

03095



Universidad Nacional Autónoma de México  
Programa de Posgrado en Ciencias de la Tierra

---

Tectonic implications of geomorphologic  
and structural characteristics  
of the Morelia–Acambay fault system,  
central Trans-Mexican Volcanic Belt.

TESIS  
Doctorado en Ciencias  
(Geología Estructural y Tectónica)

*Ewa Szyndkaruk*



Universidad Nacional  
Autónoma de México



**UNAM – Dirección General de Bibliotecas**  
**Tesis Digitales**  
**Restricciones de uso**

**DERECHOS RESERVADOS ©**  
**PROHIBIDA SU REPRODUCCIÓN TOTAL O PARCIAL**

Todo el material contenido en esta tesis esta protegido por la Ley Federal del Derecho de Autor (LFDA) de los Estados Unidos Mexicanos (México).

El uso de imágenes, fragmentos de videos, y demás material que sea objeto de protección de los derechos de autor, será exclusivamente para fines educativos e informativos y deberá citar la fuente donde la obtuvo mencionando el autor o autores. Cualquier uso distinto como el lucro, reproducción, edición o modificación, será perseguido y sancionado por el respectivo titular de los Derechos de Autor.

ESTA TESIS NO SALE  
DE LA BIBLIOTECA

... hizo a la Dirección General de Bibliotecas de la  
UNAM a difundir en formato electrónico e impreso el  
contenido de mi trabajo recepcional.

NOMBRE: EWA ILONA

SZYNKARUK

FECHA: 22.03.2004

FIRMA: Ewa Szykaruk

*Rodzicom i Ani*

## Contents

List of figures, tables and abbreviations .....	v
Agradecimientos.....	vii
Resumen .....	ix
Abstract .....	xi
1. Introduction .....	1
1.1 Does the basement of the volcanic arc influence the present-day topography and intra-arc fault pattern? .....	3
1.2 What is the kinematics of the intra-arc faulting: extension, strike-slip or both? .....	4
1.3 What drives the intra-arc faulting? .....	5
1.4 Is morphostructural analysis useful in a youthful volcanic terrain? .....	5
2. Geological setting of the Morelia–Acambay fault system.....	7
2.1 Previous work .....	7
2.2 Stratigraphy .....	8
2.2.1 <i>Pre-volcanic basement</i> .....	8
2.2.2 <i>Sierra Madre Occidental to transitional volcanic units</i> .....	12
2.2.3 <i>TMVB volcanic units</i> .....	12
2.2.4 <i>Fluviolacustrine and surficial deposits</i> .....	13
3. General information and basic topographic features .....	15
3.1 Study area .....	15
3.2 Major MAFS faults.....	15
3.3 Segmentation of the MAFS: major tectono-topographic domains .....	16
4. Materials and methods.....	21
4.1 Digital elevation model (DEM) and digital vector data: morphometric analysis .....	21
4.1.1 <i>Shaded images: searching for topographic lineaments</i> .....	21
4.1.2 <i>Longitudinal river profiles</i> .....	22
4.1.3 <i>Elevation map and topographic profiles</i> .....	22
4.1.4 <i>Relief map</i> .....	22
4.1.5 <i>Slope gradient map</i> .....	22
4.1.6 <i>Drainage density map</i> .....	23
4.1.7 <i>Fault scarp and lineament density maps</i> .....	23
4.2 Aerial photographs and field data: geomorphologic mapping.....	23
4.3 Field data: structural analysis .....	24
4.4 The DEM of central Mexico: topographic profiles across the volcanic arc and its vicinity .....	25
5. Results .....	27
5.1 Topography of the Morelia-Acambay fault system .....	27
5.1.1 <i>Fault scarp and lineament orientation</i> .....	27

5.1.2 Longitudinal river profiles.....	28
5.1.3 Distribution of morphometric values.....	30
5.1.4 Morphometry of the tectono-topographic domains .....	37
5.1.5 Distribution of landforms .....	38
5.1.6 Fault scarp degradation.....	42
5.2 Structural geology .....	43
5.2.1 Fault geometry and associated strata at outcrop scale.....	43
5.2.2 Normal, strike-slip and reverse faults at outcrop scale.....	44
5.2.3 Strata attitude: a summary (regional variation).....	49
5.2.4 Fault kinematics .....	51
5.3 Topography across the Trans-Mexican Volcanic Belt, and the location of the intra-arc faulting .....	59
6. Discussion .....	61
6.1 Active fault systems .....	61
6.1.1 Fault pattern within the central TMVB .....	61
6.2 Tectono-topographic remodeling of the central TMVB .....	62
6.3 Preliminary MAFS chronology in the westernmost study area .....	63
6.4 MAFS subsurface geometry and slip rates .....	64
6.4.1 Magnitude of displacements .....	64
6.4.2 Listric versus planar fault geometry.....	65
6.4.3 Modeled structural cross-sections.....	66
6.4.4 Slip rates.....	68
6.5 Kinematics of deformation .....	68
6.5.1 Temporal and spatial relation between contractional and extensional structures.....	68
6.5.2 Regional fault systems: initiation and kinematics .....	70
6.5.3 Coeval activity of different fault systems: What model would explain it? .....	70
6.6 What drives the deformation of the central TMVB? .....	73
6.7 Advantages and disadvantages of applied morphostructural analysis in the central TMVB.....	75
7. Conclusions .....	79
8. Reference list.....	81
<b>Appendix 1</b> An exercise in combining and classifying morphometric maps: factor and principal component analysis, mean of normalized morphometric maps, continuous classification.....	89
<b>Appendix 2</b> Filters used for calculation of shaded relief images.....	97
<b>Appendix 3</b> Calculation of depth to detachment .....	99
<b>Appendix 4</b> Structural stations listing.....	101

## List of figures, tables and abbreviations

### Figures

Fig. 1. (A) Tectonic outline map of central Mexico. (B) Shaded relief image of the vicinity of the study area	2
Fig. 2A. Geologic map of the study area	9
Fig. 2B. Comparison of stratigraphic columns west, east and at Los Azufres caldera	11
Fig. 3. Shaded relief images of the study area	17, 19
Fig. 4. (A) Rose diagram of fault scarp traces. (B) Rose diagram of lineament traces	28
Fig. 5. Longitudinal river profiles	29
Fig. 6. Elevation and relief maps	31
Fig. 7. Topographic profiles	33
Fig. 8. Slope gradient and drainage density maps	35
Fig. 9. Fault scarp density and lineament density maps	39
Fig. 10. Distribution (histograms) of elevation and relief values at each tectono-topographic domain	41
Fig. 11. Strata tilt and roll-over structures at western Cuitzeo fault	45
Fig. 12. Cross-cutting reverse and normal fault planes at Jaripeo fault	46
Fig. 13. Examples of subhorizontal strata near fault scarps east of Los Azufres caldera	47
Fig. 14. Examples of Quaternary contractional structures	48
Fig. 15. NW-striking, oblique-normal faults displacing the base of Holocene soil	49
Fig. 16. Striae superposition indicating first lateral and then normal faulting, and late Quaternary cinder cones displaced by normal faults	50
Fig. 17. Measured strata attitude and fault planes without striae	52
Fig. 18. Measured fault slip planes with striae	53-55
Fig. 19. Rose diagrams illustrating distribution of strikes of fault slip planes (separated into right-lateral, left-lateral, reverse, and normal)	57
Fig. 20. Rose diagrams illustrating distribution of strikes of kinematic axes (time-dependent)	58
Fig. 21. Shaded relief image of central Mexico	59
Fig. 22. N-S Topographic profiles across the Trans-Mexican Volcanic Belt	60
Fig. 23. Throw / length scatter diagram of major faults	65
Fig. 24. Structural cross-sections	67
Fig. 25. Rose diagram illustrating distribution of strikes of (A) fault and lineament traces (structures visible at map scale), and (B) striated fault planes (structures visible at outcrop scale)	69
Fig. 26. (A) Illustration of releasing and restraining bend at a fault with strike-slip component of motion. (B) Stereoplot of a fault pattern predicted in 3-D strain	71
Fig. 27. Plate configuration and volcanic arc location in the Oligocene, the middle/late Miocene, and present	76
Fig. 28. Appendix 1: Value distributions (histograms) of elevation, relief, and slope gradient maps	90
Fig. 29. Appendix 1: Color composites of principal components and factors	91
Fig. 30. Appendix 1: (A) Unsupervised classification (clustering) of factor maps. (B) Supervised classification of factor maps. (C) Means of normalized morphometric maps	93
Fig. 31. Appendix 3: Graphic illustration of the calculation of detachment depth of a listric normal fault	99

### Plates

Loose illustrations included at the end of this work.

Plate 1. Location of the main topographic and geologic features of the study area (transparency film that can be overlaid on the other study area maps).

Plate 2. Major topographic lineaments.

Plates 3-7. Geomorphologic maps of the study area.

Plate 8. Explanation of geomorphologic maps.

## Tables

Tab. 1. Correlation coefficients between morphometric maps .....	38
Tab. 2. Morphologic features at the main fault scarps.....	43
Tab. 3. Results of kinematic analysis of striae data.....	56
Tab. 4. Friction coefficient-dependent stress field solution for complete fault slip data set collected at the study area, (obtained with SoftStructure of Z. Reches) .....	72
Tab. 5. Appendix 1: Transformation coefficients (loadings) between elevation, relief and slope gradient maps, and the principal components.....	90
Tab. 6. Appendix 1: Transformation coefficients (loadings) between elevation, relief and slope gradient maps, and the factor maps .....	90
Tab. 7. Appendix 1: Correlation coefficients between the factor maps.....	90
Tab. 8. Appendix 4: Structural stations sorted according to site number .....	101
Tab. 9. Appendix 4: Structural stations sorted according to age of displaced rocks .....	105

## Abbreviations

B&R – Basin and Range (extensional province)  
FS – fault system  
MAFS – Morelia–Acambay fault system  
MGVF – Michoacán–Guanajuato volcanic field  
SMO – Sierra Madre Occidental  
TMVB – Trans-Mexican volcanic belt



## Agradecimientos

Este trabajo fue desarrollado gracias a la invitación de mi Tutor, el Dr. Víctor Hugo Garduño Monroy, a participar en sus proyectos de investigación de la tectónica del fallamiento intra-arco en el centro de México. Durante el trabajo de campo que hicimos juntos aprendí a distinguir y a entender los rasgos de la deformación activa. Me da mucho gusto reconocer que las discusiones que tuvimos en éstas y muchas otras ocasiones me permitieron formar buena parte de las ideas, expuestas en esta tesis. Mil gracias por el apoyo académico incondicional, así como por la hospitalidad y la compañía de la familia Garduño–Israde durante mis estancias en Morelia.

Mi aprendizaje de los aspectos teóricos del proceso de fallamiento, en buena medida es producto de las discusiones, que tuve suerte tener con el Dr. Gustavo Tolson, quien además nunca se cansó de atender mis preguntas e inquietudes. Estas discusiones y su apoyo académico constante fueron fundamentales para mi formación a lo largo de estos años. Gracias también por la paciencia para revisar mis manuscritos y por ayudarme a entender y enfrentar toda clase de procesos y sucesos, que me han tocado vivir en la Universidad Nacional.

La parte geomorfológica de este trabajo fue elaborada bajo la tutela del Dr. Gerardo Bocco. Aprecio y agradezco su empeño en guiarme a través de los temas para mi nuevos y fascinantes. Otras personas cuya ayuda fue muy importante para esta parte del trabajo son el Dr. Mario Arturo Ortiz Pérez y el Dr. Manuel Mendoza Cantú.

Este trabajo se benefició enormemente de los comentarios y las discusiones con los demás sinodales: el Dr. Jorge Aranda Gómez, el Dr. Oscar Campos Enríquez, la Dra. Lucia Capra Pedol, el Dr. Duncan Keppie con quien estoy en deuda por su revisión exhaustiva y cuidadosa que mejoró considerablemente el manuscrito, y el Dr. Max Suter cuya revisión de mi trabajo predoctoral me ayudó a mantener el rumbo. Al Dr. Luca Ferrari le agradezco haberme proporcionado la base de datos digitales de fechamientos isotópicos en México y al Dr. Juan Contreras su ayuda con la modelación de secciones estructurales.

Agradezco sobremanera a todos los que me acompañaron durante mi trabajo de campo: a Edgar Angeles con quien hicimos buena parte del trabajo y a cuya vista aguda le debo el descubrimiento de algunos de los afloramientos más importantes, a Eleazar Arreygue, Angel David Hurtado, Lucy Mora, Marco Rubio y Margarita Treviño.

Agradezco el apoyo logístico del Posgrado en Ciencias de la Tierra, particularmente del Dr. Oscar Campos Enríquez, Norma Bravo, Araceli Chaman y Mónica Salgado del Instituto de Geofísica, Enrique Gonzalez Torres del Instituto de Geología y las demás personas que cuya buena voluntad y amabilidad ha hecho grata mi estancia en la Universidad Nacional. Agradezco además el apoyo del personal de la Universidad Michoacana de san Nicolás de Hidalgo en Morelia y a la Gerencia de Proyectos Geotermoeléctricos de la Comisión Federal de Electricidad.

Este trabajo fue financiado de los proyectos del Consejo Nacional de Ciencia y Tecnología Nos. 28764-T y 37334-T a cargo del Dr. Víctor Hugo Garduño Monroy, de los cuales recibí becas y apoyo; y del proyecto del Programa de Apoyo a los Estudios de Posgrado de la UNAM No. 107302 a mi cargo. También recibí beca de la Dirección General de Estudios de Posgrado de la UNAM.

Mi estancia en México ha sido inolvidable gracias a la generosa compañía de mis amigos. Entre ellos no puedo dejar de mencionar a Elisa Fitz, Andrea Herre, Ania Jurek, Lupita Maldonado, Lucy Mora, Carlos Ortega, Laura Rosales, Marco Rubio, Monika Żukowska, las familias Juárez-Álvarez y Casas-Álvarez. A ellos y a todos los que han compartido su tiempo conmigo mil gracias.

A mis queridos Padres y a mi hermana Ania, quienes siempre me han apoyado y fortalecido, aún cuando mis decisiones significaban separaciones largas y angustiosas, les expreso mi suma gratitud y admiración. Agradezco a Marcin por compartir e impulsar mi vida.

## Resumen

El estudio geomorfológico y estructural, realizado en la parte central del Cinturón Volcánico Trans-Mexicano (CVTM), permitió evaluar el patrón, la geometría y la cinemática de la deformación intra-arco, así como las razones de esta deformación. Se encontró que tres sistemas regionales de fallas, con diferentes sentidos (y tazas) de movimiento deforman la parte central del Cinturón Volcánico Trans-Mexicano (CVTM) y modifican su topografía. Dos de estos sistemas – las fallas de la provincia de Cuencas y Sierras orientadas NNW-SSE y fallas orientadas NE-SW – son anteriores al arco volcánico y controlan contrastes morfométricos mayores así como los mayores dominios tectono-topográficos. Estos últimos a su vez están siendo fragmentados por las fallas más recientes y más activas – el sistema de fallas Morelia–Acamabý (SFMA), orientado W-E.

La coexistencia de tres sistemas de fallas activas implica que la región experimenta una deformación en 3-D, donde planos de debilidad predefinidos controlan el patrón de deformación. Discontinuidades de basamento pre-existentes aparentemente controlan fallas más antiguas. Debilitamiento termal debido a la actividad volcánica controla la orientación del SFMA

La geometría sub-superficial del SFMA cambia de un lado de la caldera de Los Azufres al otro. Hacia oeste el sistema se compone de fallas lítricas con la zona de despegue poco profunda. Hacia el este se tienen fallas de alto ángulo que (dada su longitud) probablemente cortan toda la parte frágil de la corteza. Diferente geometría de las fallas puede deberse a diferente litología del subsuelo (las rocas volcánicas sobreyacen una secuencia de capas rojas con fuertes contrastes litológicos hacia el oeste y una secuencia de metasedimentos relativamente uniformes hacia el este de Los Azufres), diferente posición topográfica de fallamiento (cortando laderas norte del arco en la parte occidental y cortando su porción más elevada en la parte oriental), o ambos.

Estructuras contraccionales y extensionales coexisten en una relación espacio-temporal muy estrecha, a lo largo de la existencia del arco. Esto se debe al alargamiento regional, orientado NNW-SSE, acompañado por el acortamiento subordinado, orientado NNE-SSW. La convergencia oblicua a lo largo de la Trinchera de Acapulco así como la geometría y dinámica de la subducción parecen ser el único motivo plausible del patrón de deformación observado en la parte central del CVTM.

Finalmente, este trabajo demuestra, que el uso de investigación morfoestructural en un arco volcánico activo permite detectar patrones de deformación inaccesibles con tan solo métodos geomorfológicos o estructurales.

## Abstract

Geomorphologic and structural study of the central Trans-Mexican Volcanic Belt (TMVB) allowed the evaluation of the geometry and kinematics of the fault pattern deforming the region, as well as the reasons for these phenomena. It was found that three regional fault systems, with different senses (and rates) of motion deform the central Trans-Mexican Volcanic Belt (TMVB) and modify its topography. Two of these systems – the NNW-striking Basin and Range faults and the NE-striking faults – pre-date the volcanic arc and control major morphometric contrasts, and major tectono-topographic domains of the region. These domains are being fragmented by the youngest and most active faults – the E-striking Morelia–Acambay fault system (MAFS).

Coeval activity of the three fault systems implies that the region is deforming in 3-D strain, where not-randomly oriented planes of weakness control the deformation pattern. Pre-existing basement discontinuities apparently control the older faults, and thermal weakening of the crust due to volcanic activity controls the orientation of the arc-parallel MAFS.

The geometry of the MAFS changes across the Los Azufres caldera. To the west, the system is made up of listric faults with a shallow detachment zone, whereas to the east it is made up of planar faults, most probably (given their length) cutting the entire brittle upper crust. The different fault geometries may be due to different basement lithology (volcanic rocks overlie red beds with strong lithologic contrasts to the west, and relatively uniform metasediments to the east of Los Azufres), different topographic location of faulting within the arc (on its northern slopes to the west of Los Azufres, and cutting its most elevated portion to the east of it), or both.

Contractional and extensional structures coexist in close space-time relationship in the central TMVB and during the entire time-span of the arc. This is due to the oblique, NNW-SSE oriented, regional stretching, accompanied by the subordinate NNE-SSW oriented shortening. Oblique convergence at the Acapulco Trench and subduction geometry and dynamics seems to be the only plausible main genesis of the deformation pattern observed in the central TMVB.

Finally, this work proves that applying morphostructural investigation to a youthful volcanic arc permits detection of deformation patterns inaccessible by structural or geomorphic tools alone.

# 1. Introduction

Intra-arc faulting affecting the Trans-Mexican Volcanic Belt (TMVB) – an active volcanic arc extending from the Pacific coast to the Gulf of Mexico along *ca.* 20° parallel N (Fig. 1) – is the key to understand the tectonics of central Mexico. The main question here is the nature of interaction (or lack of interaction, as argued by some) between subduction along Mexican Pacific coast and the intra-arc deformation; *i.e.*, the reasons for this deformation, which has been subject to long and hot debate (Menard, 1955; Mooser *et al.*, 1958; Demant, 1978; Cebull and Shurbet, 1987; Nixon *et al.*, 1987; Ferrari *et al.*, 1990, 1994a, 1999, 2001; Suter *et al.*, 1992, 2001; Ramírez-Herrera *et al.*, 1994; Soler-Arechalde, 1997; Márquez, 1999a,b; Wallace and Carmichael, 1999; Langridge *et al.*, 2000; Ego and Ansan, 2002; Verma, 1999, 2000, 2002; Ferrari, 2004a; and many others). Understanding these reasons would broaden our knowledge about the processes not only in this particular area, but possibly also in volcanic arcs elsewhere. Shedding light on this problem requires thorough understanding of geometry, kinematics and evolution of the fault pattern affecting the arc.

In the central, E-trending TMVB the main component of the intra-arc faulting is the arc-parallel Morelia–Acambay fault system (MAFS). Earliest sediments associated with these faults are of the upper Miocene age [*ca.* 6 Ma (Israde-Alcantara and Garduño-Monroy, 1999; Suter *et al.*, 2001), and historic seismicity registered on some of the MAFS faults (Urbina and Camacho, 1913; Astiz, 1980) proves its ongoing activity. Hence, this fault system modifies the topography, and controls deformational history and most of the sedimentary record of the central TMVB since the late Miocene *i.e.*, during the time-span of the arc activity (Ferrari *et al.*, 1994b).

However, NNW- and NE-trending regional fault systems have also been recognized within the central TMVB (Demant, 1978; Campa and Coney, 1983; De Cserna *et al.*, 1988; Pasquaré *et al.*, 1991; Garduño and Gutierrez, 1992; Suter *et al.*, 1992; Ferrari *et al.*, 1994a; Huizar-Álvarez *et al.*, 1997; García-Palomo *et al.*, 2000, 2002; Campos-Enríquez *et al.*, 2003). The interplay between these fault systems, and the contribution which they make to deformation is another focus of this work.

This work addresses a few questions regarding the deformation process affecting the central TMVB, which can be evaluated by structural and geomorphologic methods. Below I present these questions, describing published answers and discussing unclear and/or unanswered aspects, which are the reason for this study. The last subsection of Introduction treats an additional problem studied in this work: is it reasonable to apply morphostructural tools to a very complex setting such as a youthful volcanic terrain? If so, what are we likely to gain using such approach?

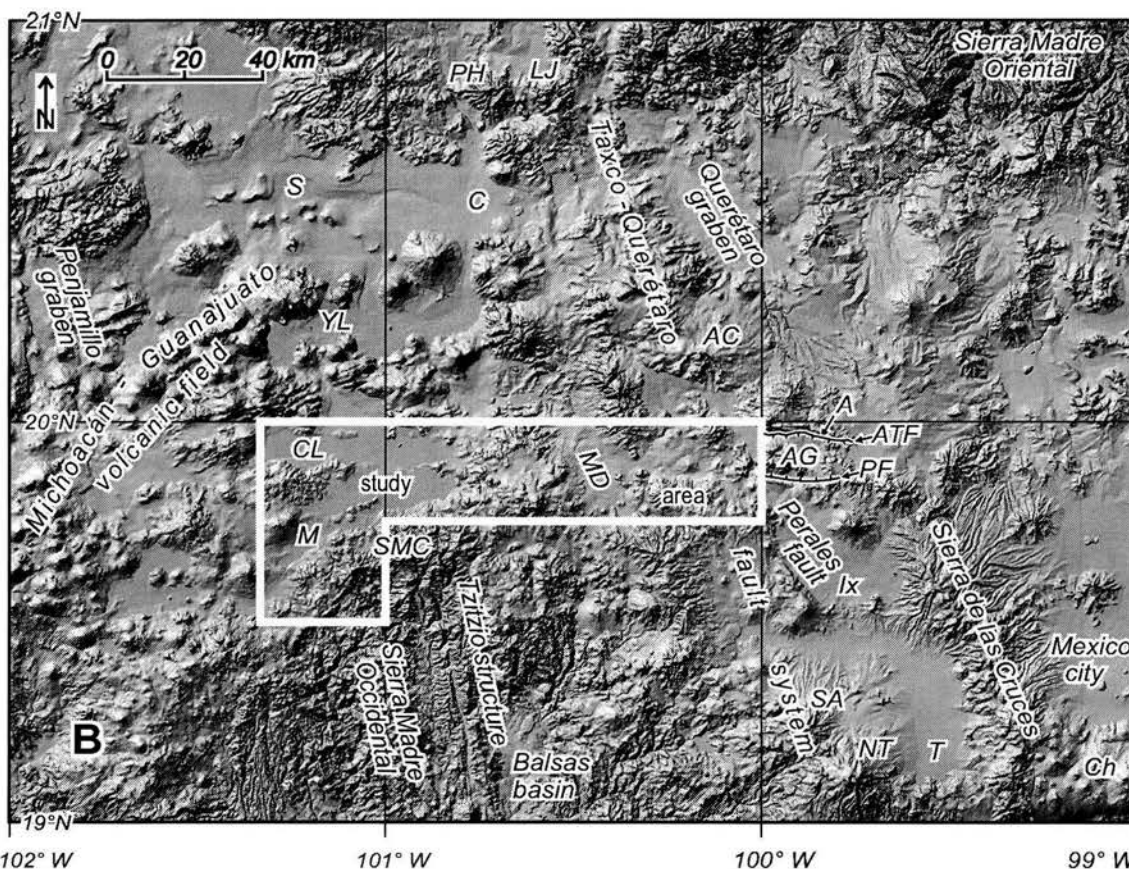
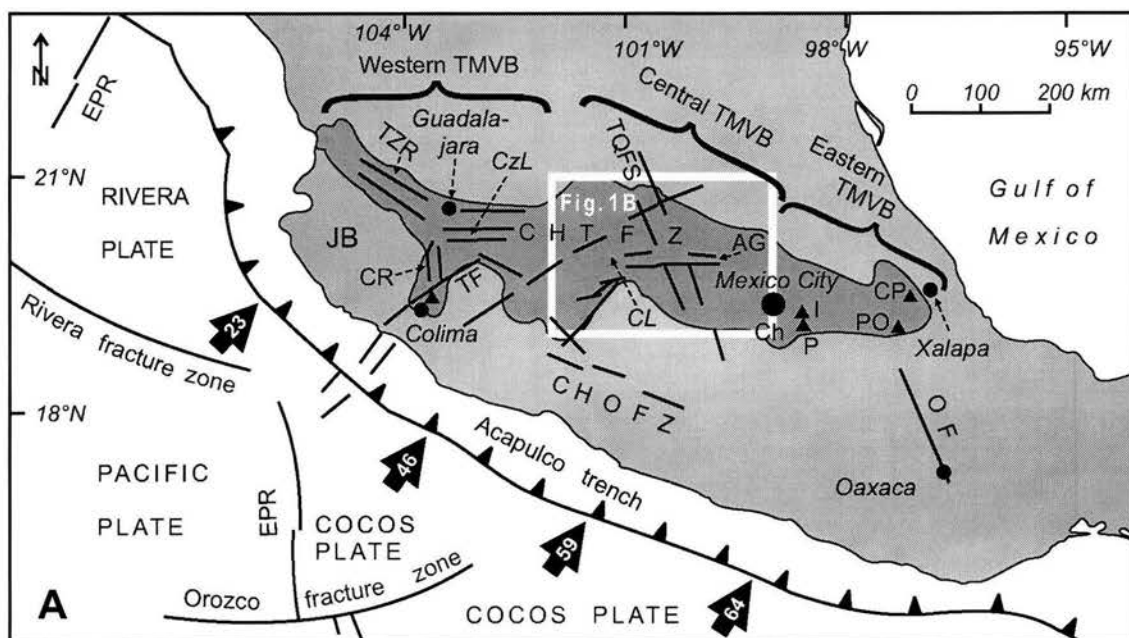


Figure 1. **(A)** Tectonic outline map of central Mexico. Thick black arrows mark relative convergence rates (in mm/yr) between oceanic and continental plates. CzL Chapala lake, CL Cuitzeo lake, JB Jalisco block. Major fault systems are: TZR Tepic-Zacoalco rift, CR Colima rift, TF Tamazula fault, CHTFZ Chapala-Tula fault zone, AG Acambay graben, TQFS Taxco-Querétaro fault system, CHOFZ Chapala-Oaxaca fault zone, Ch Chichinautzin volcanic field, P Popocatepetl volcano, Ixtachihuatl range, PO Pico de Orizaba (Citlaltepetl), CP Cofre de Perote, OF Oaxaca fault, EPR East Pacific Rise. The Trans-Mexican Volcanic Belt is marked in dark grey. White rectangle marks the area of Fig. 1B. **(B)** Shaded relief image of the vicinity of the study area (the latter outlined in white). CL, AG and Ch as above, PH Palo Huerfano volcano, LJ La Joya volcano, S Salamanca, C Celaya, YL Yuriria lake, AC Amealco caldera, MD Maravatío depression, A Acambay, ATF Acambay-Tixmadejé fault, PF Pastores fault, M Morelia, SMC Sierra Mil Cumbres, Ix Ixtlahuaca, SA San Antonio volcano, NT Nevado de Toluca volcano, T Toluca. Modified from: Pasquaré et al. (1991), Ortega-Gutiérrez et al. (1992), Suter et al. (1995), Aguirre-Díaz and McDowell (2000), Ego and Ansan (2002), Garduño-Monroy, personal communication.

## 1.1 Does the basement of the volcanic arc influence the present-day topography and intra-arc fault pattern?

The mean thickness of the crust below the central TMVB, according to seismic (Valdés and Meyer, 1996; Campillo *et al.*, 1996; Rivera-Hernandez and Ponce, 1986; Iglesias *et al.*, 2001), and gravimetric data (Urrutia-Fucugauchi, 1986; Molina-Garza and Urrutia-Fucugauchi, 1993; Urrutia-Fucugauchi and Flores-Ruiz, 1996; Flores-Ruiz, 1997; Campos-Enríquez and Sánchez-Zamora, 2000) is about 40 km. The crust thins both toward the west and east of the arc to attain *ca.* 10 km below the Jalisco block close to the Pacific coast, and *ca.* 15 km close to the Gulf of Mexico (Urrutia-Fucugauchi, 1986; Molina-Garza and Urrutia-Fucugauchi, 1993; Urrutia-Fucugauchi and Flores-Ruiz, 1996; Flores-Ruiz, 1997) (Fig. 1). According to Campos-Enríquez and Sánchez-Zamora (2000), the upper brittle crust below the central TMVB is *ca.* 20 km thick, and the lower crust reaches the depth of *ca.* 45 km. A low velocity zone (that would signify partial melting) is lacking at the interface between the two (Gomberg and Masters, 1988, Campillo *et al.*, 1996), but instead may be present at the base of lower crust (Campos-Enríquez and Sánchez-Zamora, 2000).

The TMVB is superimposed on an older structural grain that constitutes the basement of the arc. This basement is apparently made up of Guerrero terrain to the west of the NNW-striking (arc-transverse) Taxco–Querétaro fault system (Taxco–Querétaro FS) (Demant, 1978; Campa and Coney, 1983; Pasquaré *et al.*, 1991; Garduño and Gutierrez, 1992; Ferrari *et al.*, 1994a) (Fig. 1), and Oaxaquia microcontinent to the east of it (Ortega-Gutierrez *et al.*, 1995). Notably, outcrops of pre-volcanic basement within the central TMVB are associated with the Taxco–Querétaro FS and also NNW-striking Tzitzio structure (Pasquaré *et al.*, 1991; Mooser *et al.*, 1996) (Fig. 1). Several volcanic centers (La Joya volcano, Amealco caldera, San Antonio and Nevado de Toluca volcanoes) are aligned along the former (Johnson and Harrison, 1990; Suter *et al.*, 1992; Valdéz-Moreno *et al.*, 1998; García-Palomo *et al.*, 2000) (Fig. 1). Gravimetric data of Urrutia-Fucugauchi and Flores-Ruiz (1996) and Flores-Ruiz (1997) also suggest major crustal discontinuity across the Taxco–Querétaro FS. According to them, the crust thins from 40-50 km east of this fault system, to 30-40 km to the west of it. Campos-Enríquez and Garduño-Monroy (1995) attributed the thinner crust below the TMVB west of the Taxco–Querétaro FS, to the normal faulting affecting central and western portions of the arc. Nonetheless, this normal faulting extends about 150 km to the east of the Taxco–Querétaro FS.

The Taxco–Querétaro FS is considered part of the Basin and Range extensional province (B&R) (Suter *et al.*, 1995b), the latter active in the USA and northern Mexico between the Oligocene and present (Henry and Aranda-Gomez, 1992, 2000; Suter and Contreras, 2002). Faults of this system are found to the north and south of the TMVB (Fig. 1). García-Palomo *et al.* (2000) considered that the Taxco–Querétaro FS was initiated during latest Oligocene. Nonetheless, its location suggests that it might be a reactivated terrane boundary (see above). Most authors agree that Taxco–Querétaro FS was active during the middle Miocene (Pasquaré *et al.*, 1987b, 1988, 1991; Ferrari *et al.*, 1990; Henry and Aranda-Gomez, 1992). At present, faults of this system are active at the northern edge of the volcanic arc (*i.e.* Querétaro graben, Fig. 1), simultaneously with E-striking faults (Aguirre-Díaz *et al.*, 2003). Although Alaniz-Alvarez *et al.* (1998) have suggested that faults with *ca.* N-S orientation may still be active within the TMVB, it remains to be proven if such faults are active within the region deformed by the E-striking Morelia–Acambay fault system (MAFS). If this were the case, faults pre-dating the appearance of the volcanic arc would influence the deformation pattern affecting the arc.

Another set of arc-oblique faults in the central TMVB strike NE-SW. They underlie Mexico City [Tenochtitlán shear zone of De Cserna *et al.* (1988)], and extend to northeast of it (Huizar-Álvarez *et al.*, 1997; García-Palomo *et al.*, 2002; Campos-Enríquez *et al.*, 2003). They were also documented in the vicinity of the Nevado de Toluca volcano (García-Palomo *et al.*, 2000). Moreover, the late Quaternary cinder cones of the eastern TMVB form NE-striking alignments (Siebert and Carrasco-Núñez, 2002). In the westernmost portion of the study area, and further to the west of it in the Michoacán–Guanajuato volcanic field (MGVF) (Fig. 1), faults with this orientation control cinder cone alignments (Connor, 1990). This structural trend (underlying the Michoacán–Guanajuato volcanic field) also seems to separate the Chapala half-graben from the Cuitzeo half-graben, marking the shift in the position of their axes (Israde-Alcantara and Garduño-Monroy, 1999, their Fig. 1) (Fig. 1). Further to the west, the NE-striking faults were documented between Chapala lake and Colima (Fig. 1) (Garduño-Monroy *et al.*, 1998). Furthermore, the aeromagnetic maps of the

central TMVB (CRM, 1996, 1998) show alignments of magnetic anomalies oriented NE-SW in the western portion of the study area. According to Israde-Alcantara and Garduño-Monroy (1999), the NE-striking faults were formed as left-lateral strike-slip faults during the middle-late Miocene (*i.e.*, are almost contemporaneous with the onset of the TMVB), and were reactivated with normal sense of movement during the early Pliocene. To the east of the MAFS, these faults are still active (García-Palomo *et al.*, 2002). Again, it remains to be proven, if such faults are active within the area deformed by the MAFS.

In older works, the E-striking MAFS was also proposed to be a reactivated, pre-TMVB basement structure (*e.g.*, Mooser, 1969; Cebull and Shurbet, 1987). However, field-based studies suggest that the MAFS originated during the TMVB activity. Pasquaré *et al.* (1988) state that the formation of the MAFS took place in the Pliocene. Ferrari *et al.* (1990) state that these faults appeared in early Pleistocene, Ferrari *et al.* (1994a) place initiation of the MAFS in the middle Miocene, and Israde-Alcantara and Garduño-Monroy (1999), from the age of syntectonic deposits believed to be associated with the MAFS, consider that it initiated in the late Miocene at *ca.* 6-8 Ma. Suter *et al.* (2001) calculate initiation of the Acambay-Tixmadejé fault (one of the largest MAFS faults) (Fig. 1) at *ca.* 6 Ma, based on its Quaternary slip rate (Langridge *et al.*, 2000), and total displacement estimated to be double of the scarp height.

Simultaneous activity of three different fault systems within the central TMVB, if it exists, would indicate that we have to reconsider existing models of deformation pattern affecting the arc, which would have to be explained with 3D strain model. Such deformation pattern would also have an impact on the tectono-topographic architecture of the central TMVB.

## 1.2 What is the kinematics of the intra-arc faulting: extension, strike-slip or both?

A few studies claim that the MAFS was formed as left-lateral faults, and then reactivated as normal faults (Ferrari *et al.*, 1990, 1994a; Israde-Alcantara and Garduño-Monroy, 1999) or gradually transformed to normal faults (Pasquaré *et al.*, 1988). The present-day kinematics of the MAFS was inferred to be either purely dip-slip (normal), predominantly strike-slip (usually left-lateral), or normal-oblique slip.

The conclusion that the MAFS is generally an extensional (dip-slip) feature was presented by Suter *et al.* (1995b) on the basis of (limited) fault striae data. Langridge *et al.*, (2000) on the basis of paleoseismologic data (trenching across the Acambay fault) state that motion of Acambay-Tixmadejé fault (Fig. 1) is dip-slip (extension is NNE oriented), and lateral motion only occurs where master fault deviates from its usual WNW-ESE strike. Suter *et al.* (1992, 2001), on the basis of striae and focal mechanisms of earthquakes, consider the MAFS an extensional fault system with minor, left-lateral component.

Ramírez-Herrera (1994) and Ramírez-Herrera *et al.*, (1994) on the basis of morphologic data (landforms associated with fault scarps) state that the MAFS is “...consistent with systems of faults which have experienced transtensive, large-scale, left-lateral shear...”. Although stressing the lateral component of motion, these authors state, that the MAFS faults combine normal and lateral movement. Recently, Ego and Ansan (2002), on the basis of slip partitioning due to oblique convergence at Acapulco trench, conclude that the left-lateral slip rate of the MAFS should be over two times greater than the vertical slip rate. Their present-day least principal stress, obtained by inversion of intraplate earthquakes within central TMVB, is oriented *ca.* 45° to the strike of the MAFS.

These partly contradictory interpretations of the kinematics of the MAFS, and published data showing apparent coexistence of normal and strike-slip faults in the central TMVB suggest a series of questions: (i) Are normal and strike-slip faults truly coeval? (ii) If so, what model(s) would explain their coexistence? (iii) If they are not, can we clearly separate strike-slip and normal faulting in time and/or space? (iv) Except for strike-slip faults, are there other contractional structures? If so, what do they tell us? These questions are addressed in this work.

### 1.3 What drives the intra-arc faulting?

To answer the question stated in the title of this section we first need to answer the long-debated problem: does the location of the TMVB depend on the structure of the upper plate or does it depend on the geometry of the subducted slab? This problem provokes much discussion, because the TMVB seems to be an unusual volcanic arc: its greater portion is *ca.* 20° oblique to the subduction zone (Fig. 1), and oceanic-island and mid-ocean ridge type basalts were intruded within the arc (Ferrari and Rosas-Elguera, 1999; Ferrari *et al.*, 20001; Márquez *et al.*, 1999a).

The idea that the structure of the upper plate, and particularly the E-striking intra-arc faults, control the location of the TMVB was advocated by Johnson and Harrison (1989, 1990) and Ferrari *et al.* (1994a). Márquez *et al.* (1999a,b), Márquez and De Ignacio (2002) and Verma (1999, 2000, 2002), whose argument is made on geochemical basis, even state that the TMVB is unrelated to subduction.

Nonetheless, a growing body of evidence makes it clear that the peculiarities of the TMVB location and geochemistry can be explained by subduction process peculiarities. In particular, Pardo and Suárez (1995), on the basis of subduction earthquake distribution, concluded that the dip of subducted slab shallows toward the east, hence the slab reaches the depth where melting occurs progressively further away from the trench (although lack of subduction earthquakes below the TMVB makes somewhat problematic the reconstruction of subduction geometry below the arc). Guzman-Speziale (2003) presented a geometric argument supporting the shallowing of the subduction angle of Cocos plate toward the east. Geochemical evidence coupled to tectonic evolution of this part of Mexico shows that oceanic-island and mid-ocean ridge type basalts, encountered within the TMVB, can be explained by either (1) slab window formation: part of a subducted slab tears off and sinks, so hot asthenospheric mantle from below the slab flows upward through the slab window (Ferrari, 2004a), or (2) by melting and/or advection of asthenospheric mantle from behind the arc (Wallace and Carmichael, 1999; Ferrari *et al.*, 2001, Gómez-Tuena, 2002; Gómez-Tuena *et al.*, 2004, Siebe *et al.*, 2004). Moreover, some geochemical characteristics of the TMVB magmas indicate the effect of subduction (Cervantes and Wallace, 2000; Schaaf *et al.*, 2001).

Coupling volcanic vent distribution to fault mapping and subsurface fault geometry permits assessment of the scale and level of interaction between faulting and volcanism, (*e.g.*, such interaction might be restricted to the upper part of the crust). These in turn can contribute arguments on driving forces of faulting. This approach is used in this work.

Finally, recent works of Suter *et al.* (2001), and Ego and Ansan (2002) seek to explain the E-striking, intra-arc faults as a consequence of the TMVB existence. The former authors consider these faults to be an expression of gravitational collapse of the arc. This possibility will be investigated in this work using mean topography across the TMVB, along with published gravimetric data. Ego and Ansan (2002) conclude that the oblique convergence along the Acapulco trench leads to slip partitioning: the slip vector of subduction earthquakes is not parallel to oblique convergence vector, but instead is rotated toward normal to the trench (Fig. 1). This leaves coast-parallel, left-lateral slip component, which is released along the TMVB, because the arc is a weakness zone due to high heat flow. Data on fault kinematics presented here permit placing of constraints on this proposal.

### 1.4 Is morphostructural analysis useful in a youthful volcanic terrain?

An additional problem addressed in this work consists of applying morphostructural tools to a youthful volcanic terrain. Most morphotectonic studies expressly avoid such settings (*e.g.*, Burbank and Anderson, 2000). The reason is lithologic and bedrock age variability, which usually precludes finding a reasonably widespread, single reference level and hence precludes quantifying the deformation. Moreover, such variability makes it difficult to distinguish between tectonic and lithologic influence on topography. This means that features likely related to active tectonics must first be proven to be independent of lithology and/or bedrock age, and that quantifying deformation rates from topography is difficult or impossible.



Nonetheless, morphostructural analysis offers enough advantages over the purely structural one, to be worthwhile checking if it makes sense in a given setting. The most important of these advantages is an ability of morphostructural tools to detect active deformation obscured at the surface by sedimentation and/or young volcanism. In an active volcanic arc, where both processes are intense, such tools might detect deformation patterns inaccessible by traditional means (except geodetic studies that are unavailable in the area). Such a possibility will be explored in this work.

It also should be mentioned that, although at first sight morphostructural analysis of a young volcanic arc appears discouraging, it also offers an advantage: in such setting relative bedrock age can easily be estimated from topography (*e.g.*, from erosional degradation of cinderic cones). This provides an easy method of dating of the relative time of deformation.

## 2. Geological setting of the Morelia–Acambay fault system

### 2.1 Previous work

Early work on the seismicity and geology of the region comprising the Morelia–Acambay fault system date back to the end of XIX century (Urquiza, 1872; Ramírez and Reyes, 1873). During the second and third decade of the XX-th century more studies were conducted on seismicity, deformation, and stratigraphy of the region. Urbina and Camacho (1913) provided detailed description and mapping of the ground deformation associated with the 1912 Acambay earthquake nucleated on the Acambay fault. Flores (1920) described the stratigraphy and seismicity of the El Oro–Tlalpujahua mining district located to the east of San Miguel volcano (Plates 1, 7), and Camacho (1925) mapped faults in Morelia region. The latter author was apparently the first to point out that the regional, E-striking, normal faulting is deforming the region in question (Suter *et al.*, 2001).

Mooser (1969) made the first fault trace map of the central TMVB, Johnson and Harrison (1989, 1990) traced lineaments on Landsat images, and Martínez-Reyes and Nieto-Samaniego (1990) provided a more detailed fault trace map. Pasquaré *et al.* (1991) published geologic and tectonic map of the region. Suter *et al.* (2001) provided fault trace maps and a regional neotectonic study of the MAFS. More detailed maps and neotectonic research of the eastern portion of the MAFS are included in Suter *et al.* (1992, 1995b). Fault traces in Suter *et al.* (1992, 1995b, 2001) and fault scarps mapped in this work (Plates 3-8) bear strong resemblance, although the latter is more detailed. Pasquaré *et al.* (1988) studied the stress pattern evolution in the central TMVB. Israde (1995) and Israde-Alcantara and Garduño-Monroy (1999) studied lacustrine sequences associated with MAFS faulting in Morelia region. The first published paleoseismologic study in the region is that of Langridge *et al.* (2000) who trenched the Acambay fault.

Pasquaré *et al.* (1987a,b) conducted a regional scale morphological and structural analysis of the central sector of the TMVB, where they distinguished various erosional and depositional surfaces and related them to the volcanism and regional tectonics. Ortiz and Bocco (1989) studied morphostructural segmentation of the eastern part of the MAFS. Ortiz *et al.* (1994) provided geomorphologic evidence of tectonic displacement on normal faults between Ixtlahuaca and Toluca, to the SE of the Acambay graben (Fig. 1). Ramírez-Herrera (1990, 1994, 1998), and Ramírez-Herrera *et al.* (1994) assessed the relative activity and sense of motion of the Acambay graben faults on the basis of morphological evidence. Ramírez-Herrera's (1994) work includes

morphotectonic maps of the eastern portion of the MAFS from Maravatío depression in the west to the Acambay graben in the east (Plate 1).

Geologic mapping of the region, except the one by Pasquaré *et al.* (1991), includes those by Aguirre-Díaz (1996), and Silva-Mora (1995). Stratigraphic and petrologic work on local and regional scales were done by Fries *et al.* (1965), Ferrari *et al.* (1991), Pantoja-Alor (1994), Pradal and Robin (1994), Aguirre-Díaz (1995), Aguirre-Díaz and McDowell (2000), Aguirre-Díaz *et al.* (2000), and also as thesis projects (Silva-Mora, 1979; Dobson, 1984; Sánchez-Rubio, 1984; Carrasco-Núñez, 1988; Pradal, 1990; Aguirre-Díaz, 1993; Norato-Cortez, 1998). Ferrari *et al.* (1999) provided the compilation of the isotopic ages of volcanic rocks in central Mexico.

Geophysical investigations of the shallow crust of the MAFS region include those by Ballina-López (1987a,b), De Cserna *et al.* (1988), Copley and Orange (1991), Campos-Enríquez and Garduño-Monroy (1995), Campos-Enríquez *et al.* (1990, 2000). Comisión Federal de Electricidad also produced some geophysical data (unpublished). Soler-Arechalde (1997), and Soler-Arechalde and Urrutia-Fucugauchi (2000) presented paleomagnetic, magnetometric and gravimetric data from central TMVB.

## 2.2 Stratigraphy

### 2.2.1 Pre-volcanic basement

The oldest rocks of the study area are the upper Jurassic-lower Cretaceous (Pasquaré *et al.*, 1991) Tlalpujahua metamorphic-plutonic complex (Flores, 1920; Aguirre-Díaz *et al.*, 2000) (Fig. 2). The complex is exposed in the footwall of Venta de Bravo fault and in the southern part of the Maravatío depression where it is associated with NW-striking faults. It forms the basement of the TMVB to the east of the Los Azufres caldera (Fig. 2). This complex is composed of more or less uniform succession of greenschist-facies metasediments and metavolcanics (Flores, 1920), which belong to the Guerrero terrane of Campa and Coney (1983). The metasediments are white through yellow and brown to black schists, mainly of volcanoclastic origin, with lenses of black graphitic limestone. Andesitic, rhyolitic and mafic dikes and sills cut this sequence. The complex shows at least four deformation phases, the oldest being two generations of isoclinal and disharmonic folding formed during the Laramide orogeny (Corona-Chavez, 1999). Intensely deformed brittle-ductile shear zones cut these isoclinal folds and are cut by brittle fault planes. The latter strike NE-SW and E-W (Flores, 1920; this study).

To the west of the Los Azufres caldera, pre-volcanic basement rocks are not exposed within the study area. Nevertheless, the contemporaneous, although less metamorphosed and less deformed rocks, crop out at the Tzitzio structure to the southeast of Morelia (Figs. 1, 2). These rocks are flysch-like deposits composed of thick sequences of siltstones and calcareous siltstones with occasional beds of sandstones (Corona-Chavez, 1999).

Continental red beds of Tzitzio formation, made up of conglomerates, sandstones and siltstones with one horizon of calcareous conglomerate (Altamira-Areyán, 2002), overlie the former sequences. Although Pasquaré *et al.* (1991) assigned it to the Eocene, Altamira-Areyán (2002) obtained Paleocene pollen from the lower part of this sequence. At Tzitzio the red beds are over 1.5 km thick (Pasquaré *et al.*, 1991). To the east of Los Azufres, the red beds are lacking within the study area (the volcanic sequence directly overlies the Tlalpujahua complex (Fig. 2), although they are observed locally in close vicinity to the area [Perales fault, and to the SE of the Maravatío depression (Fig. 1)], where they are less than 40 m thick (Garduño-Monroy, Instituto de Investigaciones Metalúrgicas UMSNH, 2003, personal communication). Strong lithologic contrasts characterize this sequence.

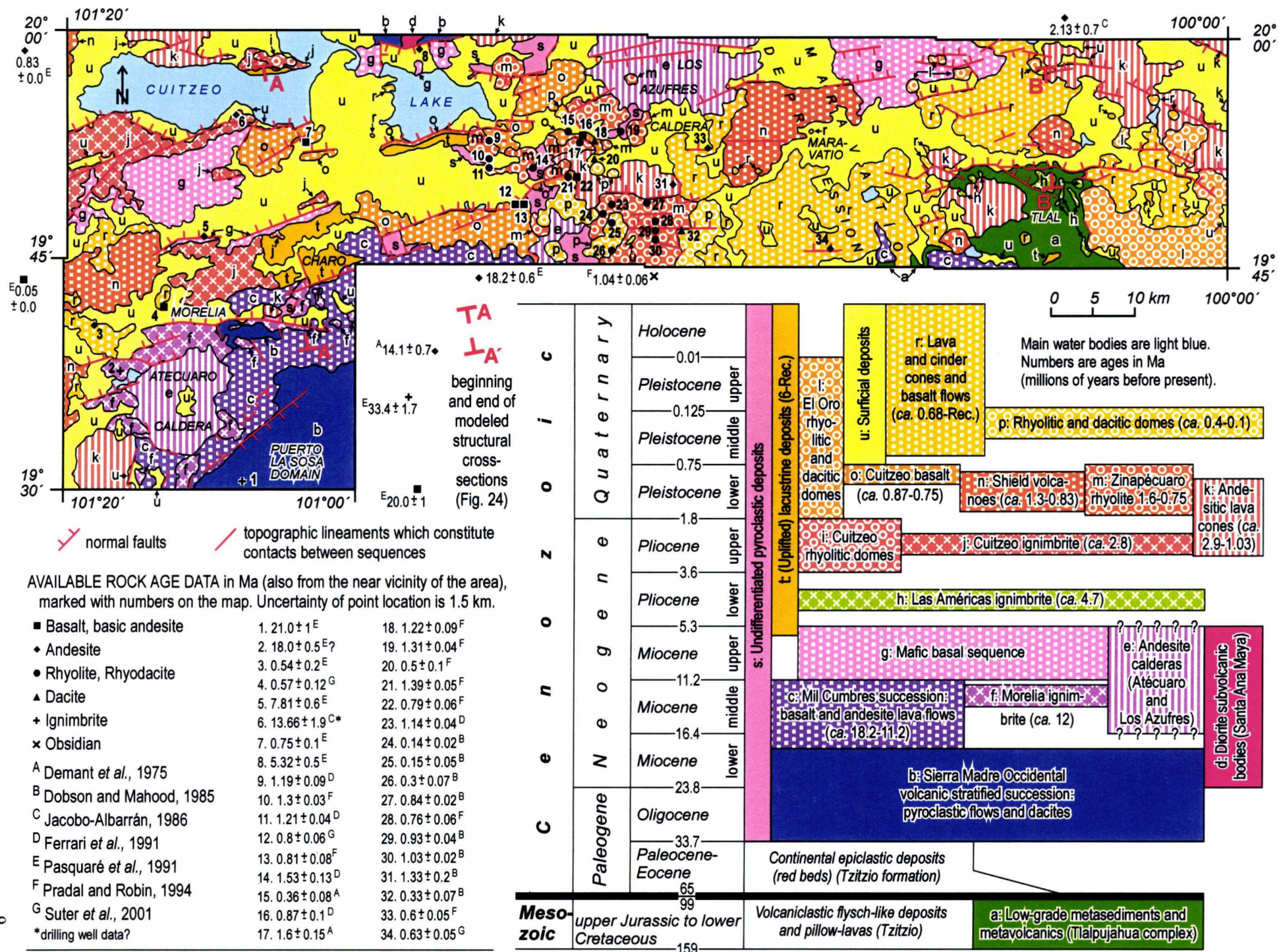


Fig. 2A. Geologic map of the study area. Sequences, whose names in the column are given in italics do not outcrop at the study area. TLAL - Tlalpujahua. Modified from: Pasquaré *et al.* (1991); Aguirre-Díaz (1996); Ferrari *et al.* (1999) and references therein (cited above); Israde-Alcantará and Graduño Monroy (1999); Altamira-Areyán (2002), M. Suter (2002), personal communication.

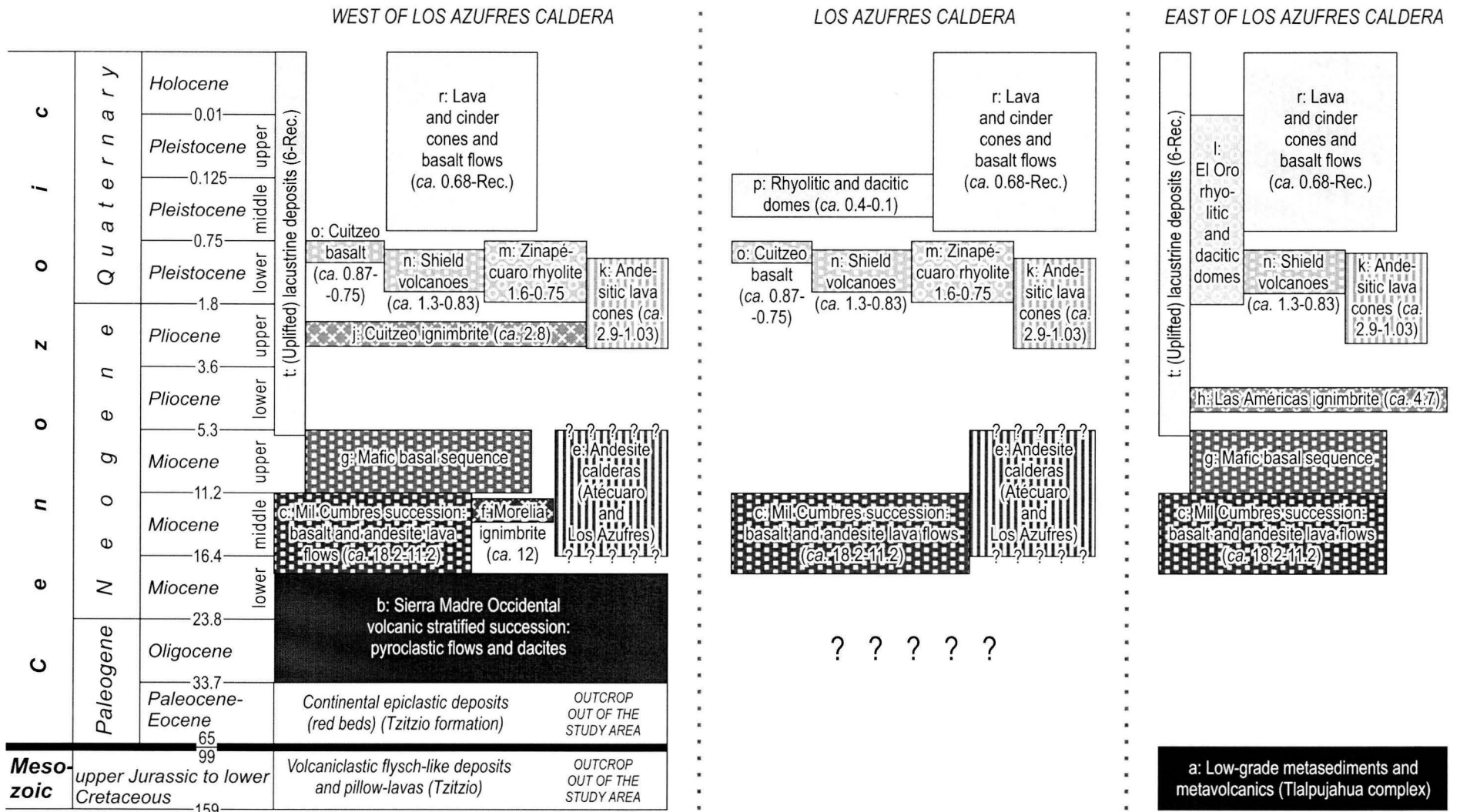


Fig. 2B. Comparison of stratigraphic columns west, east, and at Los Azufres caldera. Units d: dioritic subvolcanic bodies, i: Cuitzeo rhyolitic domes, s: undifferentiated pyroclastic deposits, and u: surficial deposits were eliminated from this comparison. The former two because of their very limited spatial extend, the latter two because of their limited use for depicting the differences in stratigraphy of the area. Numbers are ages in Ma (millions of years before present).

### 2.2.2 Sierra Madre Occidental to transitional volcanic units

The Oligocene-lower Miocene stratified succession belongs to the NNW-striking Sierra Madre Occidental (SMO) volcanic arc and is exposed in the western portion of the study area. To the north of eastern Cuitzeo lake it is composed of deformed and hydrothermally altered andesite. Dioritic subvolcanic bodies of Miocene age intrude these rocks (Fig. 2, Plate 1). The age of this succession was inferred by Pasquaré *et al.* (1991) on the basis of numerous isotopic data (Fig. 2).

Somewhat younger [mostly middle Miocene according to isotopic data of Pasquaré *et al.* (1991)] Sierra de Mil Cumbres basaltic and andesitic lava flows (Fig. 2, Plate 1) form extensive outcrops in the footwalls of normal faults, immediately to the south and southeast of Morelia. This succession is also locally observed in the eastern part of the study area, where it overlies metamorphic basement rocks (Fig. 2, Plate 1). These rocks might represent the transition from the NNW-striking SMO volcanic arc to the E-striking TMVB.

Still younger, and apparently also marking the transition from SMO to TMVB are andesitic Atécuaro and Los Azufres calderas (Fig. 2). Pasquaré *et al.* assign them a late(?) Miocene age. Nonetheless, given that the Atécuaro caldera produced the uppermost middle Miocene (aged 12 Ma, Suter, Instituto de Geología UNAM, 2001, personal communication) Morelia ignimbrite, encountered in the southwestern part of the area (Fig. 2), here they are considered middle(?) to late(?) Miocene.

### 2.2.3 TMVB volcanic units

On regional scale, the mafic basal sequence, which is inferred to mark the onset of TMVB activity (Ferrari *et al.*, 1994b), outcrops to the north of the present-day volcanic front. Its distribution is particularly clear at the eastern portion of the study area (Fig. 2), where this sequence is composed of olivine basalt flows [Río Lerma basalts of Pasquaré *et al.* (1991)]. West of Los Azufres this sequence is made up of highly fractured andesitic lava flows with minor basaltic intercalations [the Tarímbaro andesite of Pasquaré *et al.* (1991)].

Early Pliocene volcanism is present only in the eastern part of the study area as Las Américas ignimbrite (Fig. 2). According to Aguirre-Díaz *et al.* (2000), the greater part of this succession, composed of characteristic black and white pumice and fiamme, originated from the Amealco caldera located to the north of the study area (Fig. 1). A white pumice ignimbrite, intercalated in the lower part of the succession, probably originated at Brockman dam caldera located to the south of Tlalpujahua (Aguirre-Díaz *et al.*, 2000). The sequence is 4.7 Ma old (Aguirre-Díaz *et al.*, 2000), and is over 30 m thick. Recent unpublished studies indicate that this ignimbrite originated from El Capulín caldera located to the east of Tlalpujahua (Garduño-Monroy, Instituto de Investigaciones Metalúrgicas UMSNH, 2003, personal communication).

Late Pliocene felsic volcanism is represented by two small rhyolitic domes located in the northeastern part of the Cuitzeo lake, and by thick ignimbrite, ash flow and fall deposits located to the south and southwest of Cuitzeo lake [2.8 Ma old Cuitzeo ignimbrite of Pasquaré *et al.* (1991)] (Fig. 2). The ignimbrites are highly to slightly welded. Very strongly welded ignimbrites can be observed to the southwest of the lake, where they form resistant, subhorizontal mesas (Fig. 2, details on Plate 4).

Late Pliocene-early Pleistocene volcanism produced a few andesitic lava cones of various dimensions, aged 2.9-1.03 Ma (Pasquaré *et al.*, 1991) (Fig. 2). They are located in the southern part of Los Azufres caldera, to the southeast of Maravatio depression (San Miguel volcano, Plate 1) and further east (Altamirano volcano, Plate 1) (Fig. 2).

Quaternary volcanism is bimodal given that it produced rhyolitic and dacitic domes as well as mafic lava and cinder cones (Fig. 2). The former are concentrated at the southern and western rims of the Los Azufres caldera, where they constitute post-caldera activity. In this location radiometric ages of rhyolitic and dacitic domes cluster in two groups: 1.6-0.75 Ma and 0.4-0.1 Ma (various authors, see Fig. 2). These two groups are discernible by difference in morphology of the domes (Fig. 2). Another group of rhyolitic and dacitic domes is located in the easternmost study area, and was assigned Pleistocene age by Pasquaré *et al.* (1991).

Quaternary mafic volcanics are widespread throughout the area and range into the Holocene. The oldest [1.3-0.83 Ma (Pasquaré *et al.*, 1991)] are a few shield volcanoes found throughout the area (Fig. 2). The Cuitzeo basalt of Pasquaré *et al.* (1991) is found in the vicinity of central and eastern Cuitzeo lake where all published radiometric ages of mafic rocks fall within the 0.87-0.75 Ma range (various authors, Fig. 2). Hence, basalt flows and scoria cones in this region were assigned to this unit, although some scoria cones might be younger. The youngest are widespread mafic volcanics easily recognizable in topography, which were considered the 0.5 Ma to Recent by Pasquaré *et al.* (1991). Suter *et al.* (2001) dating of a scoria cone south of Maravatío extends the lower age boundary of this unit to 0.68 Ma (Fig. 2). Various pyroclastic fall deposits are encountered throughout the study area. They were produced during the volcanic activity of the region and range in age from Oligocene to present (Pasquaré *et al.*, 1991) (Fig. 2).

#### 2.2.4 *Fluviolacustrine and surficial deposits*

Fluvial and lacustrine sedimentation accompanies the TMVB volcanism (Israde-Alcantara and Garduño-Monroy, 1999) (Fig. 2). The oldest lacustrine sediments are found in the vicinity of Charo (Fig. 2) [upper Miocene Charo basin of Israde-Alcantara and Garduño-Monroy, (1999)]. They overlie 8±2 Ma old volcanic succession, and 3.6 Ma ash layer is intercalated in the upper part of this sequence. Israde-Alcantara and Garduño-Monroy, (1999) consider this basin to be associated with the MAFS and hence be the evidence of the MAFS initiation.

The youngest lacustrine sediments are presently forming in the Cuitzeo lake. The thickest pile of lacustrine sediments is encountered in the central part of the Cuitzeo lake. Gravity data across and around the western Cuitzeo lake imply at least 1000 m of lacustrine sediments in front of the eastern portion of western Cuitzeo fault (Plate 1), the greatest negative anomaly being shifted towards the southern shore of the lake (Arredondo, CFE, 2001, personal communication). Unfortunately well data are lacking at, or in the vicinity of this gravimetric low, so this value cannot be corroborated directly. Gravimetric data suggest that lacustrine sediments at the westernmost portion of the lake are only slightly thinner. Other depressions of the western part of the study area are filled with fluviolacustrine sediments (marked as surficial deposits in Fig. 2), which are progressively thinner in each consecutive depression to the south. Well data (provided by Garduño-Monroy, Instituto de Investigaciones Metalúrgicas UMSNH, 2003, personal communication, and collected by CNA, OOPAS and private companies) indicate ≤250 m of fluviolacustrine sediments in front of the Tarímbaro–A. Obregón fault, and 126 m in front of Morelia fault (these faults are named in Plate 1). In both cases the greatest thickness occurs not in the middle of the depressions but towards the southern, north-facing, bounding faults. In front of Jaripeo and Cointzio faults well data indicate *ca.* 80 and 40 m of fluvio-lacustrine deposits, respectively.

The eastern part of the Maravatío depression is filled with lacustrine sediments, and is presently a swamp. My observations at the riverbeds at the western part of this depression revealed that shallow-lying basalt lava flows are covered by a maximum of 2 m of low-energy fluvial sands, silts and fine gravel intercalated with ash and pumice fall deposits. This sequence is composed of partly reworked volcanic ash, pumice and basaltic and andesitic clasts of up to 2 cm of diameter. Another 3 m of high-energy fluvial conglomerate made up of slightly rounded basalt blocks up to 1 m in diameter cover those low-energy deposits. A similar sequence was observed in the northeastern Maravatío depression, but there the low-energy sands, silts and gravels are made up of felsic ash, pumice and lithics and high-energy conglomerates are made up of rhyolitic lava and obsidian fragments and are at least 15 m thick. This sequence passes laterally to rhyolitic domes and obsidian flows. Lack of sufficiently deep well data precludes inferring the presence of fluvial or lacustrine sediments below the lava fill of the western and northern Maravatío depression.

Thin surficial deposits overlying pyroclastic fall and shallow-lying basaltic lavas fill the proximal Venta de Bravo hangingwall (Fig. 2A, Plate 1). The Lerma river and its tributaries drain it as bedrock channels toward the Maravatío depression (Plate 1). Fluviolacustrine sediments fill the Acambay graben in the easternmost study area (Fig. 2A, Plate 1).

## 3. General information and basic topographic features

### 3.1 Study area

The study area is located *ca.* 150 km to the WNW of Mexico city. It spans almost 5000 km<sup>2</sup> of volcano-sedimentary terrain belonging to the late Miocene-Quaternary TMVB and to the Paleogene-Neogene Sierra Madre Occidental (SMO) volcanic arcs. The area is located between 19° 30' N and 20° 00' N, and 100° 00' W and 101° 20' W, and covers five 1:50,000-scale topographic map sheets, of the Instituto Nacional de Estadística, Geografía e Informática (INEGI): E14-A13 (Cuitzeo), E14-A14 (Zinapécuaro), E14-A15 (Maravatío), E14-A16 (El Oro), and E14-A23 (Morelia) (INEGI, 1998a-d, 1999). The westernmost portion of the area belongs to the Michoacán–Guanajuato volcanic field, and also includes Cuitzeo lake and Morelia depression. The Los Azufres caldera and Maravatío depression occur in the center of the area, and in the east the study area terminates at the westernmost Pastores fault without reaching the central part of the Acambay graben (Fig. 1).

The study area comprises the greater part of the major, E-striking, active, intra-arc fault system that affects the central Trans-Mexican Volcanic Belt (Suter *et al.*, 2001). It is located on the intersection of three regional fault systems (Fig. 1) and features various types of volcanism. Such a location permits investigation of the interplay between the various fault systems and the contributions they make to the deformation. It also allows evaluation of the relation between the tectonic and the surficial processes shaping the region.

### 3.2 Major MAFS faults

The main faults scarps forming the MAFS in most cases act as borders of the depressions. They are highlighted in shaded relief images (Fig. 3; location of the faults is shown in Plate 1 – a transparency film included at the end of this work) and mapped in detail in Plates 3-8. These scarps are as follows:

- In the western portion of the study area: 300 m high western Cuitzeo fault scarp, 200 m high Tarímbaro–A. Obregón fault scarp (Fig. 3, Plates 1, 4), 200 m high Morelia–Jaripeo fault scarp, 80 m high Charo fault scarp, and 140 m high Cointzio fault scarp (Fig. 3, Plates 1, 3), 500 m high Santa Ana Maya fault scarp, 120 m high eastern Cuitzeo fault scarp, and 100 m high Queréndaro fault scarp (Fig. 3, Plates 1, 5),



- In the center: 280 m high Curinhuato fault scarp, 220 m high La Trasuquila fault scarp, and 120 m high Agua Fría fault scarps (Fig. 3, Plates 1, 5, 6).
- In the eastern part: 300 m high Venta de Bravo fault scarp and various shorter fault scarps including 140 m high Zirizicuaro fault scarp (Fig. 3, Plates 1, 6, 7).

Most of these fault scarps face north, which suggest that they are associated with asymmetric half-grabens. Nevertheless, faults facing south also exist within the MAFS. These faults appear at the eastern end of the Cuitzeo lake (*i.e.*, Santa Ana Maya or Araró faults) (Fig. 3, Plates 1, 5) and at the Los Azufres caldera (Curinhuato and a few Agua Fría faults) (Fig. 3, Plates 1, 5, 6). To the east of the study area, the Acambay graben is bordered by south-facing Acambay–Tixmadejé fault and north-facing Pastores fault, and is the classic example of a depression with graben geometry (Fig. 1).

### 3.3 Segmentation of the MAFS: major tectono-topographic domains

Suter *et al.* (1992) observed that the MAFS is segmented along-strike, and that the limits between the segments coincide with the extrapolated NNW-striking Taxco-Querétaro FS structures. They divided the MAFS into three areas: western, located west of Los Azufres; central between Maravatío in the west and Altamirano volcano in the east (Plate 1); and eastern which is the Acambay graben *sensu stricto* (Fig. 1). Suter *et al.* (2001) observed that the limit between western and central segment is the NNW-striking, Maravatío depression. They state that it is of Basin and Range orientation, but does not seem to be fault bounded. Garduño-Monroy (1988) observed that N-S elongation of the Los Azufres caldera that borders the Maravatío depression to the west, occurs at the intersection of two fault systems, one striking NW-SE and another one striking W-E. Alongstrike segmentation of the MAFS, apparently controlled by conspicuous, transverse structures with Basin and Range orientation, suggests that tectono-topographic configuration of the area is more complex than simply made up of the MAFS-bounded fault blocks.

In this study, a combination of published MAFS segments, major topographic features of the region and first-order topography [elevation, slope, relief (see section 5.1.3: “Distribution of morphometric values” and Appendix 1)] renders several tectono-topographic domains transverse to the strike of the TMVB and the MAFS, with major MAFS faults subdividing these domains into sub-domains. Three largest of the latter, controlled by the longest MAFS faults, are described here together with major domains, in order to subsequently evaluate the influence of the MAFS-controlled and MAFS-perpendicular structures on topography (see section 5.1.4 “Morphometry of the tectono-topographic domains”). Approximate borders between the domains were placed along topographic lineaments and pronounced, linear breaks in slope, and MAFS faults in the case of sub-domains.

The domains are (Plate 1):

- The western depressions [western MAFS of Suter *et al.* (1992)] which include five depressions separated by uplifted and tilted normal fault footwalls. These depressions are, from north to south: the Cuitzeo lake, the Tarímbaro-Queréndaro depression, the Charo depression, the Morelia depression, and the Cointzio depression. The latter four are distributed in an *en échelon*, left-stepping arrangement.
  - The largest of the uplifted normal fault footwalls is the western Cuitzeo fault footwall, and is considered a sub-domain.
- The roughly N-S oriented Los Azufres caldera (Garduño-Monroy, 1988) located approximately in the middle of the study area.
- NNW-SSE oriented Maravatío depression (Suter *et al.*, 2001) located to the east of the former.
- Venta de Bravo area is located to the east of the Maravatío depression, and is made up of
  - the Venta de Bravo fault hangingwall (a sub-domain), and
  - the Venta de Bravo fault footwall (sub-domain).
- Westernmost Acambay graben (westernmost eastern MAFS of Suter *et al.*, (2001)] occupies the north-easternmost portion of the study area.
- Puerto la Sosa area, located to the SE of Morelia is a very steep topographic slope that marks the transition from the TMVB plateau at *ca.* 2000 m asl to the Balsas basin at *ca.* 200 m asl (Fig. 1). A series of NE-striking fault scarps and E-striking line of erosional cirques bound this domain (Plates 1, 3).

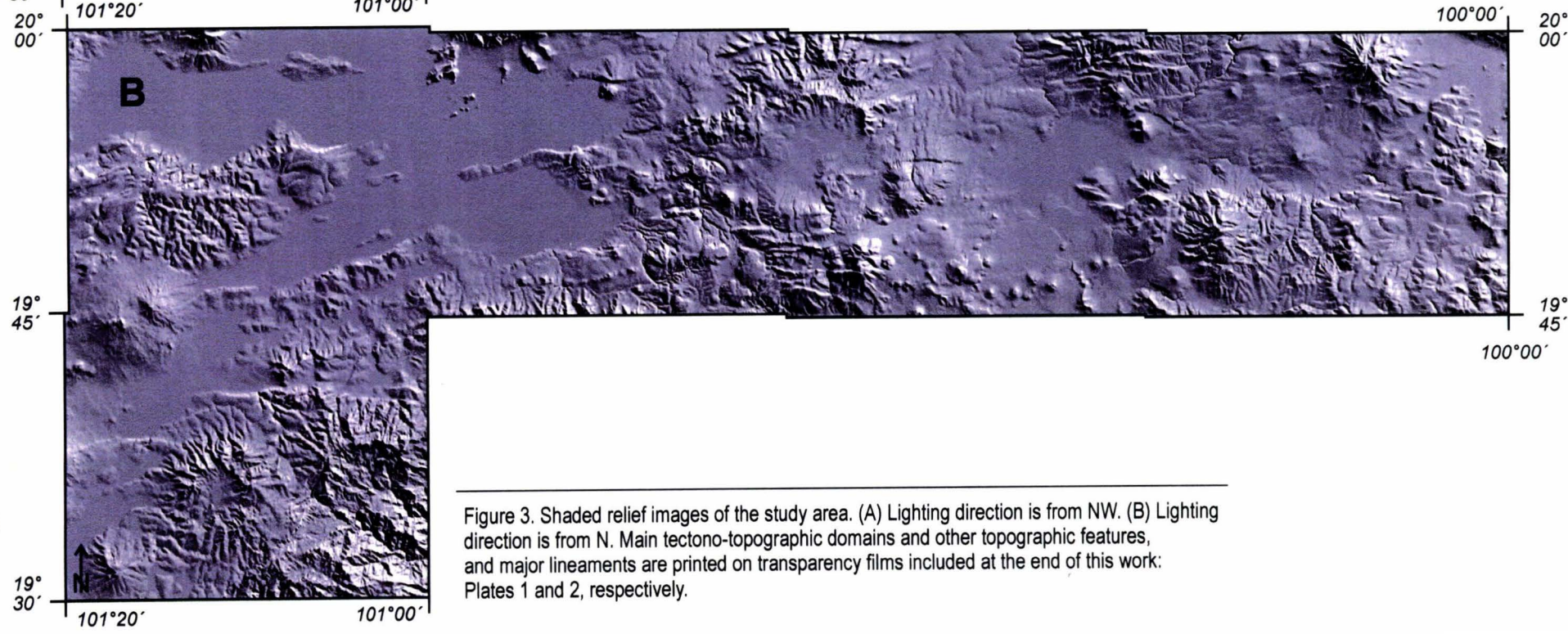
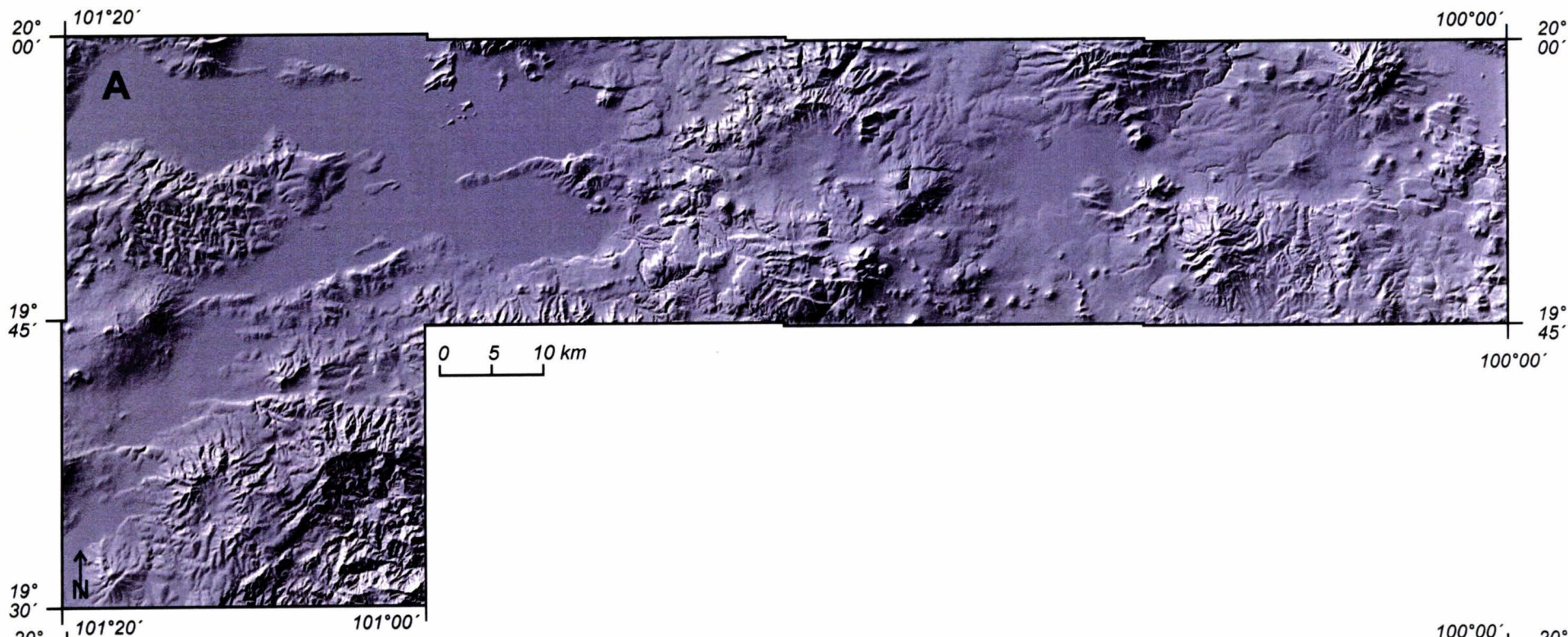


Figure 3. Shaded relief images of the study area. (A) Lighting direction is from NW. (B) Lighting direction is from N. Main tectono-topographic domains and other topographic features, and major lineaments are printed on transparency films included at the end of this work: Plates 1 and 2, respectively.

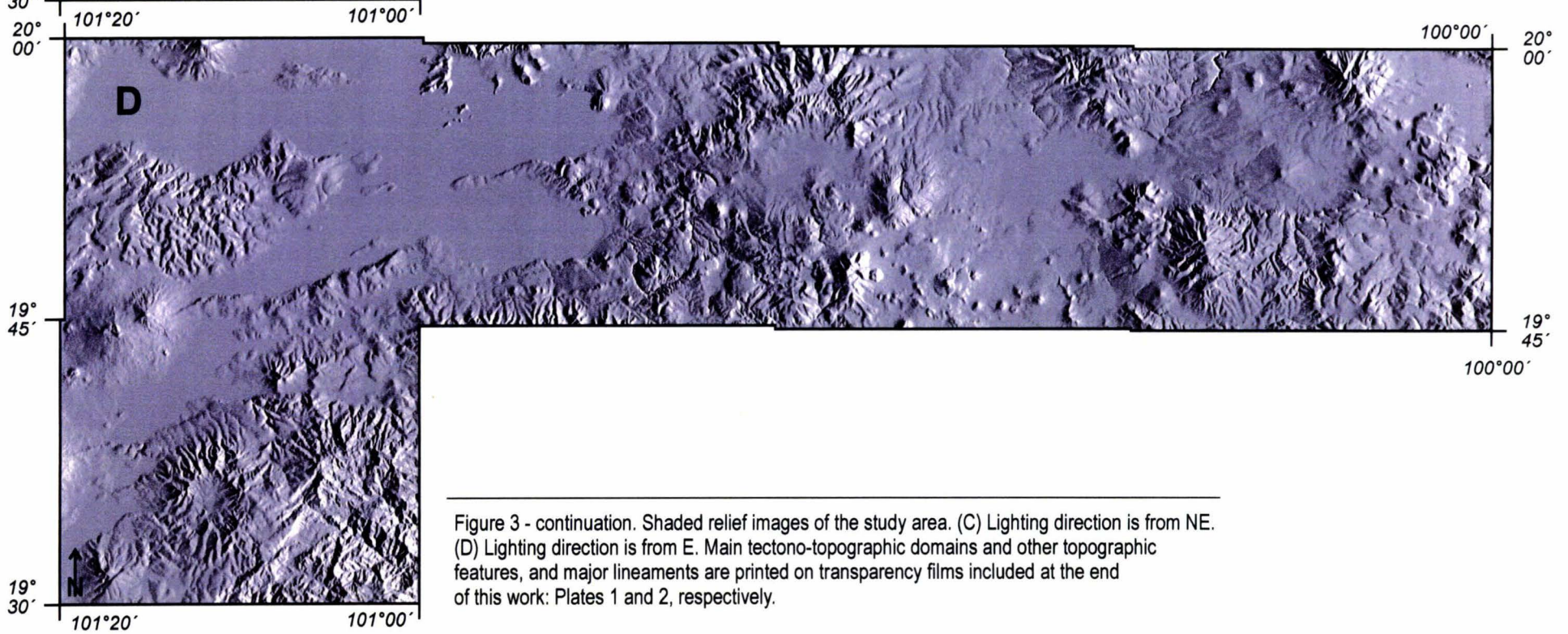
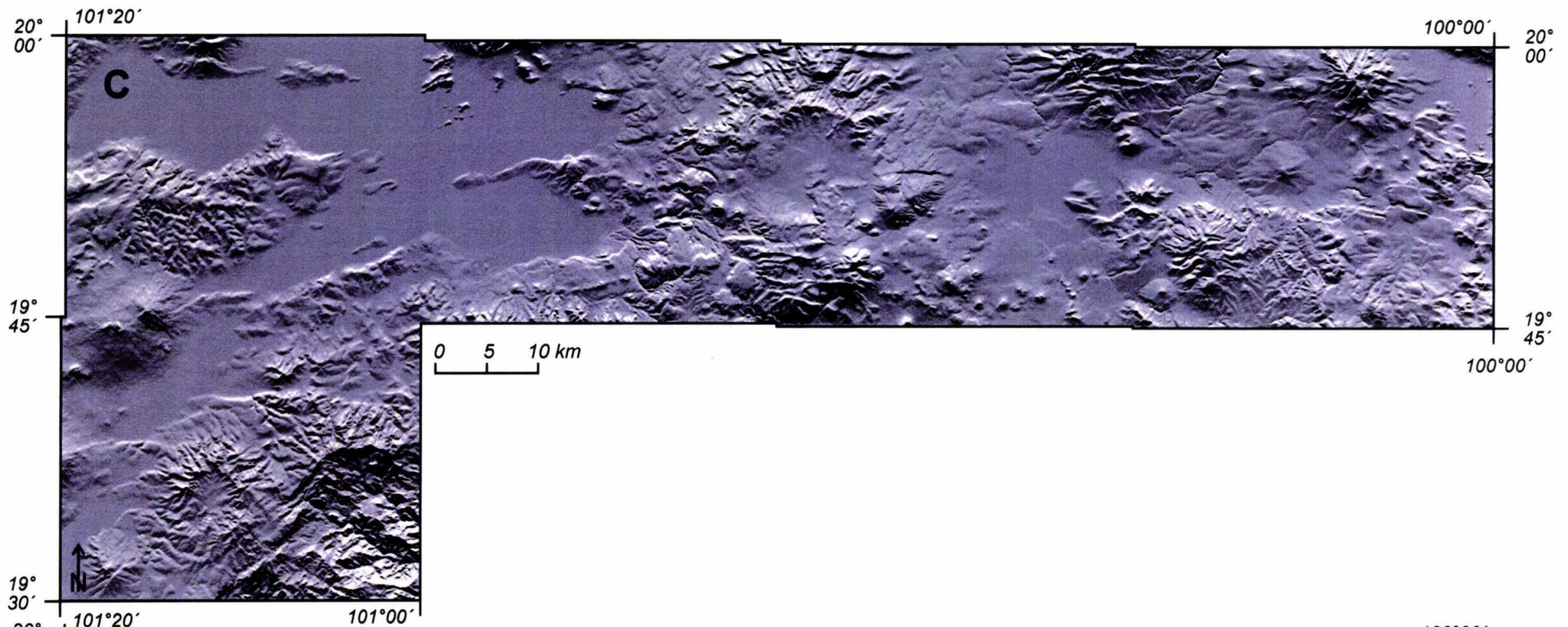


Figure 3 - continuation. Shaded relief images of the study area. (C) Lighting direction is from NE. (D) Lighting direction is from E. Main tectono-topographic domains and other topographic features, and major lineaments are printed on transparency films included at the end of this work: Plates 1 and 2, respectively.

## 4. Materials and methods

### 4.1 Digital elevation model (DEM) and digital vector data: morphometric analysis

The quantitative analysis of topography consisted of processing and interpreting digital elevation models (DEMs), with a resolution of 50 m, produced by the Instituto Nacional de Estadística, Geografía e Informática (INEGI) from 1:50,000-scale topographic maps (INEGI, 1998a-d, 1999). First, the DEM mosaic of the whole area was generated using the Integrated Land and Water Information System (ILWIS). The five input DEMs are placed in topographic (metric) coordinates, which are slightly oblique to geographic (degrees/minutes/seconds) coordinates, what resulted in step-like outline of output DEM and derived morphometric maps. The DEM was semi-manually corrected and filtered with 3x3 pixel average filter to eliminate major artifacts appearing on the model due to the interpolation from isolines. The result of this operation was used for the production of DEM-derived morphometric maps and topographic profiles. Shaded images were obtained from unfiltered DEM because average filtering blurs the image. Although I also tested the weighted average filtering (as it is expected to smooth the model without blurring it) some blurring remained, and the smoothing was less effective. The output DEM and morphometric maps use the Universal Transverse Mercator projection (zone 14), and Clarke 1866 ellipsoid.

The digital vector data used in this study consists of drainage network maps produced by the Instituto Nacional de Estadística, Geografía e Informática (INEGI) from 1:50,000-scale topographic maps (INEGI, 1998a-d, 1999), a fault trace map and a lineament map. The drainage network map of the whole area was made by joining the five map sheets that cover the study area. The fault trace map was extracted from the geomorphologic maps produced in this study (see below), and lineament trace map was interpreted from the DEM (see below).

#### 4.1.1 *Shaded images: searching for topographic lineaments*

The DEM was filtered to obtain shaded relief images with four lighting directions (from NW, N, NE, and E, with artificial light source 45° above the horizon) (Fig. 3, Appendix 2), which were used for lineament identification (Oguchi *et al.*, 2003). Shaded relief images highlight lineaments roughly perpendicular to lighting orientation, so these 4 directions are sufficient to identify all major lineaments. The traced lineaments

correspond to alignments of scarps, straight reaches of rivers or streams, and alignments of scoria cones. The latter two were also identified on air photos (at 1:75 000 scale).

#### *4.1.2 Longitudinal river profiles*

Twenty nine longitudinal river profiles were obtained using the DEM and the drainage network map, so all channels marked as perennial on the drainage network map were investigated. After selecting 10 most relevant cases, river profiles were re-plotted by reading the values directly from 1:50,000-scale topographic maps. This ensured that necessary detail was preserved, and that no artifacts due to DEM structure are present in the data [for discussion of difficulties with DEM-based longitudinal river profiles see Montgomery and López-Blanco (2003)].

Longitudinal channel profiles provide data on river profile irregularities that may be due to active tectonics or volcanism. As longer bedrock rivers have greater erosive power, they obliterate any imposed profile deformation more quickly than shorter, seasonal streams (Keller and Pinter, 1996). Therefore, if any deformation of a river longitudinal profile is preserved, it is more meaningful as an indicator of active tectonics than such a feature encountered at a seasonal stream. This is qualitative distinction only, because the differences of fluvial erosion rates between perennial and ephemeral streams in the region are unknown.

#### *4.1.3 Elevation map and topographic profiles*

The DEM was classified into altitude intervals (color-coded) and generalized (majority filtered) for visual interpretation purposes. The chosen altitude intervals produce approximately normal histogram distribution in an attempt to illustrate the peculiarities of the terrain configuration more clearly than the unclassified DEM. The unclassified DEM was used to evaluate correlation between morphometric maps.

The DEM was also used to construct histograms of elevation values for the whole area (Appendix 1) and for each tectono-topographic domain and sub-domain. For this purpose elevation values were grouped every 20 m, which is the vertical separation of isolines of the original topographic maps. This eliminates the sawtooth effect resulting from interpolation of the DEM from isolines.

Topographic profiles were obtained by reading elevation values from the DEM every 100 m along desired paths. They were used to further visualize the topography of the area and search for possible relations between topography and faulting

#### *4.1.4 Relief map*

Using the moving window method, a relief map was produced from the DEM by subtracting the minimum from the maximum height value encountered within a square of 1km<sup>2</sup>, and replacing the value of the central pixel of the square with the output. This operation was repeated for each map pixel. The size of the square provides reasonable local relief estimation, and is computationally rational at the given map resolution. Similar procedure was used by Johansson (1999) to produce what he called a “relative relief” map. For presentation purposes, this map was classified into desired ranges and generalized. The unclassified relief map was used to evaluate correlation between morphometric maps. For histogram construction, relief values were grouped every 10 m, which is the finest resolution that eliminates sawtooth effect in the case of this map.

#### *4.1.5 Slope gradient map*

To produce the slope gradient map, I calculated the first derivative per cell of the DEM in two horizontally perpendicular directions: W-E and N-S. Slope angle in degrees was computed from the two resulting maps (using the Pythagorean rule). Finally, the map was generalized with median 5x5-pixel filter, and classified into desired ranges.

The chosen slope gradient ranges fit the typical variations between landforms of the region (Bocco *et al.*, 2001), and are the following: 0°-3° – fluvioacustrine plains, or lava or ignimbrite plains or mesas; 3.01°-6° – lava or ignimbrite plains or mesas, or footslope; 6.01°-10° – mostly footslope; 10.01°-20° – moderately inclined mountainsides and fault scarps; 20.01°-30° – steep mountainsides and fault scarps; >30° – very steep mountainsides and fault scarps. The 3.01°-6° class is particularly sensitive to the DEM production process, namely the digitizing of isolines, so its extent should be viewed with caution.

Slope gradient map was produced in order to (i) further characterize the morphometry of the area, (ii) check if any regional-scale breaks in slope (abrupt changes of slope gradient) are encountered in the area, (iii) delimit flat surfaces (especially topographically high), (iv) visualize the distribution of fault scarps, volcanic cones and domes and limits of lava flows.

#### 4.1.6 Drainage density map

The drainage density map was calculated from the digital drainage network map by counting the total length of streams within squares of 4km<sup>2</sup>, and storing the resulting value in the raster map with resolution of 4 km<sup>2</sup>. 4-km<sup>2</sup> square was chosen to enable comparison of the drainage density map with the lineament and fault scarp density maps (see below), as possible relation of drainage and lineaments/faults is of interest in this work. Smaller square (*e.g.*, 1 km<sup>2</sup> as used for relief map) would cover only a single lineament or fault scarp, so using such square size would be unreasonable. Only natural stream/river channels were taken into account. This eliminated almost all rivers and streams crossing the fluvioacustrine plains, as they have been converted to the network of irrigation channels, but also guaranteed that no artificial channels, such as aqueducts are included in calculations.

To calculate the correlation coefficients between morphometric maps, the drainage density map was interpolated to 50 m cell size as all maps must have the same resolution for this calculation. Uninterpolated maps are presented in this work, because interpolation reduces the original value range. Nonetheless, it does not significantly alter the distribution of values that is important for correlation.

Comparison of digital drainage network maps of INEGI with paper copies of topographic maps of the same institution (INEGI, 1998a-d, 1999) and aerial photos, reveal that, although within the TMVB drainage network is reasonably well depicted, outside the TMVB, particularly at the Puerto la Sosa region, the drainage density is unrealistically low, *i.e.*, while the scaling factor of drainage density from interpreted paper topographic maps to digital drainage density map within the TMVB is 1.1, this factor is 1.7 at the outcrops of Tlalpujahuá metamorphic-plutonic complex at Tlalpujahuá, and 2.8 at Sierra Madre Occidental outcrops at Puerto la Sosa domain (Fig. 2). Therefore, it is considered that only within the TMVB are the depicted variations of drainage density meaningful.

#### 4.1.7 Fault scarp density and lineament density map

Fault scarp density and lineament density maps were constructed from the fault trace map (extracted from geomorphologic map, see below) and the lineament trace map (interpreted from the DEM, see above), respectively. The total length of fault scarps and lineaments within squares of 4 km<sup>2</sup> was counted, and the resulting values were stored in the raster map with resolution of 4 km<sup>2</sup>. For calculation of correlation coefficients between morphometric maps, these maps were interpolated to 50-m cell size.

### 4.2 Aerial photographs and field data: geomorphologic mapping

The geomorphologic map was produced by interpreting 1:75,000-scale aerial photographs, and by subsequent field verification. The mapping scheme adopted for this study is a modification based on the general guidelines of Van Zuidam (1979). The classification of the terrain is twofold: color illustrates the distribution of surface classes, that is weathering- and erosion-dominated surfaces (summits and slopes); transitional surfaces (talus, colluvium, and footslope); and deposition-dominated surfaces (fluvioacustrine plain, and alluvial and proluvial fans). The pattern represents easily recognizable volcanic landforms (scoria cones, lava

cones, lava domes, lava flows, lava plains, and ignimbrite plains/mesas or undifferentiated pyroclastic flow and fall deposits).

The maps also show linear features associated with active deformation (fault scarps, rounded/lowered fault scarps, triangular facets at fault scarps, entrenched streams, and topographic surface tilt), linear features that can be related to active deformation (collapse scars and fluvial erosional cirques), and lithologic linear features (lithologic scarps and lava fronts).

Field verification of these maps consisted of describing surficial deposits to compare them with mapped units. Additionally, slopes on different surface units were measured in the field, in order to compare the results with slope gradient map, and verify the ranges of slope gradients of mapped units. I also field mapped fault scarp features such as some triangular facets and free rock face, impossible to identify on the air photos for scale reasons.

This mapping scheme seeks to combine morphodynamics and morphogenesis, in order to illustrate tectonic influence over landscape formation. The distribution of mapped surface classes reveals possible tectonic controls over landscape dynamics, such as sedimentation at fault-controlled lacustrine basins, or erosion and weathering at upthrown footwalls of normal faults. Nonetheless, mapped surface classes can also be examined in terms of morphogenesis, given that formation of fluviolacustrine plains, alluvial/proluvial fans, footslopes, colluvium, taluses and slopes and summit surfaces is largely tectonics- and volcanism-controlled in the region where both processes are active. The distribution of volcanic landforms reveals possible tectonic controls over landscape morphogenesis. In the study area it applies principally to the scoria cone distribution because they tend to be aligned parallel to the regional fault systems. Potentially, lava flows are also tectonic indicators when erupted from fissures. An additional advantage of this mapping scheme is that it can be easily modified to suit particular research needs, *e.g.*, specific features associated with deformation can be added/eliminated, any specific landform can be added/eliminated, if morphogenesis is of greatest interest color/pattern code can be swapped, etc.

### 4.3 Field data: structural analysis

Structural data collected during fieldwork consist of measurements of fault slip planes, position of layered deposits, outcrop descriptions and stratigraphic observations. The total number of observation points is 312, of which 63 have fault plane and striae orientations, and 25 have fault plane orientations. Strata attitudes were measured at 116 observation points. 87 verification points were devoted solely to lithologic and geomorphologic observations. All measurements take into account magnetic deviation, which is 8° west in central Mexico.

Outcrop descriptions provide illustration of fault and strata geometries and fault kinematics. They also served for verification of existing geologic maps of the region, and for subsequent assessment of rock ages by comparison with existing geologic data.

Direction of motion on faults was assessed on the basis of striae orientation. Sense of motion was determined with the following criteria: tectonic tool marks, Riedel shears, conjugate shear fractures, alternating polished and rough facets, mineral steps, and parabolic marks (Angelier, 1994). Faults with striae pitches (rakes) less than 40° are considered strike-slip, faults with striae pitches between 40° and 50° are considered reverse-oblique or normal-oblique, faults with striae pitches over 50° are considered reverse or normal. Where striae was absent, it was usually possible to assess normal or reverse components of motion on the basis of stratigraphic separation.

Almost all fault plane and striae orientations were measured in the upper Miocene to Recent rocks, so the slip on the faults is contemporaneous with the TMVB. In the few cases where data was collected in older rocks, it corresponds to the brittle faulting of the last deformation phase that cuts the foliation and older folds and shear zones, hence these faults are also probably contemporaneous with the TMVB.

Fault slip data (striae) inversion was carried out with the STRESS software of T. Villemin and H. Charlestone, using right dihedral (also called P-T axes) method of Angelier and Mechler (1977) in which the fault plane

and the auxiliary plane perpendicular to striae divide 3-D space into four right dihedral. Two of these dihedral are in contraction and the other two in extension. They are computed for all faults in population and orientations of contraction (shortening) and extension (stretching) are the geometrical centers of areas of respective dihedral overlap. Usage of this method assume local plane strain (Reches, 1983). Directional diagrams (*e.g.*, rose diagrams of fault planes or kinematic axes) were calculated with Stereonet software.

Strata attitudes were measured in layered deposits such as pyroclastic flows and falls, bases of lava flows, and lacustrine deposits. Obvious primary, sedimentary dip (such as in scoria cones, surficial deposits inclined in accordance with present topographic slope, pyroclastic fall deposits draping pre-existing topography, or flow folds in lavas) were not measured, because they would have given an erroneous impression of tectonic deformation. Most of the strata attitudes were measured in extensive outcrops and show an association with faulting [see sections 5.2.1: "Fault geometry and associated strata at outcrop scale" and 5.2.3: "Strata attitude: a summary (regional variation)"], so I believe that most of the dips are of tectonic origin. Nonetheless, some primary dips or combined effect of primary dips and tectonic tilting might be present within the data set as the distinction between the two is not always possible. Strata dips were not measured in poly-deformed Tlalpujahuá metamorphic-plutonic complex as the deformation associated with the MAFS could not be separated from previous deformation stages. Where several data were collected at one or neighboring outcrops, the averaging of strata attitude was calculated using Stereonet computer software, and density plots.

Stratigraphic data include rock descriptions such as rock type and primary structures, and sketches of stratigraphic columns. These permitted investigation of possible tectonic controls over sedimentation process. These data were collected primarily in the riverbeds of the depressions of the study area, and close to fault scarps.

Structural and stratigraphic data were used for forward modeling of (balanced) structural cross-sections. This was done with public-domain software FBF (Contreras, 2002; <http://www.cicese.mx/~juanc/fbf/fbf.html>).

#### 4.4 The DEM of central Mexico: topographic profiles across the volcanic arc and its vicinity

The topographic data from central Mexico is presented at the end of the Results chapter, because it spans much wider region than the actual study area, and seeks to contribute data for the discussion of the deformation of central Mexico in a broader perspective.

The digital elevation model of 30 arc second grid showing continental elevations of central Mexico, was constructed by extracting parts of GTOPO30, public domain data tiles W100N40 and W140N40, generated by the United States Geological Survey. The resulting DEM used for analysis of elevation has the same projection parameters as the raw data *i.e.*, geographic projection, WGS84 datum, and WGS84 spheroid. The 30 arc second cells of the DEM measure *ca.* 875 m east-west, and *ca.* 912.5 m north-south, at 20° latitude in central Mexico.

Several topographic profiles were derived from the DEM along north-trending lines, roughly perpendicular to the analyzed portion of TMVB. The lines are spaced *ca.* every 90 km in east-west direction. Two lines are located at the eastern portion of the western TMVB, four at the central TMVB, and two at the eastern TMVB.

In order to construct topographic profiles, the average filter with window size of *ca.* 90 km in east-west direction per *ca.* 4.5 km in north-south direction was applied to the DEM. This operation determines the mean value of all pixels covered by the filter window, and stores it in the central pixel of the window, repeating the procedure for each pixel of the map. Topographic profiles were produced by reading values from filtered DEM, every 4.5 km along the south-north trending lines.

The output profiles show mean elevations at 90-km wavelength (elevation is averaged over 45 km to the east and west of each line), determined in 4.5-km segments along the line. The size of the filtering window and the spacing of the lines, allow all elevation data between the paths to be considered. The profiles, wherever the



distance from the coast permits it, extend to the south and the north of the arc at least as far, as is the width of the arc along the path of each profile.

Mean elevations of the portions of TMVB and its vicinities, represented on each profile, were also calculated. This was done by averaging the values corresponding to the TMVB, and to the terrain south, and north of the TMVB shown on each profile. In the latter two cases the portion of the profile taken into account does not exceed the width of TMVB along the path of a given profile.

The software used for processing of digital topography, digitizing of the geomorphologic map, and spatial data integration was the Integrated Land and Water Information System (ILWIS) of ITC, The Netherlands.

## 5. Results

### 5.1 Topography of the Morelia–Acambay fault system

#### 5.1.1 *Fault scarp and lineament orientation*

The most common fault scarp orientation throughout the study area is ENE-WSW to ESE-WNW (Figs. 3, 4A, Plate 1). Most of these scarps show curvilinear, anastomosing patterns that can be observed on detailed geomorphologic maps (Plates 3-7, legend on Plate 8). Such a fault pattern is typical of 3-D extensional and oblique-extensional settings (Reches, 1983; Reches and Dieterich, 1983; Clifton *et al.*, 2000). Straight scarps appear locally, *e.g.*, at the southern part of Los Azufres caldera (Plates 5 and 6).

A few fault scarps, oriented NW to N were observed at the study area. West of Los Azufres these scarp orientations are rare, but their presence is noteworthy, because they cut recent lacustrine deposits (Garduño-Monroy, Instituto de Investigaciones Metalúrgicas UMSNH, 2003, personal communication). They become more persistent to the east of Los Azufres, where in some cases they link E-striking scarps. Such NW-striking scarps appear at the central part of Venta de Bravo fault, and in the easternmost part of the study area (Plates 1, 7). At the latter location they correspond to the major, regional fault system: NNW-striking Taxco–Querétaro FS (Fig. 1).

The NE-striking scarps are relatively common to the west of Los Azufres where they often join different segments of E-striking scarps (Plates 1, 3-5). The NE-striking scarps also separate Sierra Madre Occidental and Sierra de Mil Cumbres outcrops in the vicinity of Puerto La Sosa (Fig. 2, Plates 1, 3). To the east of the Los Azufres caldera these scarps become rare.

The topographic lineaments correspond to alignments of scarps, straight reaches of rivers or streams, and alignments of scoria cones (Plate 2). The later are indicative of faulting less than 0.87 Ma old (such is the age of recognizable scoria cones, Fig. 2). Notably NW-striking alignments of scoria cones cluster in both edges of the Maravatio depression (Plates 1, 2).

In general, while W-E directions are normally represented by the MAFS fault scarps (Fig. 4A) the lineaments usually strike NW-SE to NNE-SSW (Fig. 4B). The NE-SW tectonic trends are distributed between fault scarps and topographic lineaments.

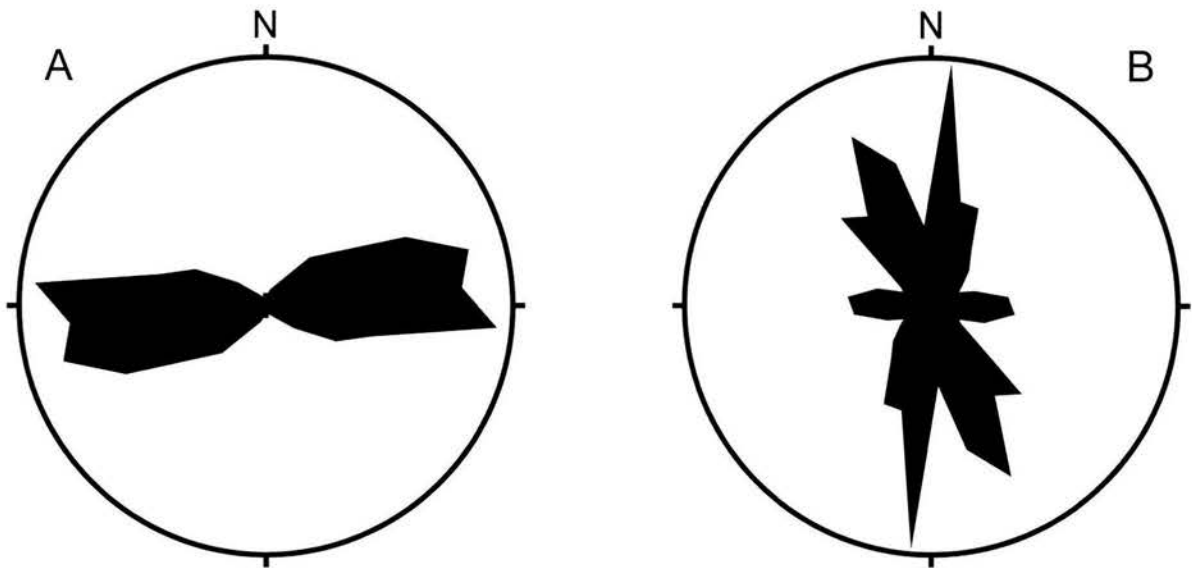


Figure 4. (A) Rose diagram illustrating distribution of strikes of fault scarp traces, extracted from detailed geomorphologic maps (Plates 3-7). The diameter of ring is 10% of fault frequency. (B) Rose diagram illustrating distribution of strikes of lineament traces, interpreted from shaded images (main lineaments in Plate 2). The diameter of ring is 8% of lineament frequency.

### 5.1.2 Longitudinal river profiles

Longitudinal channel profiles of the rivers of the study area are likely to provide data on stream profile deformation that may be due to active tectonics or volcanism. Ten most relevant cases, which were selected from 29 DEM-based profiles of perennial channels and re-plotted by hand (see section 4.1.2 in Materials and Methods chapter) are shown in Figure 5. Location of these rivers is shown in Plate 1.

El Limón river (No. 1 in Fig. 5 and Plate 1) is one of very few rivers of the study area with well-graded longitudinal profiles. This river does not cross any fault or topographic lineament (although part of it flows along a lineament). However, it flows over different lithologies (basalt-andesite and fluviolacustrine plain, Fig. 5), with resistant bedrock of upper Miocene basalts and andesite. Note that profile deformation due to lithologic contrasts across the course of this river is absent.

The rivers of Morelia region (Río Chiquito and El Rile-Jaripeo: Nos. 2 and 3, respectively, in Fig. 5 and Plate 1) show profile deformations associated with Morelia–Jaripeo fault scarp. The longitudinal profile of the former river is convex upward in its lower part, and has a small knickpoint directly above the E-striking Morelia fault scarp. A very small knickpoint can also be seen above small, NE-striking fault further upstream (Fig. 5). The profile of El Rile-Jaripeo river shows knickpoints at, and above, Jaripeo fault scarp. Notably, there is no knickpoint associated with Charo fault scarp (Fig. 5).

Queréndaro river profile (No. 4 in Fig. 5 and Plate 1) is straight and has several small knickpoints. They seem to be associated with the Queréndaro fault, the alignment of 12 cineritic cones located 3 km to the south of it, and the ENE-striking lineament located further upstream. The knickpoints located between the latter two might have migrated upstream from the scoria cone alignment, or be due to stacking of lava flows at the lava plain.

The two rivers that flow down the northwestern slopes of the Los Azufres caldera (Las Navajas and Rosas Amarillas: Nos. 5 and 6, respectively, in Fig. 5 and Plate 1) have very pronounced knickpoints. Las Navajas knickpoint is located where the river crosses the NNW-striking lineament (Fig. 5, Plates 1, 2). Rosas Amarillas knickpoint is located at the NE-striking La Trasuquila fault (Fig. 5, Plate 1).

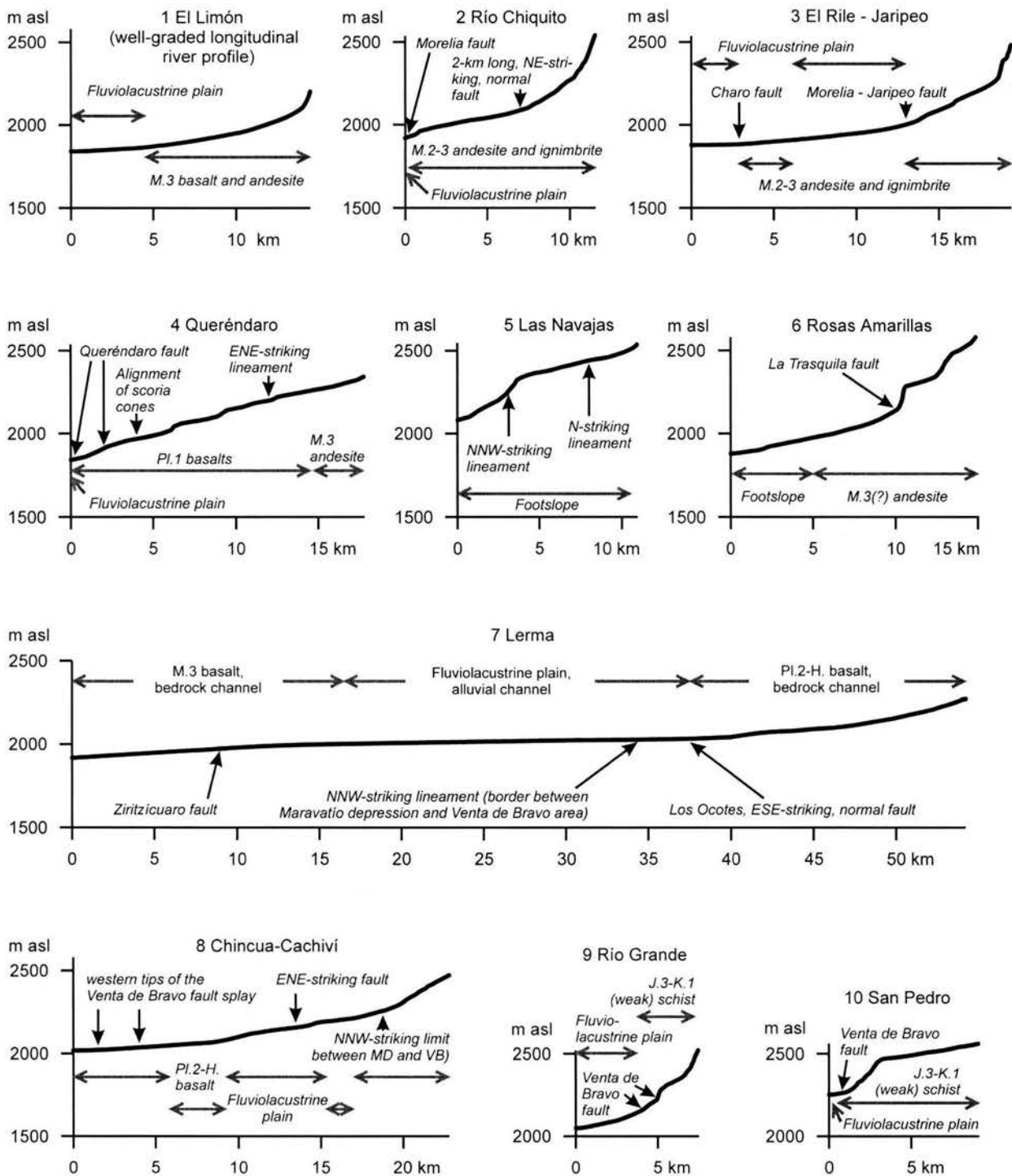


Figure 5. Longitudinal river profiles. Vertical exaggeration is 10x, m asl = meters above sea level. For location of the rivers see Plate 1 (river numbers are the same). Age of bedrock: J.3 – upper Jurassic; K.1 – lower Cretaceous; M.2-3 – middle-upper Miocene; Pl.2 – middle Pleistocene; H. – Holocene. Footslope and fluviolacustrine plain are considered middle Pleistocene to Holocene. MD – Maravatio depression, VB – Venta de Bravo area. Note knickpoints associated with faults and lineaments of various strikes.

The largest river of the study area – the Río Lerma (No. 7 in Fig. 5 and Plate 1) – has convex upward profile, upstream of the E-striking Zirizícuaru fault. Fluvial regime of this river changes from bedrock to alluvial channel in across the ESE-striking Los Ocotes fault, and from alluvial to bedrock channel in the vicinity of Zirizícuaru fault (Fig. 5, Plate 1).

Chincua-Cachiví river (No. 8 in Fig. 5 and Plate 1) flows around the western tip of the Venta de Bravo fault scarp without profile deformation. The clearest profile alteration is seen where the river leaves the lava plain and enters the El Fresno reservoir fluviolacustrine plain. Further upstream are two knickpoints, apparently associated with a short ESE-striking fault, and the boundary between the Maravatío depression and the Venta de Bravo domain.

The rivers that cross Venta de Bravo fault scarp (Río Grande and San Pedro: Nos. 9 and 10, respectively, in Fig. 5 and Plate 1) have pronounced knickpoints associated with this fault. Noteworthy, the San Pedro knickpoint is considerably larger than the Río Grande knickpoint. Moreover, bedrock strength is similar across these knickpoints (Fig. 5), because upstream of the fault these rivers run over usually highly fractured and relatively weak schists of Tlalpujahua complex (see Fig. 2 and Plate 1). The former river crosses the fault in the middle of the central Venta de Bravo fault scarp. The latter river crosses it at the boundary between the western and the central Venta de Bravo fault scarp (segment boundary) (Plate 1).

In summary, very few rivers draining the study area have well-graded, concave upward longitudinal profiles without signs of profile deformation. Notably, bedrock strength variations alone do not produce departures from such profiles (Fig. 5, profile 1), unless the harder bedrock is of late (?) Quaternary age (*e.g.*, Fig. 5, profile 8). Instead, profile convexities and knickpoints are usually directly associated with normal fault scarps and topographic lineaments, or located only slightly upstream of them (Fig. 5). One or more knickpoints located upstream of the main knickpoint are also observed at several fault scarps (Fig. 5). Lithologic variations are commonly associated with knickpoints crossing roughly E-striking fault scarps, and rarely with knickpoints crossing roughly N-striking topographic lineaments (Fig. 5).

### 5.1.3 Distribution of morphometric values

#### *Elevation and topographic profiles*

The lowest terrain within the study area is the Puerto La Sosa domain (Plate 1), which is part of a very abrupt southern slope of the TMVB (Fig. 6A, Plate 1; Fig. 7, profile F-F'). Lowest altitude here is 1140 m asl (above sea level). The rest of the area, belonging to the TMVB and Sierra Mil Cumbres, lies between 1837 m asl (the Cuitzeo lake) and 3600 m asl (the top of San Andrés volcano – the volcanic cone in the southern part of Los Azufres caldera) (Fig. 6A, Plate 1). Altitude distribution within this area is described below.

The depressions of the area are elongated roughly W-E. An exception to this rule is the Maravatío depression. The latter is oriented NNW-SSE, and its SW border is particularly linear and well defined (Figs. 3, 6A, Plate 1). Nevertheless, superposed topographic steps striking W-E can be noticed in the northern and southern part of this depression, in both cases with altitude drop of *ca.* 80 m toward the north (Fig. 7, profile C-C'). Although relatively depressed, the topography of the downthrown block of the Venta de Bravo fault (Venta de Bravo fault hangingwall in Plate 1) is exceptionally rugged, when compared to other depressions of the region (Fig. 7, profile D-D').

As noted by previous workers, mean topographic elevation of the TMVB drops toward the west (Ramírez-Herrera, 1994; Suter *et al.*, 2001). In particular, the floor of central MAFS-controlled depression descends in a step-like manner toward the west. This descent is systematic, given that the floor of each depression is *ca.* 100-200 m lower than the floor of its eastern neighbor (Fig. 7, profile A-A'). The floors of the depressions of the western part of the area are progressively lower from south to north (Fig. 7, profile B-B'). The southernmost Cointzio depression lies at 2000 m asl, the Morelia depression at 1900 m asl, and the Tarimbaro-Queréndaro depression and Cuitzeo lake lay at *ca.* 1840 m asl.

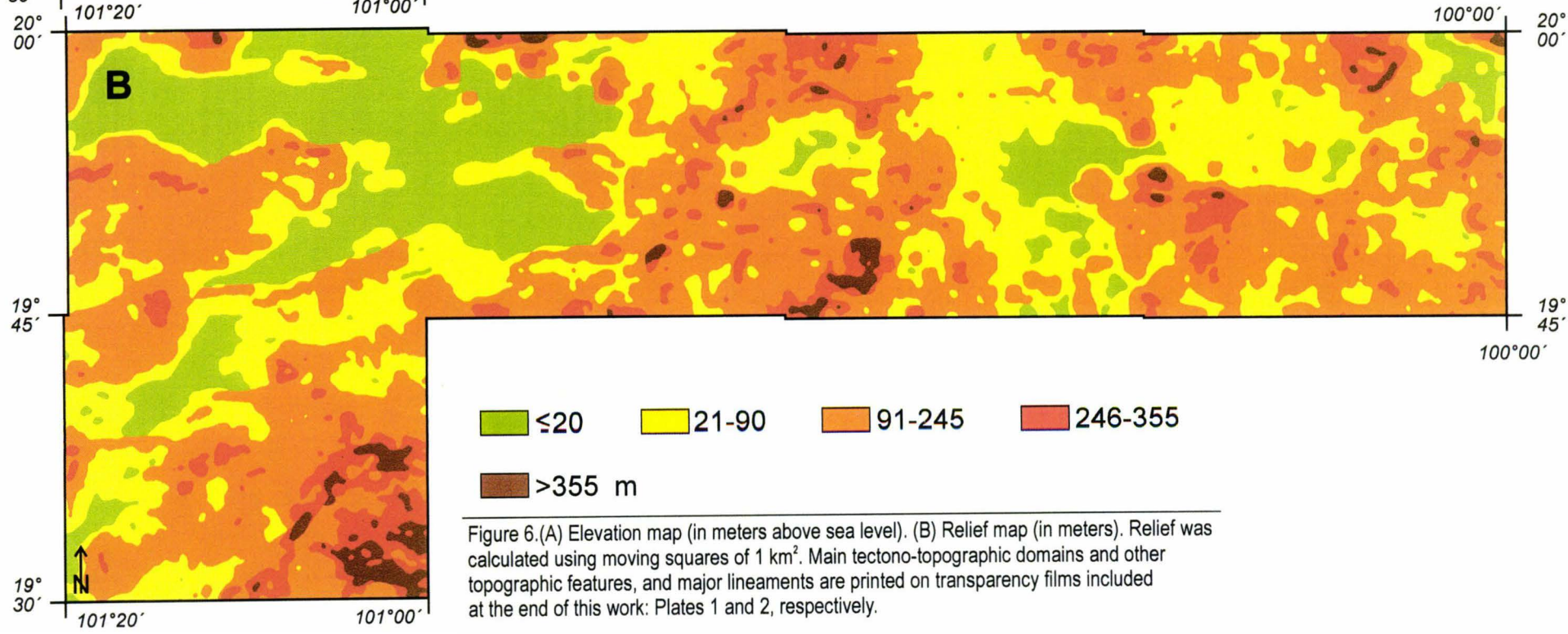
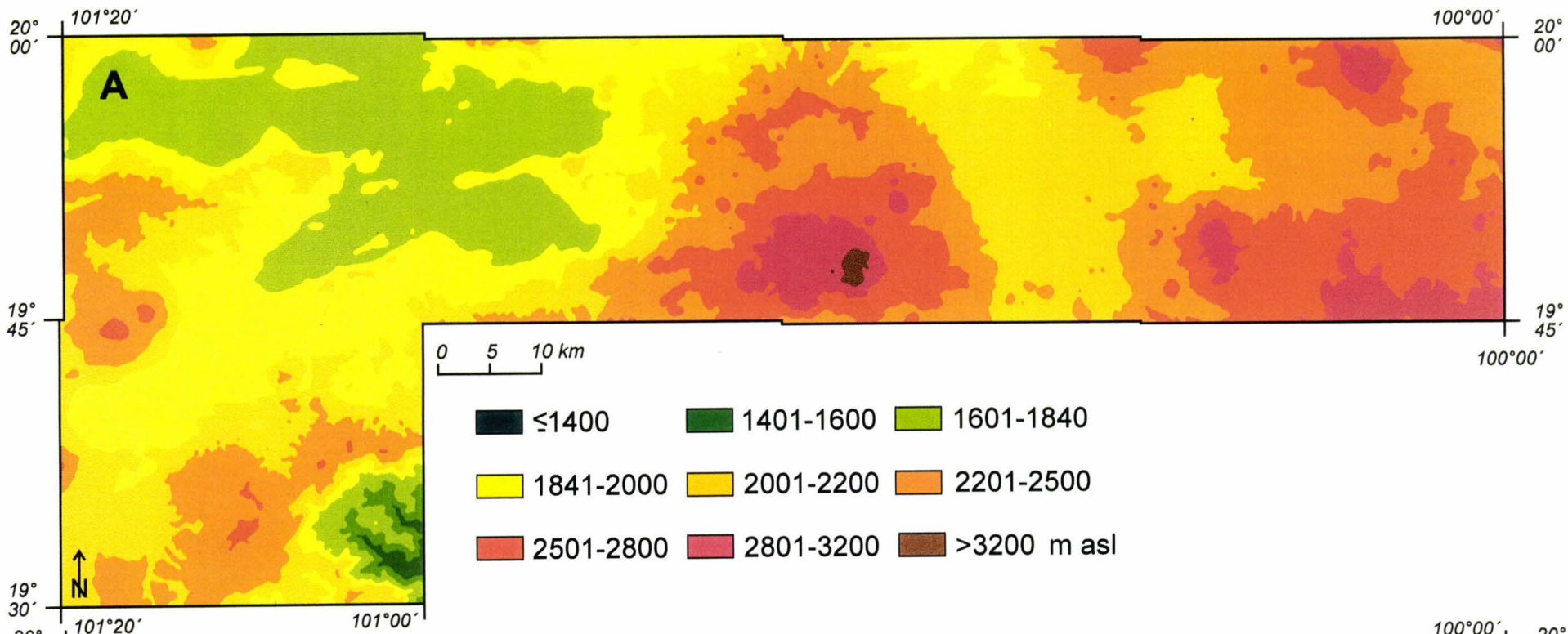


Figure 6.(A) Elevation map (in meters above sea level). (B) Relief map (in meters). Relief was calculated using moving squares of 1 km<sup>2</sup>. Main tectono-topographic domains and other topographic features, and major lineaments are printed on transparency films included at the end of this work: Plates 1 and 2, respectively.

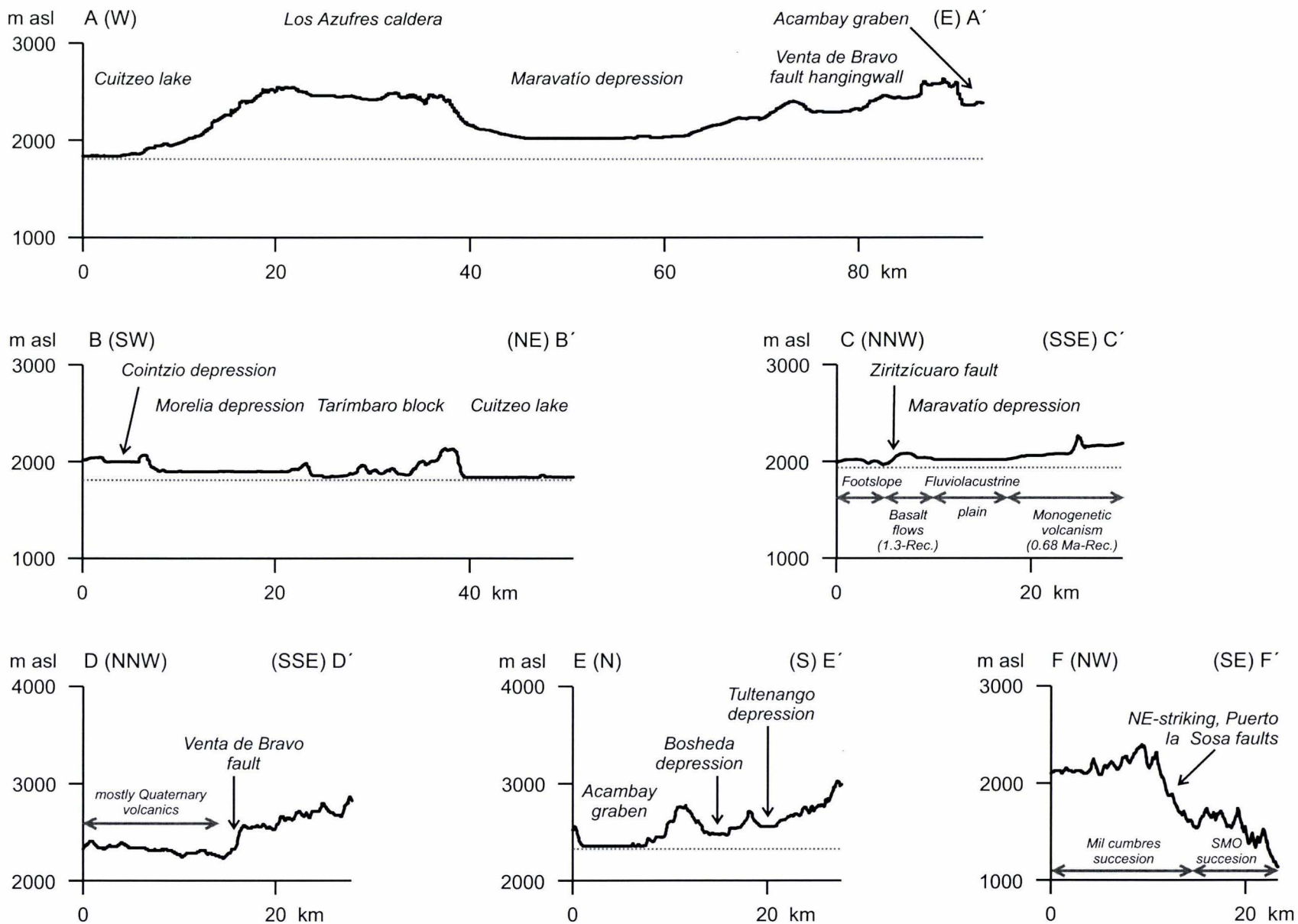


Figure 7. Topographic profiles (vertical exaggeration 10x). See Plate 1 for location of the profiles. Gray broken line below a few profiles is added to highlight lowering of depression floors from east to west and from south to north. Note very smooth topography of depression floors (mostly filled with fluvio-lacustrine sediments), and rugged topography of the Venta de Bravo hangingwall (profile D-D'). Lithologic information deemed necessary for correct interpretation of the features is marked on a few profiles. The short-wavelength step-like noise is due to the DEM structure.

Similar, step-like lowering of depression floors toward the north is encountered in the easternmost study area. Here, the small Tultenango depression is the highest (2560 m asl), the Bosheda depression lies at 2460 m asl, and the Acambay graben floor is the lowest (2360 m asl) (Fig. 7, profile E-E'). As in the case of the western depressions, the northern depression is the largest.

Los Azufres caldera and Venta de Bravo domain are oriented *ca.* N-S, hence orthogonal to the TMVB and the MAFS, and disrupt the central depression of the MAFS (Fig. 6A, Plate 1). The central, flat part of the Los Azufres caldera, occupied by fluviolacustrine sediments, lies *ca.* 400 m above the Maravatío depression and *ca.* 600 m above Cuitzeo lake (Fig. 6A, Plate 1; Fig. 7, profile A-A'). A series of volcanoes and lava flows constitute the SW border of the Venta de Bravo domain. This topographic high is disrupted in the middle where the Lerma river (No. 7 in Plate 1) crosses it. The flat part of the topographic high that separates the Venta de Bravo fault hangingwall from the Acambay graben, lies *ca.* 200 m above the graben and *ca.* 270 m above the central, flat portion of the Venta de Bravo hangingwall (Fig. 7, profile A-A').

### ***Relief***

The study area lies between 0 and 696 m of the relief values. The former are encountered at the depression floors, and the latter at the southern slope of the TMVB (Puerto la Sosa domain, Plate 1).

Throughout the TMVB, elevation generally correlate with variations in the relief values. Low-lying parts of the area are characterized by low relief values: at the basinal parts of the central depression the values are usually below 20 m. Only the northern and southern portions of the Maravatío depression show values slightly above 20 m. High-lying portions of the TMVB have high relief values, mostly above 90 m (Fig. 6B). The noteworthy exception from this rule is the Venta de Bravo hangingwall that is relatively depressed, but its relief values are almost always above 20 m.

Most of the southern slope of the TMVB [Puerto la Sosa tectono-topographic domain (Plate 1)] lies within the upper range of relief values – above 245 m (Fig. 6B). Notably, it is the lowest portion of the area, so the relation between altitude and relief at this domain is incompatible with the TMVB (see also section 5.1.4 below: “Morphometry of the tectono-topographic domains”).

### ***Slope gradient***

The study area lies within 0 to 49° range of slope gradient values. The highest values are observed at the Puerto la Sosa domain. Elevated TMVB tectono-topographic domains [Los Azufres and Venta de Bravo (Plate 1)] usually exhibit high slope gradients. A notable exception is the inner part of the Los Azufres caldera (Fig. 8A, Plate 1). Up-thrown MAFS footwalls usually exhibit high slope gradient values, regardless of their position within basinal domains (*e.g.*, at the western depressions), although in these cases values above 20° are relatively rare (Fig. 8A, Plate 1).

The slope gradient map highlights various linear features, *e.g.*, fault scarps or edges of lava flows. Lava and scoria cones, and volcanic domes are also highlighted: they form circles of highly inclined slopes. Where the cones suffered collapse, the marks are horseshoe-shaped (compare Fig. 8A, and Plates 3-7).

A conspicuous feature visible on slope gradient map is an alignment of (fault) scarps, which start at the southern border of eastern Cuitzeo lake, crosses the northern side of the Los Azufres caldera and the northern part of the Maravatío depression, and terminate as Ziritzicuaro fault scarp (Fig. 8A, Plate 1).

### ***Drainage density***

As noted in Materials and Methods chapter, the description below treats variations of drainage density within the TMVB only. I exclude Puerto la Sosa domain from this description due to incorrectly depicted drainage network in available digital maps.



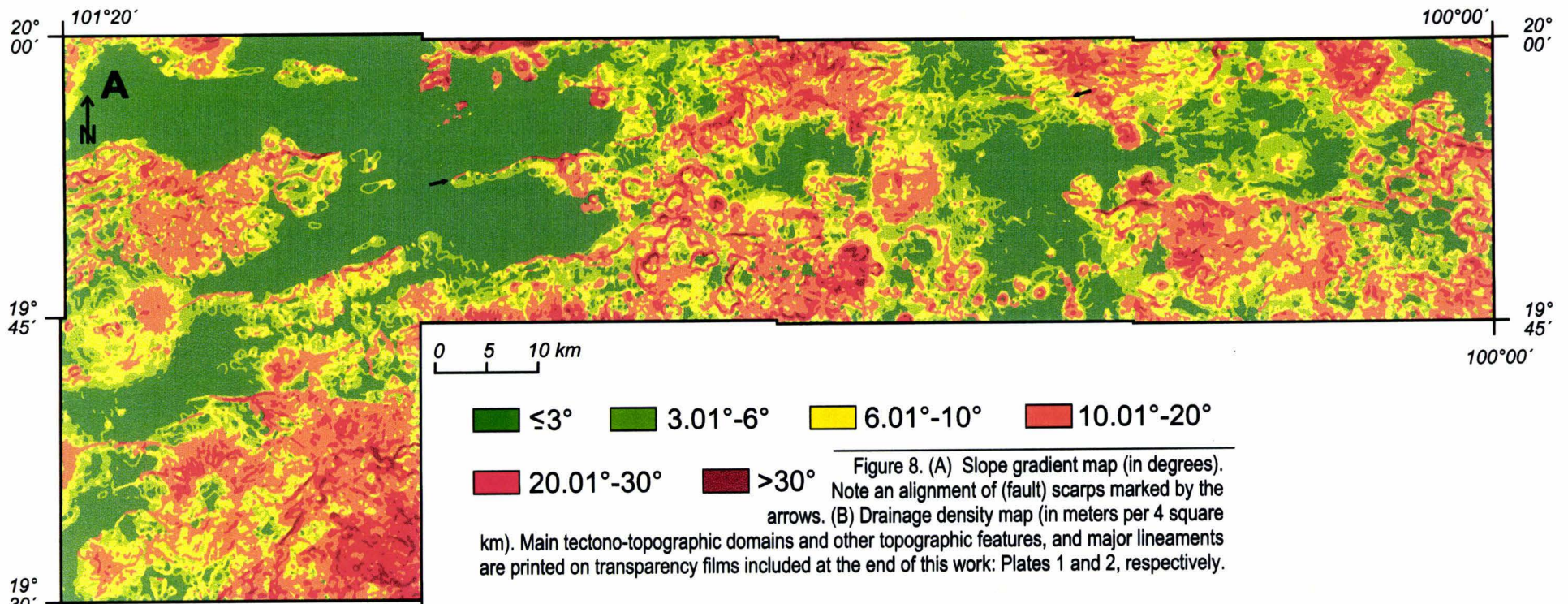
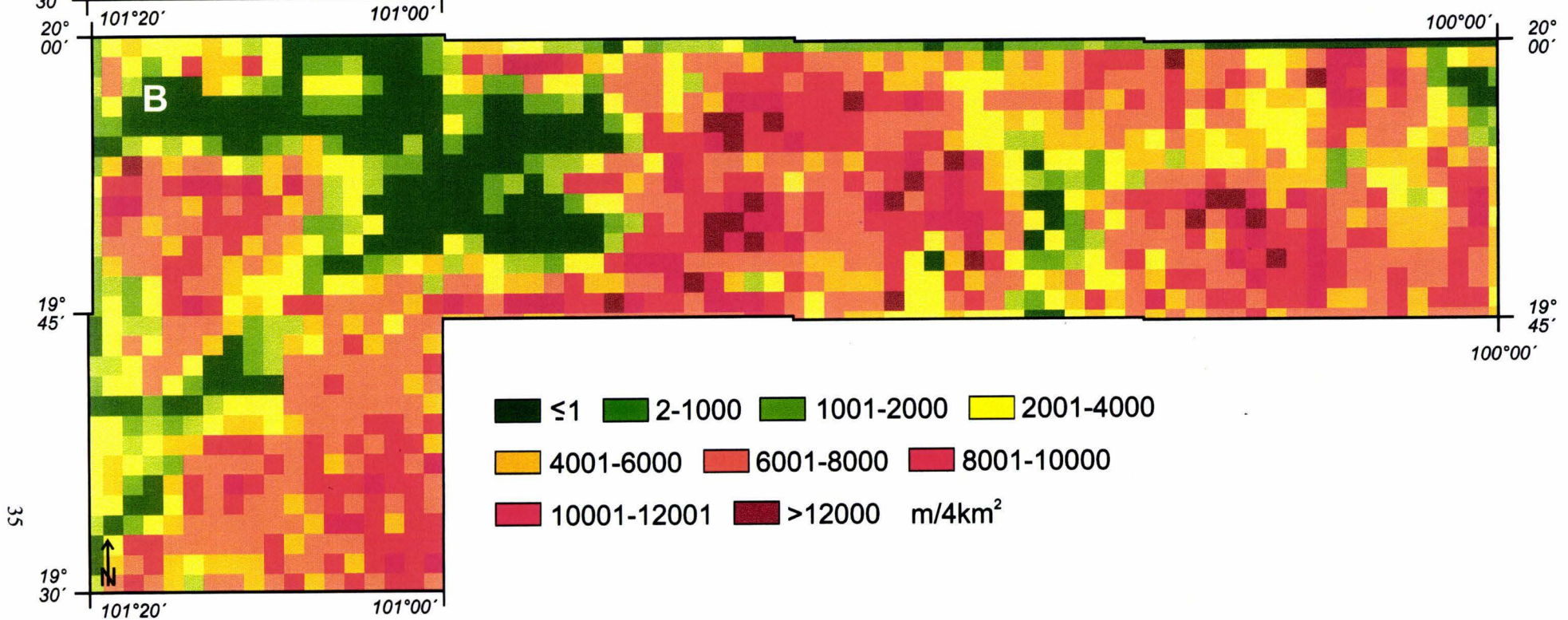


Figure 8. (A) Slope gradient map (in degrees). Note an alignment of (fault) scarps marked by the arrows. (B) Drainage density map (in meters per 4 square km). Main tectono-topographic domains and other topographic features, and major lineaments are printed on transparency films included at the end of this work: Plates 1 and 2, respectively.



The drainage density within the TMVB spans the values between 0 and slightly over 15000 m/4 km<sup>2</sup>. The former are encountered at fluviolacustrine plains. Low drainage densities are also typical at very youthful volcanic terrain, *e.g.*, parts of lava flow north of Cointzio fault scarp (Fig. 8B, Plate 1, also compare Fig. 8B and Plate 3). Relatively low drainage densities are encountered in footwalls of normal faults of Morelia region (Fig. 8B, Plate 1).

High drainage densities (over 10000 m/4km<sup>2</sup>) are encountered at several MAFS fault scarps: western Cuitzeo, Santa Ana Maya, eastern Queréndaro, Charo, La Trasuila, and central Venta de Bravo (Fig. 8B, Plate 1). The latter features have the highest values: slightly over 15000 m/4km<sup>2</sup>. Notably, the drainage density is also high in both edges of the Los Azufres caldera, where it displays trends transverse to the MAFS (Fig. 8B, Plate 1).

#### ***Fault scarp density***

The density of fault scarps varies in the MAFS. In the basinal parts of the system, the scarps are usually concentrated in narrow zones that border the depressions. In the transverse high-lying areas (Los Azufres and Venta de Bravo domains) the scarps are distributed more or less uniformly across the whole system (Fig. 9A, Plate 1). The mean density of fault scarps is 480 m/4km<sup>2</sup>, with minimum value of 0 m/4km<sup>2</sup>, and maximum of 7920 m/4km<sup>2</sup>.

A few zones of the study area show increased fault scarp density, which is usually due to the appearance of many relatively small faults instead of a single fault scarp. These scarps can be observed on detailed geomorphologic maps (loose illustrations at the end of this thesis: Plates 3-8). They are (see Fig. 9A, Plate 1 for general location): immediately southwest of the Cuitzeo lake (Plate 4); immediately southwest of the Santa Ana Maya fault (Plate 5); at the Queréndaro fault scarp, where very many small faults cut the lava flow that entered the lacustrine zone (Plate 5); in the southern part of Los Azufres caldera (Plates 5 and 6); and northeast of Venta de Bravo, where these faults are the NE boundary of the Venta de Bravo domain (Plate 7).

#### ***Lineament density***

The density of lineaments varies between 0 and 4327 m/4km<sup>2</sup>, with mean value of 200 m/4km<sup>2</sup>. Low values correspond to the depressions of the area. High values correspond to the outcrops of pre-Pliocene rocks: the mafic basal sequence in the footwall of western Cuitzeo fault, the upper Miocene-lower Pliocene lacustrine deposits in the vicinity of Charo, the Atécuaro caldera andesites, Sierra Madre Occidental outcrops at the Puerto la Sosa domain, upper Miocene mafic basal sequence northeast of Maravatío, middle(?)-upper(?) Miocene andesites at northern Los Azufres caldera, and Tlalpujahuá complex in the footwall of Venta de Bravo fault (compare Fig. 2 with Fig. 9B and Plates 1, 2). High lineament density southwest of the Los Azufres caldera and in its southeastern boundary is due to the alignments of scoria cones (Fig. 9B, Plates 1, 2).

### ***5.1.4 Morphometry of the tectono-topographic domains***

The spatial distribution of elevation, relief, and slope gradient values shows strong dependence on previously described, major tectono-topographic domains in the region (Figs. 6, 8A, Plate 1, Appendix 1). Drainage density, fault density and lineament density maps apparently depend on other factors. The drainage density is meaningful only at the TMVB outcrops (see scaling factors in section 4.1.6) and within this terrain the distribution of values seems to be mostly MAFS-controlled (see above). The fault density is mainly describing the peculiarities of the MAFS, and the lineament density depends mainly on substrate age.

Relief and slope gradient maps show strong correlation of 0.86 (Tab. 1), so it is reasonable to use only one of them for characterization of morphometry of these domains. Given that the slope gradient map is more sensitive to the influence of small structures, so its dependency on major structures is somewhat less marked, elevation and relief maps were used for comparison of morphometry between tectono-topographic domains and sub-domains.

For efficient comparison of the morphometry between the domains and subdomains, illustration of value distributions (histograms) was combined with scatter diagrams, by setting the elevation and relief histograms

along horizontal axes with the same origin and scale (Fig. 10). The data have non-gaussian distributions except in the case of Puerto la Sosa relief values (Fig. 10), and log transform of it did not produce gaussian distributions from the data of basinal domains. Therefore, it is impossible to use means ( $\mu$ ) and standard deviations ( $\sigma$ ) to characterize all domains and find out if the differences between them are statistically significant ( $\mu$ - $\sigma$  in a few cases is lower than the real lower limit of values at a given domain). Even if I find the narrowest continuous ranges that cover 68% of the area at each domain (same % as  $\mu \pm \sigma$  in the case of gaussian distribution), these ranges would not necessarily be meaningful in the case of non-gaussian distributions. Therefore, the comparison that follows is qualitative. Nonetheless, I marked the narrowest continuous ranges that cover 95% of each population (dark gray in Fig. 10), as I consider that it is a reasonable approximation of the scatter of values at each domain. The scatter of elevation values is equal to the relief amplitude of Bocco *et al.* (2001) of each domain.

Table 1  
Correlation coefficients between morphometric maps.

	Elevation	Relief	Slope gradient	Drainage density	Fault density	Lineament density
Elevation	1.00	0.40	0.34	0.46	0.13	0.16
Relief		1.00	0.86	0.61	0.17	0.19
Slope gradient			1.00	0.54	0.14	0.20
Drainage density				1.00	0.14	0.27
Fault density					1.00	-0.12
Lineament density						1.00

The correlation coefficients are generated in two steps: first covariance matrix of the maps is calculated, and then each (covariance<sub>map1map2</sub>) value is divided by a square root of (variance<sub>map1</sub>\*variance<sub>map2</sub>). The coefficients should be taken with caution due to non-gaussian distributions of values of the maps (see Appendix 1 for further reasoning and histograms of the entire elevation, relief, and slope gradient maps).

The Puerto la Sosa domain (southern slope of the TMVB) has the lowest elevation of all domains, reaches the highest relief, and shows the highest scatter of both elevation and relief values, although it is the second-smallest domain of the region. The relief values at this domain have an almost normal distribution (Fig. 10).

The distribution of elevation and relief values at the major, TMVB domains differ from basinal to high-lying domains (Fig. 10). In the former, the distributions of both elevation and relief are strongly skewed towards the low values and show much less scatter of elevation values, and less scatter of relief values than at elevated TMVB domains. The relief values distribution at the Venta de Bravo area is skewed, but the scatter resembles those of the Los Azufres caldera.

Among the MAFS-controlled sub-domains, the distributions of values at the up-thrown, western Cuitzeo fault footwall are similar to the transverse high-lying domains, but the scatter of both elevation and relief values is considerably smaller than in these domains (hence, rather typical of basinal domains). The Venta de Bravo fault hangingwall (down-thrown side) shares some of the basinal domains characteristics (*e.g.*, skewness of relief values), but the scatter of both elevation and relief values is typical for high-lying domains. The distributions of values at the Venta de Bravo fault footwall resemble high-lying domains (as expected).

### 5.1.5 Distribution of landforms

Distribution of landforms is illustrated in detailed geomorphologic maps (loose illustrations included at the end of this work: Plates 3-7, legend in Plate 8). Various features described here are located only on these maps for scale reason. As anticipated in Materials and Methods chapter, these maps provide data on possible tectonic controls over landform distribution and surficial processes shaping the region.

To the west of Los Azufres caldera almost all fluviolacustrine plains and a considerable part of footslopes developed in the hangingwalls of normal faults (Plates 3-5, 8). Noteworthy, in the western portion of this region almost all faults are north-facing and all fluviolacustrine plains are located to the north of them (Plates

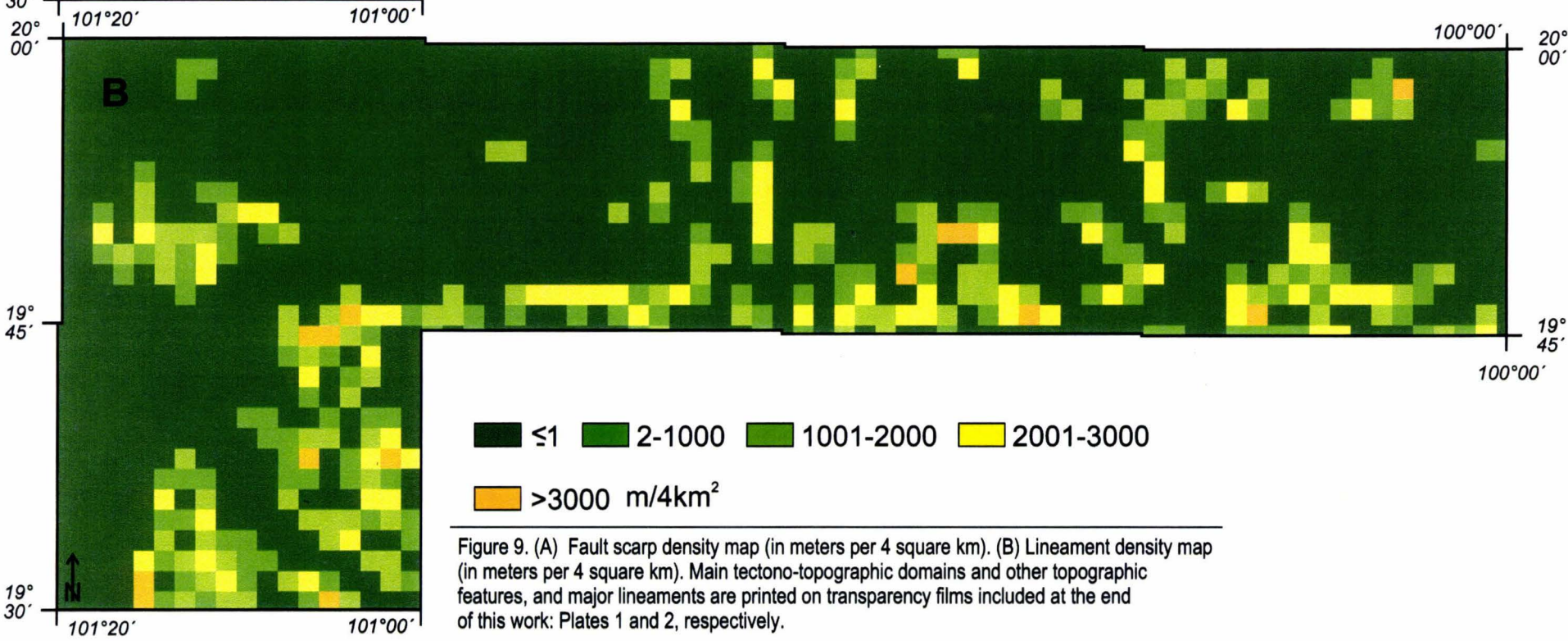
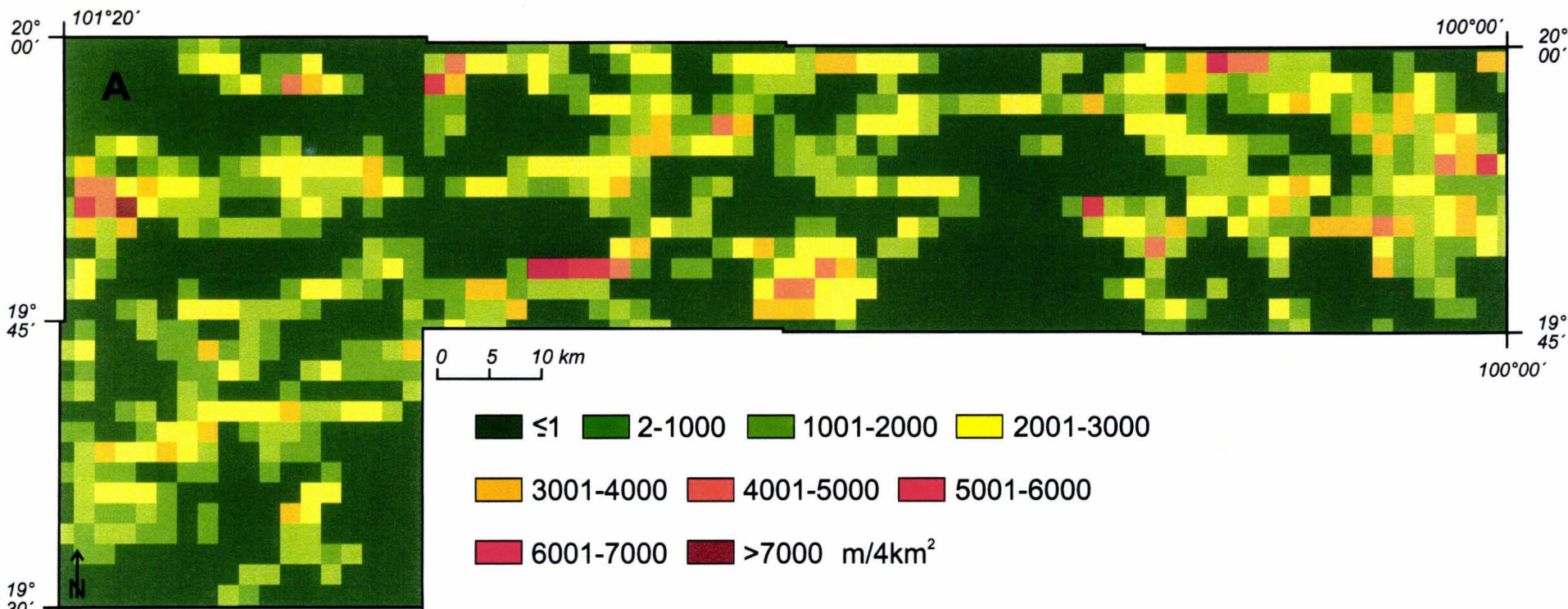


Figure 9. (A) Fault scarp density map (in meters per 4 square km). (B) Lineament density map (in meters per 4 square km). Main tectono-topographic domains and other topographic features, and major lineaments are printed on transparency films included at the end of this work: Plates 1 and 2, respectively.

MAJOR, TRANVERSE MEXICAN VOLCANIC BELT DOMAINS  
 MAFS-controlled sub-domains  
 southern slope of the TMVB

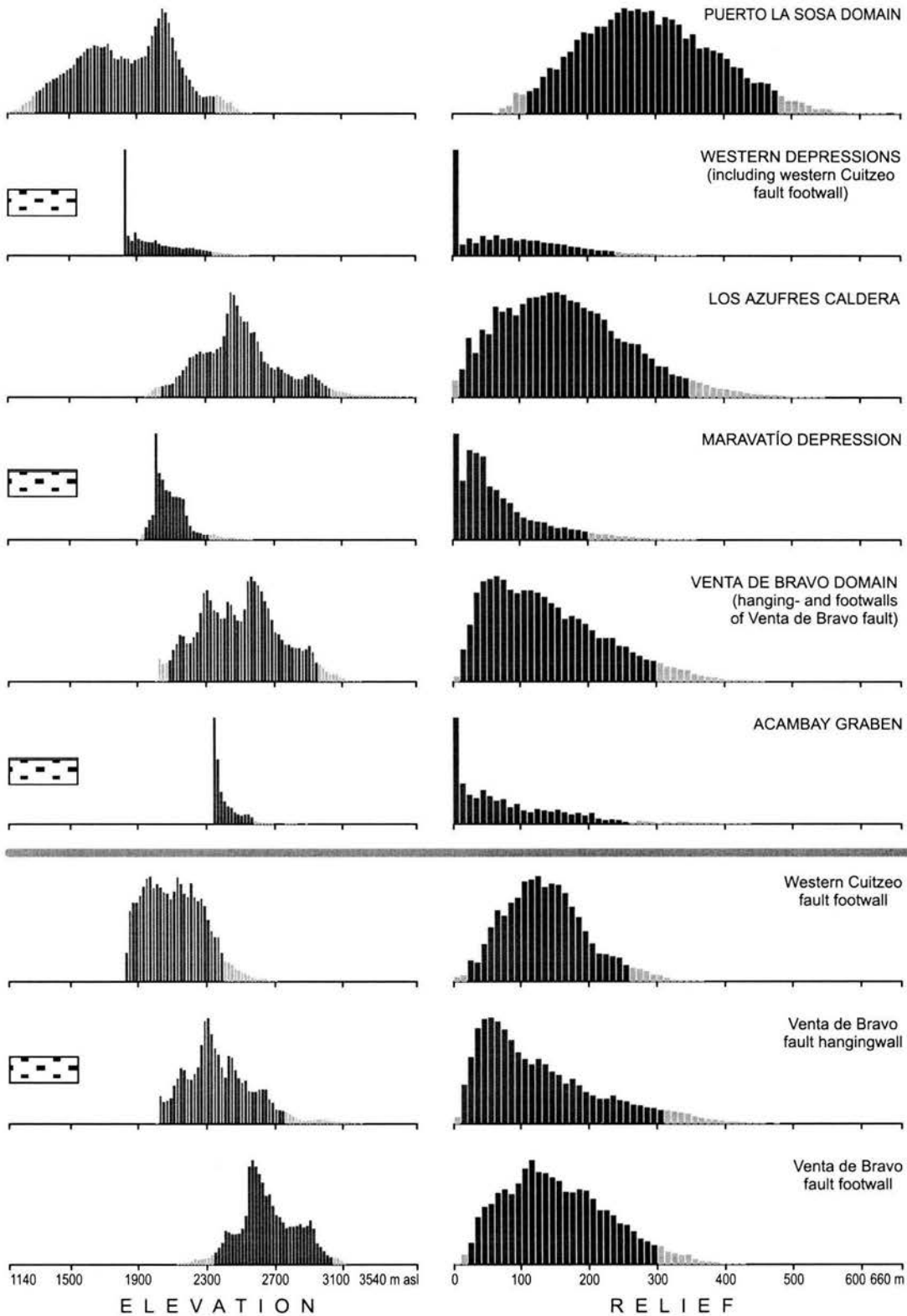


Figure 10. Distribution of elevation and relief values in each tectono-topographic domain (see Plate 1 for location of the domains). Histogram bars represent 20-m intervals of elevation, and 10-m intervals of relief. Height of histogram bars is proportional to the percent of area of each domain covered by the interval. Elevation and relief histograms are set along axes with the same origin and scale, in order to evaluate shifts between the domains. Dark gray bars sum 95% of area at each domain. Stippled rectangles mark basinal domains and the Venta de Bravo fault hangingwall (down-thrown block of the largest MAFS fault). Note westward lowering of the TMVB domains (toward the top of the page, see Plate 1). See text for discussion.

3, 4, 8). A south-tilted weathering/erosion-dominated topographic surface (slope and summit surface) separates these plains (Plate 4). South of the Morelia–Jarapeo fault scarp, the tilt of topographic surface is lacking (Plate 3). At the eastern part of western depressions (Plate 5), close to the Los Azufres caldera faults are south- (Santa Ana Maya and Araró), and north-facing, fluviolacustrine plain and a footslope is located between them. The tilt of weathering/erosion-dominated topographic surface is mostly to the NW, except in the near footwall of the eastern Cuitzeo fault scarp (Plate 5). Puerto de Cabras N- (B&R) striking fault scarp (NW corner of Plate 5) apparently marks the boundary between the south- and north- tilted topographic surfaces (Plates 4, 5). It also separates footslope and fluviolacustrine plain developed in its hangingwall (to the east) from erosion-dominated slope area of its footwall (to the west) (Plate 5). The Cuitzeo lake preserves the water column during the wet season and the eastern part of this lake is filled with water most of the year. The southernmost Queréndaro depression is also flooded during the wet season (Plates 4, 5, 8).

Most of the Los Azufres caldera (Plates 5, 6, 8) is being eroded, except for its inner part and eastern flank, where footslope and fluvio-lacustrine sedimentation are taking place. Also, several small fluviolacustrine plains developed in the hangingwalls of the MAFS and the NE-SW fault scarps, in southern Los Azufres caldera (Agua Fria area) (Plates 5, 6, 8).

In the Maravatío depression, located to the east of the Los Azufres caldera (Plates 6, 8), fluvio-lacustrine and footslope deposition is distributed in W-striking belts, or in the hangingwalls of the MAFS faults. It is most notable in the case of footslope to the north of the Uripitío–Zirizicuaro fault scarps, but is also visible in the case of fluviolacustrine plain pushed to the north by basaltic lavas that erupted from scoria cones aligned at E-striking faults in the southern part of the depression (Plates 6, 8). The ESE-striking Los Ocotes fault is the NE boundary of the Maravatío depression fluviolacustrine plain at the Venta de Bravo domain (Plates 7, 8). Nevertheless, some fluvio-lacustrine and footslope deposition does take place in the southern (erosion-dominated) Maravatío depression (Plates 6, 8). The E-striking, erosion-dominated (slope) area between Zirizicuaro fault scarp and Maravatío (Plates 6, 8) is also noteworthy.

Further east, in the Venta de Bravo domain and the western Acambay graben (Plates 7, 8), the deposition-dominated surfaces and footslopes are located in front of the Venta de Bravo fault scarp (proximal part of the Venta de Bravo fault hangingwall), inside of the Acambay graben, and they partly fill the distal Venta de Bravo fault hangingwall. The MAFS-controlled distribution of these deposition surfaces is quite clear, although some of them are also due to volcanic landforms, most notably the footslopes and fluviolacustrine plains skirting Altamirano and San Miguel volcanoes, and also El Oro volcanic domes (Plates 7, 8). The weathering- and erosion-dominated surfaces follow a similar pattern, *i.e.*, is their distribution is MAFS and volcanic landform controlled. In particular, erosion takes place in the footwall of Venta de Bravo fault, but also at lava cones, domes and basalt-filled, distal Venta de Bravo fault hangingwall. The tilt of topographic surface is only observed in the highly deformed relay ramp between the eastern Venta de Bravo, and the Pastores fault scarps (Plates 7, 8).

Finally, Plates 5-8 illustrate that normal faulting control location of many cineritic cones built on the traces of major faults. Most of these cones are subsequently displaced by the same faults that led to their construction.

In summary, Plates 3-8 show that throughout the study area almost all of fluvio-lacustrine and the greater part of footslope and colluvial sedimentation is confined to the E-striking belts in front of the MAFS faults. The only exceptions are the internal parts of Atécuaro and Los Azufres calderas (Plates 3 and 6, respectively), where fluvio-lacustrine sedimentation is due to volcanic landforms, and footslopes that skirt major volcanoes of the region.

### 5.1.6 *Fault scarp degradation*

Several mapped features allow assessment of the degree of fault scarp degradation. They are: free rock faces, collapse scars carved in the scarps, talus accumulation/footslope deposits at the scarp feet, erosion cirques, rounding and/or lowering of the scarps, triangular facets, and fluvial dissection of the scarps.

These features are mapped in Plates 3-8. The exceptions are: (1) free faces that were identified in the field and cannot be represented at the map scale and (2) fluvial dissection, which is almost always accompanied by

triangular facets so the latter is the substitute for the former, unless the contrary is indicated (Tab. 2). The presence or absence of these features at the main fault scarps of the study area is summarized in Table 2.

Table 2  
Morphologic features at the main fault scarps of the study area.

		<b>Morphologic feature</b>						
		<b>Fault Name</b>	<i>fluvial dissection</i>	<i>erosional cirques</i>	<i>talus accumulation</i>	<i>collapse scars</i>	<i>triangular facets</i>	<i>free rock face</i>
West of Los Azufres caldera	N	Western Cuitzeo	√√	√√	√√		√√	
		Tarimbaro–A. Obregón	√	√	√	√	√	
	Western portion of the western depressions	Charo	√√ (along whole fault)	√	√√		√ (only E portion)	
		S	Morelia–Jaripeo	√ (cuts consequently an old volcanic slope)		√	√√	√√
	Cointzio				√			
	Eastern western depressions	Santa Ana Maya	√√		√√		√√	
		Eastern Cuitzeo			√	√		
		Queréndaro			√			
	Los Azufres caldera	Curinhuato	√√		√		√√	√√
		La Trascuila	√		√		√	
Agua Fria		√		√				
East of Los Azufres caldera	Central Venta de Bravo	√√	√	√√	√√	√√		
	Western Venta de Bravo						√√	
	Eastern Venta de Bravo			√			√√	

√ indicates presence of the respective feature, and √√ indicates relatively intense development of the feature. For generalized traces of fault scarps see Plate 1, details are mapped in Plates 3-7.

Free rock faces and collapse scars are indicative of fresh and/or active scarps. Triangular facets are indicative of active fault scarps and are only present at dissected scarps (hence relatively degraded, or consequently cutting previously dissected slope). Significant talus accumulation is likely at degraded and/or active scarps. Lack of talus signifies a fresh scarp if conditions do not allow fast deposit removal, *i.e.*, there is no river running along the scarp foot. Erosion cirques and scarp rounding/lowering (the latter marked in Plates 3-8) indicate degraded scarps.

## 5.2 Structural geology

### 5.2.1 Fault geometry and associated strata at outcrop scale

Outcrops observed in the study area reveal a surprising picture because although located within the same fault system, most outcrops to the west of Los Azufres caldera feature highly dipping strata, whereas strata in outcrops located to the east of the caldera strata is usually subhorizontal or its inclination is clearly primary (*e.g.*, dipping layers in cineritic cones). Such differences might be due to several causes: (1) pre-existing structures to the west of Los Azufres, (2) primary high dips to the west of Los Azufres, (3) younger rocks outcropping to the east of Los Azufres, or (4) different fault geometry in these two areas. Below I describe a few examples of fault geometries that permit evaluation of these possibilities.

A detailed survey along the western Cuitzeo fault (Plate 1), where high strata dips cluster, reveals that the strikes of individual normal (MAFS) fault planes and strikes of dipping strata in front of them, are in most cases similar (the difference do not exceed 20°), but the dips of the two are opposite. One example of such behavior is shown in Figure 11, where also the deflection of a fault plane on the stratification can be observed.

Moreover, at three locations along the western Cuitzeo fault roll-over structures were observed (Fig. 11). The footwall of this fault is mostly made up of upper Pliocene (*ca.* 2.8 Ma old) Cuitzeo ignimbrite (Fig. 2). Given the opposite dips of strata and faults, a plausible explanation seems to be listric fault geometry, which produces roll-over structures (also called reverse drag anticlines) in fault hangingwalls (Fig. 11). Such associations indicate that strata is tilted by the activity of the MAFS faults, and is not due to pre-MAFS tectonics or primary dips.

An unusual case of fault geometry was observed at the Jaripeo fault east of Jaripeo village (Fig. 12). At this location the topographic drop is to the north, triangular facets at fault scarp indicate N-dipping normal fault, and the western prolongation of Jaripeo fault – the Morelia fault – is a major, normal, N-dipping fault (Fig. 12). Nonetheless, at outcrop scale the principal fault plane is an S-dipping reverse fault: 12 Ma old Morelia ignimbrite is thrust over the fault talus made mainly of ignimbrite clasts and subordinate amount of basaltic clasts (the latter probably coming from 18.2-11.2 Ma old Mil Cumbres succession) (Fig. 12). Other faults in this outcrop include S-dipping reverse faults and N-dipping normal faults. These two sets are mutually cross-cutting, and therefore coeval. One explanation of this configuration is local fault plane dip sense reversal close to the surface, and the formation of fault splays (Fig. 12). Such reversals (especially at ridges) have been documented (*e.g.*, Tibaldi, 1995, 1998; Miller and Dunne, 1996). A very steep upper part of a fault plane, needed for such reversal, is characteristic of listric faults. Alternatively, this site could also possibly be an expression of alternating contraction and extension.

East of Los Azufres, as anticipated above, strata at, and in front of fault scarps are usually subhorizontal (Fig. 13). In the case of late Quaternary rocks it is not surprising, given that young strata is obviously less displaced (hence less tilted) by faults whose activity dates back to the late Miocene. In fact, late Quaternary strata are also usually subhorizontal west of Los Azufres. Nevertheless, as can be seen in Figure 13, subhorizontal strata at normal MAFS faults east of Los Azufres date back to the late Miocene.

### 5.2.2 Normal, strike-slip and reverse faults at outcrop scale

Previous studies suggest that strike-slip and reverse faults affecting the Neogene and in some cases also early Pleistocene rocks appear to be absent in younger rocks in central TMVB (*e.g.*, Pasquaré *et al.*, 1988; Ferrari *et al.*, 1990, 1994a; García-Palomo *et al.*, 2000, 2002). Hence, these authors consider that contractional structures are characteristic of early phases of deformation of the central TMVB.

However, during this study reverse and strike-slip faults were also found in late Quaternary rocks, both close to major normal faults and within basin fill. A few examples are shown in Figure 14. The first of them (Fig. 14A) is a reverse-oblique, NW-striking left-lateral reverse fault within the basin fill in the central Maravatio depression, which produced folding of basaltic lava flow, welded volcanic ash and surficial deposits. The volcanics are 1.3 Ma or younger (Pasquaré *et al.*, 1991). Two other examples (Fig. 14B and D) are reverse faults encountered in the vicinity of normal fault scarps. In Figure 14B reverse faults cut a cineritic cone located in proximal hangingwall of the Queréndaro fault and considered 0.81-0.79 Ma (from isotopic ages 12, 13 and 22 in Fig. 2). In Figure 14D reverse faults cut and fold the 0.87-0.75 Ma basalts south of the eastern tip of the western Cuitzeo fault. Another example are conjugate, subvertical, left-, and right-lateral faults observed at the eastern Cuitzeo fault (Fig. 14C). These faults cut volcanic ash deposits of the last phase of a cineritic cone built on the trace of the eastern Cuitzeo fault, and 0.87-0.75 Ma or younger.

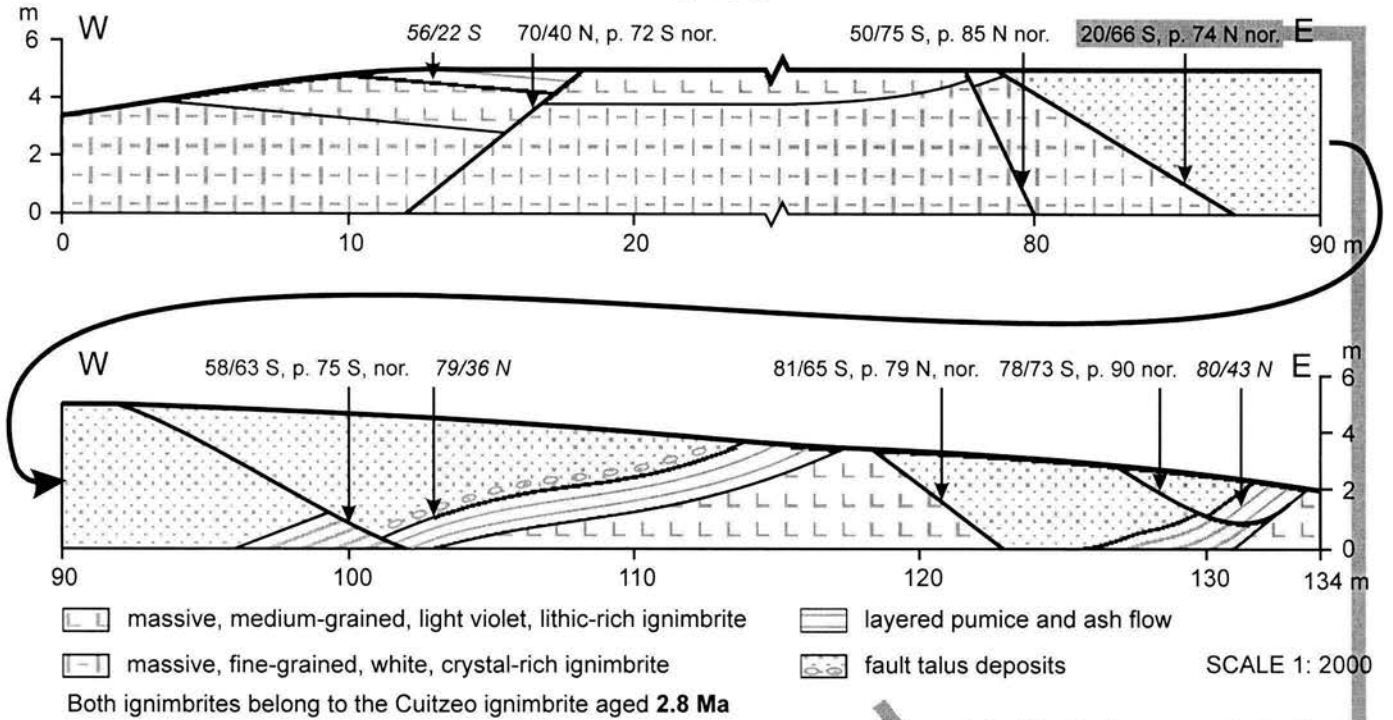
The last example of contractional structures, in this case affecting Holocene soil, is also one of the key outcrop for understanding the deformation pattern in the area. In Figure 15 the set of oblique-normal faults displace the base of Holocene soil and underlying volcanic ash and paleosol layers, which in nearby (a few km away) outcrops contain upper Pleistocene mammal bones (Garduño-Monroy, Instituto de Investigaciones Metalúrgicas UMSNH, 2000, and Pantoja-Alor, Instituto de Geología UNAM, 2003, personal communication). The site is located at a valley side, and on some of the faults progressive deformation (lower layers displaced more than upper layers) is observed (Fig. 15). These factors rule out the possibility, that the faulting is due to, or is enhanced by human activity, namely water extraction from unconsolidated sediments, which accelerates displacement rates of faults by over one order of magnitude in many fluvio-lacustrine plains in central TMVB (Suter *et al.*, 2001). At this site one fault strikes NNE-SSW and has left-lateral displacement.



Strata tilt in front of western Cuitzeo fault segments (outcrop sketch).

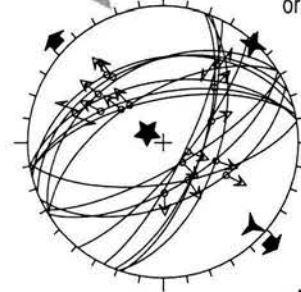
Note similar strikes and opposite dips of strata and corresponding fault segment.

Site 29 in Fig. 18, Appendix 4



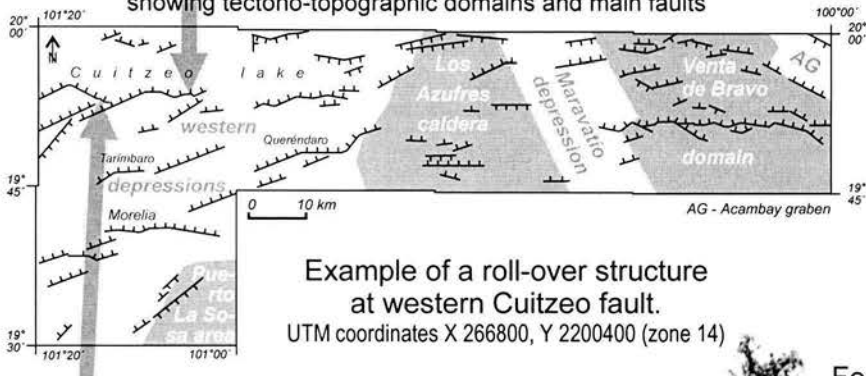
Stereoplot of fault planes collected at the outcrop sketched above.

Note that 3 to 4 sets of faults can be distinguished, and that NW-SE local extension is in accord with orientation of the major fault segment



Drag folds at a fault plane in outcrop sketched above

Study area map showing tectono-topographic domains and main faults



Formation of a roll-over structure.

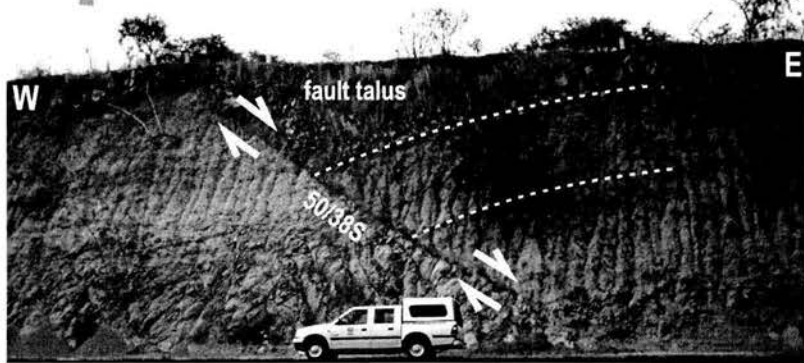
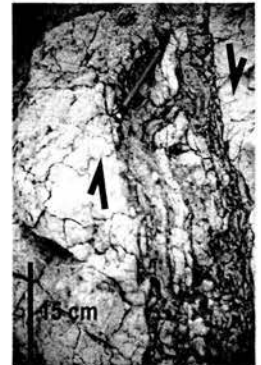
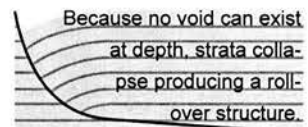
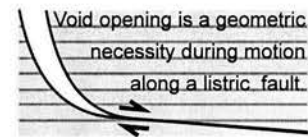
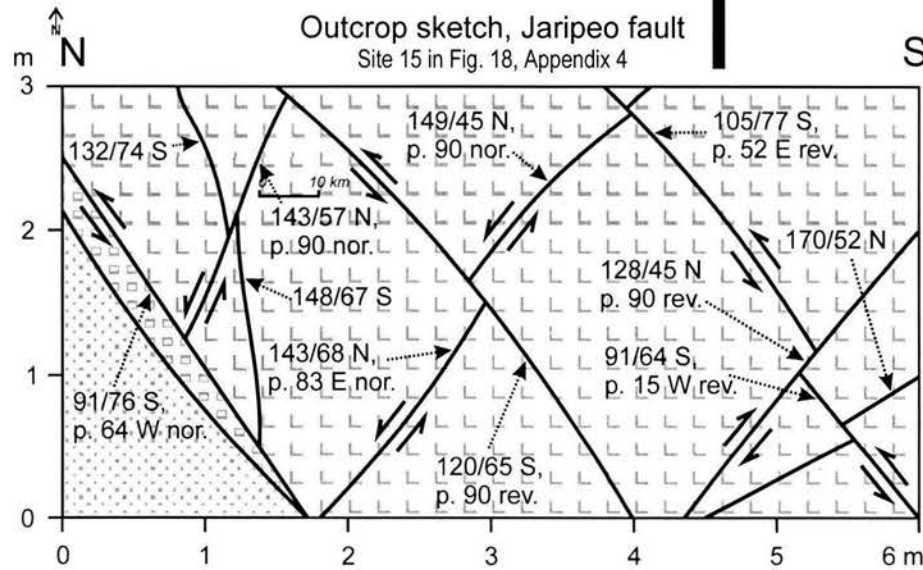
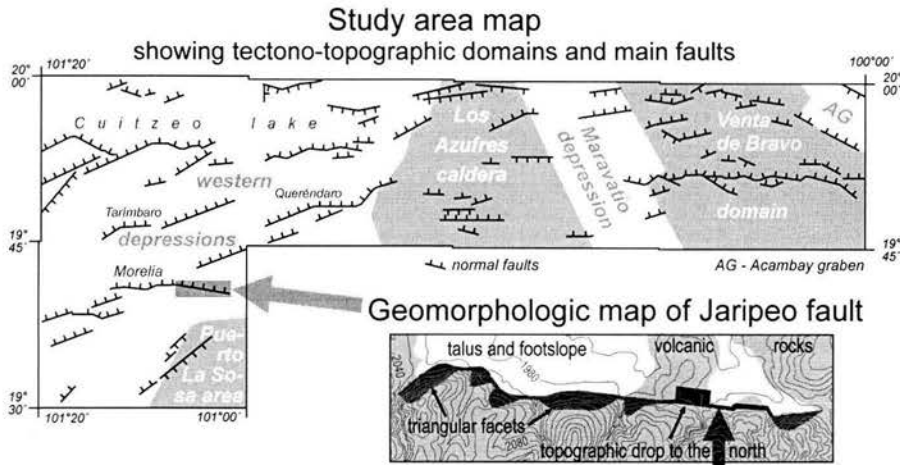
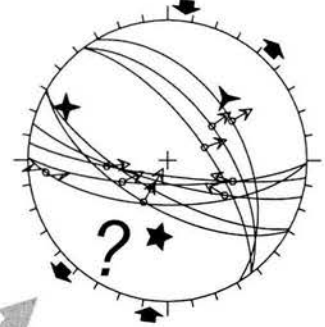


Figure 11. Strata tilt and roll-over structures at western Cuitzeo fault, indicating listric subsurface fault geometry. Fault plane measurements are given in strike/dip/dip sense, pitch/fault type format. Strata position measurements are given in strike/dip/dip sense format. Stereoplot of fault planes is lower hemisphere, equal angle, five-, four- and three-point stars are contraction, intermediate and extension axes, respectively. See text for discussion.



**Stereoplot of fault planes**  
collected at the site  
sketched below

Note that from simultaneous normal and reverse faults, striae inversion cannot produce reasonable extension/contraction orientations.



- fault talus deposits
- fault gauge (breccia)
- massive, fine-grained, white, crystal-rich, slightly welded ignimbrite, belonging to Morelia ignimbrite aged **12 Ma**

SCALE 1: 5

**What happens in this outcrop?**



- (1) Major reverse fault?
  - (2) Alternating contraction and extension?
  - (3) Local reversal of fault plane dip sense close to the topographic surface?
- Note that option (3) is consistent with triangular facets along fault scarp and with regional fault pattern. This option suggest listric (rather than planar) fault geometry, where very steep upper part is more likely.

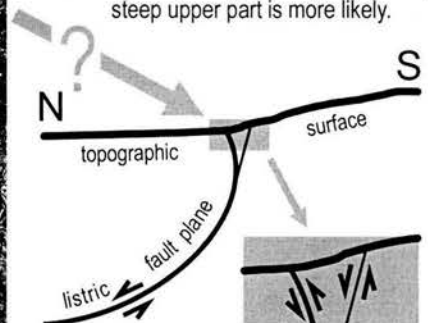


Figure 12. Cross-cutting reverse and normal fault planes at Jaripeo fault. Sense of slip was obtained from kinematic indicators in fault planes and from sense of displacement of pre-existing faults. Fault measurements are given in strike/dip/dip sense, pitch/fault type format. Stereoplot is lower hemisphere, equal angle, five-, four- and three-point stars are contraction, intermediate and extension axes, respectively. See text for discussion.

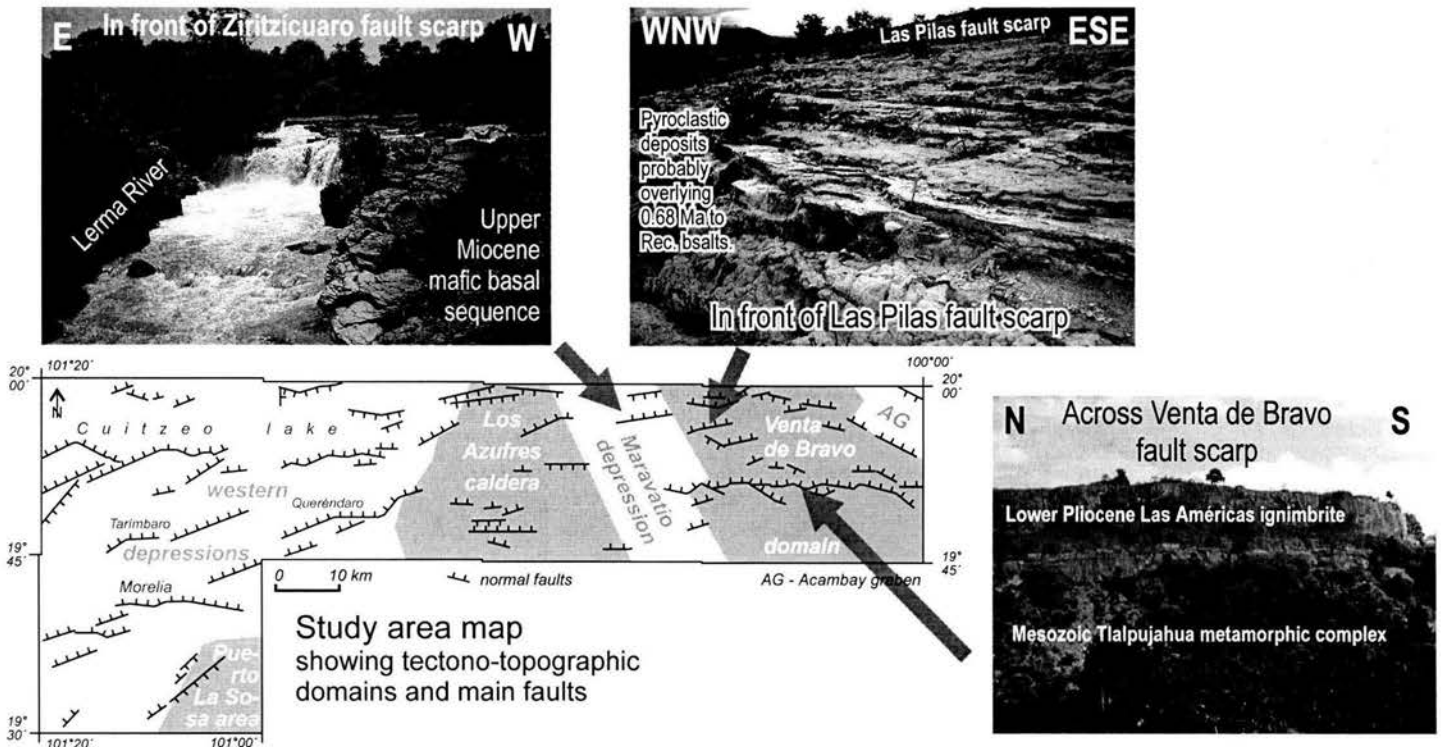


Figure 13. Examples of subhorizontal strata near fault scarps east of Los Azufres caldera.

The remaining faults strike NNW-SSE to NW-SE. Among them faults dipping to the NE are dextral-normal (the majority), and those dipping to SW are sinistral-normal. There are also two faults without striae. Striae inversion of NW-striking dextral faults and NNE-striking sinistral fault gives NNE-trending contraction and ESE-trending extension shown on stereoplot in Figure 15, consistent with conjugate faults. The entire population, which also includes sinistral-normal, NW-striking faults, does not give a reasonable result with right-dihedra inversion (as expected), neither is it coherent with orthorhombic fault pattern developing in 3-D strain (Reches, 1998; Reches and Dieterich, 1983). Hence, the only plausible explanation seems to be that at least at the scale of individual small faults, slip plane geometry and/or faulted blocks configuration control slip direction and sense. *E.g.*, a block bounded by SW-dipping fault and WNW-dipping fault (faults 1 and 2 on stereoplot in Fig. 15) slides parallel to fault intersection (Nieto-Samaniego, 1999).

Very young contractional structures described above extend the strike-slip and reverse faulting throughout the MAFS activity. However, striae superposition encountered in six sites throughout the study area indicates that strike-slip and reverse faults may pre-date some normal faulting in the area – in all these cases subhorizontal striae is older than subvertical striae. One example is shown in Figure 16A.

The youngest volcanic rocks in the area, late Quaternary cinder cones and basalt flows (Fig. 2), are commonly affected by normal faults. In many cases, these cinder cones were built on the traces of normal faults, which later displaced them. For scale reasons, this is easiest to observe in detailed geomorphologic maps (Plates 3-8). Nonetheless, at outcrop scale the relation between cone construction and faults can also be observed. One example has been found in southern Maravatio depression, where three cinder cones are aligned in W-E direction and are displaced by E-striking fault (Plate 6). Many fault planes displace the strata of these cinder cones right to the present topographic surface (*e.g.*, Fig. 16B). Nevertheless, a fault plane active during the construction of the cone was also found (Fig. 16C). The latter indicates temporal (and obviously also spatial) association of cone construction with faulting.

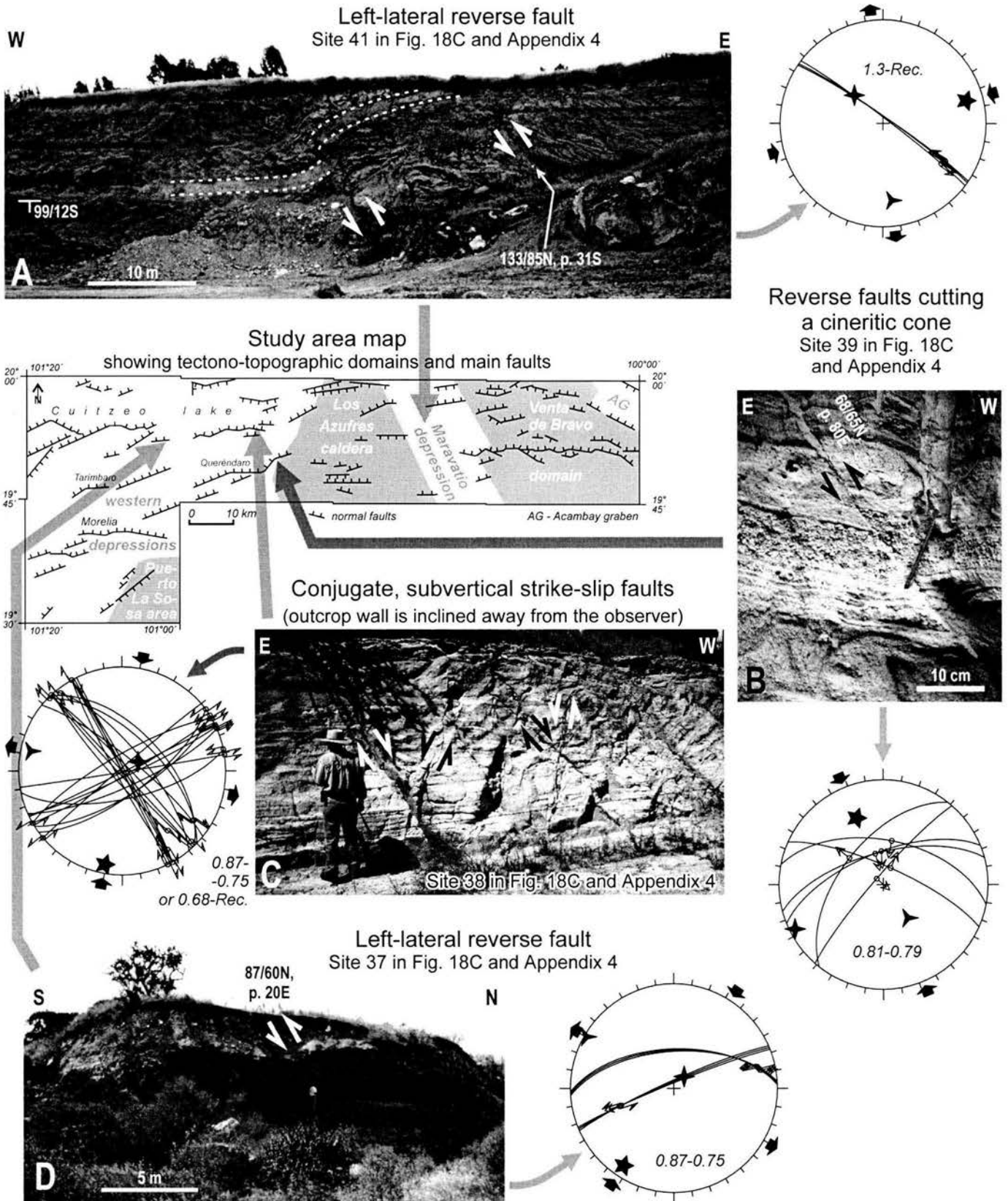


Figure 14. Examples of contractional structures affecting Quaternary rocks. Numbers inside or aside of stereoplots are ages of affected rocks in Ma. Fault measurements are given in strike/dip/dip sense, pitch/fault type format. Stereoplots are lower hemisphere, equal angle, five-, four- and three-point stars are contraction, intermediate and extension axes, respectively. See text for discussion.

### NW-striking faults cutting Holocene soil (outcrop sketch).

Note progressive deformation on faults A, B and C (lower layers displaced more than upper layers).  
Site 47 in Fig. 18, Appendix 4

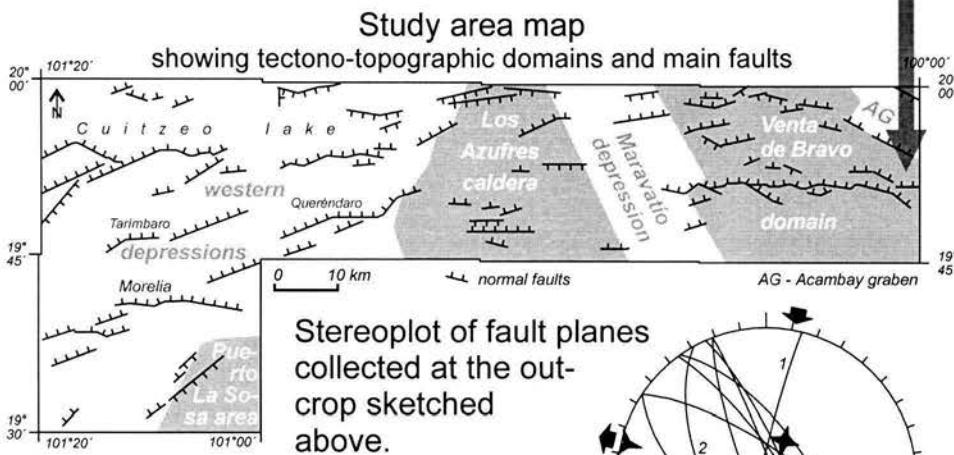
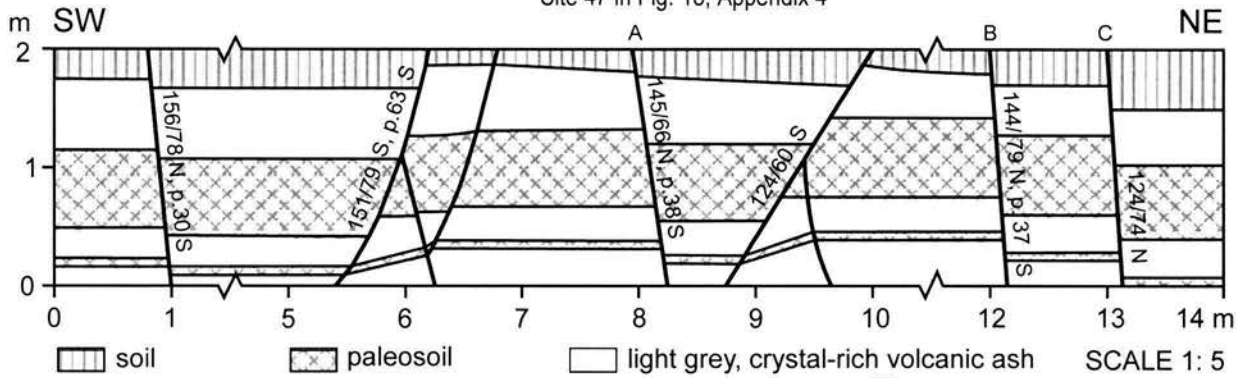
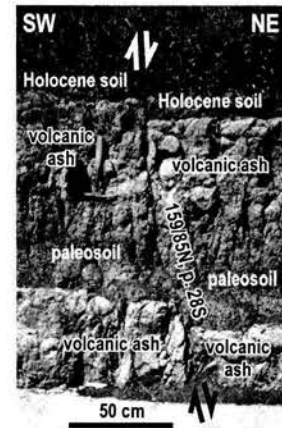


Photo of one of the faults in the outcrop sketched above



Note that NW-striking faults are oblique-normal: those dipping to NE (majority) are dextral-normal, and those dipping to SW are sinistral-normal. The latter were eliminated for calculation of strain orientations, because they produce unreasonable results. See text for discussion.

Figure 15. NW-striking, oblique-normal faults displacing the base of Holocene soil. Fault measurements are given in strike/dip/dip sense, pitch/fault type format. Stereoplot is lower hemisphere, equal angle, five-, four- and three-point stars are contraction, intermediate and extension axes, respectively. See text for discussion.

Another important case is a cineritic cone located between western and eastern Cuitzeo fault scarps, although closer to the latter (Fig. 16D). Although, at map scale, no fault scarp can be seen here (La Mina cone in Plate 5), this cone is cut by three major and a few minor normal faults, that together produce a minimum of 15 m of vertical displacement (Fig. 16D). This cone seems to indicate that the western and eastern Cuitzeo faults are propagating towards each other, and might be already linked in subsurface.

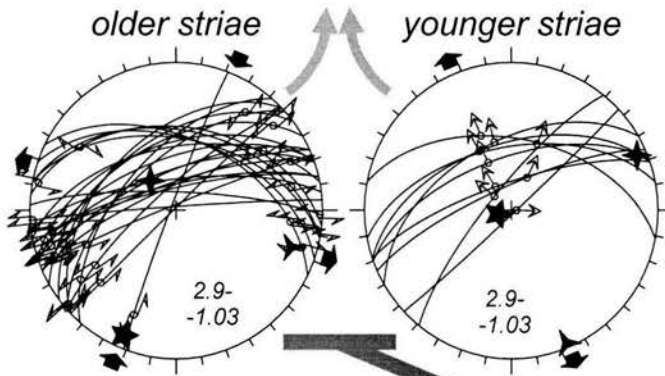
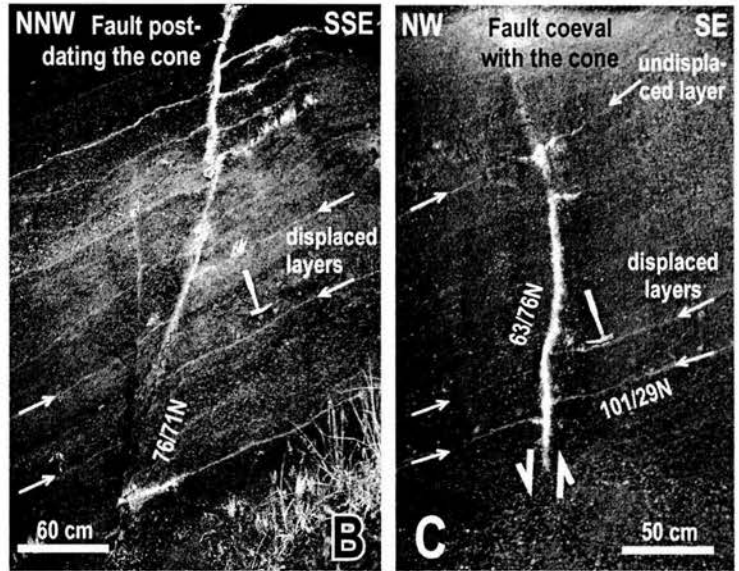
### 5.2.3 Strata attitude: a summary (regional variation)

Highly dipping strata, locally up to 50°, are encountered within the western depressions tectono-topographic domain (Fig. 17, Plate 1). The highest dips cluster at, and in front of, the western Cuitzeo fault. Although strikes and dips of strata vary significantly along this fault, the strike of strata is usually subparallel to the strike of the corresponding major segment of the fault and the dips of the two are usually opposite (Fig. 17).



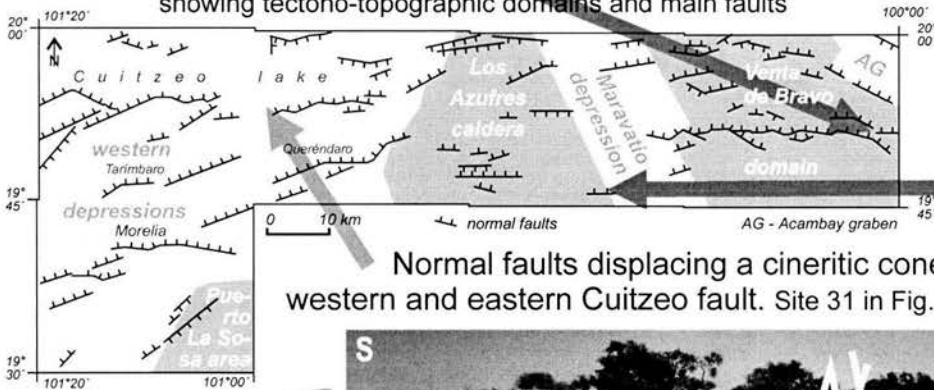
Site 21 in Fig. 18B and Appendix 4

Normal faults displacing a cineritic cone  
0.63 Ma old (dated by Suter et al., 2001)  
Site 45 in Fig. 18C and Appendix 4



Study area map

showing tectono-topographic domains and main faults



Normal faults displacing a cineritic cone between western and eastern Cuitzeo fault. Site 31 in Fig. 18C and Appendix 4

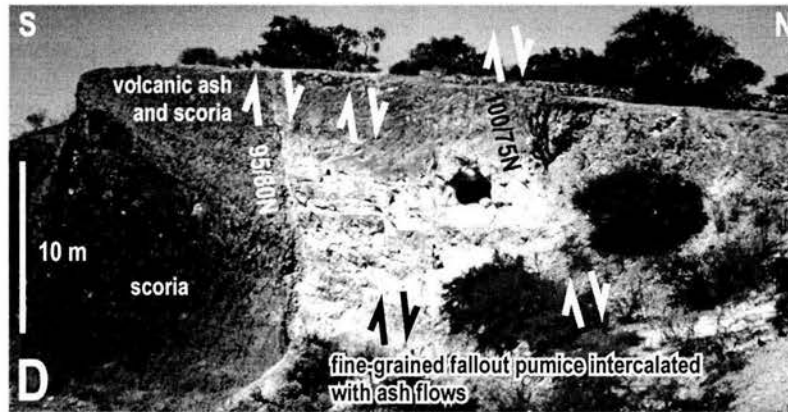
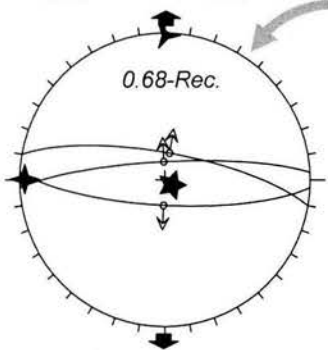
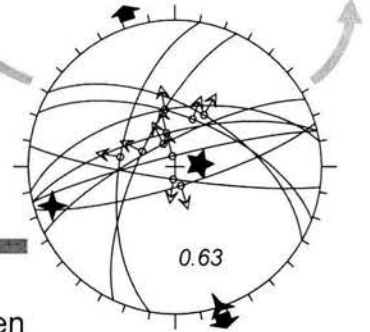


Figure 16. Striae superposition indicating first lateral and then normal faulting, and late Quaternary cinder cones displaced by normal faults. Numbers inside or aside of stereoplots are ages of affected rocks in Ma. Fault measurements are given in strike/dip/dip sense, pitch/fault type format. Stereoplots are lower hemisphere, equal angle. Five-, four- and three-point stars are contraction, intermediate and extension axes, respectively. See text for discussion.

A particular case of such behavior was described above and illustrated in Fig. 11. The measurements within the hangingwall of western Cuitzeo fault to the north of the lake give the SE-dipping strata, opposite to the dip of the major faults of the region (Fig. 17). As noted before, in volcano-sedimentary terrain primary dips are not always easily separated from tectonic tilt. Nonetheless, notorious high dips consistent with orientation of faulting, and some of these dips higher than upper bound of primary dips (which is *ca.* 32°), indicate tectonic tilt of strata. I consider that 25° toward the SSE is a safe estimation of tectonic strata tilt in front of the western Cuitzeo fault.

South of the western Cuitzeo fault and in front of the Tarímbaro fault safe estimation of tectonic strata tilt is 12° towards the south (Fig. 17). South of the Tarímbaro fault, and in front of the Morelia–Jarípeo fault strata dips *ca.* 10° to the south. South of the Morelia–Jarípeo fault strata lay subhorizontal (Fig. 17).

Around the eastern Cuitzeo lake, in front of south-facing faults, strata dips between 6 and 9 degrees to the north, so again opposite to the dip of principal faults. Towards the south of eastern Cuitzeo lake, strata lay subhorizontal (Fig. 17).

To the east of the Los Azufres caldera, strata mostly are subhorizontal. Rarely the inclinations of a few degrees to the south appear close to the Venta de Bravo fault. The exception is the cluster of dipping beds at the central Venta de Bravo fault, which was collected in basaltic/andesitic breccia, along the *ca.* 350 m transect. It forms an asymmetric anticline with axis oriented W-E, located between two rhomb-shaped segments of this fault (Fig. 17). Dipping strata was also encountered in north-eastern Los Azufres caldera, and at the central part of Maravatío depression (Fig. 17). At the latter location the 12° to SSW measurement is associated with the NW-striking left-lateral reverse fault described in detail above and illustrated in Figure 14A.

In summary, highly dipping strata are found almost exclusively within western depressions domain (to the west of Los Azufres caldera). Moreover, within this domain reversal of the dip direction of strata and principal faults is observed. At western Cuitzeo lake, principal faults dip to the north and northwest, and strata generally dip to the south and southeast. At eastern Cuitzeo lake, principal faults dip to the south and southeast, and strata generally dip to the north and northwest. The axis of this reversal corresponds to the narrowest and shallowest portion of the Cuitzeo lake. Hence, dipping strata appear to be the effect of tectonic tilting by major MAFS faults. To the east of Los Azufres caldera strata usually are subhorizontal (Fig. 17).

#### 5.2.4 *Fault kinematics*

448 fault slip planes with striae were measured at 63 structural stations. Grouping measurements from closely spaced and apparently related stations yields 58 stereograms. These stereograms make up 52 measurement sites because at six sites superposition of striae was observed (these sites are marked with the same number in Fig. 18 and Appendix 4, letter “a” designating younger striae) (Fig. 18, Appendix 4). At 3 sites (17 fault planes) striae inversion with the right-dihedra method of Angelier and Mechler (1977) (see section 4.3 for explanation of this method) did not yield satisfactory results, due to contemporary normal and reverse, or left- and right-lateral faults. These sites are excluded from the comparison below, but one of them (site 15 in Fig. 18, Appendix 4) is described in detail in section 5.2.1 above and illustrated in Figure 12.

The data presented in this section is relevant to possible temporal variations of fault kinematics. To evaluate it, we first have to see what temporal constraints these data can provide. First of all, reverse, strike-slip and normal faults affect Miocene to Holocene rocks. Hence, none of them can be assigned a younger limit. Nonetheless, as faults can only be as old as affected rocks, evaluating possible changes in fault kinematics through time will be attempted below on this basis. Finally, striae superposition always indicates first strike-slip or reverse faulting and then normal faulting. Hence, contractional structures may pre-date extensional ones, so will be considered first. Nonetheless, such superposition (hence fault reactivation with different sense of motion) is found up to the Quaternary (Fig. 18).

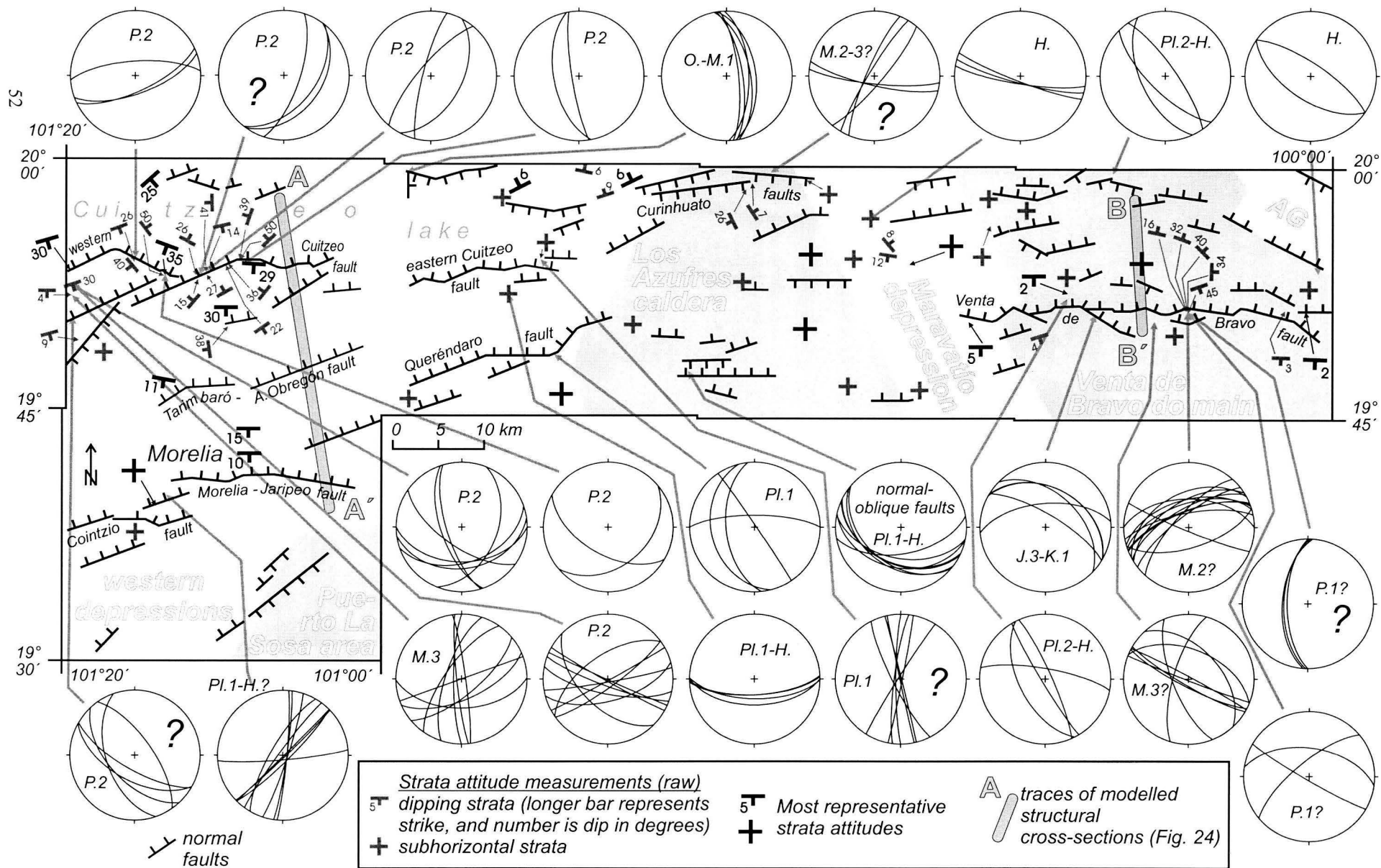


Figure 17. Measured strata attitude (symbols on the map), and fault planes without striae (stereograms: lower hemisphere, equal area). Stereograms with question marks show faults where sense of displacement is unknown, other stereograms represent faults with normal component of displacement. Letters inside or beside each diagram indicate the age of the youngest rocks cut by the faults: J.3 - upper Jurassic; K.1 - lower Cretaceous; O. - Oligocene; M.1 - lower Miocene; M.3 - upper Miocene; P.2 - upper Pliocene; PI.1 - lower Pleistocene; PI.2 - middle Pleistocene; PI.3 - upper Pleistocene; H. - Holocene. Normal fault traces and tectono-topographic domains (the latter in light gray and white) are added for orientation. AG - Acambay graben.



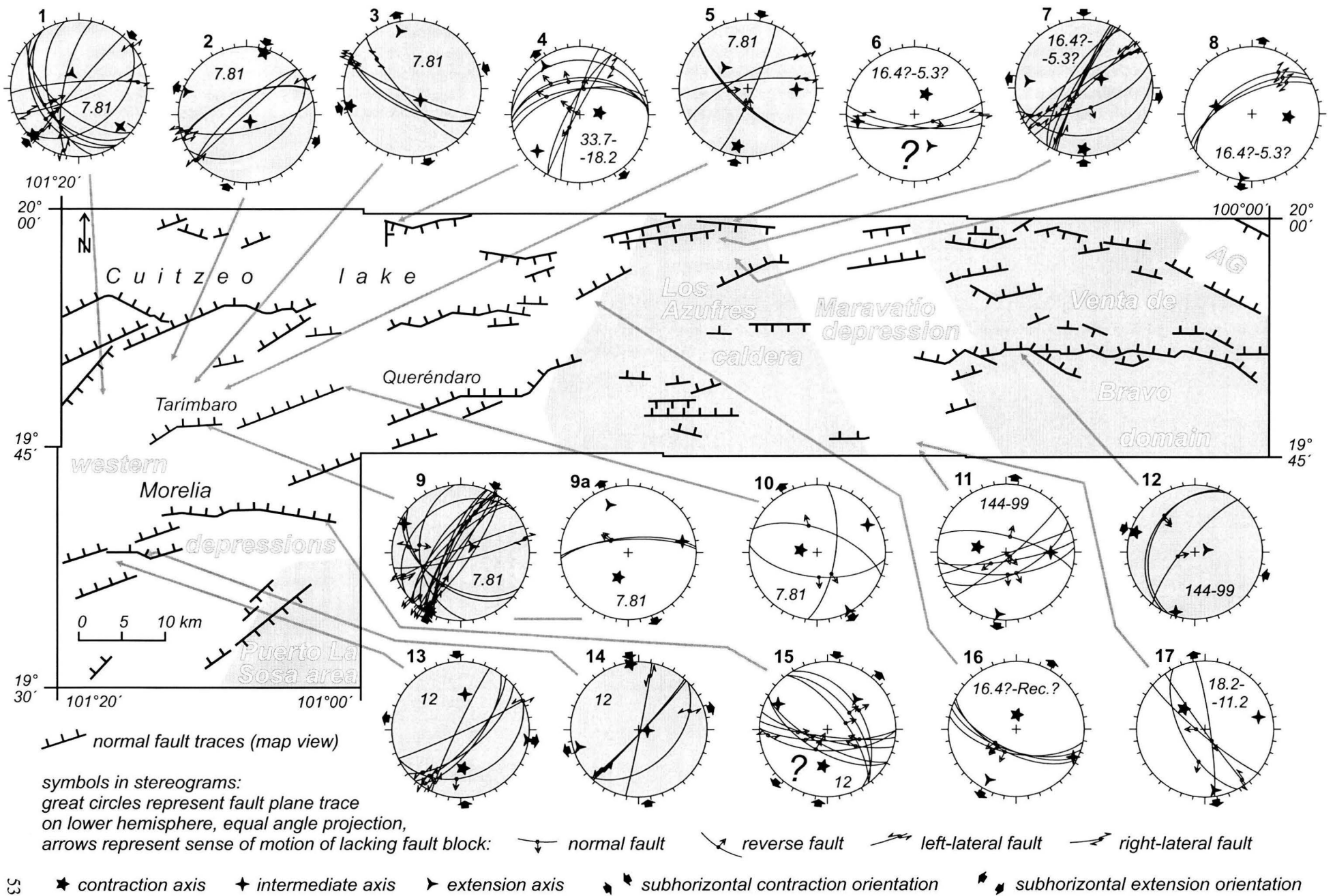


Figure 18A. Measured fault slip planes and striae collected in rocks of the upper Jurassic to Miocene age. Stereograms show slip planes and sense of displacement. Extension, contraction and intermediate axes were calculated with right dihedral (P-T axes) method. Gray-filled stereograms show reverse and/or strike-slip faults (contraction), unfilled stereograms show normal faults (extension). Question marks mark stereograms where available data did not produce coherent results. Bold numbers identify measurement sites (see Appendix 4 for corresponding numeric values). Stereograms identified with the same number illustrate superposition of striae, and the letter "a" marks younger striae. Numbers in italics located inside or beside each diagram indicate ages in Ma of the youngest rocks cut by the faults. Normal fault traces and tectono-topographic domains (in light gray and white) are added for orientation. AG - Acambay graben.

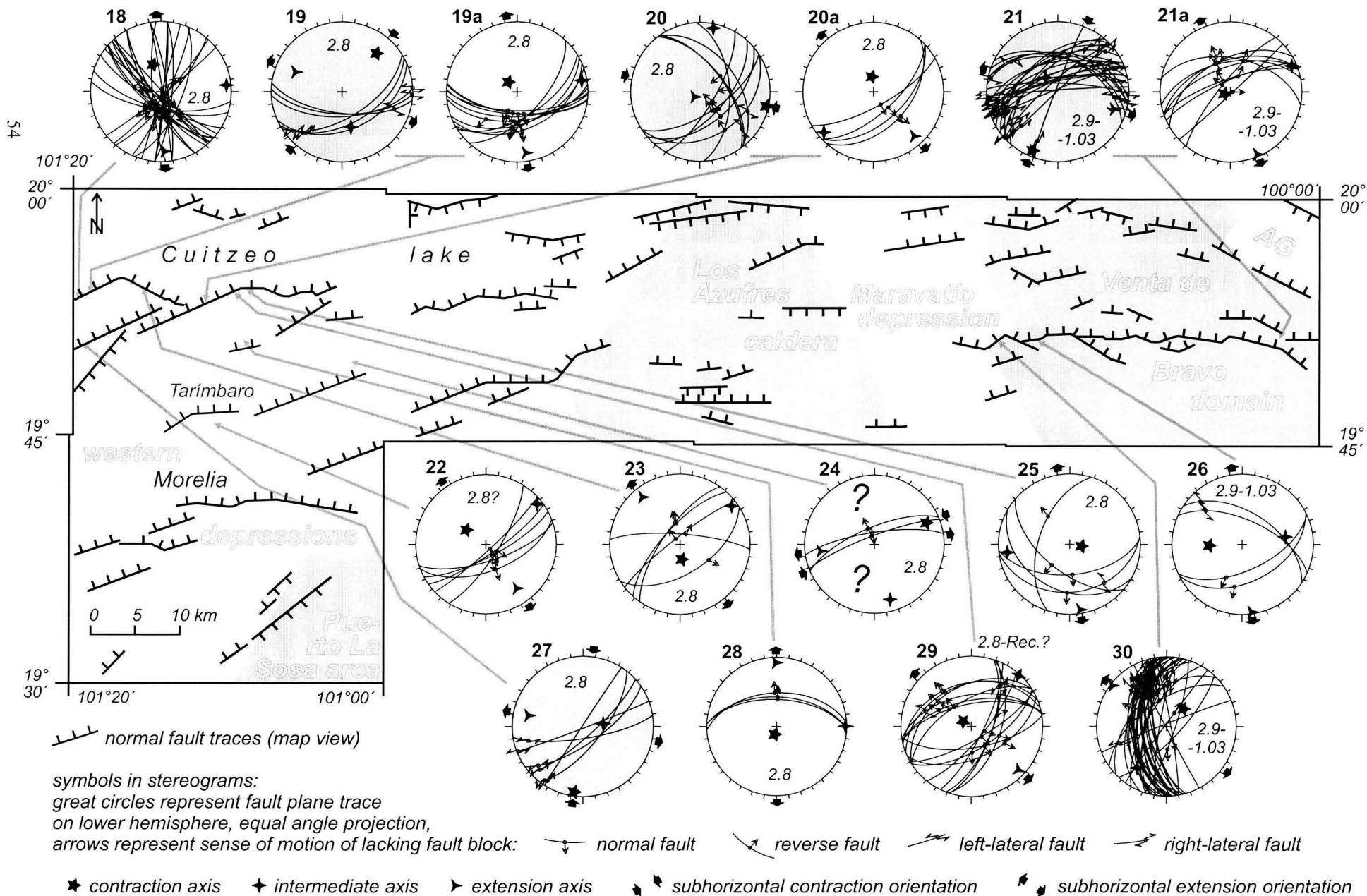


Figure 18B. Measured fault slip planes and striae collected in rocks of the upper Jurassic to Miocene age. Stereograms show slip planes and sense of displacement. Extension, contraction and intermediate axes were calculated with right dihedral (P-T axes) method. Gray-filled stereograms show reverse and/or strike-slip faults (contraction), unfilled stereograms show normal faults (extension). Question marks mark stereograms where available data did not produce coherent results. Bold numbers identify measurement sites (see Appendix 4 for corresponding numeric values). Stereograms identified with the same number illustrate superposition of striae, and the letter "a" marks younger striae. Numbers in italics located inside or beside each diagram indicate ages in Ma of the youngest rocks cut by the faults. Normal fault traces and tectono-topographic domains (in light gray and white) are added for orientation. AG - Acambay graben.

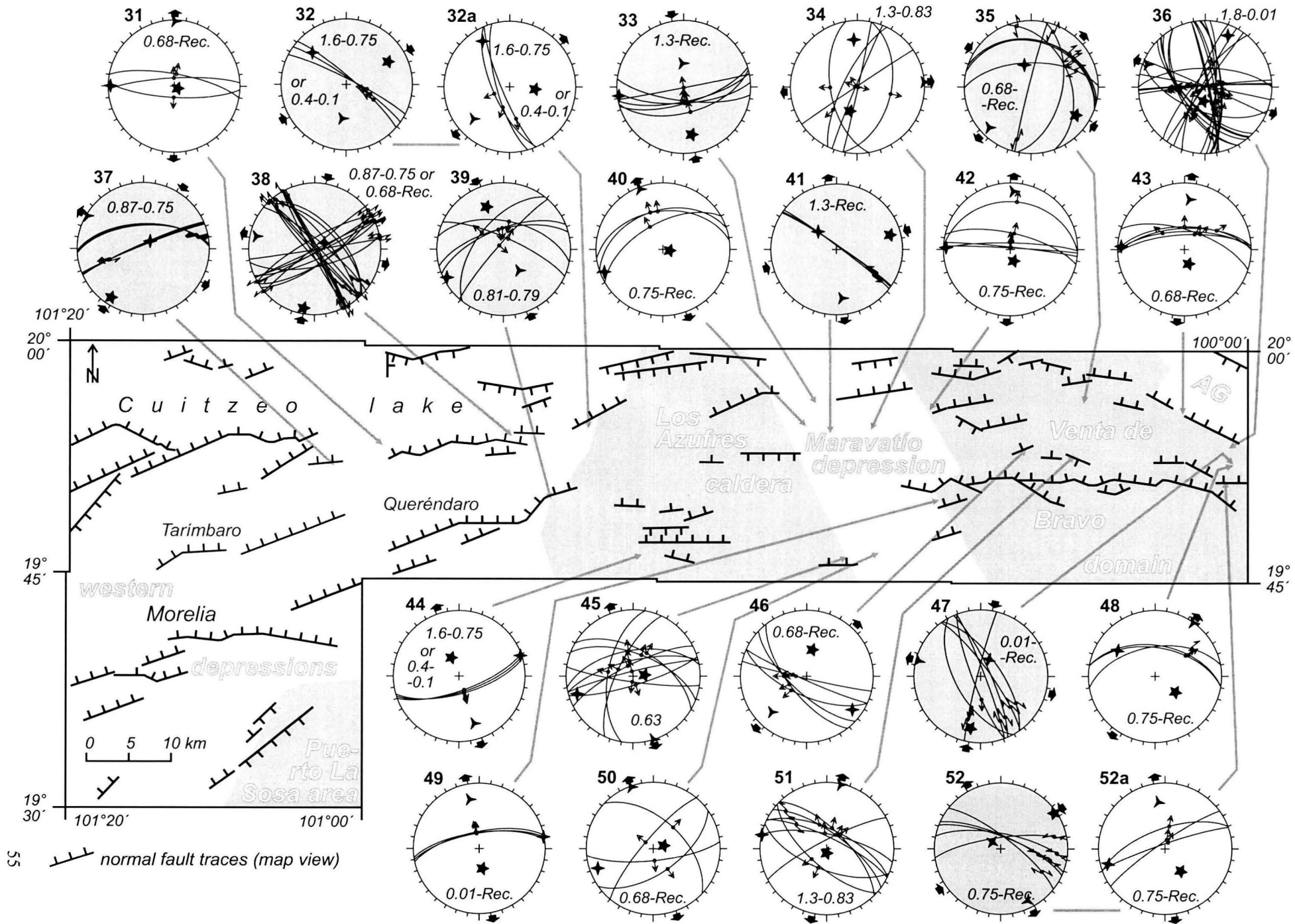


Figure 18C. Measured fault slip planes and striae collected in rocks of the Quaternary age. Stereograms show slip planes and sense of displacement. All symbols and explanations as in Figs. 18A and B.

Strike-slip and reverse striated faults constitute 44.5% of the entire dataset, 38% of the slip planes affecting Plio-Quaternary rocks, and 34% of the slip planes affecting Quaternary rocks (Tab. 3). The remaining data correspond to normal and normal-oblique striated faults. Considering that strike-slip and reverse faults indicate contraction, these data suggest waning of tectonic shortening during the arc evolution, and progressive increase of the role of tectonic stretching. Notably, after separating these faults into three groups: right-lateral, left-lateral and reverse (Fig. 19A, B, C), mean strikes are NNW-SSE, NE-SW and NW-SE, respectively, what means that they are consistent with NNE-SSW to NE-SW oriented contraction (see also next paragraph). Although considerable scatter is observed, especially in the case of reverse faults, this variation lacks any temporal trend (in other words: strikes of right-lateral, left-lateral and reverse fault are independent of faulted rock age). The strikes of normal striated faults are widely scattered, although WNW-ESE to ENE-WSW strikes predominate (Fig. 19D). Also in this case fault strikes are independent of faulted rock age.

Note that faults are assigned to different types solely on the basis of striae orientation, *i.e.*, this assignment is independent of the kinematics of an entire fault population at a given site (*e.g.*, a stereogram indicating contraction can contain a few normal-oblique faults, which are counted in Table 3 as faults indicating extension). Hence, the calculations of proportions between (1) strike-slip and reverse, to normal faults, and (2) stereograms indicating contraction to stereograms indicating extension, give two independent criteria to estimate the role of contractional and extensional structures in the deformation process.

Table 3  
Results of kinematic analysis of striae data.

	Data indicating contraction			Data indicating extension		
	No. and % of strike-slip and reverse faults	No. and % of stereograms indicating contraction	~contraction orientation	No. and % of normal faults	No. and % of stereograms indicating extension	~extension orientation
Only faults cutting Quaternary rocks	51 (34%)	9 (37%)	218/13	99 (66%)	15 (63%)	341/1
Only faults cutting Plio- Quaternary rocks	121 (38%)	13 (33%)	191/8	196 (62%)	26 (67%)	308/3 341/1
Total dataset	188 (44.5%)	22 (40%)	186/9	234 (55.5%)	33 (60%)	160/0 172/9 309/2

Separation to strike-slip, reverse and normal faults was done on the basis of striae pitch (also called rake). Strike-slip faults are those with pitches less than 40°, reverse and normal faults are those with pitches over 50°. Note that stereograms indicating contraction, although mostly having strike-slip and reverse faults, may include some normal faults; and that stereograms indicating extension (mostly having normal faults) may include some strike-slip and/or reverse faults. Number of faults in total dataset sum up to 422 (instead of 448 measured faults) because 26 faults with oblique pitches (40°-50°) were not assigned to any fault type. Number of stereograms in total dataset sum up to 55 because in 3 cases kinematic analysis of fault populations did not produce reasonable results. See Fig. 20 for rose diagrams of contraction and extension axes.

Kinematic analysis (inversion of striae data), shown on stereograms in Figure 18, give subhorizontal contraction predominantly oriented NNE-SSW to NE-SW (Tab. 3, Fig. 20A, C, E) and subhorizontal extension predominantly oriented NNW-SSE (Tab. 3, Fig. 20B, D, F). At sites with mostly left-lateral faults, the contraction is accompanied by roughly NW-SE oriented, subhorizontal extension (Fig. 18). The contraction seems to rotate clockwise through time (Tab. 3, Fig. 20A, C, E). However, the few data points and their wide scatter in Quaternary rocks makes this observation uncertain (Fig. 20A, C, E). Moreover, extension is constant through time (rose diagrams B, D, F in Fig. 20 are almost identical) hence, renders unlikely the

rotation of contraction, assuming that the two are related. The extension axes are widely scattered (Fig. 20B, D, F), as are the strikes of normal slip planes described above. Also in this case most of the scatter is found in Quaternary rocks.

Notably, when the number of stereograms indicating contraction is compared to the number of stereograms indicating extension (instead of comparing the number of strike-slip and reverse to normal faults), waning of tectonic shortening during the arc evolution is much less clear (Tab. 3). The implications of this difference will be further discussed in section 6.5.1: “Temporal and spatial relation between contractional and extensional structures”.

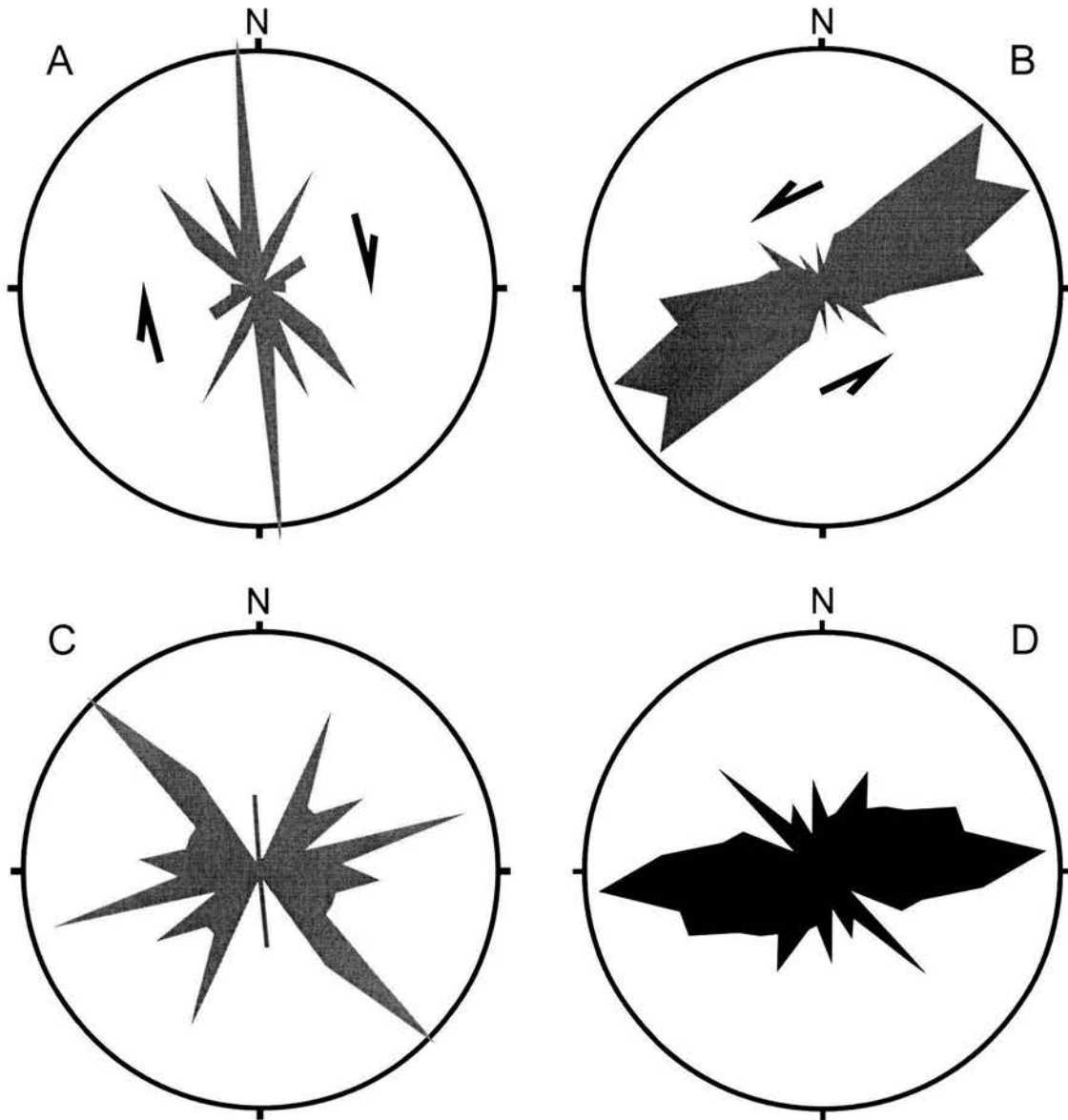


Figure 19. Rose diagrams illustrating distribution of strikes of four types of fault slip planes: (A) right-lateral, 39 data points, diameter of ring is 12% of fault frequency; (B) left-lateral, 112 data points, diameter of ring is 8% of fault frequency; (C) reverse, 37 data points, diameter of ring is 8% of fault frequency; (D) normal, 234 data points, diameter of ring is 7% of fault frequency. Separation to strike-slip, reverse and normal faults was done on the basis of striae pitch (also called rake). Number of faults sum up to 422 (instead of 448 measured faults) because 26 faults with oblique pitches ( $40^{\circ}$ - $50^{\circ}$ ) were not assigned to any fault type.

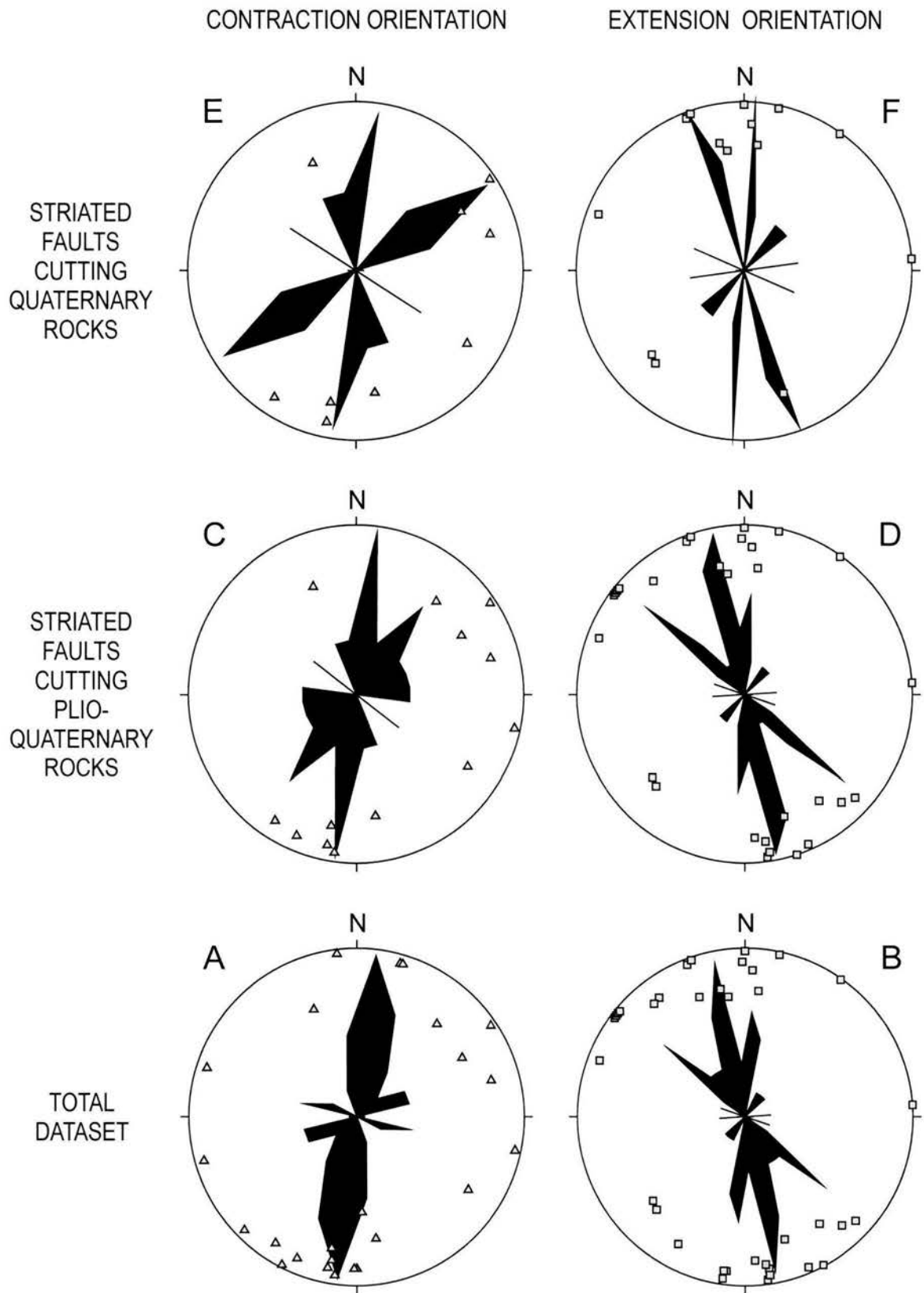


Figure 20. Stereoplots (lower hemisphere, equal angle) of contraction axes (small triangles) and extension axes (small squares) and their respective rose diagrams that illustrate mean strikes of these axes. Note that both contraction and extension is significant up to the Quaternary, and that contraction might be rotating through time, and extension is constant through time. Ring diameter for rose diagrams is the following % of axes frequency: (A) 13%, (B) 9%, (C) 12%, (D) 9%, (E) 12%, (F) 11%.

### 5.3 Topography of the Trans-Mexican Volcanic Belt and its vicinity, and the location of the intra-arc faulting

The western and central TMVB are affected by major, normal, intra-arc faults. Within the western TMVB these faults are associated with extensional tectonics around Jalisco block (*e.g.*, Rosas-Elguera *et al.*, 1996). Intra-arc faults of the central TMVB, which are the subject of this study, were proposed to be an expression of gravitational collapse of the arc (Suter *et al.*, 2001) or the effect of slip partitioning due to oblique convergence along Acapulco trench (Ego and Ansan, 2002). Data below provides some constraints on the first proposal, and therefore, on the reasons for the intra-arc faulting of the central TMVB.

The whole TMVB is elevated above the terrain to the south of it. The eastern half of the TMVB (eastern portion of the central TMVB, and the eastern TMVB), is also elevated above the terrain bordering it to the north (Figs. 21, 22). The western half of the TMVB (western portion of the central TMVB, and the western TMVB) is either lower or located at almost the same elevation as the terrain to the north of it (Figs. 21, 22). The most abrupt elevation drop is seen to the south of the arc at the longitude of Mexico City (Fig. 22, profile F), where it is more than 1800 m across *ca.* 50-km long stretch (in terms of averaged elevation values, as seen on the profiles in Fig. 22).

Within the central TMVB, documented faults (Pasquaré *et al.*, 1988; Martínez-Reyes and Nieto-Samaniego, 1990; Suter *et al.*, 1992, 1995a,b, 2001; Huizar-Álvarez *et al.*, 1997; García-Palomo *et al.*, 2000, 2002; Campos-Enríquez *et al.*, 2003; this study) usually cut the northern slopes of the topographic culmination of the arc (Fig. 22, profiles A, C, D, F) (Suter *et al.*, 2001), and most of the faults dip to the north. The exception occurs at the longitude of Acambay graben (eastern central TMVB), where documented faults dip to the north and to the south and cut the most elevated portion of the arc (Fig. 22, profile E). Only in the easternmost central TMVB faulting reaches the northern portion of the arc (Fig. 22) (Suter *et al.*, 1995a). Notably, major, normal fault scarps at abrupt, southern slopes of the arc have only been documented west of line D (Fig. 21, Plates 1, 3).

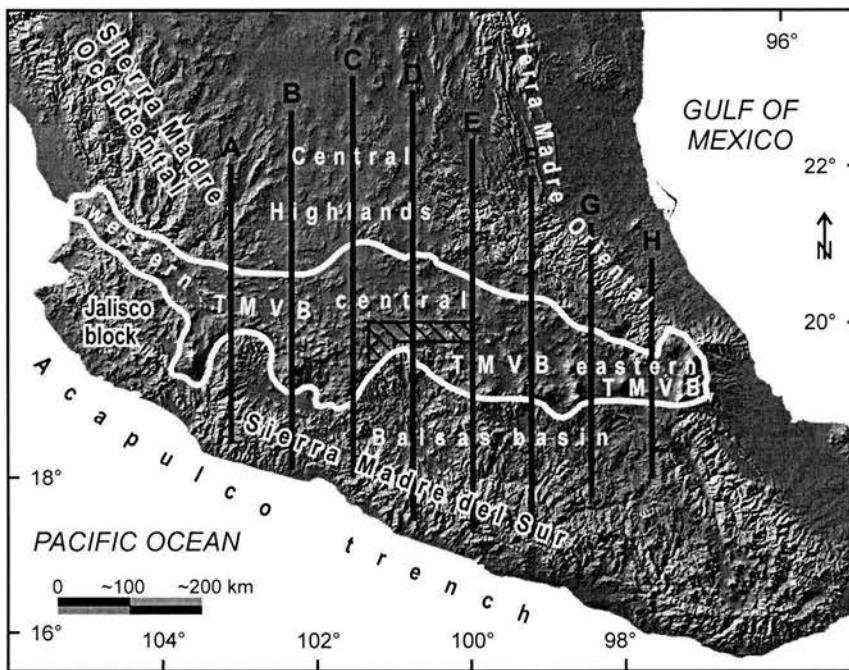


Figure 21. Shaded relief image of central Mexico, 30 arc second resolution. The Trans-Mexican Volcanic Belt is outlined in white (modified from Pasquaré *et al.*, 1991; and Ortega-Gutiérrez *et al.*, 1992). Thick black lines mark paths of topographic profiles, letters above them are symbols of the profiles (as in Fig. 22). The study area is hatched. Geographic projection, WGS84 datum and spheroid.

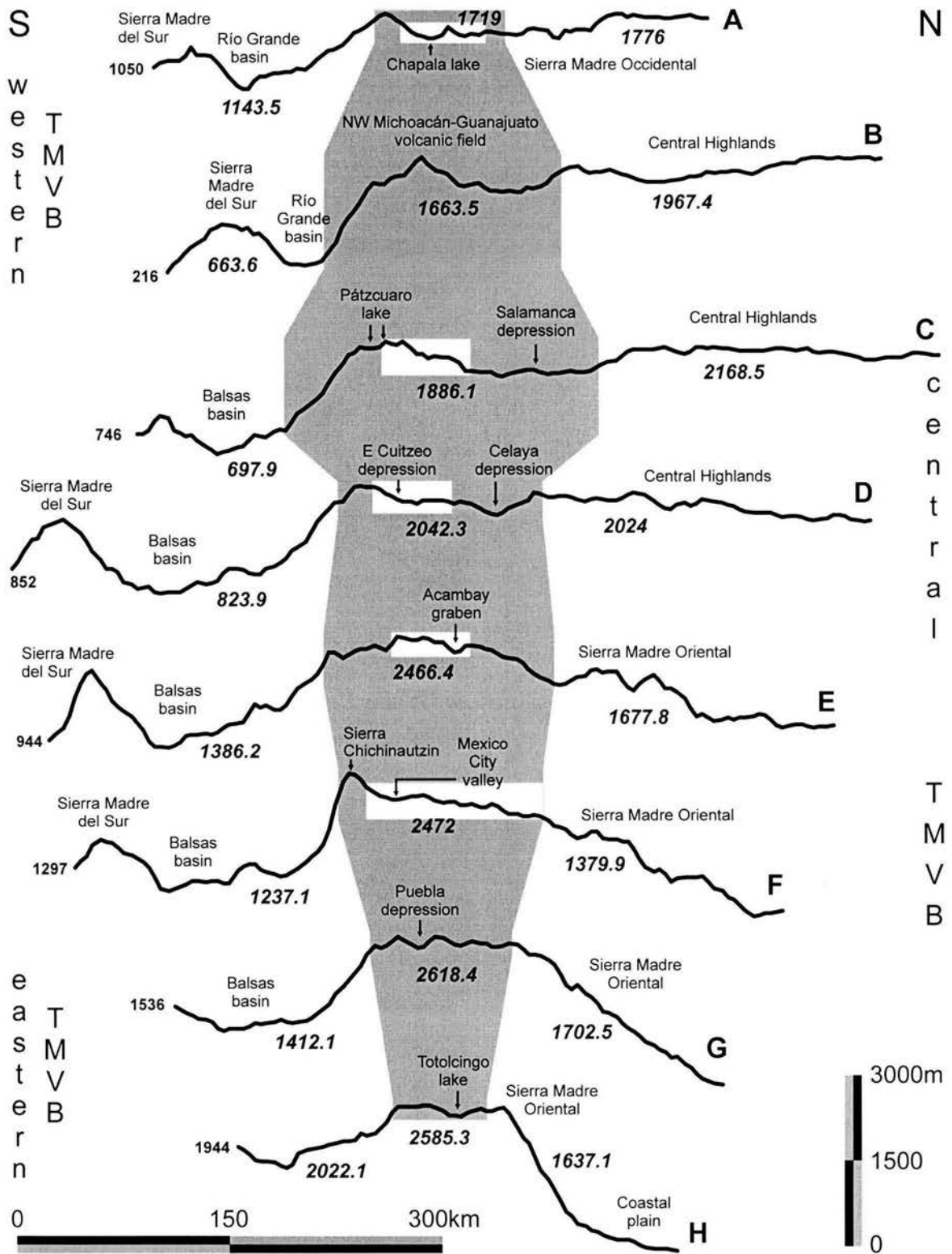


Figure 22. Topographic profiles across the Trans-Mexican Volcanic Belt (vertical exaggeration is 40x; see Fig. 21 for location of paths). Profiles show mean elevation, averaged over ~45 km to the east and the west of each line and over ~4.5 km along each line. The extent of the TMVB at each profile is marked in gray. The zone of intra-arc faulting along each path is marked in white. Bold italic numbers are the mean elevations of the entire portions of the TMVB and its vicinities, represented on each profile. Numbers to the left of the profiles are the elevations of the southernmost point of each profile. Main topographic features encountered along the paths of the profiles are added for orientation.



## 6 Discussion

### 6.1 Active fault systems

#### 6.1.1 *Fault pattern within the central TMVB*

In the central TMVB, the activity of the E-striking MAFS is widely accepted, and historic seismicity registered on these faults (Urbina and Camacho, 1913; Astiz, 1980) confirms it without doubt. Nonetheless, doubt remains whether other regional fault systems are also active within the area affected by the MAFS. Roughly N-striking, (Basin and Range trend) faults are active at the northern margin of the central TMVB, to the north of the MAFS (Orozco-Esquivel *et al.*, 2001; Aguirre-Díaz *et al.*, 2003). Moreover, Quaternary faults with Basin and Range strikes are encountered in the near vicinity, or at the edges of the MAFS: the N-striking Penjamillo graben to the NW of the MAFS, and the NW-striking Perales fault in the SE portion of the MAFS (Fig. 1). The NE-striking faults are active within the TMVB to the east of the MAFS (De Cserna *et al.*, 1988; Huizar-Álvarez *et al.*, 1997; García-Palomo, *et al.*, 2002; Campos-Enríquez *et al.*, 2003) and most probably to the west of the MAFS (Connor, 1990). Below, I discuss the possibility that both systems are also active within the central MAFS.

The majority of the departures from graded longitudinal river profiles, seen throughout the area, are directly associated with fault scarps or topographic lineaments parallel to all three regional fault systems. Given that knickpoints of the longitudinal stream profiles, including those formed due to lithologic variability alone, migrate upstream (Burbank and Anderson, 2000), associations of knickpoints with faults argue in favor of the ongoing activity of the latter. Moreover, in the area lithologic variations which are not related to Quaternary volcanic rocks, does not cause departures from graded river profiles (Fig. 5, profile 1), including where the contact is an apparently inactive fault (Fig. 5, profile 3: Charo fault). The latter argues against lithologic control of the knickpoints at the study area, where pre-Quaternary rocks are involved. Knickpoints do appear due to lithologic control where Quaternary volcanic rocks are involved, but in such cases they are often unrelated to recognizable fault scarps or topographic lineaments. Different bedrock strength across the fault scarps or (rarely) lineaments probably enhance the knickpoints. Nonetheless, the most pronounced knickpoints are unrelated to considerable variation in bedrock strength (Fig. 5, profiles 5, 6, 10). Only where Quaternary volcanic rocks outcrop in fault footwalls, lithologic contrast could possibly be the only factor controlling the location of the knickpoint at a fault scarp (*e.g.*, Fig. 5, profile 4).

Other geomorphic arguments suggesting the activity of NE-SW and NNW-SSE fault systems in the area are: the NE-striking fault scarps at the boundary between Puerto la Sosa and western depressions; the step-like lowering of depression floors toward the west (Fig. 7); the abrupt shifts of morphometric values across the (transverse to the MAFS) boundaries of the tectono-topographic domains; and the high drainage densities at the sides of the Los Azufres caldera (Fig. 8B).

Structural evidence of the activity of the NNW- to NW- and the NE-striking faults at central TMVB are measured fault planes, cutting the Quaternary (mostly  $\leq 870$  ka old) rocks (Figs. 17, 18, Appendix 4). NW-striking faults at Bosheda displacing Holocene soil (Fig. 15), are the particularly clear proof of the activity of faults transverse to the MAFS. Moreover, Urbina and Camacho (1913) mark NW-striking fault trace at Huapango plain (easternmost Acambay–Tixmadejé fault, to the east of the study area) ruptured during the 1912 Acambay earthquake. Langridge *et al.* (2000) found repeated Holocene displacements on this fault trace. Furthermore, NW-striking Perales fault, located to the SE of the study area (Fig. 1), tilts soils containing prehispanic ceramics (Garduño-Monroy, Instituto de Investigaciones Metalúrgicas UMSNH, 2003, personal communication).

In summary, geomorphic and structural evidence points to the activity of the NNW-SSE, NE-SW and E-W faults within the central TMVB. The different topographic expression of these systems *i.e.*, topographic lineaments at NNW-striking faults, and fault scarps up to 500 m high at E-striking faults suggest differences in the present-day displacement rates and/or displacement senses between these fault systems. The striae data (Fig. 18) confirm this observation, as the slip on NW- and NE-striking faults is usually highly oblique.

## 6.2 Tectono-topographic remodeling of the central TMVB

Comparison of the morphometric values between the tectono-topographic domains (Fig. 10) shows that the topography of the southern slope of the TMVB (Puerto la Sosa domain, Plate 1) is incompatible with the TMVB domains.

The histograms of the MAFS-controlled subdomains (Fig. 10) confirm their subordinate character with respect to the major, transverse domains. Little scatter of elevation values at the western Cuitzeo fault footwall is particularly interesting because it means that the activity of the MAFS produced considerably less relief than the transverse structures. Similarly, the Venta de Bravo fault hangingwall resembles high-lying domains, although it should be a basin, if the MAFS were as efficient in controlling the distribution of elevation and relief values as the transverse structures are. Instead, together with the Venta de Bravo fault footwall, it represents the NNW-striking, partially fragmented tectono-topographic high. Hence, the domains associated with the largest morphometric contrasts are transverse to the MAFS and parallel to the pre-MAFS fault systems. Although these contrasts may be due to a combination of tectonics, volcanism, and lithology, the pre-MAFS fault systems appear to be the controlling factor. Nevertheless, the control may be partly indirect, *e.g.*, by controlling magma paths leading to construction of volcanic edifices such as Los Azufres caldera.

Throughout the study area, the MAFS faults control almost all fluviolacustrine deposits and a large number of footslopes and talus units whose distribution is illustrated in detailed geomorphologic maps (Plates 3-8). The exceptions are the internal parts of the Atécuaro and Los Azufres calderas, and footslopes that skirt major volcanoes of the region, (Plates 3-7). In both cases, sedimentation is due to volcanic landforms. The absence of a fluviolacustrine plain in front of the longest continuous MAFS fault scarp in the area – the Venta de Bravo fault scarp – is surprising, given the development of this type of basin in fault hangingwalls elsewhere. Instead, bedrock channels drain the Venta de Bravo fault hangingwall toward the Maravatio depression. These factors suggest that the entire Venta de Bravo domain constitutes active tectono-topographic high, inherited from Basin and Range trends. Alternatively, the Venta de Bravo fault hangingwall topography may be due to the young (mostly  $\leq 680$  ka) basaltic volcanism that covers a considerable portion of this area. Nevertheless, such volcanism also fills the Maravatio depression, without turning it a topographic high.

In summary, the spatial distribution of the morphometric properties analyzed at the scale of major tectono-topographic domains indicate the role of the pre-MAFS fault systems in shaping the topography of the area,

while the spatial distribution of the erosion- and sedimentation-dominated surfaces indicate the role of the MAFS in this process. The Maravatío depression is a good illustration of this process, because it is a NNW-striking depression, with *ca.* 400 m relief on both sides, where sedimentation and erosion take place mostly in E-striking, MAFS-controlled belts. I believe that the morphometry and the distribution of landforms reflect the re-shaping of the pre-existing, Basin and Range topography. Apparently, this pre-TMVB topography, although already intensely fragmented by the MAFS, is discernible due to the ongoing activity of the older fault systems.

### 6.3 Preliminary MAFS chronology in the westernmost study area

Excluding the Charo fault scarp whose greater part seems inactive (see below), the primary fault scarp morphology described in section 5.1.6 suggests that in western depressions main fault scarps are progressively less degraded towards the south (Tab. 2, Plates 3-5). The apparently inactive portion of the Charo fault scarp [lack of knickpoint at the El Rile–Jarapeo river crossing it (Fig. 5) and lack of triangular facets at this portion of the scarp (Tab. 2, Plate 3)] is located between the Tarimbaro–A. Obregón and the Morelia–Jarapeo scarps that are active – the latter displace soils with pre-hispanic ceramics (Garduño-Monroy, Instituto de Investigaciones Metalúrgicas UMSNH, 2003, personal communication). The switching off of the Charo fault after formation of neighboring faults is consistent with models of stress shadow fault interaction concept (Willemsse *et al.*, 1996; Cowie, 1998; Gupta and Scholz, 2000), and is likely the reason why the upper Miocene lacustrine deposits formed in front of Charo fault can be seen at the surface (see section 2.2.4 and Fig. 2).

The degree of scarp degradation in western depressions seems to depend only partly on lithology, *e.g.*, the most resistant rocks outcropping at the study area (very strongly welded upper Pliocene Cuitzeo ignimbrites) form the southwestern edge of the degraded western Cuitzeo fault scarp. Nevertheless, when the resistant bedrock is of Quaternary age, it does seem to considerably influence the preservation potential of fault scarps, *e.g.*, all scarps formed in Quaternary basalts, such as easternmost western Cuitzeo fault scarp or Queréndaro fault scarp, are relatively fresh (compare Fig. 2 with Plates 4 and 5).

The degree of destruction of the western Cuitzeo, Tarimbaro–A. Obregón, Morelia–Jarapeo and Cointzio fault scarps correlates with their maximum displacement (see section 6.4.1 below), *i.e.*, the northern, most degraded fault scarp shows the greatest total displacement, and the southern, least degraded scarp shows the smallest displacement. Such association suggests that the age of the initiation of the respective faults diminishes towards the south (rather than slip rate increases, in which case the greatest displacement should be found at least degraded scarp). However, the lifetime of at least some mapped features is clearly less than the age of the faults [the MAFS initiated in the late Miocene, at about 6 Ma (Israde-Alcantara and Garduño-Monroy, 1999; Suter *et al.*, 2001)], the features were mapped for the regional overview at 1:75,000-scale, and the time since last rupture may influence or even control the preservation of the scarps. Finally, talus instability may also influence or control the distribution of mapped features.

To the east of Los Azufres systematic variation of the degree of destruction between different fault scarps is absent but, at least in the case of the Venta de Bravo fault scarp, the alongstrike variation is clear. The tips of this scarp are fresh, and the central part is degraded (Tab. 2, Plates 6-7). Nonetheless, in this case lithologic control of scarp preservation cannot be discounted, given that central Venta de Bravo fault scarp is made up of pre-Quaternary rocks, while tips of this scarp are made up of Quaternary basalts (compare Fig. 2 with Plates 6 and 7).

## 6.4 MAFS subsurface geometry and slip rates

### 6.4.1 Magnitude of displacements

The displacements on the pre-MAFS faults are very poorly constrained. Campos-Enríquez and Garduño-Monroy (1995) found that the resistive basement is *ca.* 1500 m lower in western depressions (in Araró, Plate 5) than in Los Azufres caldera. Although these authors do not state which fault system is responsible for the observed displacement (all three are present at Los Azufres), those transverse to the MAFS faults (NNW- or NE-striking, or their combination) are more likely, given the configuration. This displacement is possibly responsible for the disappearance of red beds (which are *ca.* 1500 m thick at Tzitzio) to the east of the caldera (Fig. 2). From gravity data, De Cserna *et al.* (1988) infer several km of displacement on NE- and NW-striking faults below the basin fill of Mexico City valley, to the east of the MAFS (Fig. 1). The thickness of the sedimentary fill of Ixtlahuaca–Toluca depression (located to the east of the MAFS), bounded by NNW-striking faults, was proposed by Soler-Arechalde (1997) to be almost 6 km (Soler-Arechalde, 1997, her Fig. 3.10). Alaniz-Álvarez *et al.* (2001) reports displacements of up to 450 m on *ca.* N-striking faults in the Querétaro–San Miguel de Allende region to the north of the MAFS (northern edge of the TMVB). These values cannot, of course, be applied directly to my study area, but they do give the idea of the magnitude of displacements on the Basin and Range faults in central Mexico.

The magnitude of vertical displacements on some of the MAFS faults in western depressions can be roughly estimated from existing subsurface (well) and geophysical data. Sediment thickness in front of these faults, along with sources of these data, were described in section 2.2.4: “Fluviolacustrine and surficial deposits”. Below I repeat these values because thickness of syntectonic deposits (fluviolacustrine sediments are syntectonic in these cases) complemented by topographic relief of fault scarps, allow estimation of minimum vertical component of total displacement of these faults.

In front of the eastern part of western Cuitzeo fault (Plate 1), thickness of fluviolacustrine deposits is at least 1000 m, and topographic relief of the fault scarp at this point is *ca.* 300 m. Hence, the total throw on this fault is at least 1300 m. Well data indicates 250 m of maximum thickness of fluviolacustrine sediments in front of the Tarímbaro–A. Obregón fault, and 126 m in front of Morelia fault. In both cases the greatest thickness is shifted from the middle of the depressions towards the southern, north-facing, bounding faults. Both fault scarps have a topographic relief of *ca.* 200 m, which gives 450 and 350 m of displacement, respectively. At Jaripeo fault (Plate 1), at least 200 m of maximum displacement should be a reasonable estimation, given *ca.* 120 m scarp height and *ca.* 80 m of syntectonic deposits. At Cointzio fault (Plate 1) a single well indicates 40 m of syntectonic deposits. The scarp height (measured at the top of the middle Miocene Morelia ignimbrite) is 140 m, which gives *ca.* 180 m of maximum displacement. The greatest thickness of basin fill close to the bounding faults supports the half-graben geometry. Lack of gravimetric and well data at eastern Cuitzeo lake precludes assessment of subsurface geometry, where structural data indicates reversal of dip direction of faults and strata.

To the east of the Los Azufres caldera, the magnitude of vertical displacements is unknown because wells never perforate the basalt fill of the Venta de Bravo fault hangingwall. Nevertheless, topographic relief of the Venta de Bravo fault scarp (Plate 1), measured on the top of flat, lower Pliocene ignimbrite sheets is *ca.* 300 m. Doubling this value, as did Suter *et al.* (2001) to roughly estimate displacement of the Acambay–Tixmadejé fault east of the study area (Fig. 1), we obtain at least 600 m of maximum displacement on the Venta de Bravo fault.

Figure 23 is a comparison between lengths and displacements of the major faults of the area. The lengths of these faults were measured as straight line from tip to tip, and the displacement is the one calculated above. The data point corresponding to the total length of the Cuitzeo faults (western + eastern) is used because major normal faults cut a cineritic cone located between these two fault scarps (Fig. 16D; site 31 in Fig. 18 and Appendix 4), which indicate that these two faults are linked in subsurface. Although the available data is insufficient for statistical analysis, excellent correlation ( $R^2 = 0.98$ ) for western depressions faults, where throw is reasonably well estimated with subsurface data, suggests that displacement-length relations (Cartwright *et al.*, 1995; Dawers and Anders, 1995; Wojtal, 1996; Gross *et al.*, 1997; Cowie *et al.*, 2000;

Ackermann *et al.*, 2001; and others) are constant in this area. Figure 23 reveals that either these relations are different east of Los Azufres [a reasonable possibility given different subsurface fault geometry (see next section)], or the Venta de Bravo fault is underdisplaced [*e.g.*, due to recent alongstrike linking (Dawers and Anders, 1995)], or its displacement is higher than the 600 m calculated by doubling the scarp height.

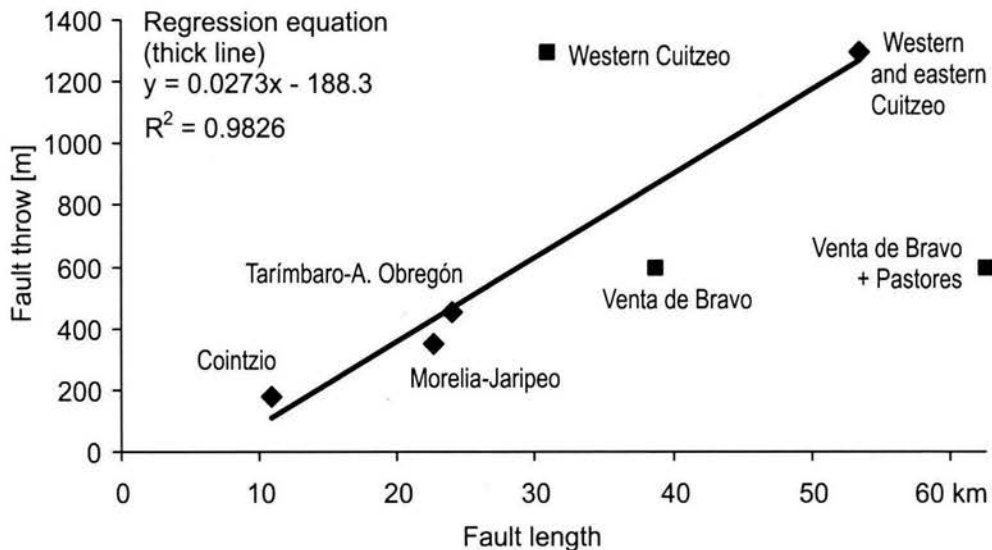


Figure 23. Throw / length scatter diagram of major faults of the study area. Only faults marked with diamonds were taken into account for calculation of regression line and correlation coefficient ( $R^2$ ).

### 6.4.2 Listric versus planar fault geometry

The tilt of the topographic surfaces (Plates 3-8), high to moderate dip of strata (locally up to  $50^\circ$ ) (Fig. 17) and observed rollover structures (Fig. 11) all point to listric faulting in the western depressions. The highest tilt of strata is seen at the western Cuitzeo fault (Plate 1). Further south, the Tarimbaro–A. Obregón and Morelia–Jaripeo faults also tilt the strata, although to a lesser degree (Fig. 17). Also, an S-tilted topographic surface is obvious in front of these faults (Plates 3, 4). In the case of the Cointzio fault, the absence of observable tilt of strata is most probably due to little displacements (see above). The absence of S-dipping faults in this area, along with S-dipping strata, indicates that the detachment fault dips to the north.

At the eastern portion of the Cuitzeo lake, I observed the reversal of the strata (Fig. 17) and topographic surface (Plate 5) tilt, and appearance of antithetic, S-dipping faults. The tilt of the topographic surface seems to be meaningful only to the north-east of Araró and toward the Santa Ana Maya and Puerto de Cabras faults (Plate 5). The tilt of volcanic domes at the western and southwestern part of Los Azufres caldera may be due to young magmatic activity in this region (intrusions below the southern caldera that feed the domes). The described reversal of strata tilt and fault polarity may be due to the activity of the antithetic MAFS faults or, alternatively, to the collapse of the northern margin of the Los Azufres caldera. Without data on the subsurface geometry around the eastern Cuitzeo lake this problem cannot be resolved. Nonetheless, only slightly curved traces of the Curinhuato faults (Fig. 17, Plate 1) do not justify the latter possibility.

The flat-lying strata of the central and eastern portion of the study area [usually not more than  $5^\circ$  dip ( $7^\circ$  in Suter *et al.*, 1995)], and at least 600 m of throw on the Venta de Bravo fault, compared to, 450 m of throw and at least  $12^\circ$  strata dip on the Tarimbaro fault rule out the possibility that to the west and east of Los Azufres the geometry of faulting is the same. Instead, this evidence points to listric faults to the west, and planar faults to the east of Los Azufres. In such case, the 40-km long Venta de Bravo fault should cut the entire brittle upper crust (*e.g.*, Nicol *et al.*, 1996; their Fig. 2), *ca.* 20 km thick below the central TMVB (Campos-Enriquez

and Sánchez-Zamora, 2000). A few locations with high dips of strata east of Los Azufres seem to be due to contraction, or interaction between fault segments, not tilting on normal faults.

The different style of deformation to the west and to the east of the Los Azufres caldera may be the effect of different pre-volcanic basement lithology. To the west of Los Azufres, the pre-volcanic basement is made up of continental red beds with strong lithologic contrasts, that are likely to favor the appearance of bedding-parallel detachments and thus listric faulting. To the east of the caldera, the more-or-less homogenous and strongly deformed sequence of metasediments forms the pre-volcanic basement, which do not favor bedding-parallel detachment.

Alternatively, a different fault geometry may be related to the arc topography and the location of faulting. As described in section 5.3, towards the west of Los Azufres normal faulting cuts the northern slopes of the arc and faults preferably dip to the north, while to the east of the caldera it cuts the most elevated portion of the arc and faults dip to the north and the south. Notably, at the longitude of Mexico City, where García-Palomo *et al.* (2002) report listric faults, faulting again cuts the northern slopes of the arc (Figs. 21, 22, profile F).

### 6.4.3 Modeled structural cross-sections

The inferred fault geometry and fault displacements, known thickness of strata (see section 2.2: "Stratigraphy"), and calculations of detachment depth (see below) permitted forward modeling of balanced, structural cross-sections (Fig. 24). These cross-sections illustrate subsurface MAFS geometry, and schematic stratigraphy, to the west, and to the east of the Los Azufres caldera.

Calculation of depth to detachment (Ramsay and Huber, 1987, Appendix 3) at the western Cuitzeo fault (based on an estimation of 1300 m of displacement, fault plane inclination of 60° and pre-tectonic strata dip of 25°) gives the value of *ca.* 3 km (Fig. 24A). At Tarímbaro–A. Obregón fault this calculation gives the value of *ca.* 2.5 km [450 m of displacement, fault plane inclination of 67° (because upper part of a listric fault is steeper, less displacement require higher fault dip for this calculation, see Appendix 3) and pre-tectonic strata dip of 12°]. Such configuration implies the detachment dipping *ca.* 2° to the north.

The southernmost tip of section A-A' in Figure 24 is located at the geographic longitude of Tzitzio structure, where Tzitzio formation (red beds) outcrops at *ca.* 800 m asl (Fig. 1). Hence, the calculated depth to detachment would correspond to the upper part of the Tzitzio formation, if we assume its monotonous dip of *ca.* 2° to the north, (Garduño-Monroy, Instituto de Investigaciones Metalúrgicas UMSNH, 2003, personal communication). Upper part of this formation is made up of indurated, resistant microconglomerate, underlain by thick sequence of relatively weak sandstones and siltstones (Pasquaré *et al.*, 1991). This lithologic contrast might control the detachment.

The cross-section across western depressions (Fig. 24A) is better constrained than the cross-section across Venta de Bravo region (Fig. 24B) because fault throws and thickness of sequences can be estimated more accurately. Unfortunately, modeling deformation across eastern Cuitzeo lake was impossible because fault displacements and detachment depth cannot be estimated due to the lack of subsurface data. Moreover, the software does not permit the introduction of antithetic faults (displacement must be from left to right).

Forward modeling of the section across western depressions (Fig. 24A) assumed horizontal roof of volcanic (pre-tectonic) sequence at 2200 m asl, and uniform increase of thickness of this sequence toward the north, due to the dip of red beds (see Fig. 24A for sections before and after deformation). Given that this does not need to be the case after adding the present topography the extent of modeled fluviolacustrine depressions filled with lacustrine and/or surficial sediments, does not match reality (compare Figs. 2 and 24A). It also shall be noted that at western Cuitzeo fault, maximum modeled strata dip is *ca.* 20° (Fig. 24A), not 25° shown by structural data (Fig. 17). The latter may signify even more displacement on this fault (*ca.* 2000 m of displacement was needed to obtain strata dip of 25°, with present fault geometry), and/or different subsurface fault geometry: steeper upper part of fault produces higher strata dips, but also means greater depth of detachment. Both alternatives are impossible to evaluate with available data. Modeling resulted in 5.3% (1.86 km) of extension at this section, which is a minimum value given that only large faults were taken into account.

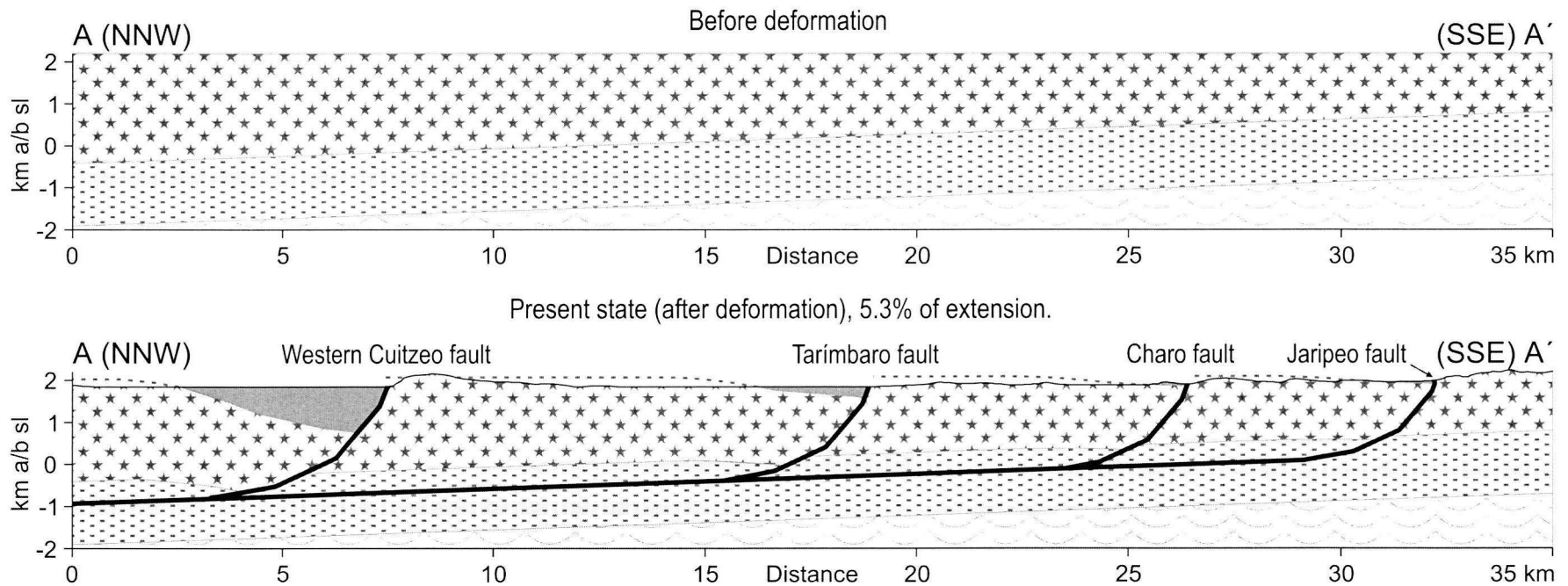
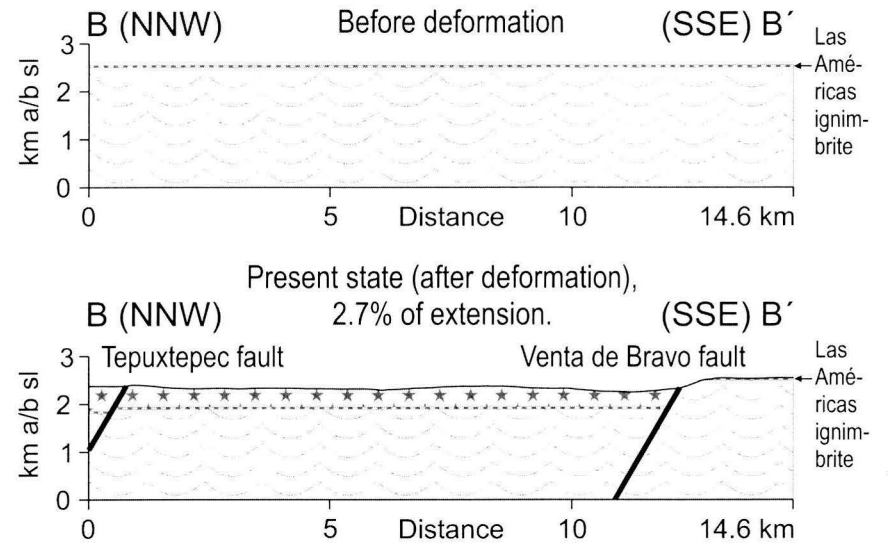
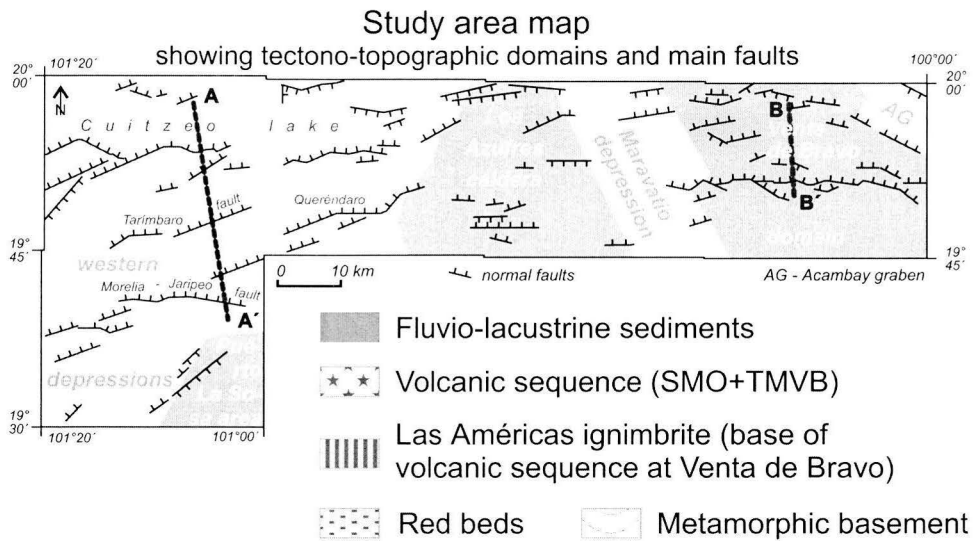


Figure 24. Forward modeling of (balanced) structural cross-sections. Traces of these sections are also marked in Figs. 2 (geologic map) and 17 (strata attitude). Broken dark gray lines in sections mark eroded roof of volcanic sequence. Vertical scale in km above/below sea level. Forward modelling was done with FBF software by J. Contreras, CICESE, Mexico. In section A-A' it is assumed that all volcanic rocks are pre-tectonic and that their thickness increase uniformly northward due to lowering of red beds roof (both assumptions are obviously a simplification). Note thinning of volcanic sequence due to the formation of roll-over structure in front of the western Cuitzeo fault.

A noteworthy output of the modeling of listric faults at western depressions is a thinning of volcanic sequence due to formation of roll-over structure (compare strata thickness across the western Cuitzeo fault in Fig. 24A). Such thinning is a logical consequence of the collapse of strata into the “void” (see Fig. 11) during the motion along the curved portion of a listric fault.

It shall also be mentioned, that the subhorizontal detachment modeled at western depressions is unlikely to extend beyond the northern boundary of active volcanic front of the TMVB. It is also unlikely to be rooted in a ductile layer which could accommodate displacement by crustal flow, because brittle/ductile transition within the crust is supposed to be *ca.* 20 km deep (Campos-Enríquez and Sánchez-Zamora, 2000), and the detachment is much shallower. Hence, amount of displacement on this detachment probably diminishes downward, similar as in the case of an elliptical planar fault (*e.g.*, Nicol *et al.*, 1996; Willemse *et al.*, 1996).

The section across Venta de Bravo region (Fig. 24B) was modeled assuming horizontal pre-tectonic strata. Modeling at this section resulted in minimum 2.7% (0.4 km) of extension on planar, 60° dipping faults. This section roughly illustrates faulting geometry east of the Los Azufres caldera.

#### 6.4.4 Slip rates

Extension in roughly N-S oriented cross-sections at western depressions and Venta de Bravo domain (Fig. 24) was modeled to be 5.3% and 2.7%, respectively. Average value of 4%, mean width of the MAFS, which is 40 km (Suter *et al.*, 2001), and 6 Ma of the MAFS existence permit calculation of mean N-S horizontal slip rate which is *ca.* 0.2 mm/yr. On 60° dipping faults this gives vertical slip rate of *ca.* 0.3 mm/yr across the whole of the MAFS (that is this slip rate should be divided between all faults encountered along a transect in N-S direction).

This rate is consistent with Quaternary rates for single faults: Langridge *et al.* (2000) found 0.18 mm/yr vertical slip rate at Acambay fault at easternmost MAFS, where the system is narrowest and features only two major faults: Acambay–Tixmadejé and Pastores (Fig. 1), the former being considerably larger. Hence, the remaining 0.12 mm/yr is likely to be distributed between Pastores fault and smaller structures. Suter *et al.* (2001) calculated *ca.* 0.05 mm/yr Quaternary vertical slip rate for single faults in Morelia region, where their map show 5-7 faults along N-S transect (Suter *et al.*, 2001; their Fig. 2). Hence, Quaternary slip rate is apparently representative for the time-span of the MAFS.

### 6.5 Kinematics of deformation

#### 6.5.1 Temporal and spatial relation between contractional and extensional structures

Figure 25A shows a rose diagram illustrating distribution of strikes of fault scarp and lineament traces (per length), and Figure 25B shows a rose diagram illustrating distribution of strikes of striated fault planes. Comparison between the two roses indicates that striated fault planes parallel to the E-striking, normal-oblique MAFS are undersampled with respect to the map-scale structures. Hence, it is reasonable to suppose that the E-striking MAFS and NNW-SSE oriented oblique extension registered on these faults, contribute more to the deformation than can be deduced from fault kinematics analysis presented in section 5.2.4. This reinforces the subordinate character of contractional structures.

The percentage of measured contractional faults decreases progressively during the TMVB development (Tab. 3). This decrease is much less clear when we consider the number of sites (stereograms) indicating contraction and extension (Tab. 3). One possible explanation is that in some sites successive reactivations has not been recognized, *i.e.*, contraction and extension orientations were calculated for a population of faults that should have been separated into two or more populations.



Strike-slip and reverse faults may precede normal faults, given that left-lateral strike-slip and (rarely) reverse faults form older striae in all sites where striae superposition was encountered (Figs. 16A, 18, Appendix 4). Nonetheless, striae superposition is most notable in Pliocene rocks and is found even in Quaternary rocks (Fig. 18C). Contractional faults are also present in Quaternary rocks (Fig. 18C). Hence, neither the process of fault inversion nor contractional deformation can be confined to early stages of the TMVB development.

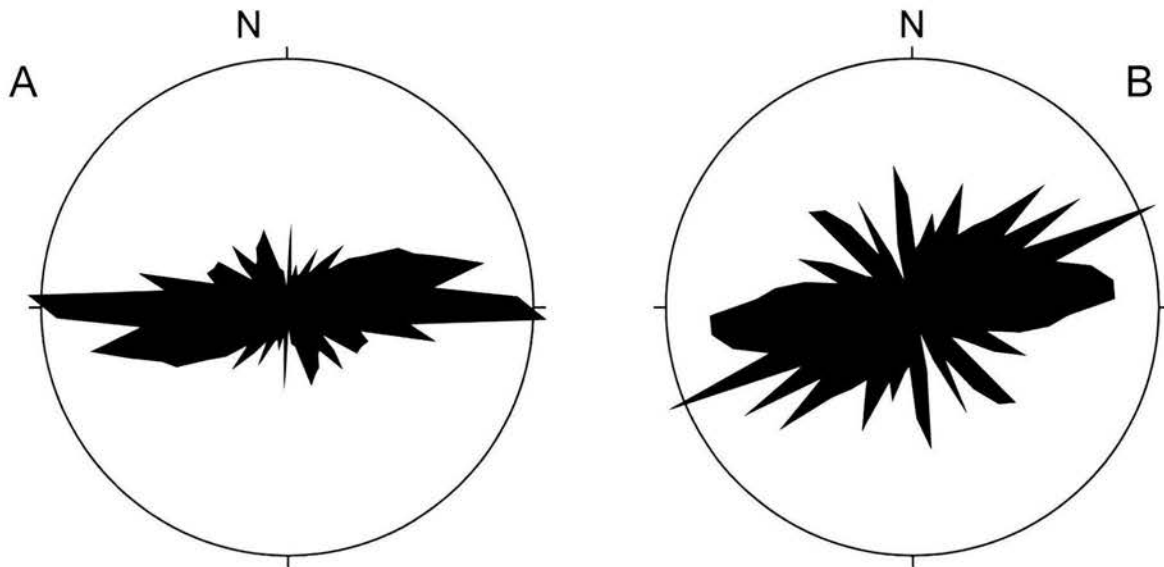


Figure 25. (A) Rose diagram illustrating distribution of strikes of fault and lineament traces (structures visible at map scale). Diameter of ring is 4% of fault and lineament length. (B) Rose diagram illustrating distribution of strikes of striated fault planes (structures visible at outcrop scale), 448 data points. Diameter of ring is 3% of striated fault plane frequency.

Predominantly normal MAFS originated in the late Miocene (*ca.* 6 Ma) (Israde-Alcantara and Garduño-Monroy, 1999; Suter *et al.*, 2001). Hence, since then strike-slip, reverse and normal faults are active within the study area. This implies that the deformation pattern since the establishment of the TMVB consists of interacting contractional and extensional structures, with the latter more accentuated in (Plio)-Quaternary.

Furthermore, as seen in Fig. 20, contraction and extension directions are almost constant through time, the former being preferably oriented NNE-SSW, and the latter being preferably oriented NNW-SSE. These imply roughly constant deformation pattern through the late Miocene to present, that is during the time-span of the arc.

This deformation pattern is dominated by oblique extension of the E-striking MAFS. In such cases left-lateral component on major faults is likely to produce subordinate contractional structures where main normal-oblique fault trace is curved to form restraining bend, just like in the case of strike-slip faults (*e.g.*, Christie-Blick and Biddle, 1985) (Fig. 26A). However, only 5 of 22 sites where reverse or strike-slip faults were measured can be considered as developed within restraining fault bends (sites 14, 20, 21, 38 and 47 in Fig. 18, of which only sites 14 and 21 are without doubt located within restraining bends). Most of the sites appear either unrelated to a major fault scarps (sites 1, 2, 3, 5, 12, 13, 32, 33, 35, 37, 41 in Fig. 18), associated with straight, E-striking fault segment (site 9 in Fig. 18) or even located within a releasing fault bend (sites 7, 19, 27, 39, 52 in Fig. 18 and the anticline between rhomb-shaped segments at Venta de Bravo fault in Fig. 17). Hence, strike-slip and reverse faults cannot be explained as subordinate accommodation structures required by strain compatibility (Ramsay and Huber, 1983) because most of them is apparently unrelated to (restraining) fault bends.

Instead, contractional structures, which are unrelated to MAFS segments, suggest component of shortening independent of major fault geometry. Rotations around vertical axis found by Soler-Arechalde and Urrutia-

Fucugauchi (2000) in Acambay graben further reinforce NNE-SSW contraction accompanying NNW-SSE oriented extension. Possible reasons behind such deformation pattern are further discussed in the section 6.6: “What drives the deformation of the central TMVB?”.

### 6.5.2 Regional fault systems: initiation and kinematics

The NNW-striking faults are apparently controlled by the pre-TMVB basement discontinuities, namely the Paleogene-Neogene Basin and Range extensional province, upon which the TMVB has been superimposed (Henry and Aranda-Gomez, 1992, 2000). Some of these faults may also be related to the (older) terrane boundaries, *e.g.*, a likely candidate is the NW-striking Perales fault to the east of the study area (Fig. 1), which is located above abrupt shift in crustal thickness (Molina-Garza and Urrutia-Fucugauchi, 1993; Urrutia-Fucugauchi and Flores-Ruiz, 1996) and approximately above the boundary between Guerrero terrane and Oaxaquia microcontinent (Ortega-Gutierrez *et al.*, 1995). Figure 19 shows that faults with this orientation are usually reverse or right-lateral.

The nature of the NE-striking, predominantly left-lateral, strike-slip faults is more difficult to constrain. They seem to be contemporaneous with, or only slightly older than the initiation of the TMVB, and therefore should rather be related to the processes that finally resulted in arc formation. I hypothesize, that the initiation of the present-day oblique, shallow-dip convergence along Acapulco trench in the middle-late Miocene (Morán-Zenteno *et al.*, 1996), might have resulted in shortening of the upper plate, and the development of strike-slip NE-striking faults (see also section 6.6: “What drives the deformation of the central TMVB?”).

Given the same orientations of the MAFS and the TMVB, some sort of interplay between the two is inevitable. This interplay, which includes factors controlling the MAFS, will be further discussed in section 6.6: “What drives the deformation of the central TMVB?”. Let me only anticipate it here, that geometric, spatial and temporal characteristics of the MAFS suggest that it originated, and develops in strict association with the TMVB, and that its orientation appears to be controlled by thermal weakening of the crust due to volcanic activity. However, in such a case, shallow, listric MAFS in western depressions should be a superficial expression of a deeper deformation, which should include (low-angle?) brittle faults between ductile lower crust, and the MAFS detachments. The MAFS motion is normal with subordinate left-lateral component.

### 6.5.3 Coeval activity of different fault systems: What model would explain it?

Coeval activity of the three fault systems deserves consideration. In this section I will discuss models that may explain such activity. First, I will review those models that are based on kinematic (strain) approach, and then those based on dynamic (stress) approach, and finally I will direct attention to the points of convergence between the two.

Any fault pattern, different from one subparallel fault set or conjugate fault system imply 3-D strain (Nieto-Samaniego, 1999). The study area, where three different fault systems are active, must therefore deform in 3-D strain. When such a strain field acts upon intact rock, or rock containing many randomly oriented planes of weakness, 4 sets of faults (2 oblique conjugate systems) with orthorhombic symmetry develop (Fig. 26B), as predicted by the slip model of Reches (1978, 1983) and the odd-axis model (further development of the former) of Krantz (1988). In practice, 3-D strain field may also result in 3 sets of faults (Reches and Dieterich, 1983). However, measured slip planes lack clearly recognizable orthorhombic symmetry, nor the three regional fault systems possess it. Only locally the MAFS resemble the fault pattern shown in Figure 26B *e.g.*, along western Cuitzeo fault (Plate 1). Moreover, regional evidence points to the reactivation of pre-existing and activation of existing, not randomly oriented planes of weakness (see section 6.5.2. above), and, according to Krantz (1988): “Systems produced by (...) reactivation of pre-existing faults may present geometric and kinematics patterns that cannot be understood in the context of simple orthorhombic or conjugate faulting.”

To my knowledge, the only model that directly address the possibility that faulting is controlled by pre-existing planes of weakness, which are not randomly oriented, is the interacting block model of Nieto-

Samaniego and Alaniz-Alvarez (1997). According to this model, the interplay between such pre-existing planes determines slip directions of faults. Given that in the central TMVB major fault systems are apparently controlled by either the pre-existing planes of weakness (NE-striking system, and NNW- to NW-striking Basin and Range faults) or existing weakness zone (the MAFS) (Ego and Ansan, 2002), this model seems the most viable explanation of the coeval activity of faults with different orientations.

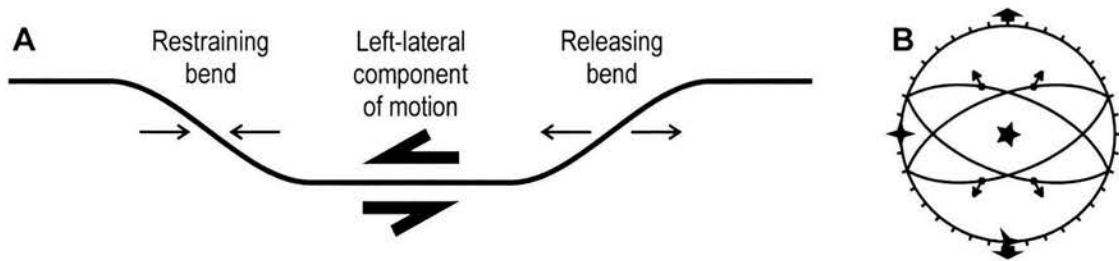


Figure 26. (A) Schematic illustration of releasing and restraining bend at a fault with left-lateral component of motion. (B) Stereoplot of a fault pattern predicted in 3-D strain with horizontal, N-S oriented greatest stretching. Note that two conjugate fault systems with oblique slip are formed. Three-point star and thick arrows represent N-S oriented stretching (extension axis), four-point star represents W-E oriented intermediate distortion (in this case contraction), and five-point star represents greatest shortening (vertical contraction). Angle between strikes of the two conjugate fault systems depends on strain ratio between intermediate and greatest contraction. Modified from Reches (1983) and Krantz (1988).

Notably, this model implies truly simultaneous movement of intersecting faults. Urbina and Camacho (1913) and Langridge *et al.* (2000) map *ca.* 10-km long, NW-striking fault trace that ruptured together with E-striking faults during the 1912 Acambay earthquake. This suggests that differently oriented faults do move simultaneously in the central TMVB. On the other hand side, at the northern edge of the central TMVB, Aguirre-Díaz (Centro de Geociencias UNAM, 2003, personal communication) found that the seismicity on nearly orthogonal fault systems (*ca.* E- and *ca.* N-striking) alternate, that is only one system moves at a time. If the simultaneous movement were indeed the case, and the model could be applied, then regional stretching and shortening directions can only be roughly determined from displacement of major faults. This is because accurate determination of strain (or stress) field is impossible in the case of interacting faults, unless we can establish relative motions of all fault-bounded blocks in the area (Nieto-Samaniego and Alaniz-Alvarez, 1997; Nieto-Samaniego, 1999). Such rough determination would result in NNW-SSE oriented stretching, observed on the most of major, E-striking faults (Fig. 18). It shall be stressed, that NNW-SSE oriented regional extension and NNE-SSW oriented contraction are coherent with (reactivated) fault kinematics.

An alternative to the kinematics approach is a dynamic (stress field) approach by Reches (1987) and Alaniz-Alvarez *et al.* (2000), based on the Coulomb-Mohr failure criterion, uniform stress field (lack of interaction between faults), and several other conditions and parameters. Again, if faults interact, the assumptions are not satisfied. Nonetheless, as fault interaction has not been proved without doubt, I discuss some options that use this approach.

Faults analyzed by Reches (1987) have variable orientations, and the author obtains satisfactory results fitting regional extension direction when both misfit angles are minimized and reasonable friction coefficient value [ $\sim 0.85$ , see Byerlee (1978)] is incorporated. Reches (1987) also observes that previous inversion methods [*e.g.*, P-T axes (or dihedral) by Angelier, 1979]] are valid only for cases with friction coefficient near 0 [*e.g.*, fault surfaces that developed thick fault gouge (Byerlee, 1978)]. Indeed, the complete fault slip data set collected in the study area, when analyzed with SoftStructure software by Z. Reches (shareware in: <http://earth.es.huji.ac.il/reches/soft.html>), returns stable solution for 0.5-1.3 range of friction coefficients (Tab. 4), after eliminating most of the reverse and lateral faults (*ca.* 30% of the data set, Tab. 4). Best solution [least principal angle misfit (Reches *et al.*, 1992)] gives NW-SE oriented, subhorizontal  $\sigma_3$  (Tab. 4). This solution further reinforces oblique (left-lateral) extension (assuming that  $\sigma_3$  parallels extension) at the central TMVB, and is similar to the results obtained by Ego and Ansan (2002). Data deleted in the first step (reverse and

lateral faults), did not return stable solution (with default misfit angles, the software eliminated 80% of the data).

Alaniz-Alvarez *et al.* (2000), and Tolson *et al.* (2001) provide computer software (ReActiva) (shareware in: <http://geologia.igeolcu.unam.mx/Tolson/SoftWare/ReActivaV24Es.exe>) that permits visualizing reactivation of pre-existing planes of weakness in a given stress field. In the case of normal faults, reactivation domains grow with decreasing depth, friction coefficient ( $\mu$ ), cohesion, stress ratio [ $R=(\sigma_2-\sigma_3)/(\sigma_1-\sigma_3)\approx 0$ , hence  $\sigma_2\approx\sigma_3$ ], and mean rock density (similar to depth decrease, in the sense that it lowers the confining pressure), and with increasing pore pressure, reaching, *e.g.*, 95% of the stereonet area at 1 km depth, other parameters kept at default levels (see Tolson *et al.*, 2001). Given many independent parameters, it is difficult to find out which in particular (if any) of these factors may be the controlling one. Nonetheless, I discuss a few possibilities below.

Table 4

Friction coefficient-dependent stress field solution for complete fault slip data set collected in the study area.

FA	STATUS	FRICTION COEF.	MISFITS		STRESS MAGNITUDE			Phi	STRESS ORIENTATIONS		
			PRINC	SLIP	1	2	3		1	2	3
448	LEAST	0	45.91	49.32	-100	-98	-98	0.11	89/265	0/15	0/105
301	LEAST	0	33.9	27.01	-100	-98	-98	0.11	89/329	0/217	0/127
301	LEAST	0.1	32.43	27.04	-100	-81	-78	0.09	88/323	0/215	1/125
301	LEAST	0.2	30.95	27	-100	-64	-61	0.08	88/324	0/215	1/125
301	LEAST	0.3	29.66	27.71	-100	-52	-48	0.08	87/326	0/215	2/125
301	LEAST	0.4	28.59	28.17	-100	-42	-38	0.07	87/329	1/215	2/125
<b>301</b>	<b>LEAST</b>	<b>0.5</b>	<b>27.76</b>	<b>28.7</b>	<b>-100</b>	<b>-34</b>	<b>-30</b>	<b>0.07</b>	<b>86/332</b>	<b>1/216</b>	<b>3/126</b>
<b>301</b>	<b>LEAST</b>	<b>0.6</b>	<b>27.17</b>	<b>29.27</b>	<b>-100</b>	<b>-28</b>	<b>-24</b>	<b>0.06</b>	<b>86/334</b>	<b>1/217</b>	<b>3/127</b>
<b>301</b>	<b>LEAST</b>	<b>0.7</b>	<b>26.78</b>	<b>29.85</b>	<b>-100</b>	<b>-23</b>	<b>-19</b>	<b>0.06</b>	<b>85/335</b>	<b>1/219</b>	<b>3/129</b>
<b>301</b>	<b>LEAST</b>	<b>0.8</b>	<b>26.55</b>	<b>30.42</b>	<b>-101</b>	<b>-19</b>	<b>-15</b>	<b>0.05</b>	<b>85/336</b>	<b>2/221</b>	<b>4/130</b>
<b>301</b>	<b>LEAST</b>	<b>0.9</b>	<b>26.44</b>	<b>30.91</b>	<b>-101</b>	<b>-16</b>	<b>-11</b>	<b>0.05</b>	<b>84/337</b>	<b>2/222</b>	<b>4/132</b>
<b>301</b>	<b>LEAST</b>	<b>1</b>	<b>26.43</b>	<b>31.3</b>	<b>-101</b>	<b>-13</b>	<b>-9</b>	<b>0.05</b>	<b>84/337</b>	<b>2/224</b>	<b>4/134</b>
<b>301</b>	<b>LEAST</b>	<b>1.1</b>	<b>26.49</b>	<b>31.59</b>	<b>-101</b>	<b>-11</b>	<b>-6</b>	<b>0.05</b>	<b>84/337</b>	<b>2/226</b>	<b>5/135</b>
<b>301</b>	<b>LEAST</b>	<b>1.2</b>	<b>26.59</b>	<b>31.8</b>	<b>-101</b>	<b>-9</b>	<b>-4</b>	<b>0.04</b>	<b>84/337</b>	<b>1/227</b>	<b>5/137</b>
<b>301</b>	<b>LEAST</b>	<b>1.3</b>	<b>26.72</b>	<b>31.95</b>	<b>-101</b>	<b>-7</b>	<b>-3</b>	<b>0.04</b>	<b>84/336</b>	<b>1/229</b>	<b>5/138</b>
287	LEAST	1.4	28.18	29.02	-101	-5	-1	0.04	84/335	1/230	5/140
262	LEAST	1.5	31.05	25.18	-101	-4	0	0.04	84/335	1/231	5/141

Selected pore pressure is 0 and mean cohesion is 0.

Solution was obtained with SoftStructure by Z. Reches (shareware in: <http://earth.es.huji.ac.il/reches/soft.html>). Program was run with default values, including 60° and 90° for principal and slip angle misfits, respectively. Changing other values influences stress magnitudes, but does not change stress axes orientations. The range of  $\mu$  that returns stable solution is bold, and best solution is underlined. Note that *ca.* 30% of the data was eliminated (most of reverse and lateral slip planes).

For reactivation at shallow depth to be the case, we need pre-existing relatively high-angle planes of weakness at shallow depth, which in a youthful volcanic terrain could only be thermal joints. Therefore it is clear, that at least map-scale faults with unfavorable orientations were reactivated below volcanic cover and propagated upwards.

Minimizing friction coefficient, which also increases reactivation domains, means either the increase of confining pressure, and therefore depth (up to  $\mu\approx 0.8$ ) (in which case asperities of fault plane cease to be an obstacle to slip), or development of fault gouge (Byerlee, 1978). Given that faults in the area commonly develop gouge, it is a possible reason for variable fault orientation. However, the solution presented in Tab. 4 is stable at  $\mu>0.5$ , suggesting that friction coefficient is not particularly low.

Minimizing stress ratio ( $R \approx 0$ , so  $\sigma_2 \approx \sigma_3$ ) also increases reactivation domain (to 81% of the stereonet at  $R=0$ , other parameters kept at default levels). In the latter case, vertical faults, which do appear in the study area, are not permitted. Nevertheless  $R=0$  and, for example, 5 km depth of faulting increases reactivation domain to 91% of stereonet and permit such faults, covering the entire range of observed slip planes.  $R \approx 0$ , and therefore  $\sigma_2 \approx \sigma_3$  implies (almost) axisymmetric stress, which is likely to produce permutations of the intermediate and least stresses, due to stress relaxation when one of nearly orthogonal fault systems ruptures. Such permutations were proposed by Suter *et al.* (1995a), to explain the activity of E- and N-striking faults at Aljibes half-graben located at the northern edge of the central TMVB. 3-D strain field was proposed by Alaniz-Alvarez *et al.* (2001) to explain the same fault pattern. According to Reches (1983), 3-D strain field requires  $\sigma_2 = \sigma_3$  [3D strain requires 3 to 4 sets of faults oblique to principal strain axes; 3D stress field requires 2 sets of faults that include intermediate stress axis; axisymmetric stress field generates infinite number of faults, of which 4 sets minimize deviatoric stress and energy dissipation; see Reches (1983) for full reasoning of the problem]. In this sense,  $\sigma_2 = \sigma_3$  is necessary for 3-D strain, and implies it (with infinite number of faults of varying orientations plane strain is inconceivable). Therefore, axisymmetric stress (stress ratio = 0), implying 3-D strain, and combined with some other factor(s) is likely to be responsible of the observed fault pattern, provided that faults do not interact. This option is also compatible with  $\sigma_2$  and  $\sigma_3$  permutations proposed by Suter *et al.* (1995a) at the northern edge of the central TMVB.

The remaining issue is the relationship between the directions of principal stresses and strains. In pure shear (unrotational strain), stress axes orientations are parallel to strain axes orientation, hence both approaches give equivalent results as far as orientations of stress/strain principal axes are concerned. Obviously, the results are not equivalent in terms of magnitudes, or senses of principal stresses and strains. However, in the study area most faults dip to the north, hence strain is not truly unrotational. Moreover, given that striae in the first term indicates displacement direction of a fault (Twiss and Unruh, 1998; Gapais *et al.*, 2000), discussing the results in terms of kinematics (strain) is more straightforward and sufficient if we are interested in orientations only.

In summary, there are two conceivable (and partially incompatible) models that can explain coeval activity of three highly oblique fault systems in the central TMVB:

- (i) Faults are controlled by not-randomly oriented planes of weakness implying 3-D strain. All three fault systems can move in a single event, hence these faults behave according to the interacting block model of Nieto-Samaniego and Alaniz-Alvarez (1997). In such a case stretching and shortening directions can only be roughly estimated. This estimation would result in NNE-SSW oriented, subordinate contraction, and NNW-SSE oriented, extension, coherent with observed fault pattern. Given that the studied faults are apparently controlled by planes of weakness and faults with different orientations apparently move simultaneously, this is my preferable option.
- (ii) Faults move in (almost?) axisymmetric stress field ( $\sigma_2 \approx \sigma_3$ ), implying 3-D strain. Additional factor(s) favoring fault reactivation, such as relatively shallow depth of nucleation or low friction coefficient, make possible the observed fault pattern. In such case faults can (but not have to) be controlled by not-randomly oriented planes of weakness. However, faults do not interact, hence only one fault system can move in a single event. Alternating events on almost perpendicular fault systems are likely due to stress relaxation and therefore intermediate and least stress permutations.

## 6.6 What drives the deformation of the central TMVB?

The results of this work permit one to make a few observations regarding the much discussed (see sec. 1.3 in Introduction) issue of whether the MAFS orientation is controlled by the strike of the TMVB, or the TMVB is controlled by the orientation of the MAFS. If the geometry of the western MAFS is listric with shallow detachment zone, then at least in this area the MAFS is unlikely to control the location of the TMVB, because these faults do not cut the upper part of the crust so cannot provide effective conduits for magma ascent. Nonetheless, they do seem to provide paths for magma within the upper part of the crust, given that many monogenetic cones are seated on the traces of the MAFS. Indeed, according to Takada (1994), in the case of monogenetic volcanoes, cracks that provide paths for magma ascent tend to interact (coalesce) until in the upper parts of the crust. Such a configuration suggests a scale-dependent phenomena: at regional scale, the TMVB (and hence the MAFS) are related to the subduction geometry, namely decrease of dip angle of

subducted slab towards the east. Nevertheless, on a local scale of individual fault segments, the latter influence the distribution of volcanism.

Moreover, growing body of geochemical data confirms that the TMVB is indeed related to subduction (Wallace and Carmichael, 1999; Cervantes and Wallace, 2000; Ferrari *et al.*, 2001; Schaaf *et al.*, 2001; Gómez-Tuena, 2002; Gómez-Tuena *et al.*, 2004; Siebe *et al.*, 2004). Subsequently, the MAFS appears to be an effect of the TMVB existence. Two explanations of the intra-arc faulting as a result of the arc existence have been proposed: (1) the MAFS is an expression of gravitational collapse of the arc (Suter *et al.*, 2001) and (2) the MAFS is an effect of far-field plate tectonics, namely convergence along Acapulco trench, accommodated along the TMVB because, due to high heat flow, it is a weakness zone (Ego and Ansan, 2002). I discuss these options below, and also propose other mechanisms that may play a role in the deformation of the central TMVB.

The available data shows that: (i) The TMVB is characterized by the negative Bouguer gravimetric anomaly (De la Fuente-Duch *et al.*, 1994a). (ii) The TMVB as a whole does not produce a residual isostatic gravimetric anomaly (Airy's model). The greatest observed residual isostatic anomalies are roughly perpendicular or oblique to the arc (de la Fuente-Duch *et al.*, 1994b). (iii) The distribution of major normal faults within the TMVB is inconsistent with residual isostatic anomalies. (iv) These faults usually dip towards the terrain whose mean elevation is higher than, or similar to the arc. Even if the topography alone does not provide an argument against or in favor of the gravitational collapse because the terrain elevated above its vicinity might be compensated in which case there is no reason for collapse (García, CFE, 2003, and Mena, Instituto de Geofísica UNAM, 2003, personal communication), fault system dipping toward higher terrain (higher at spatial scale relevant to geophysical investigation) is unlikely to be an expression of the gravitational collapse.

These data argue against the possibility that the MAFS is an expression of (or its motion is enhanced by) a gravitational collapse of the TMVB. If the latter were the case, one would expect positive gravimetric anomalies, and a general lack of isostatic compensation of the TMVB, which is not the case. There exists a possibility, that the lack of compensation is operating on local scales (and the compensation surface is shallow), but at the present state of knowledge there are no data to support such an option. Moreover, in such a case the rigidity of the crust is supposed to be sufficient to support surface loads at least in the case of planar, high-angle faults (García, CFE, 2003, and Mena, Instituto de Geofísica UNAM, 2003, personal communication). Hence, if the TMVB deformation is not due to the gravitational collapse, then we need some kind of far-field force related to plate motions to explain the activity of the MAFS.

As shown above, the relation of the MAFS to plate tectonics is, in the light of the data presented here, the only plausible option. Given that Acapulco trench at Pacific coast is the nearest plate boundary, and subduction zone along it is responsible for the TMVB, there is little doubt that this plate boundary is the first candidate to examine. According to Ego and Ansan (2002), who base their conclusions on geometric relationships between convergence vector between North America and Cocos plates and slip vector of subduction earthquakes, oblique convergence along Acapulco trench is not totally released by subduction earthquakes, leaving left-lateral, coast-parallel slip component, which must be accommodated within the upper plate (slip partitioning concept). These authors point out the TMVB as the most likely candidate to accommodate this slip, because it is a weakness zone [thermal weakening of the crust due to volcanic activity, which lowers the crust viscosity (Klepeis *et al.*, 2003), controls the orientation of the MAFS, constituting kind of "plane of weakness" in comparison with more rigid neighboring terrain].

This is no doubt a very appealing proposal because it explains the MAFS existence and activity with a precise, subduction-related mechanism. However, it poses a data compatibility problem: coast-parallel, WNW-ESE oriented motion postulated by Ego and Ansan (2002) signify that the ratio of left-lateral to vertical slip rate along the E-striking and 60° dipping MAFS should be 5:2 (Ego and Ansan, 2002). This is inconsistent with structural data, both published (Pasquaré *et al.*, 1988; Suter *et al.*, 1992, 1995a,b, 2001; Ferrari *et al.*, 1994a; Israde-Alcantara and Garduño-Monroy, 1999; Langridge *et al.*, 2000; García-Palomo *et al.*, 2000, 2002) and presented in this work. These structural data indicates NNW-striking extension, which on E-striking fault with 60° dip gives a ratio of left-lateral to vertical slip of *ca.* 1:4. Moreover, vertical slip rate calculated in section 6.4.4 (0.3 mm/yr) means that with NNW-SSE oriented extension lateral component on the MAFS is 0.075 mm/yr. Ego and Ansan's (2002) calculation of left-lateral slip component along the

MAFS gives 7.5 mm/yr, which is 2 orders of magnitude greater. In terms of the vertical slip rate the difference is one order of magnitude [0.3 mm/yr in this work and 3 mm/yr in Ego and Ansan's (2002) work] because of different extension orientation. Hence it seems obvious, that most of trench-parallel motion is accommodated between the trench and the TMVB, possibly along the Xolapa mylonite, where Tolson-Jones (1998) found active left-lateral motion.

Vertical slip rates and ratios of lateral to vertical slip described above predict that an additional motion component must exist (possibly trench- or arc-perpendicular), in order to rotate motion vector from coast-parallel WNW-ESE to NNW-SSE position observed in structural data. A factor that might introduce such motion component was recently proposed by Ferrari (2004b). This author states that arc-perpendicular rollback of the leading edge of subducted slab below central TMVB may influence intra-arc faulting, although it is not clear how the two processes would be linked. Moreover, NNE-SSW contraction must also be accounted for in a model for the intra-arc deformation. Shallow-dip subduction, which often leads to shortening of upper plate (e.g., Gutscher *et al.*, 1999), might account for this (perpendicular to the trench) shortening.

Finally, given that the TMVB (and hence the deformation affecting it) appears strictly connected with subduction along Mexican Pacific coast, its evolution should show dependence on the Miocene to Recent subduction geometry and kinematics. According to Morán-Zenteno *et al.* (1996), the present-day convergence pattern initiated after major reorganization of the subduction kinematics, which started with fragmentation of the Farallon plate during the Oligocene and subsequent eastward movement of the Chortis block. It resulted in the development of the Acapulco trench during the middle/late Miocene at the site of the previous transform between North America and the Chortis block (Morán-Zenteno *et al.*, 1996) (Fig. 27). Alternatively, subduction erosion could produce the present-day position of the arc (Keppie, Instituto de Geología UNAM, 2004, personal communication). Regardless of which process is responsible for the initiation of subduction at the Acapulco trench, this subduction led to the establishment of the TMVB in the late Miocene (Ferrari *et al.*, 1994a). Since then there were no major shifts in subduction geometry in front of the central Mexico. Nonetheless, subducted slab detachment, propagating from W to E below the TMVB (Ferrari, 2004a), and subsequent slab rollback were proposed to influence intra-arc faulting (Ferrari, 2004b). These processes plus growth of the volcanic arc, and associated thermal weakening of the crust [TMVB has high heat flow according to Prol and Juarez (1985)] might be responsible for waning of the NNE-SSW shortening and dominance of the NNW-SSE stretching.

## 6.7 Advantages and disadvantages of applied morphostructural analysis in the central TMVB

As anticipated in introduction, morphostructural analysis resulted highly useful data to detect deformation obscured by young sedimentary and volcanic products. In particular, longitudinal river profiles coupled to bedrock lithology and age, produced the conclusion that three different fault systems are active within the study area. Hard-rock (structural data) proof of this conclusion (e.g., Fig. 15) are rare and might be difficult to find in neighboring areas.

Moreover, morphometric parameters permitted detection of unexpected morphotectonic configuration of the area, namely arc-transverse structures, which dominate arc-parallel ones. In this case Maravatío depression is an excellent example of the advantage of morphostructural investigation when compared to purely structural one. According to Suter *et al.* (2001), it is a major depression of pre-MAFS Basin and Range trends (NNW-striking), which nonetheless does not seem to be fault-controlled. Indeed, NNW-striking faults with Holocene displacement has been found in the easternmost study area (Fig. 15), where they are associated with the NE edge of Venta de Bravo domain, but not at the edges of Maravatío depression. However, both morphometry of this depression compared to its neighbors, and fluvial regime changes across its eastern edge suggest that it is active fault bound. Recent, intense volcanism and sedimentation in both edges of this depression (illustrated in Fig. 2 and Plates 1, 6 and 8) are most probably responsible for obscuring structural evidence of these faults.

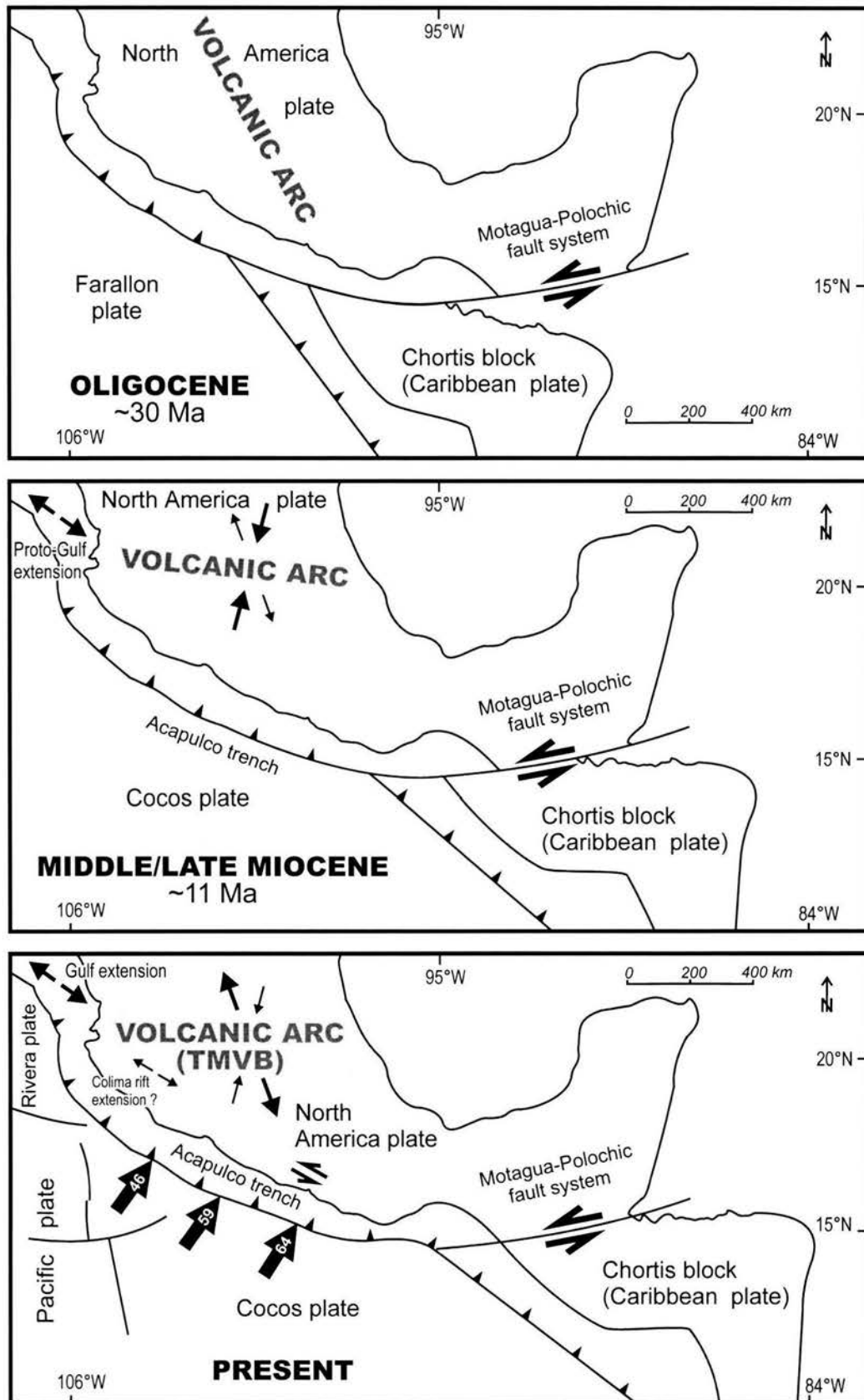


Figure 27. Plate configuration and volcanic arc location in Oligocene, middle/late Miocene and present. Thick arrows are relative convergence rates between oceanic and continental plates (in mm/yr). Modified from: Ego and Ansan (2002), Morán-Zenteno *et al.* (1996), Rosas-Elguera *et al.* (1996), Ferrari *et al.* (1999).



When these morphometric data were coupled with geomorphologic (surface class) map and data on fault activity, it was possible to show that arc-transverse structures are being fragmented by arc-parallel ones, but still take up part of the deformation process. It would most probably be impossible to detect and/or prove such a configuration with structural or geomorphic data alone.

Volcanic landforms in geomorphologic maps (Plates 3-8) to some extent permitted verification of existing geologic maps, which in turn allowed more accurate dating of deformation. Furthermore, fault scarp degradation coupled with fault throw data permitted to hypothesize about fault growth pattern in western portion of the area, where scarp degradation does not show direct dependence on lithology or bedrock age. Nevertheless, lithologic and bedrock age variability precluded quantitative evaluations. This case clearly shows an advantage of combining structural and geomorphic data which permits distinction if variable scarp degradation is an effect of fault initiation or slip rate. With paleoseismologic data a third possible variable (time since last rupture) can be evaluated.

In summary, in a youthful volcanic arc, where active structures are partly obscured by sediments and volcanic products, morphometry and geomorphologic mapping permit detection of structural patterns undetectable by other means. Longitudinal river profiles permit qualitative assessment of fault activity. Fault scarp degradation coupled with bedrock lithology and structural data are likely to allow inferences about fault growth pattern and/or relative fault displacement rates.

## 7 Conclusions

The following conclusions, concerning the tectono-topographic configuration of the central TMVB, the deformation pattern affecting the region, and the reasons behind these phenomena, can be made based on the geomorphic and structural data presented here:

- (i) A complex deformation pattern affects the central TMVB. Instead of a collapse of volcanic arc on arc-parallel faults, three active regional fault systems – NNW-striking Basin and Range faults, NE-striking faults, and E-striking MAFS – with different rates and/or senses of motion are deforming the region and modifying its topography.
- (ii) Pre-TMVB structures, mainly Basin and Range, NNW-striking horsts and grabens, control major tectono-topographic elements that build up the study area. These elements are being fragmented and overprinted by the MAFS, but still take up part of the deformation process, hence their persistence.
- (iii) The subsurface geometry of the MAFS changes across the Los Azufres caldera. To the west, the system is made up of listric faults with shallow detachment zone, to the east it is made up of planar faults, most probably (given their length) cutting the entire brittle upper crust.
- (iv) The different fault geometry may be due to different basement lithologies, different location of faulting within the arc (on its northern slopes to the west of Los Azufres, and cutting its most elevated portion to the east of it), or both.
- (v) The NNW-SSE oriented, subhorizontal, regional stretching, accompanied by subordinate NNE-SSW oriented, subhorizontal, shortening are responsible for the coexistence of contractional and extensional structures in close space-time relationship at the central TMVB.
- (vi) Coeval activity of three regional fault systems can be explained as the effect of the interaction between (pre)-existing planes of weakness or, alternatively, as the effect of very low stress ratio, plus some other factors such as shallow faulting, low friction coefficient, or high pore pressure. In both cases the region must be deforming in 3-D strain, although if the former is the case, principal strains can only roughly be estimated. Nonetheless, this rough estimation is consistent with the one given above.
- (vii) The MAFS apparently originated in association with the volcanic arc. Thermal weakening of the crust due to volcanic activity seems to condition its appearance and orientation.
- (viii) Oblique convergence at the Acapulco Trench and subduction geometry and dynamics are the most plausible sources of the deformation pattern observed in the central TMVB.

- (ix) In a youthful volcanic arc, regardless (and in some cases due to) its lithologic complexity and variable substrate age, a combination of geomorphic and structural data permits determination of deformation patterns inaccessible with geomorphic or structural tools alone.

## 8 Reference list

- Ackermann, R.V., Schlische, R.W., Withjack, M.O., 2001. The geometric and statistical evolution of normal fault systems: an experimental study of the effects of mechanical layer thickness on scaling laws. *Journal of Structural Geology*, 23(11): 1803-1819.
- Aguirre-Díaz, G.J., 1993. The Amealco caldera, Querétaro, México: Geology, geochronology, geochemistry, and comparison with other silicic centers of the Mexican Volcanic Belt. PhD Thesis, University of Texas, Austin, USA, pp. 401.
- Aguirre-Díaz, G.J., 1995. La toba Amealco y su correlación con la formación Las Américas a través del graben de Acambay, estados de México, Michoacán y Querétaro, México. *Revista Mexicana de Ciencias Geológicas*, 12(1): 17-21.
- Aguirre-Díaz, G.J., 1996. Volcanic stratigraphy of the Amealco caldera and vicinity, central Trans-Mexican Volcanic Belt. *Rev. Mex. de Cie. Geol.*, 13(1): 10-51.
- Aguirre-Díaz, G.J., McDowell, F.W., 2000. Volcanic evolution of the Amealco caldera, central Mexico, *in* Delgado-Granados H., Aguirre-Díaz, G., and Stock, J.M., eds., *Cenozoic Tectonics and Volcanism of Mexico*: Boulder, Colorado, GSA Spec. Paper 334.
- Aguirre-Díaz, G.J., Urrutia-Fucugauchi, J., Soler-Arechalde, A.M., McDowell, F.W., 2000. Stratigraphy, K-Ar ages, and magnetostratigraphy of the Acambay graben, central Mexican Volcanic Belt, *in* Delgado-Granados H., Aguirre-Díaz, G., and Stock, J.M., eds., *Cenozoic Tectonics and Volcanism of Mexico*: Boulder, Colorado, GSA Spec. Paper 334.
- Aguirre-Díaz, G.J., Nieto-Obregón, J., Zuñiga, R., 2003. The Querétaro graben: Basin and Range faulting in the central-northern portion of the Mexican Volcanic Belt. *GSA Abstracts with programs*, 35(4): 57.
- Alaniz-Alvarez, S.A., Nieto-Samaniego, A.F., Ferrari, L., 1998. Effect of strain rate in the distribution of monogenetic and polygenetic volcanism in the Transmexican volcanic belt. *Geology*, 26(7): 591-594.
- Alaniz-Alvarez, S.A., Tolson, G., Nieto-Samaniego, A.F., 2000. Assessing fault reactivation using the ReActiva program. *Journal of Geoscience Education*, 48(5): 651-657.
- Alaniz-Álvarez S.A., Nieto-Samaniego, A.F., Reyes-Zaragoza, M.A., Orozco-Esquivel, M.A., Ojeda-García, A.C., Vassallo, L.F., 2001. Estratigrafía y deformación extensional en la región San Miguel de Allende-Querétaro, México. *Revista Mexicana de Ciencias Geológicas*, 18(2): 129-148.
- Altamira-Areyán, A., 2002. Las litofacies y sus implicaciones de la cuenca sedimentaria Cutzamala – Tiquicheo, estados de Guerrero y Michoacán, México. McS thesis, UNAM, Mexico, 79 pp.
- Angelier, J., 1979. Determination of the mean principal directions of stresses for a given fault population. *Tectonophysics*, 56: T17-T26.

- Angelier, J., 1994. Fault slip analysis and paleostress reconstruction. In: P.L. Hancock (Editor), *Continental Deformation*. Pergamon Press, Oxford, UK, p. 53-100.
- Angelier, J., Mechler, P., 1977. Sur une méthode graphique de recherche des contraintes principales également utilisable en tectonique et en sismologie: la méthode des dièdres droits, *Bull. Soc. géol. France*, 19(7): 1309-1318.
- Astiz, L.M., 1980. Sismicidad en Acambay, Estado de México. El temblor del 22 de febrero de 1979, B.S. thesis, 130 pp., UNAM, Mexico City.
- Ballina-López, H.R., 1987a. Perfiles gravimétricos y magnetométrico en el campo geotérmico Los Azufres, Michoacán. *Geotermia, Rev. Mex. Geoenergía*, 3(3): 275-283.
- Ballina-López, H.R., 1987b. Estudio geoelectrico de resistividad en la zona occidente de Los Azufres, Mich. *Geotermia, Rev. Mex. Geoenergía*, 3(3): 145-154.
- Bocco, G., Mendoza, M., Velázquez, A., 2001. Remote sensing and GIS-based regional geomorphological mapping – a tool for land use planning in developing countries. *Geomorphology*, 39: 211-219.
- Burbank, D.W., Anderson, R.S., 2000. *Tectonic geomorphology*. Blackwell Science, Massachusetts, USA.
- Burrough, P.A., van Gaans, P.F.M., MacMillan, R.A., 2000. High-resolution landform classification using fuzzy k-means. *Fuzzy Sets and Systems*, 113: 37-52.
- Byerlee, 1978. Friction of Rocks. *Pure Appl. Geoph.*, 116(4-5): 615-626.
- Camacho, H., 1925. Las aguas subterráneas del valle de Morelia, Estado de Michoacán. *Anales del Instituto Geológico*, 2: 6-17.
- Campa, M.F., Coney, P.J., 1983. Tectonostratigraphic terranes and mineral resource distributions in Mexico. *Canadian Journal of Earth Sciences*, 20: 1040-1051.
- Campillo, M., Singh, S., Shapiro, N., Pacheco, J., Herrmann, R., 1996. Crustal structure south of the Mexican volcanic belt, based on group velocity dispersion. *Geof. Int.*, 35(4): 361-370.
- Campos-Enríquez, J.O., Alatorre-Zamora, M.A., 1998. Shallow crustal structure of the junction of the grabens of Chapala, Tepic-Zacoalco and Colima, Mexico. *Geofísica Int.*, 37(4): 263-282.
- Campos-Enriquez, J.O., Garduño-Monroy, V.H., 1995. Los Azufres silicic center (Mexico): Inference of caldera structural elements from gravity, aeromagnetic, and geoelectric data. *Jour. of Volcan. and Geotherm. Res.*, 67: 123-152.
- Campos-Enriquez, J., Sánchez-Zamora, O., 2000. Crustal structure across southern Mexico inferred from gravity data. *Journal of South American Earth Sciences*, 13: 479-489.
- Campos-Enriquez, J., Arroyo-Esquivel, M., Urrutia-Fucugauchi, J., 1990. Basement, Curie isotherm and shallow-crustal structure of the Trans-Mexican Volcanic Belt, from aeromagnetic data. *Tectonophysics*, 172: 77-90.
- Campos-Enriquez, J.O., Rodríguez, M., Delgado-Rodríguez, O., Milán, M., 2000. Contribution to the tectonics of the northern portion of the central sector of the trans-Mexican Volcanic Belt, in Delgado-Granados H., Aguirre-Díaz, G., and Stock, J.M., eds., *Cenozoic Tectonics and Volcanism of Mexico*: Boulder, Colorado, GSA Spec. Paper, 334.
- Campos-Enríquez, J.O., Alatrístre-Vilchis, D.R., Huizar-Álvarez, R., Marines-Campos, R., Alatorre-Zamora, M.A., 2003. Subsurface structure of the Tecocomulco sub-basin (northeastern Mexico basin), and its relationship to regional tectonics. *Geofísica Internacional*, 42(1): 3-24.
- Carrasco-Núñez, G., 1988. *Geología y petrología de los campos volcánicos de Los Azufres (Mich.), Amealco y Zamorano (Qro.)*. Ms. Thesis, Fac. de Ingeniería, UNAM, Mexico City, pp. 148.
- Cartwright, J.A., Trudgill, B.D., Mansfield, C.S., 1995. Fault growth by segment linkage: an explanation for scatter in maximum displacement and trace length data from Canyonlands Grabens of SE Utah. *J. Struct. Geol.*, 17(9): 1319-1326.
- Cebull, S.E., Shurbet, D.H., 1987. Mexican Volcanic Belt: an intraplate transform? *Geofísica Internacional*, 26: 1-14.
- Cervantes, P., Wallace, P., 2000. Water in Subduction Zone Magmatism: New Insights From Melt Inclusions in High-Mg Basalts From Central Mexico. *EOS*, 81: 1370 (Abstract).
- Christie-Blick, N., Biddle, K.T., 1985. Deformation and basin formation along strike-slip faults. In: R.L. Ethington (Ed.), *Strike-slip Deformation, Basin Formation, and Sedimentation*. Society of Economic Paleontologists and Mineralogists, Spec. Publ., 37.
- Clifton, A.E., Schlische, R.W., Withjack, M.O., Ackermann, R.V., 2000. Influence of rift obliquity on fault-population systematics: results of experimental clay models. *Journal of Structural Geology*, 22: 1491-1509
- Connor, C.B., 1990. Cinder cone clustering in the TransMexican Volcanic Belt: Implications for Structural and Petrologic Models. *J. Geophys. Res.*, 95(B12): 19,395-19,405.

- Contreras, J., 2002. FBF: a software package for the construction of balanced cross-sections. *Computers & Geosciences*, 28: 961-969.
- Copley, J.H., Orange, A.S., 1991. Final report: magnetotelluric survey. Los Azufres and Araro. CFE, México, Internal report, pp. 22.
- Corona-Chavez, P., 1999. El Basamento Litológico y Tectónico del Estado de Michoacán, in Corona-Chavez, P., Israde-Alcantará, I., eds., *Carta Geológica de Michoacán*. Univ. Mich. De San Nicolás de Hidalgo, México.
- Cowie, P., 1998. A healing-reloading feedback control on the growth rate of seismogenic faults. *J. Struct. Geol.*, 20(8): 1075-1087.
- Cowie, P.A., Gupta, S., Dawers, N.H., 2000. Implications of fault array evolution for synrift depocentre development: insights from a numerical fault growth model. *Basin Res.*, 12: 241-261.
- CRM, 1996. Carta magnética de campo total reducido al polo. Sheet Querétaro, F14-10.
- CRM, 1998. Carta magnética de campo total reducido al polo. Sheet Morelia, E14-1.
- Dawers, N.H., Anders, M.H., 1995. Displacement-length scaling and fault linkage. *J. Struct. Geol.*, 17(5): 607-614.
- De Cserna, Z., De La Fuente-Duch, M., Palacios-Nieto, M., Triay, L., Mitre-Salazar, L.M., Mota-Palomino, R., 1988. Estructura Geológica, Gravimetría, Sismicidad y Relaciones Neotectónicas Regionales de La Cuenca de México. *Boletín del Instituto de Geología, UNAM, México*, 104: 1-71.
- De la Fuente-Duch, M., Aiken, C.L.V., Mena-J., M., 1994a. Cartas Gravimétricas de la República Mexicana. I Carta de Anomalía de Bouguer. Escala 1:3000000. Instituto de Geofísica, UNAM, Mexico.
- De la Fuente-Duch, M., Aiken, C.L.V., Mena-J., M., 1994b. Cartas Gravimétricas de la República Mexicana. III Carta de Anomalía Residual Isostática. Escala 1:3000000. Instituto de Geofísica, UNAM, Mexico.
- Demant, A., 1978. Características del Eje Neovolcánico Transmexicano y sus problemas de interpretación. *UNAM, Inst. Geol. Revista*, 2(2): 172-187.
- Demant, A., Mauvois, R., Silva, M.L., 1975. Estudio geológico de las hojas Morelia y Maravatío (1/100000), estado de Michoacán. Reporte de la Universidad Nacional Autónoma de México, 40 pp.
- Dobson, P.F., 1984. Volcanic stratigraphy and geochemistry of Los Azufres geothermal center, Mexico. M.S. Thesis, Stanford University, pp. 58.
- Dobson, P.F., Mahood, G.A., 1985. Volcanic stratigraphy and geochemistry of Los Azufres geothermal area, Mexico. *J. Volc. And Geothermal Res.*, 25: 273-287.
- Ego, F., Ansan, V., 2002. Why is the Central Trans-Mexican Volcanic Belt (102°–99°W) in transtensive deformation? *Tectonophysics*, 359: 189– 208.
- Ferrari, L., 2000. Avances en el conocimiento de la Faja Volcánica Transmexicana durante la última década. *Boletín de la Soc. Geol. Mex.*, LIII: 84-92.
- Ferrari, L., 2004a. Slab detachment control on mafic volcanic pulse and mantle heterogeneity in central Mexico. *Geology*, 32 (1): 77–80.
- Ferrari, L., 2004b. Geologic evolution of the Trans-Mexican Volcanic Belt – Tectonic and petrogenetic implications. Penrose Conference on Neogene-Quaternary Continental Margin Volcanism, Metepec, Mexico, (Abstract).
- Ferrari, L., Rosas-Elguera, J., 1999. Alcalic (ocean-island basalt type) and calc-alkalic volcanism in the Mexican volcanic belt: a case for plume-related magmatism and propagating rifting at an active margin?: *Comment. Geology*, 27: 1055.
- Ferrari, L., Pasquaré, G., Tibaldi, A., 1990. Plio-Quaternary tectonics of the central Mexican Volcanic Belt and some constraints on its rifting mode. *Geofísica Internacional*, 29(1): 5-18.
- Ferrari, L., Garduño, V.H., Pasquaré, G., Tibaldi, A., 1991. Geology of Los Azufres caldera, Mexico, and its relationships with regional tectonics. *Journal of Volcanology and Geothermal Research*, 47: 129-148.
- Ferrari, L., Garduño, V.H., Pasquaré, G., Tibaldi, A., 1994a. Volcanic and tectonic evolution of the central Mexico: Oligocene to Present. *Geofísica Internacional.*, 33(1): 91-105.
- Ferrari, L., Garduño, V.H., Innocenti, F., Manetti, P., Pasquaré, G., Vaggelli, G., 1994b. A widespread mafic volcanic unit at the base of the Mexican Volcanic Belt between Guadalajara and Querétaro. *Geofísica Internacional.*, 33(1): 107-123.
- Ferrari, L., López-Martínez, M., Aguirre-Díaz, G., Carrasco-Nuñez, G., 1999. Space-time patterns of Cenozoic arc volcanism in central Mexico: From the Sierra Madre Occidental to the Mexican Volcanic Belt. *Geology*, 27(4): 303-306.

- Ferrari, L., Petrone, C.M., Francalanchi, L., 2001. Generation of oceanic-island basalt-type volcanism in the western Trans-Mexican volcanic belt by slab rollback, asthenosphere infiltration and variable flux melting. *Geology*, 29(6): 507-510.
- Flores, T., 1920. Estudio geológico minero del distrito El Oro-Tlalpujahua: UNAM, Instituto de Geología, Boletín, 37, pp. 87
- Flores-Ruiz, J., 1997. Estructura cortical de la FVTM. PhD thesis, UNAM, México, D.F., Mexico
- Fries, C., Ross, C.S., Obregón-Pérez, A., 1965. Mezcla de vidrios en los derrames cineríticos Las Américas de la región de El Oro-Tlalpujahua, estados de México y Michoacán, parte centromeridional de México. UNAM, Instituto de Geología, Boletín, 70, pp. 85.
- Gapais, D., Cobbold, P.R., Bourgeois, O., Rouby, D., de Urreiztieta, M., 2000. Tectonic significance of fault-slip data. *Journal of Structural Geology*, 22: 881-888.
- García-Palomo, A., Macías, J.L., Garduño, V.H., 2000. Miocene to recent structural evolution of the Nevado de Toluca volcano region, Central Mexico. *Tectonophysics*, 318(1-4).
- García-Palomo, A., Macías V., J.L., Tolson, G., Valdez, R., Mora-Chaparro, J.C., 2002. Volcanic stratigraphy and geological evolution of the Apan region, east-central sector of the Trans-Mexican Volcanic Belt. *Geofísica Internacional*, 41(2): 133-150.
- Garduño-Monroy, V.H., 1988. La caldera de Los Azufres y su relación con el sistema regional E-W. *Geotermia, Rev. Mex. de Geoenergía*, 4(1): 49-61.
- Garduño, V.H., Gutierrez, A., 1992. Magmatismo, hiatus y tectonismo de la Sierra Madre Occidental y del Cinturón Volcánico Mexicano. *Geofísica Internacional*, 31: 417-429.
- Garduño-Monroy, V.H., Saucedo-Girón, R., Jiménez, Z., Gavilanes-Ruiz, J.C., Cortés-Cortés, A., Uribe-Cifuentes, R.M., 1998. La falla Tamazula – límite suroriental del bloque Jalisco y sus relaciones con el complejo volcánico de Colima, México. *Rev. Mex. de Ciencias Geol.*, 15(2): 132-144.
- Gomberg, J.S., Masters, T.G., 1988. Waveform modelling using locked-mode synthetic and differential seismograms: applications to determination of the structure of Mexico. *Geophysical Journal*, 94: 193-218.
- Gómez-Tuena, A., 2002. Control temporal del magmatismo de subducción en la porción oriental de la Faja Volcánica Trans-Mexicana: caracterización del manto, componentes en subducción y contaminación cortical. PhD thesis, UNAM, México D.F., Mexico, pp. 113.
- Gómez-Tuena, A., LaGatta, A.B., Langmuir, C.H., Goldstein, S.L., Ortega-Gutiérrez, F., Carrasco-Núñez, G., 2004. Temporal Control of Subduction Magmatism in the Eastern Trans-Mexican Volcanic Belt: Mantle Sources, Slab Contributions and Crustal Contamination. *Geochemistry, Geophysics, Geosystems*, in press.
- Gross, M.R., Gutiérrez-Alonso, G., Bai, T., Wacker, M.A., Collinsworth, K.B., Behl, R.J., 1997. Influence of mechanical stratigraphy and kinematics on fault scaling relations. *J. Struct. Geol.*, 19(2): 171-183.
- Gupta, A., Scholz, C.H., 2000. A model of normal fault interaction based on observations and theory. *Journal of Structural Geology* 22: 865-879.
- Gutscher, M.A., Malavieille, J., Lallemand, S., Collot, J.Y., 1999. Tectonic segmentation of the North Andean margin: impact of the Carnegie Ridge collision. *Earth and Planetary Science Letters* 168: 255-270.
- Guzman-Speziale, M., 2003. Geometric aspects of the subduction of the Cocos plate: implications for the orientation of the Trans-Mexican Volcanic Belt. *GSA Abstracts with programs*, 35(4): 32.
- Henry, C.D., Aranda-Gomez, J.J., 1992. The real southern Basin and Range: Mid- to late Cenozoic extension in Mexico. *Geology*, 20: 701-704.
- Henry, C.D., Aranda-Gomez, J.J., 2000. Plate interactions control middle-late Miocene, proto-Gulf and Basin and Range extension in the southern Basin and Range. *Tectonophysics*, 318: 1-26.
- Huizar-Álvarez, R., Campos-Enríquez, J.O., Lermo-Samaniego, J., Delgado-Rodríguez, O., Huidobro-González, A., 1997. Geophysical and hydrogeological characterization of the sub-basins of Apan and Tohac (Mexico Basin). *Geofísica Internacional*, 36: 217-233.
- Iglesias, A., Cruz-Atienza, V.M., Shapiro, N.M., Singh, S. K., Pacheco, J.F., 2001. Crustal structure of south-central Mexico estimated from the inversion of surface-wave dispersion curves using genetic and simulated annealing algorithms. *Geofis. Int.*, 40(3): 181-190.
- INEGI, 1998a. Carta topográfica, hoja Cuitzeo E14-A13. Instituto Nacional de Estadística, Geografía e Informática, Mexico.
- INEGI, 1998b. Carta topográfica, hoja Zinapécuaro E14-A14. Instituto Nacional de Estadística, Geografía e Informática, Mexico.
- INEGI, 1998c. Carta topográfica, hoja Maravatío E14-A15. Instituto Nacional de Estadística, Geografía e Informática, Mexico.

- INEGI, 1998d. Carta topográfica, hoja Morelia E14-A23. Instituto Nacional de Estadística, Geografía e Informática, Mexico.
- INEGI, 1999. Carta topográfica, hoja El Oro E14-A16. Instituto Nacional de Estadística, Geografía e Informática, Mexico.
- Irvin, B.J., Ventura, S.J., Slater, B.K., 1997. Fuzzy and isodata classification of landform elements from digital terrain data in Pleasant Valley, Wisconsin. *Geoderma*, 77: 137-154.
- Israde, I., 1995. Bacini lacustri del settore centrale dell'Arco Vulcanico Messicano: Stratigrafia ed evoluzione sedimentaria basata sulle diatomee. PhD Thesis, Università degli Studi di Milano, Italia, 254 p.
- Israde-Alcántara, I., Garduño-Monroy, V.H., 1999. Lacustrine record in a volcanic intra-arc setting: the evolution of the Late Neogene Cuitzeo basin system (central western Mexico, Michoacán). *Palaeogeography, Palaeoclimatology, Palaeoecology*, 151: 209-227.
- Jacobo-Albarrán, 1986. Estudio petrogenético de las rocas ígneas de la porción central del Eje Neovolcánico. Instituto Mexicano de Petróleo, Subdirección de Tecnología de Exploración. Open File Report, Proyecto C-2006, 47 pp.
- Jensen, J.R., 1996. *Introductory Digital Image Processing A Remote Sensing Perspective*. Prentice Hall, London, UK.
- Johansson, M., 1999. Analysis of digital elevation data for paleosurfaces in south-western Sweden. *Geomorphology*, 26: 279-295.
- Johnson, C.A., Harrison, C.G.A., 1989. Tectonics and Volcanism in Central Mexico: A Landsat Thematic Mapper Perspective. *Remote Sens. Environ.*, 28: 273-286.
- Johnson, C.A., Harrison C.G.A., 1990. Neotectonics in central Mexico. *Physics Of the Earth and Planetary Interiors*, 64: 187-210.
- Keller, E.A., Pinter, N., 1996. *Active Tectonics. Earthquakes, Uplift and Landscape*. Prentice Hall, Upper Saddle River, New Jersey, pp. 338.
- Klepeis, K.A., Clarke, G.L., Rushmer, T., 2003. Magma transport and coupling between deformation and magmatism in the continental lithosphere. *GSA Today*, 13(1): 4-11.
- Krantz, R.W., 1988. Multiple fault sets and three-dimensional strain: theory and application. *J. Struct. Geol.*, 10(3): 255-237.
- Langridge, R.M., Weldon, R.J., Moya, J.C., Suárez, G., 2000. Paleoseismology of the 1912 Acambay earthquake and the Acambay-Tixmadejé fault, Trans-Mexican Volcanic Belt. *J. Geophys. Res.*, 105(B2): 3019-3037.
- Márquez, A., De Ignacio, C., 2002. Mineralogical and geochemical constrains for the origin and evolution of magmas in Sierra Chichinautzin, Central Mexican Volcanic Belt. *Lithos*, 62: 35-62.
- Márquez, A., Oyarzun, R., Doblas, M., Verma, S.P., 1999a. Alcalic (ocean-island basalt type) and calc-alkalic volcanism in the Mexican volcanic belt: a case for plume-related magmatism and propagating rifting at an active margin? *Geology*, 27(1): 51-54.
- Márquez, A., Verma, S.P., Anguita, F., Oyarzun, R., Brandle, J.L., 1999b. Tectonics and volcanism of Sierra Chichinautzin: extension at the front of the Central Trans-Mexican Volcanic belt. *Journal of Volcanology and Geothermal Research*, 93: 125-150.
- Martínez-Reyes, A., Nieto-Samaniego, A. F., 1990. Efectos Geológicos de la Tectónica Reciente en la Parte Central de México. *Rev. del Inst. Geol. UNAM*, 1: 33-50.
- Menard, H.W., 1955. Deformation of the northeastern pacific basin and the west coast of North America. *Geol. Soc. Amer. Bull.*, 66: 1149-1198.
- Miller, D.J., Dunne, T., 1996. Topographic perturbations of regional stresses and consequent bedrock fracturing. *Journal of Geophysical Research*, 101 (B11): 25,523-25,536.
- Mills, H.H., 2003. Inferring erosional resistance of bedrock units in the east Tennessee mountains from digital elevation data. *Geomorphology*, 55 (1-4): 263-281.
- Molina-Garza, R., Urrutia-Fucugauchi, J., 1993. Deep crustal structure of central Mexico derived from interpretation of Bouguer gravity anomaly data. *J. Geodyn.*, 17: 181-201.
- Montgomery D.R., and López-Blanco, J., 2003. Post-Oligocene river incision, southern Sierra Madre Occidental, Mexico. *Geomorphology*, 55: 235-247.
- Mooser, F., 1969. The Mexican volcanic belt; structure and development. In: *Proceedings, Pan-American Symposium on the Upper Mantle, Group 2, Upper Mantle, Petrology and Tectonics, Volume 2*, UNAM, Instituto de Geofísica, México D.F., 15-22.
- Mooser, F., Meyer, A.H., McBirney, A.R., 1958. Catalogue of active volcanoes of the world; Part VI, Central America, Internal. *Volc. Assoc. Pte.*, 6: 36 p.



- Mooser, F., Montiel, A., Zúñiga, A., 1996. Nuevo mapageológico de las cuencas de México, Toluca y Puebla. Estratigrafía, tectónica regional y aspectos geotérmicos. Comisión Federal de Electricidad, Mexico.
- Morán-Zenteno, D.J., Corona-Chavez, P., Tolson, G., 1996. Uplift and subduction erosion in southwestern Mexico since Oligocene: pluton geobarometry constraints. *Earth and Planetary Science Letters*, 141: 51-65.
- Nicol, A., Watterson, J., Walsh, J.J., Childs, C., 1996. The shapes, major axis orientations and displacement patterns of fault surfaces. *J. Struct. Geol.*, 18(2-3): 235-248.
- Nieto-Samaniego, A.F., 1999. Stress, strain and fault patterns. *J. Struct. Geol.*, 21: 1065-1070.
- Nieto-Samaniego, A.F., Alaniz-Alvarez, S.A., 1997. Origin and tectonic interpretation of multiple fault patterns. *Tectonophysics*, 270: 197-206.
- Nixon, G.T., Demant, A., Armstrong, R.L., Harakal, J.E., 1987. K-Ar and geologic data bearing on the age and evolution of the trans-Mexican volcanic belt. *Geof. Int.*, 26: 109-158.
- Norato-Cortez, T.A., 1998. Estudio estratigráfico-volcanológico-estructural de los volcanes San Pedro y Altamirano (estados de México y Michoacán) y su relación con la evolución tectónica del sector central del Cinturón Volcánico Mexicano. Lic. Thesis, Fac. de Ciencias de la Tierra, Universidad Autónoma de Nuevo León, Mexico.
- Oguchi, T., Aoki, T., Matsuta, M., 2003. Identification of an active fault in the Japanese Alps from DEM-based hill shading. *Computers and Geosciences* 29, 885– 891.
- Orozco-Esquivel, M.T., Alaniz-Álvarez, S.A., Nieto-Samaniego, A.F., 2001. Vulcanismo y deformación durante la transición Sierra Madre Occidental – Faja volcánica Transmexicana en el centro de México. *GEOS*, 21(3): 217.
- Ortega-Gutiérrez, F., Mitre-Salazar, L.M., Roldán-Quintana, J., Aranda, Gómez, J.J., Morán, Zenteno, D., Alaniz-Álvarez, S.A., Nieto-Samaniego, A.F., 1992. Carta geológica de la República Mexicana, escala 1:2,000,000. Instituto de Geología, UNAM, Mexico.
- Ortega-Gutierrez, F., Ruiz, J., Centeno-Garcia, E., 1995. Oaxaquia, a Proterozoic microcontinent accreted to North America during the late Paleozoic. *Geology*, 23(12): 1127-1130.
- Ortiz, M.A., Bocco, G., 1989. Análisis morfotectónico de las depresiones de Ixtlahuaca y Toluca, México. *Geof. Int.* 23(3): 507-530.
- Ortiz M.A., Zamorano J.J., Frausto O., Mendoza M.E., 1994. Evidencias de una ribera fluvial y lacustre en la cima de un pilar tectónico: Bloque Perales México. *Geografía y Desarrollo*, 11(11): 59-67.
- Pantoja-Alor, J., 1994. Formación Las Américas, Tlalpujahua, Michoacán, México – una reinterpretación de los datos petrográficos, petroquímicos, tectónicos y de los mecanismos de erupción. *Revista Mexicana de Ciencias Geológicas*, 11(2): 168-181.
- Pardo, M., Suárez, G., 1995. Shape of the subducted Rivera and Cocos plates in southern Mexico: Seismic and tectonic implications. *Jour. Geophys. Res.* 100(B7): 12,357-12,373.
- Pasquaré G., Vezzoli L., Zanchi A., 1987a. Morphological and structural model of Mexican Volcanic Belt. *Geof., Int.* 26(2): 159-176.
- Pasquaré G., Ferrari L., Perazzoli V., Tiberi M., Turchetti F., 1987b. Morphological and structural analysis of the central sector of the Transmexican Volcanic Belt. *Geof. Int.*, 26(2): 177-193.
- Pasquaré, G., Garduño, V.H., Tibaldi, A., Ferrari, M., 1988. Stress pattern evolution in the central sector of the Mexican Volcanic Belt. *Tectonophysics*, 146: 353-364.
- Pasquaré, G., Ferrari, L., Garduño, V.H., Tibaldi, A., Vezzoli, L., 1991. Geologic map of the central sector of the Mexican Volcanic Belt, states of Guanajuato and Michoacan, Mexico. *Geol. Soc. of Amer. Map and Chart Series MCH072*.
- Pradal, E., 1990. La caldera de Los Azufres (Mexico): Contexte volcanologique d'un grand champ geothermique. PhD thesis, Univ. Clermond-Ferrand, pp. 250.
- Pradal, E., Robin, C., 1994. Long-lived magmatic phase at the Los Azufres volcanic center, Mexico. *J. Volc. and Geoth. Res.*, 63: 201-215.
- Prol, R.M., Juarez, G., 1985. Silica geotemperature mapping and thermal regime in the Mexican volcanic belt. *Geof., Int.*, 24(4): 609-621.
- Ramírez, S., Reyes, V., 1873. Informe sobre los temblores y volcanes de Aguafría y Jariepo. *Bol. Soc. Geogr. Mex.*, época 3(1): 67-88.
- Ramírez-Herrera, M.T., 1990. Análisis morfoestructural de la Faja Volcánica Trasmexicana (centro-oriente). Ms. Thesis. Facultad de Filosofía y Letras., UNAM, Mexico, pp. 86.
- Ramírez-Herrera, M.T., 1994. Tectonic Geomorphology of the Acambay Graben, Central Mexican Volcanic Belt. PhD Thesis. Univ. of Edinburgh, UK.

- Ramírez-Herrera, M.T., 1998. Geomorphic assessment of active tectonics in the Acambay graben, Mexican Volcanic Belt. *Earth Surf. Process. Landforms*, 23: 317-332.
- Ramírez-Herrera, M.T., Summerfield, M.A., Ortiz-Pérez, M.A., 1994. Tectonic geomorphology of the Acambay graben, Mexican Volcanic Belt. *Z. Geomorph. N. F.*, 38(2): 151-168.
- Ramsay, J.G., Huber, M.I., 1983. *The Techniques of Modern Structural Geology, Vol.1: Strain analysis.* Academic Press, London.
- Ramsay, J.G., Huber, M.I., 1987. *The Techniques of Modern Structural Geology, Vol.2: Folads and Fractures.* Academic Press, London.
- Reches, Z., 1978. Analysis of faulting in three-dimensional strain field. *Tectonophysics*, 47: 109-129.
- Reches, Z., 1983. Faulting of rocks in three-dimensional strain fields II. Theoretical analysis. *Tectonophysics*, 95: 133-156.
- Reches, Z., 1987. Determination of the tectonic stress tensor from slip along faults that obey the Coulomb yield condition. *Tectonics*, 6(6): 849-861.
- Reches, Z., Dieterich, J.H., 1983. Faulting of rocks in three-dimensional strain fields I. Failure of rocks in polyaxial, servo-control experiments. *Tectonophysics*, 95: 111-132.
- Reches, Z., Baer, G., Hatzor, Y., 1992. Constraints on the strength of the upper crust from stress inversion of fault slip data. *J. Geophys. Res.*, 97(B9): 12,481-12,493.
- Rivera-Hernandez, J., Ponce, L., 1986. Estructura de la corteza al oriente de la Sierra Madre Occidental, México, basada en la velocidad de grupo de las ondas de Rayleigh. *Geof. Int.*, 25(3): 383-402.
- Rosas-Elguera, J., Ferrari, L., Garduño-Monroy, V.H., Urrutia-Fucugauchi, J., 1996. Continental boundaries of the Jalisco block and their influence in the Pliocene-Quaternary kinematics of western Mexico. *Geology*, 24(10): 921-924.
- Sánchez-Rubio, G., 1984. Cenozoic volcanism in the Toluca-Amealco region, central Mexico. Ms. Thesis, Imperial College of Science and Technology, University of London, pp. 275.
- Schaaf, P., Martínez, R., Solís, G., Hernández, M.S., Morales, J., Hernández, T., Siebe, C., Carrasco, G., 2001. Los volcanes Popocatepetl, Nevado de Toluca y Pico de Orizaba: Datos isotópicos de Sr, Nd y Pb y modelos genéticos (abstract). *GEOS* 21: 234.
- Siebe, C., Rodríguez-Lara, V., Schaaf, P., Abrams, M., 2004. Geochemistry, Sr-Nd isotope composition, and tectonic setting of Holocene Pelado, Guespalapa and Chichinautzin scoria cones, south of Mexico City. *Journal of Volcanology and Geothermal Research*, 130: 197-226.
- Siebert, L., Carrasco-Núñez, G., 2002. Late-Pleistocene to precolumbian behind-the-arc mafic volcanism in the eastern Mexican Volcanic Belt; implications for future hazards. *Journal of Volcanology and Geothermal Research*, 115: 179-205.
- Silva-Mora, L., 1979. Contribution a la connaissance de l'Axe Volcanique Transmexicain: etude geologique et petrologie des laves du Michoacan Oriental. PhD thesis, Université de Droit, d'Economie et des Sciences d'Aix-Marseille III, France, pp. 243.
- Silva-Mora, L., 1995. Hoja Morelia, con resumen de la geología de la hoja Morelia, estados de Michoacán y Guanajuato. Inst. de Geología, UNAM, Carta Geológica de México, serie 14Q-g(2), scale 1:100000.
- Soler-Arechalde, A.M., 1997. Paleomagnetismo y Neotectónica de la Región Acambay-Morelia. Faja Volcánica Mexicana. PhD thesis, Inst. Geofísica, UNAM, México DF., Mexico.
- Soler-Arechalde, A.M., Urrutia-Fucugauchi, J., 2000. Paleomagnetism of the Acambay graben, central Trans-Mexican Volcanic Belt. *Tectonophysics*, 318: 235-248.
- Suter M., Contreras, J., 2002. Active tectonics of Northeastern Sonora, Mexico (Southern Basin and Range Province and the 3 May 1887 Mw 7.4 Earthquake. *Bull. Seism. Soc. Amer.*, 92(2): 581-589.
- Suter M., Quintero O., Johnson C.A., 1992. Active faults and state of stress in the central part of the Trans-Mexican Volcanic Belt, Mexico, I. The Venta de Bravo fault. *J. Geophys. Res.*, 97(B8): 11,983-11,993.
- Suter, M., Carrillo-Martínez, M., López-Martínez, M., Farrar, E., 1995a. The Aljibes half-graben – Active extension at the boundary between the trans-Mexican volcanic belt and the Basin and Range Province, Mexico. *GSA Bulletin*, 107(6): 627-641.
- Suter, M., Quintero-Legorreta, O., López-Martínez, M., Aguirre-Díaz, G., Farrar, E., 1995b. The Acambay graben: Active intraarc extensión in the trans-Mexican volcanic belt, Mexico. *Tectonics*, 14(5): 1245-1262.
- Suter, M., López-Martínez, M., Quintero-Legorreta, O., Carrillo-Martínez, M., 2001. Quaternary intra-arc extension in the central Trans-Mexican volcanic belt. *GSA Bull.*, 113(6): 693-703.
- Takada, A., 1994. The influence of regional stress and magmatic input on styles of monogenetic and polygenetic volcanism. *J. Geophys. Res.*, 99(B7): 13,563-13,573.

- Tibaldi, A., 1995. Photo interpretation of active faults in regions of complex topography: possible errors in correspondence of ridges. *ITC Journal*, 1995-2: 127-132.
- Tibaldi A., 1998. Effects of topography on surface fault geometry and kinematics: examples from the Alps, Italy and Tien Shan, Kazakstan. *Geomorphology*, 24: 225–243
- Tolson-Jones, G., 1998. Deformación, Exhumación y Neotectónica de la Margen Continental de Oaxaca: Datos Estructurales, Petrológicos y Geotermobarométricos. PhD thesis, UNAM, Mexico, 98 pp.
- Tolson, G., Alaniz-Alvarez, S. A., Nieto-Samaniego, 2001. ReActiva, a plotting program for calculate the potential of reactivation of preexisting planes of weakness: Instituto de Geología, Universidad Nacional Autónoma de México, shareware in:  
<http://geologia.igeolcu.unam.mx/Tolson/SoftWare/ReActivaV24Es.exe>.
- Twiss, R.J., Unruh, J.R., 1998. Analysis of fault slip inversions: do they contain stress or strain rate? *Journal of Geophysical Research*, 103: 12205-12222.
- Urbina, F., Camacho, H., 1913. La zona megasísmica Acambay-Tixmadejé, Estado de México, conmovida el 19 de noviembre de 1912. *Bol. Inst. Geol. Méx.*, 32, 125pp.
- Urquiza M., 1872. Informe del ingeniero encargado de reconocer la sierra de Ucareo para averiguar las probabilidades de una erupción volcánica. *Bol.Soc.Geogr. Mex. época* 2(4): 586-588.
- Urrutia-Fucugauchi, J., 1986. Crustal thickness, heat flow, arc magmatism, and tectonics of Mexico – Preliminary report. *Geofis. Int.*, 25(4): 559-573.
- Urrutia-Fucugauchi, J., Flores-Ruiz, J.H., 1996. Bouguer gravity anomaly and regional crustal structure in central Mexico: *Int. Geol. Review*, 38: 176-194.
- Valdés, C.M., Meyer, R.P., 1996. Seismic structure between the Pacific coast and Mexico City from the Petatlán earthquake ( $M_s=7.6$ ) aftershocks. *Geofis. Int.*, 35(4): 377-401.
- Valdéz-Moreno G., Aguirre-Díaz, G.J., López-Martínez, M., 1998. El volcán La Joya estados de Querétaro y Guanajuato: un estratovolcán miocénico del Cinturón Volcánico Mexicano. In: *Tectonic and magmatic evolution of Mexico during the Cenozoic*, Aguirre-Díaz G.J., ed. *Revista Mexicana de Ciencias Geológicas*, spec. issue., 15(2): 181-197
- Van Zuidam, R. 1979. *Terrain Analysis*. ITC, Enschede, The Netherlands.
- Verma, S.P., 1999. Geochemistry of evolved magmas and their relationship to subduction-unrelated mafic volcanism at the volcanic front of the central Mexican Volcanic Belt. *J. Volc. and Geoth. Res.*, 93: 151-171.
- Verma, S.P., 2000. Geochemistry of the subducting Cocos plate and the origin of subduction-unrelated mafic volcanism at the volcanic front of the central Mexican Volcanic Belt. *GSA Spec. Pap.*, 334: 195-222.
- Verma, S.P., 2002. Absence of Cocos plate subduction-related basic volcanism in southern Mexico: A unique case on Earth? *Geology*, 30(12): 1095–1098.
- Wallace, P.J., Carmichael, I.S.E., 1999. Quaternary volcanism near the Valley of Mexico: implications for subduction zone magmatism and the effects of crustal thickness variations on primitive magma compositions. *Contrib. Mineral. Petrol.*, 135: 291-314.
- Willemsse, E.J.M., Pollard, D.D., Aydin, A., 1996. Three-dimensional analyses of slip distributions on normal fault arrays with consequences for fault scaling. *J. Struct. Geol.*, 18(2-3): 295-309.
- Wojtal, S.F., 1996. Changes in fault displacement populations correlated to linkage between faults. *J. Struct. Geol.*, 18(2-3): 265-279.

## Appendix 1

### An exercise in combining and classifying morphometric maps: factor and principal component analysis, mean of normalized morphometric maps, continuous (fuzzy) classification

This study includes analysis of topography based on different morphometric maps of the same area, which were derived from the base DEM (sections 4.1 and 5.1.3). Such data set permits experimenting with techniques of multivariate analysis, including standard techniques used (except many other applications) for analyzing satellite multispectral images, and (rarely) DEM-derived morphometric maps. These techniques allow combining data from various maps in one image, finding sources of most and least variation, eliminate redundant (dependent) data, test if meaningful information can be obtained based on statistics alone (clustering), classify the terrain taking into account various maps, and more.

Below, I present a few results of such experiments. The direct motivation to try these analyses was the comparison of the morphometry between tectono-topographic domains. Namely, I wanted to see if these domains can also be distinguished automatically, and if I can produce images that would highlight them better than the individual morphometric maps. In these experiments I used unclassified elevation (DEM), relief and slope gradient maps, that is the same maps that highlight the tectono-topographic domains.

In the last section of this appendix, I mention the continuous classification of multivariate data sets, which, in my opinion, is an interesting proposal of automatic classification of the terrain, that takes into account that discrete classes does not really exist in nature.

This appendix is by no means a complete review of the treatment of multivariate data sets. Its sole objective is to present a few output images of multivariate statistical analysis applied to the morphometric maps of the study area, and compare them qualitatively.

#### *Factor and principal component analysis*

Factor and principal component analyses are multivariate statistical analysis techniques that permit to identify the factors (or driving principles) that control a data set composed of many variables. They are standard procedures used to reduce the number of data, (*e.g.*, bands in a satellite image) eliminating dependent variables, they help classify the data, and they allow to identify sources of the most and least variation. Factor analysis is based on a correlation matrix (standardized variance-covariance matrix) of the input variables, and principal component analysis is based on variance-covariance matrix of the input variables; the principal components are truly orthogonal (independent, uncorrelated). Use of variance-covariance matrix implies, that input variables (maps, bands, etc.) should have approximately Gaussian distribution (Irvin *et al.*, 1997). This is not the case at the study area, where lacustrine plains constitute *ca.* 25% of the region (relief and slope gradient map histograms resemble power-law, rather than normal, distribution) (Fig. 28). It follows, that any results based on these matrices [including correlation coefficients between morphometric maps (Tab. 1 in main text)] shall be viewed with caution.

Factor and principal component analysis were performed on the three input maps and color composites were constructed of the three output factors, and the three principal components. Therefore, the data reduction potential of these analyses was not exploited, but the possibility to combine the three maps, find sources of variation, and classify the area was.

The loadings (Tab. 5) show that the principal components are almost the same as the input maps, except that the relief map is inverted. It is surprising, given that relief and slope maps are strongly correlated (Tab. 1, main text), and the principal components are uncorrelated. Subsequently, the color composite made up of the three principal components (Fig. 29A) highlights the same features as the color composite made up of the three input maps, and is not more useful for distinction of tectono-topographic domains, than raw maps.

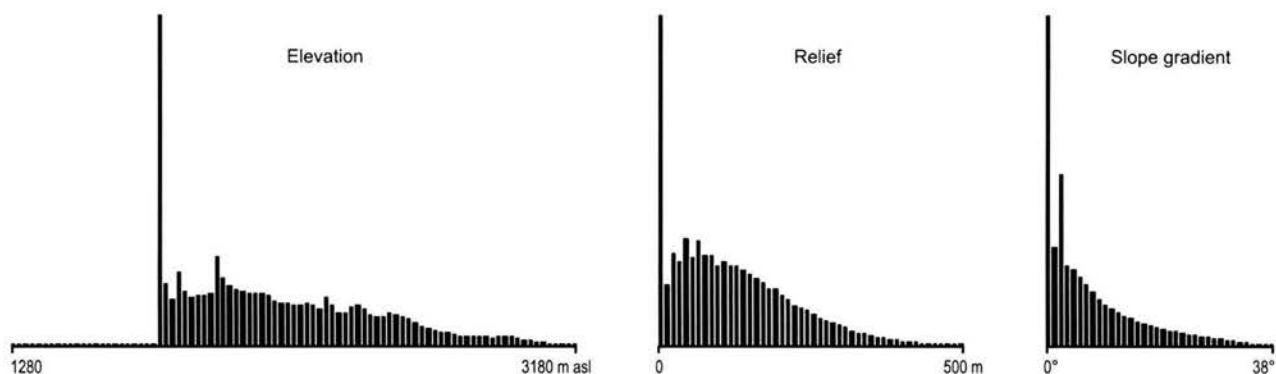


Figure 28. Distribution of elevation, relief and slope gradient values at the study area. Histogram bars represent 20-m intervals of elevation, 10-m intervals of relief, and 1° intervals of slope gradient. Height of histogram bars is proportional to the percent of area covered by the interval. Only intervals that cover more than 0.05% of the area are shown (hence shown value ranges are narrower than the real ranges).

Table 5. Transformation coefficients (loadings) between the three input morphometric maps and the principal components.

	Elevation	Relief	Slope gradient
First PC	0.991	0.131	0.009
Second PC	0.131	-0.989	-0.065
Third PC	0.000	-0.066	0.998

Variance percentages per band: 92.81 7.17 0.01

The color composite made up of the three calculated factors (Fig. 29B), to the contrary, highlights the tectono-topographic domains more clearly, than individual morphometric maps used to calculate them (compare Figs. 6, 8A, 29B, and Plate 1). The matrix containing transformation coefficients between the input maps and factors (Tab. 6) shows, that the first factor influences all input maps, second factor correlates inversely with elevation, and third factor influences relief and slope gradient maps.

Table 6. Transformation coefficients (loadings) between the three input morphometric maps and the factor maps.

	Elevation	Relief	Slope gradient
First factor	0.428	0.645	0.633
Second factor	-0.902	0.264	0.341
Third factor	-0.053	0.717	-0.695

Variance percentages per band: 70.21 25.12 4.67

The correlation matrix of the factor maps (Tab. 7) shows that the first factor correlates inversely with the second factor and the third factor is largely independent from the other two.

Table 7. Correlation coefficients between the factor maps

	First factor	Second factor	Third factor
First factor	1.00	-0.90	0.49
Second factor	-0.90	1.00	-0.06
Third factor	0.49	-0.06	1.00

Unsupervised classification (clustering) of the three factor maps did not produce any intuitively reasonable results (Fig. 30A shows division into 3 clusters). This may be due to the non-gaussian distributions of values of the factor maps (although the departure from normal distributions is less in case of factor maps, than in case of input morphometric maps).

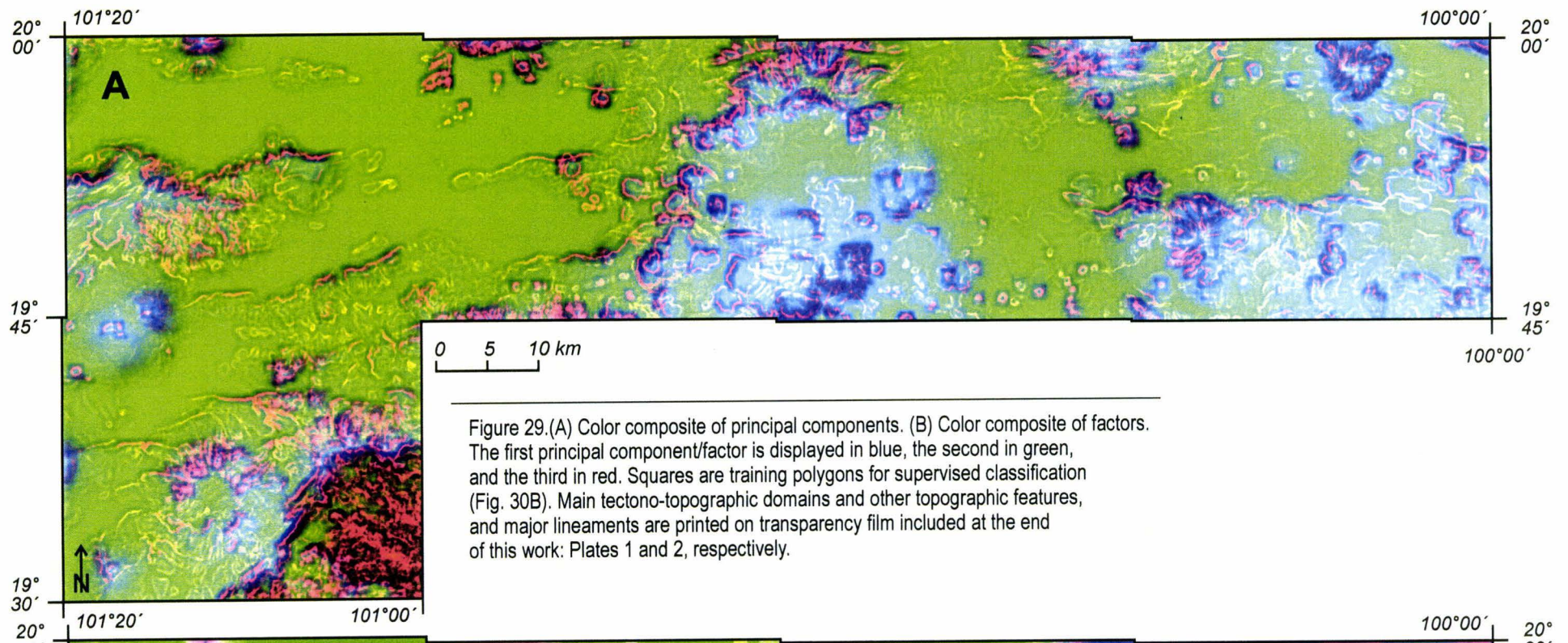
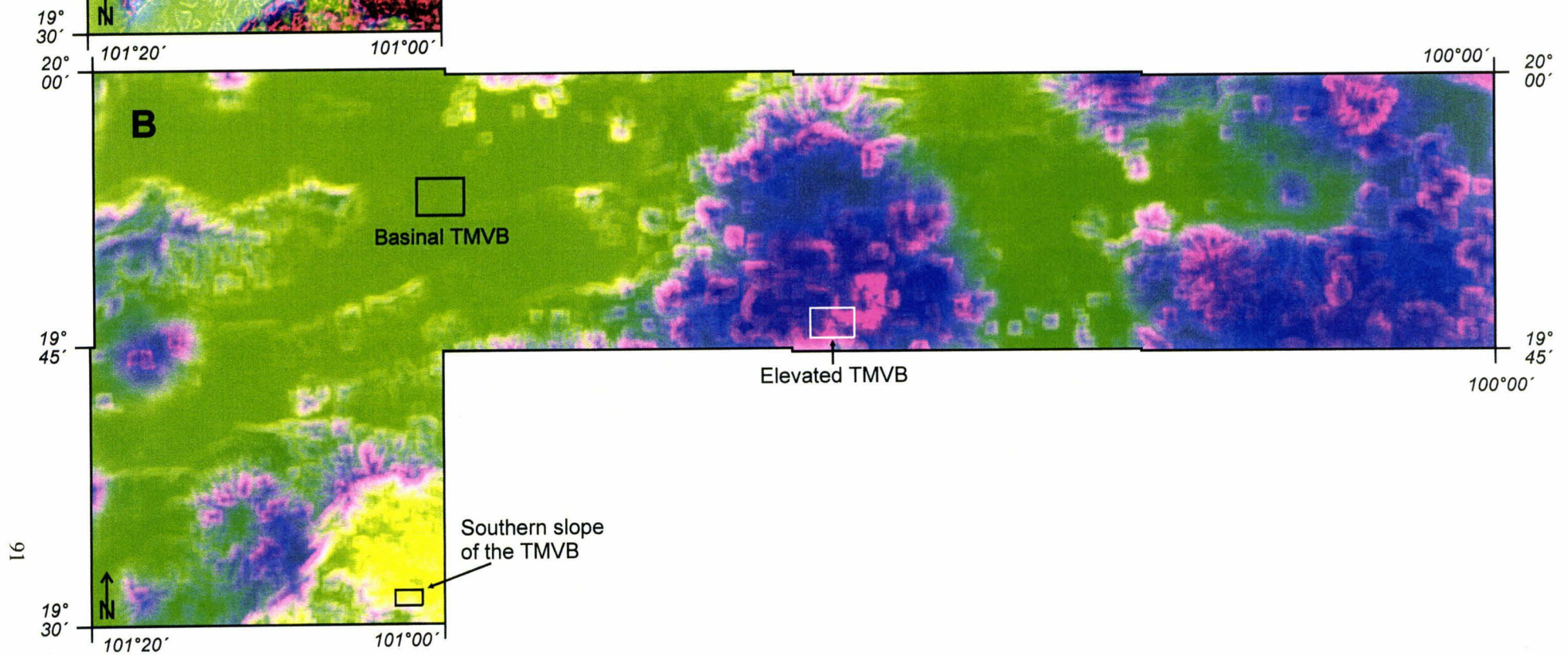


Figure 29.(A) Color composite of principal components. (B) Color composite of factors. The first principal component/factor is displayed in blue, the second in green, and the third in red. Squares are training polygons for supervised classification (Fig. 30B). Main tectono-topographic domains and other topographic features, and major lineaments are printed on transparency film included at the end of this work: Plates 1 and 2, respectively.



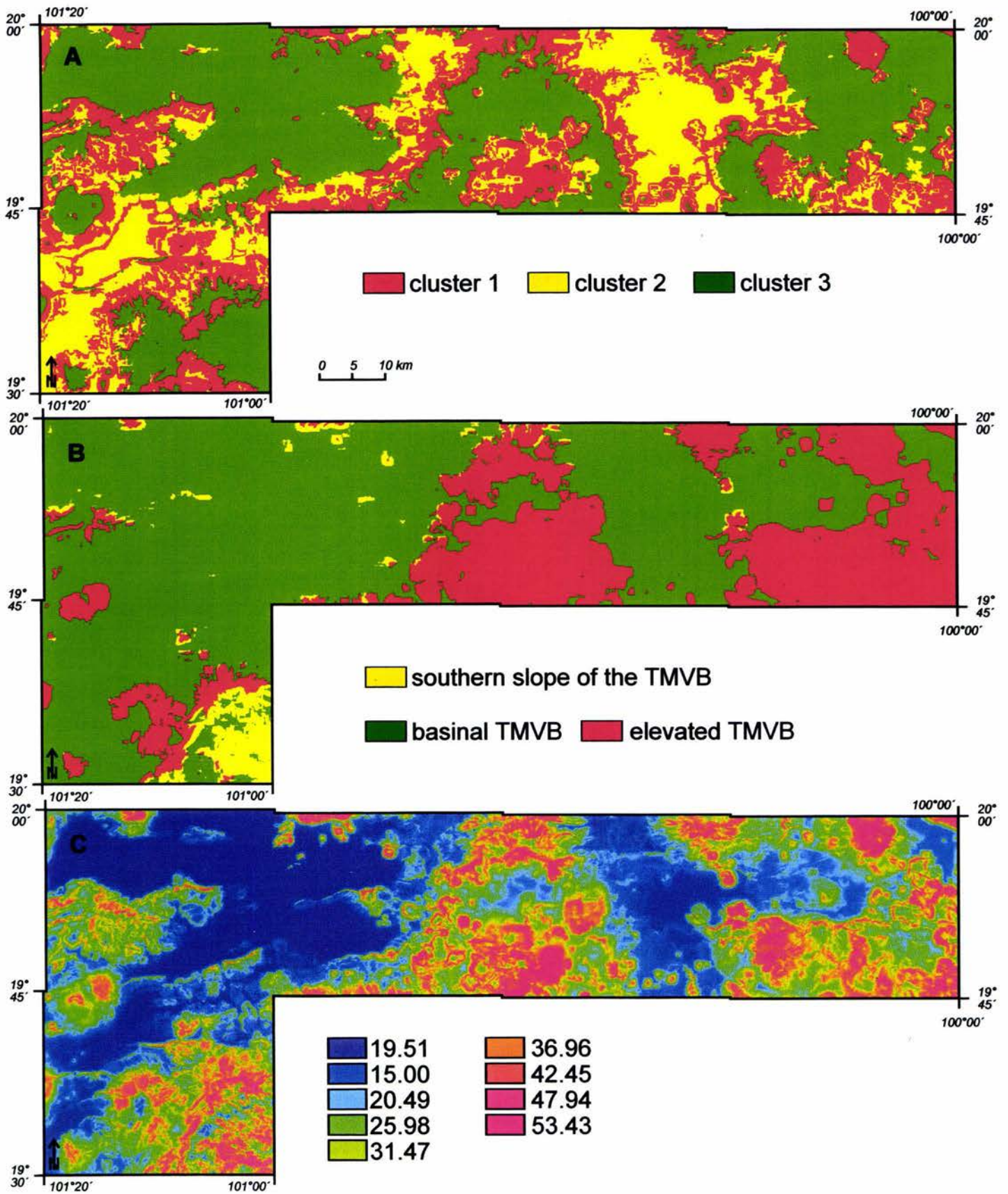


Figure 30.(A) Unsupervised classification (clustering) of the three factor maps. (B) Supervised classification of the three factor maps (see Fig. 29B for location of training polygons). (C) Means of the three normalized (to 0-100 value range) morphometric maps.

Supervised classification (minimum distance), where training polygons correspond to what was visually identified as typical values for the southern slope of the TMVB (Puerto la Sosa domain, Plate 1), basinal TMVB and elevated TMVB (Fig. 30B) makes evident the spatial distribution of the most abrupt morphometric changes at the region. Classified image also suggests transitional nature of the Venta de Bravo hangingwall domain (between basinal and elevated TMVB), and seems to reflect the degree to which the pre-existing topography, with mainly Basin and Range trends, has already been modified by the E-striking faults. *E.g.*, at the Maravatío depression this modification is less marked than at the Venta de Bravo domain (see Plate 1 for location of these domains).

Both unclassified color composite of the factors, and classified image suggest that the driving principle behind the topography of the study area are the three active fault systems, that condition the major tectono-topographic domains and subdomains.

### *Mean of normalized morphometric maps*

The last method used to combine the three morphometric maps, was normalization of the values of each of them to the 0-100 range, and then calculation of the mean of the three normalized values at each cell of the map. This procedure is similar to the calculation of the Erosional Resistance Index (ERI) of Mills (2003), except that the altitude map was used instead of regional relief, and the calculation of relief in this work is different from calculation of local relief map of Mills (2003).

Map of the mean of normalized morphometric maps (Fig. 30C) is apparently the least suitable to distinguish the topographic domains of the area. Particularly, the Puerto la Sosa domain, standing clearly out on all other maps, here is indistinguishable from, *e.g.*, most of the Los Azufres caldera.

### *Continuous (fuzzy) classification*

The reason behind fuzzy classification method of multivariate data sets is that in most natural cases the boundaries between different phenomena are transitional, so separating them into discrete classes is difficult and may be misleading, and moreover, in nature there is usually a considerable within-class heterogeneity (Jensen, 1996).

Fuzzy classification deals with this problem by assigning to each pixel of a map a percentage membership in each class (first step of analysis). The classes itself may be first designed by training polygons, or statistical procedures (clustering), where the latter may provide further insights into the data. After the first step the map can be classified into discrete classes. Nonetheless, such procedure also allows identification of pixels which have high membership in more than one class (so shall be regarded transitional), or pixels that have low membership in all classes.

Irvin *et al.* (1997) apply fuzzy classification to morphometric, DEM-derived data in a soil-landscape study of the Pleasant Valley, Wisconsin. Burrough *et al.* (2000) further develop this application, proposing methods for obtaining more meaningful (fuzzy as well) DEM-derivatives.



## Appendix 2

### Filters used for calculation of shaded relief images

Lighting from NW

-3	-2	-1
-2	1	2
-1	2	4

Lighting from N

-4	-4	-4
0	2	0
3	4	3

Lighting from NE

-1	-2	-3
2	1	-2
4	2	-1

Lighting from E

-1	-2	-3
2	1	-2
4	2	-1

Gain factor (the number the output is multiplied by) is 1 in all cases.

### Appendix 3

#### Calculation of depth to detachment

The calculation of depth to detachment at listric, normal fault is illustrated in Fig. 31. It is easy to see, that increase of fault throw results in the increase of the depth to detachment. Increase of strata dip (necessarily connected with increasing throw), and decrease of fault dip (necessarily connected with increasing throw, as displacement reaches lower, less inclined plane) both decrease detachment depth. These opposing mechanisms, make possible to maintain detachment at the same position during fault growth.

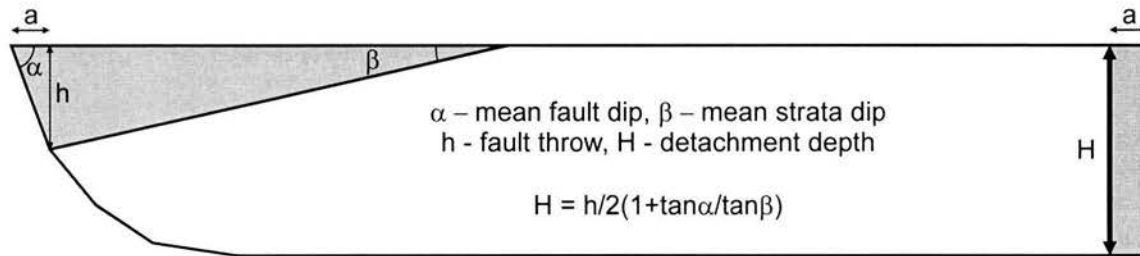


Figure 31. Graphic illustration of the calculation of detachment depth of a listric normal fault. Gray mark equal areas.

## Appendix 4

### Structural stations listing

Table 8. Structural stations sorted according to site number (numbers as in Fig. 18)

site No. (as in Fig. 18)	UTM coordinates Zone 14 (in meters)			No. of slip plane s	Contra ction axis orient.	Inter mediate axis orient.	Extensi on axis orient.	rock age (epoch)	rock age (Ma)	error	displaced lithology	Seq. symbol (as in Fig. 2)	age estimation source
	x	y	z										
1	260001	2191082	2182	10	225 6	133 19	334 70	M.3	7.81	xxx	andesite	g	Pasquaré <i>et al.</i> 1991
2	268000	2194500- 2196200	2020- 2180	6	16 6	152 81	291 7	M.3	7.81	xxx	andesite	g	Pasquaré <i>et al.</i> 1991
3	270500	2192500	1920	4	254 6	145 73	348 15	M.3	7.81	xxx	basalt/andesite	g	Pasquaré <i>et al.</i> 1991
4	294173	2211494	1946	8	84 67	229 19	324 14	O.-M.1	33.7-18.2	xxx	andesite	b	Pasquaré <i>et al.</i> 1991
5	274200	2191900	1885	5	190 15	91 30	312 53	M.3	7.81	xxx	andesite	g	Pasquaré <i>et al.</i> 1991
6	332900	2211500	2000	4	29 62	263 17	154 46	M.(2-3?)	16.4?-5.3?	xxx	andesite	e	Pasquaré <i>et al.</i> 1991, this work
7	333200- 333000	2207600- 2206900	2300- 2340	10	180 11	63 67	277 20	M.(2-3?)	16.4?-5.3?	xxx	andesite	e	Pasquaré <i>et al.</i> 1991
8	331450	2209660	2135	3	95 45	282 45	188 4	M.(2-3?)	16.4?-5.3?	xxx	andesite	e	Pasquaré <i>et al.</i> 1991, this work
9	271950	2187850	1860	16	207 2	298 9	61 75	M.3	7.81	0.6	andesite	g	Pasquaré <i>et al.</i> 1991
9a	271950	2187850	1860	2	202 57	78 20	339 25	M.3	7.81	0.6	andesite	g	Pasquaré <i>et al.</i> 1991
10	288300	2192200	1850	3	278 70	61 17	152 1	M.3	7.81	xxx	andesite	g	Pasquaré <i>et al.</i> 1991
11	354400- 359300	2184900- 2186500	2260- 2210	6	280 55	91 35	187 9	J.3-K.1	144-99	7.0-1.0	metasediments	a	Pasquaré <i>et al.</i> 1991
12	366300	2196000	2300	3	288 7	198 7	79 76	J.3-K.1	144-99	7.0-1.0	metasedimentary schist	a	Pasquaré <i>et al.</i> 1991
13	261000	2171900	2000	6	177 43	7 47	99 2	M.2	12	xxx	ignimbrite	f	M. Suter, pers. com.
14	265000	2172800	2020	4	353 3	97 80	254 10	M.2	12	xxx	ignimbrite	f	M. Suter, pers. com.
15	285700	2176800	2000	10	181 45	297 19	44 39	M.2	12	xxx	ignimbrite	f	M. Suter, pers. com.
16	317000	2202300	2200	4	2 73	116 7	208 16	M.(2- 3?)- Rec.?	16.4?-Rec.?	xxx	andesitic/basaltic volcanic breccia, and fault talus	e (and u?)	Pasquaré <i>et al.</i> 1991
17	354100	2185500	2280	4	314 55	77 21	171 10	M.2	18.2-11.2	xxx	andesite	c	Pasquaré <i>et al.</i> 1991
18	255627	2200267	1926	26	343 57	84 7	176 16	P.2	2.8	xxx	ignimbrite	j	Pasquaré <i>et al.</i> 1991
19	257300	2200700	1900	6	41 28	166 47	293 29	P.2	2.8	xxx	ignimbrite	j	Pasquaré <i>et al.</i> 1991
19a	257300	2200700	1900	11	318 75	80 8	172 13	P.2	2.8	xxx	ignimbrite	j	Pasquaré <i>et al.</i> 1991
20	270500	2200800	1840	9	102 4	12 7	228 81	P.2	2.8	xxx	ignimbrite	j	Pasquaré <i>et al.</i> 1991

Table 8 continuation. Structural stations sorted according to site number (numbers as in Fig. 18)

site No. (as in Fig. 18)	UTM coordinates Zone 14 (in meters)			No. of slip plane s	Contra ction axis orient.	Inter mediate axis orient.	Extensi on axis orient.	Rock age (epoch)	rock age (Ma)	error	displaced lithology	Seq. Symbol (as in Fig. 2)	age estimation source
20a	270500	2200800	1840	4	353 72	230 10	138 15	P.2	2.8	xxx	ignimbrite	j	Pasquaré <i>et al.</i> 1991
21	391500	2196000	2530	33	203 10	318 69	107 19	P.2-Pl.1	2.9-1.03	xxx	andesite	k	Pasquaré <i>et al.</i> 1991
21a	391500	2196000	2530	10	253 82	67 8	157 4	P.2-Pl.1	2.9-1.03	xxx	andesite	k	Pasquaré <i>et al.</i> 1991
22	271000	2186500	1910	7	306 62	52 8	145 24	P.2?	2.8?	xxx	pumice flow and fall	j?	Pasquaré <i>et al.</i> 1991
23	263000	2201800	1920	5	173 72	54 9	321 15	P.2	2.8	xxx	ignimbrite	j	Pasquaré <i>et al.</i> 1991
24	286500	2193200	1860	3	67 21	164 18	263 23	P.2	2.8	xxx	ignimbrite	j	Pasquaré <i>et al.</i> 1991
25	275000	2201200	1900	5	100 77	262 13	171 6	P.2	2.8	xxx	ignimbrite and ash flows	j	Pasquaré <i>et al.</i> 1991
26	363300	2196000	2160	4	268 51	80 39	172 03	P.2-Pl.1	2.9-1.03	xxx	andesite	k	Pasquaré <i>et al.</i> 1991
27	256070	2195609	2239	6	188 6	83 66	281 22	P.2	2.8	xxx	ignimbrite	j	Pasquaré <i>et al.</i> 1991
28	275050	2196200	1900	3	139 80	90 2	359 9	P.2	2.8	xxx	ignimbrite	j	Pasquaré <i>et al.</i> 1991
29	273500	2201000	1880	16	282 79	23 2	113 11	P.2-H.?	2.8-Rec.	xxx	ignimbrite and fault talus	j and u?	Pasquaré <i>et al.</i> 1991, this work
30	359300	2196333	2100	38	44 62	215 28	307 3	P.2-Pl.1	2.9-1.03	xxx	andesite/basalt	k	Pasquaré <i>et al.</i> 1991
31	292500	2200300	1839	3	125 85	270 4	0 2	Pl.2-H.	0.68-Rec.	xxx	volcanic ash (last phase of a scoria cone)	r	Pasquaré <i>et al.</i> 1991; Suter <i>et al.</i> , 2001
32	316900	2202400	2200	3	61 29	313 29	187 47	Pl.1 or 2	1.6-0.75 or 0.4-0.1		avalanche deposits (destruction of volcanic dome) (mainly andesite? clasts)	m or p	Demant, 1975; Pasquaré <i>et al.</i> 1991; Pradal and Robin, 1994
32a	316900	2202400	2200	3	95 58	329 20	228 27	Pl.1 or 2	1.6-0.75 or 0.4-0.1		avalanche deposits (destruction of volcanic dome) (mainly andesite? clasts)	m or p	Demant, 1975; Pasquaré <i>et al.</i> 1991; Pradal and Robin, 1994
33	343900	2205400	2095	6	171 28	262 3	358 61	Pl.1-H.	1.3-Rec.	xxx	fine-grained scoria and ash fall	n or r	Pasquaré <i>et al.</i> 1991, Suter <i>et al.</i> , 2001
34	350353	2202262	2085	6	197 59	356 29	86 0	Pl.1	1.3-0.83	xxx	andesite	n	Pasquaré <i>et al.</i> 1991, this work
35	375500	2205500	2320	7	123 22	343 62	226 14	Pl.2-H.	0.68-Rec.	Xxx	pumice flows and falls	r	Pasquaré <i>et al.</i> 1991, Suter <i>et al.</i> , 2001
36	393001	2200145	2503	31	187 73	24 17	291 08	Pl.	1.8-0.01	xxx	dacite?	L	Pasquaré <i>et al.</i> 1991
37	287400	2198200	1840	6	213 12	42 78	300 2	Pl.1	0.87-0.75	xxx	basalt	o	Pasquaré <i>et al.</i> , 1991; Pradal and Robin, 1994; Suter <i>et al.</i> , 2001; this work
38	307796	2201581	1840	21	191 10	60 76	282 11	Pl.1-H.	0.87-0.75 or 0.68-Rec.	xxx	volcanic ash (youngest portion of a cinder cone deposits)	o or r	Pasquaré <i>et al.</i> , 1991; Pradal and Robin, 1994; Suter <i>et al.</i> , 2001; this work

Table 8 continuation. Structural stations sorted according to site number (numbers as in Fig. 18)

site No. (as in Fig. 18)	UTM coordinates Zone 14 (in meters)			No. of slip plane s	Contra ction axis orient.	Inter mediate axis orient.	Extensi on axis orient.	rock age (epoch)	rock age (Ma)	error	displaced lithology	Seq. symbol (as in Fig. 2)	age estimation source
39	312737	2194084	2103	6	338 32	243 6	144 57	Pl.1	0.81-0.79	0.08-0.06	volcanic ash and scoria (last phase of a scoria cone)	o	Pradal and Robin, 1994; Suter <i>et al.</i> , 2001
40	342700	2202900	2100	3	100 82	249 7	339 4	Pl.2-H.	0.75-Rec.	xxx	reworked pumice, volcanic ash and lithics	u	this work
41	345500	2202000	2080	3	75 18	314 58	173 26	Pl.1-H.	1.3-Rec.	xxx	basalt, welded volcanic ash and surficial deposits	n (or r) and u	Pasquaré <i>et al.</i> 1991, this work
42	357000	2204400	2100	5	165 75	272 4	3 14	Pl.2-H.	0.75-Rec.	xxx	fluvial conglomerate made up of obsidian and rhyolite clasts	u (clasts from l)	Pasquaré <i>et al.</i> 1991, this work
43	387111	2204184	2460	5	164 72	273 6	6 26	Pl.2-H.	0.68-Rec.	xxx	scoria (cone)	r	Pasquaré <i>et al.</i> 1991, Suter <i>et al.</i> , 2001
44	323400	2187200	2760	3	337 65	71 2	162 25	Pl.1 or 2	1.6-0.75 or 0.4-0.1		pumice and ash fall containing rhyolite lithics	m or p	Pasquaré <i>et al.</i> 1991; Dobson and Mahood, 1985; Pradal and Robin, 1994
45	347600	2187100	2240	10	84 76	252 13	162 0	Pl.2	0.63	0.05	scoria (cone)	r	Suter <i>et al.</i> , 2001
46	369000	2200000	2200	5	11 56	126 16	224 25	Pl.2-H.	0.68-Rec.	xxx	basalt	r	Pasquaré <i>et al.</i> 1991, Suter <i>et al.</i> , 2001
47	393100	2198500	2410	7	191 22	26 67	284 5	H.	0.01-Rec.	xxx	soil (and volcanic ash)	u	this work
48	393085	2198354	2440	3	128 58	305 32	35 1	Pl.2-H.	0.75-Rec.	xxx	volcanic ash and surficial deposits (clasts from nearby El Oro domes)	u	this work
49	358500	2194000	2140	3	172 65	79 1	349 24	H.	0.01-Rec.	xxx	soil (and andesite)	u	this work
50	351300	2187600	2260	4	74 77	250 13	341 2	Pl.2-H.	0.68-Rec.	xxx	scoria (cone)	r	Pasquaré <i>et al.</i> 1991; Suter <i>et al.</i> , 2001
51	374500	2199300	2370	9	184 84	282 1	12 2	Pl.1	1.3-0.83	xxx	basalt	n	Pasquaré <i>et al.</i> 1991
52	392047	2195914	2494	5	56 4	311 77	153 13	Pl.2-H.	0.75-Rec.	xxx	fault talus	u	this work
52a	392047	2195914	2494	3	145 56	255 13	352 29	Pl.2-H.	0.75-Rec.	xxx	fault talus	u	this work

Table 9. Structural stations sorted according to displaced rock age.

site No. (as in Fig. 18)	UTM coordinates Zone 14 (in meters)			No. of slip plane s	Contra ction axis orient.	Inter mediate axis orient.	Extensi on axis orient.	rock age (epoch)	rock age (Ma)	error	displaced lithology	Seq. symbol (as in Fig. 2)	age estimation source
	x	y	z										
11	354400- 359300	2184900- 2186500	2260- 2210	6	280 55	91 35	187 9	J.3-K.1	144-99	7.0-1.0	metasediments	a	Pasquaré <i>et al.</i> 1991
12	366300	2196000	2300	3	288 7	198 7	79 76	J.3-K.1	144-99	7.0-1.0	metasedimentary schist	a	Pasquaré <i>et al.</i> 1991
4	294173	2211494	1946	8	84 67	229 19	324 14	O.-M.1	33.7-18.2	xxx	andesite	b	Pasquaré <i>et al.</i> 1991
17	354100	2185500	2280	4	314 55	77 21	171 10	M.2	18.2-11.2	xxx	andesite	c	Pasquaré <i>et al.</i> 1991
6	332900	2211500	2000	4	29 62	263 17	154 46	M.(2-3?)	16.4?-5.3?	xxx	andesite	e	Pasquaré <i>et al.</i> 1991, this work
7	333200- 333000	2207600- 2206900	2300- 2340	10	180 11	63 67	277 20	M.(2-3?)	16.4?-5.3?	xxx	andesite	e	Pasquaré <i>et al.</i> 1991
8	331450	2209660	2135	3	95 45	282 45	188 4	M.(2-3?)	16.4?-5.3?	xxx	andesite	e	Pasquaré <i>et al.</i> 1991, this work
16	317000	2202300	2200	4	2 73	116 7	208 16	M.(2- 3?)- Rec.?	16.4?-Rec.?	xxx	andesitic/basaltic volcanic breccia, and fault talus	e (and u?)	Pasquaré <i>et al.</i> 1991
13	261000	2171900	2000	6	177 43	7 47	99 2	M.2	12	xxx	ignimbrite	f	M. Suter, pers. com.
14	265000	2172800	2020	4	353 3	97 80	254 10	M.2	12	xxx	ignimbrite	f	M. Suter, pers. com.
15	285700	2176800	2000	10	181 45	297 19	44 39	M.2	12	xxx	ignimbrite	f	M. Suter, pers. com.
1	260001	2191082	2182	10	225 6	133 19	334 70	M.3	7.81	xxx	andesite	g	Pasquaré <i>et al.</i> 1991
2	268000	2194500- 2196200	2020- 2180	6	16 6	152 81	291 7	M.3	7.81	xxx	andesite	g	Pasquaré <i>et al.</i> 1991
3	270500	2192500	1920	4	254 6	145 73	348 15	M.3	7.81	xxx	basalt/andesite	g	Pasquaré <i>et al.</i> 1991
5	274200	2191900	1885	5	190 15	91 30	312 53	M.3	7.81	xxx	andesite	g	Pasquaré <i>et al.</i> 1991
9	271950	2187850	1860	16	207 2	298 9	61 75	M.3	7.81	0.6	andesite	g	Pasquaré <i>et al.</i> 1991
9a	271950	2187850	1860	2	202 57	78 20	339 25	M.3	7.81	0.6	andesite	g	Pasquaré <i>et al.</i> 1991
10	288300	2192200	1850	3	278 70	61 17	152 1	M.3	7.81	xxx	andesite	g	Pasquaré <i>et al.</i> 1991
21	391500	2196000	2530	33	203 10	318 69	107 19	P.2-Pl.1	2.9-1.03	xxx	andesite	k	Pasquaré <i>et al.</i> 1991
21a	391500	2196000	2530	10	253 82	67 8	157 4	P.2-Pl.1	2.9-1.03	xxx	andesite	k	Pasquaré <i>et al.</i> 1991
26	363300	2196000	2160	4	268 51	80 39	172 03	P.2-Pl.1	2.9-1.03	xxx	andesite	k	Pasquaré <i>et al.</i> 1991
30	359300	2196333	2100	38	44 62	215 28	307 3	P.2-Pl.1	2.9-1.03	xxx	andesite/basalt	k	Pasquaré <i>et al.</i> 1991
18	255627	2200267	1926	26	343 57	84 7	176 16	P.2	2.8	xxx	ignimbrite	j	Pasquaré <i>et al.</i> 1991
19	257300	2200700	1900	6	41 28	166 47	293 29	P.2	2.8	xxx	ignimbrite	j	Pasquaré <i>et al.</i> 1991
19a	257300	2200700	1900	11	318 75	80 8	172 13	P.2	2.8	xxx	ignimbrite	j	Pasquaré <i>et al.</i> 1991
20	270500	2200800	1840	9	102 4	12 7	228 81	P.2	2.8	xxx	ignimbrite	j	Pasquaré <i>et al.</i> 1991

Table 9 continuation. Structural stations sorted according to displaced rock age.

Site No. (as in Fig. 18)	UTM coordinates Zone 14 (in meters)			No. of slip plane s	Contra ction axis orient.	Inter mediate axis orient.	Extensi on axis orient.	Rock age (epoch)	rock age (Ma)	error	displaced lithology	Seq. Symbol (as in Fig. 2)	age estimation source
20a	270500	2200800	1840	4	353 72	230 10	138 15	P.2	2.8	xxx	ignimbrite	j	Pasquaré <i>et al.</i> 1991
22	271000	2186500	1910	7	306 62	52 8	145 24	P.2?	2.8?	xxx	pumice flow and fall	j?	Pasquaré <i>et al.</i> 1991
23	263000	2201800	1920	5	173 72	54 9	321 15	P.2	2.8	xxx	ignimbrite	j	Pasquaré <i>et al.</i> 1991
24	286500	2193200	1860	3	67 21	164 18	263 23	P.2	2.8	xxx	ignimbrite	j	Pasquaré <i>et al.</i> 1991
25	275000	2201200	1900	5	100 77	262 13	171 6	P.2	2.8	xxx	ignimbrite and ash flows	j	Pasquaré <i>et al.</i> 1991
27	256070	2195609	2239	6	188 6	83 66	281 22	P.2	2.8	xxx	ignimbrite	j	Pasquaré <i>et al.</i> 1991
28	275050	2196200	1900	3	139 80	90 2	359 9	P.2	2.8	xxx	ignimbrite	j	Pasquaré <i>et al.</i> 1991
29	273500	2201000	1880	16	282 79	23 2	113 11	P.2-H.?	2.8-Rec.	xxx	ignimbrite and fault talus	j and u?	Pasquaré <i>et al.</i> 1991, this work
36	393001	2200145	2503	31	187 73	24 17	291 08	Pl.	1.8-0.01	xxx	dacite?	L	Pasquaré <i>et al.</i> 1991
32	316900	2202400	2200	3	61 29	313 29	187 47	Pl.1 or 2	1.6-0.75 or 0.4-0.1		avalanche deposits (destruction of volcanic dome) (mainly andesite? clasts)	m or p	Demant, 1975; Pasquaré <i>et al.</i> 1991; Pradal and Robin, 1994
32a	316900	2202400	2200	3	95 58	329 20	228 27	Pl.1 or 2	1.6-0.75 or 0.4-0.1		avalanche deposits (destruction of volcanic dome) (mainly andesite? clasts)	m or p	Demant, 1975; Pasquaré <i>et al.</i> 1991; Pradal and Robin, 1994
44	323400	2187200	2760	3	337 65	71 2	162 25	Pl.1 or 2	1.6-0.75 or 0.4-0.1		pumice and ash fall containing rhyolite lithicks	m or p	Pasquaré <i>et al.</i> 1991; Dobson and Mahood, 1985; Pradal and Robin, 1994
34	350353	2202262	2085	6	197 59	356 29	86 0	Pl.1	1.3-0.83	xxx	andesite	n	Pasquaré <i>et al.</i> 1991, this work
51	374500	2199300	2370	9	184 84	282 1	12 2	Pl.1	1.3-0.83	xxx	basalt	n	Pasquaré <i>et al.</i> 1991
33	343900	2205400	2095	6	171 28	262 3	358 61	Pl.1-H.	1.3-Rec.	xxx	fine-grained scoria and ash fall	n or r	Pasquaré <i>et al.</i> 1991, Suter <i>et al.</i> , 2001
41	345500	2202000	2080	3	75 18	314 58	173 26	Pl.1-H.	1.3-Rec.	Xxx	basalt, welded volcanic ash and surficial deposits	n (or r) and u	Pasquaré <i>et al.</i> 1991, this work
37	287400	2198200	1840	6	213 12	42 78	300 2	Pl.1	0.87-0.75	xxx	basalt	o	Pasquaré <i>et al.</i> , 1991; Pradal and Robin, 1994; Suter <i>et al.</i> , 2001; this work
38	307796	2201581	1840	21	191 10	60 76	282 11	Pl.1-H.	0.87-0.75 or 0.68-Rec.	xxx	volcanic ash (youngest portion of a cinder cone deposits)	o or r	Pasquaré <i>et al.</i> , 1991; Pradal and Robin, 1994; Suter <i>et al.</i> , 2001; this work
39	312737	2194084	2103	6	338 32	243 6	144 57	Pl.1	0.81-0.79	0.08-0.06	volcanic ash and scoria (last phase of a scoria cone)	o	Pradal and Robin, 1994; Suter <i>et al.</i> , 2001

Table 9 continuation. Structural stations sorted according to displaced rock age.

site No. (as in Fig. 18)	UTM coordinates Zone 14 (in meters)		No. of slip plane s	Contra ction axis orient.	Inter mediate axis orient.	Extensi on axis orient.	rock age (epoch)	rock age (Ma)	error	displaced lithology	Seq. symbol (as in Fig. 2)	age estimation source	
40	342700	2202900	2100	3	100 82	249 7	339 4	Pl.2-H.	0.75-Rec.	xxx	reworked pumice, volcanic ash and lithics	u	this work
42	357000	2204400	2100	5	165 75	272 4	3 14	Pl.2-H.	0.75-Rec.	xxx	fluvial conglomerate made up of obsidian and rhyolite clasts	u (clasts from I)	Pasquaré <i>et al.</i> 1991, this work
48	393085	2198354	2440	3	128 58	305 32	35 1	Pl.2-H.	0.75-Rec.	xxx	volcanic ash and surficial deposits (clasts from nearby El Oro domes)	u	this work
52	392047	2195914	2494	5	56 4	311 77	153 13	Pl.2-H.	0.75-Rec.	xxx	fault talus	u	this work
52a	392047	2195914	2494	3	145 56	255 13	352 29	Pl.2-H.	0.75-Rec.	xxx	fault talus	u	this work
31	292500	2200300	1839	3	125 85	270 4	0 2	Pl.2-H.	0.68-Rec.	xxx	volcanic ash (last phase of a scoria cone)	r	Pasquaré <i>et al.</i> 1991; Suter <i>et al.</i> , 2001
35	375500	2205500	2320	7	123 22	343 62	226 14	Pl.2-H.	0.68-Rec.	xxx	pumice flows and falls	r	Pasquaré <i>et al.</i> 1991, Suter <i>et al.</i> , 2001
43	387111	2204184	2460	5	164 72	273 6	6 26	Pl.2-H.	0.68-Rec.	xxx	scoria (cone)	r	Pasquaré <i>et al.</i> 1991, Suter <i>et al.</i> , 2001
46	369000	2200000	2200	5	11 56	126 16	224 25	Pl.2-H.	0.68-Rec.	xxx	basalt	r	Pasquaré <i>et al.</i> 1991, Suter <i>et al.</i> , 2001
50	351300	2187600	2260	4	74 77	250 13	341 2	Pl.2-H.	0.68-Rec.	xxx	scoria (cone)	r	Pasquaré <i>et al.</i> 1991; Suter <i>et al.</i> , 2001
45	347600	2187100	2240	10	84 76	252 13	162 0	Pl.2	0.63	0.05	scoria (cone)	r	Suter <i>et al.</i> , 2001
47	393100	2198500	2410	7	191 22	26 67	284 5	H.	0.01-Rec.	xxx	soil (and volcanic ash)	u	this work
49	358500	2194000	2140	3	172 65	79 1	349 24	H.	0.01-Rec.	xxx	soil (and andesite)	u	this work



**Study area map**  
 showing the spatial arrangement of detailed geomorphologic maps.  
 Tectono-topographic domains and main faults are added for orientation

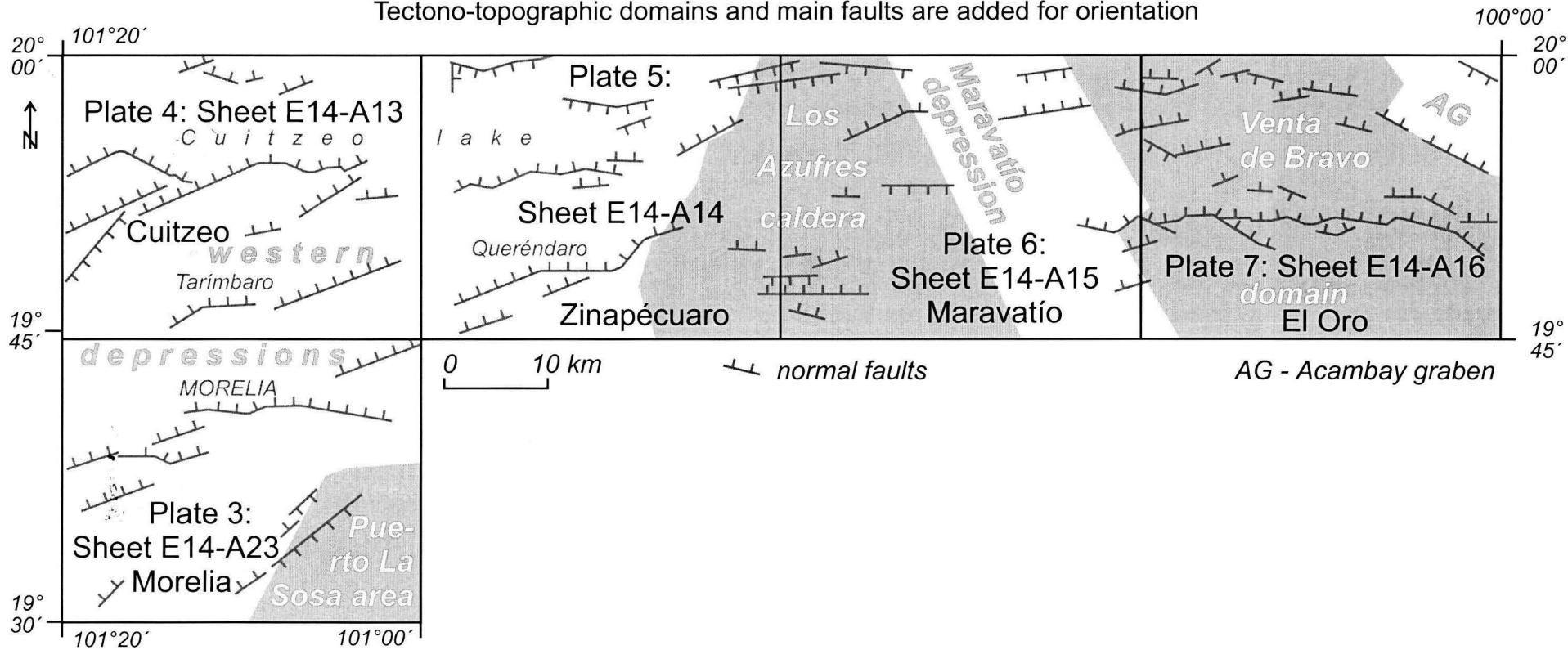


Plate 1. Location of the main topographic and geologic features of the study area.

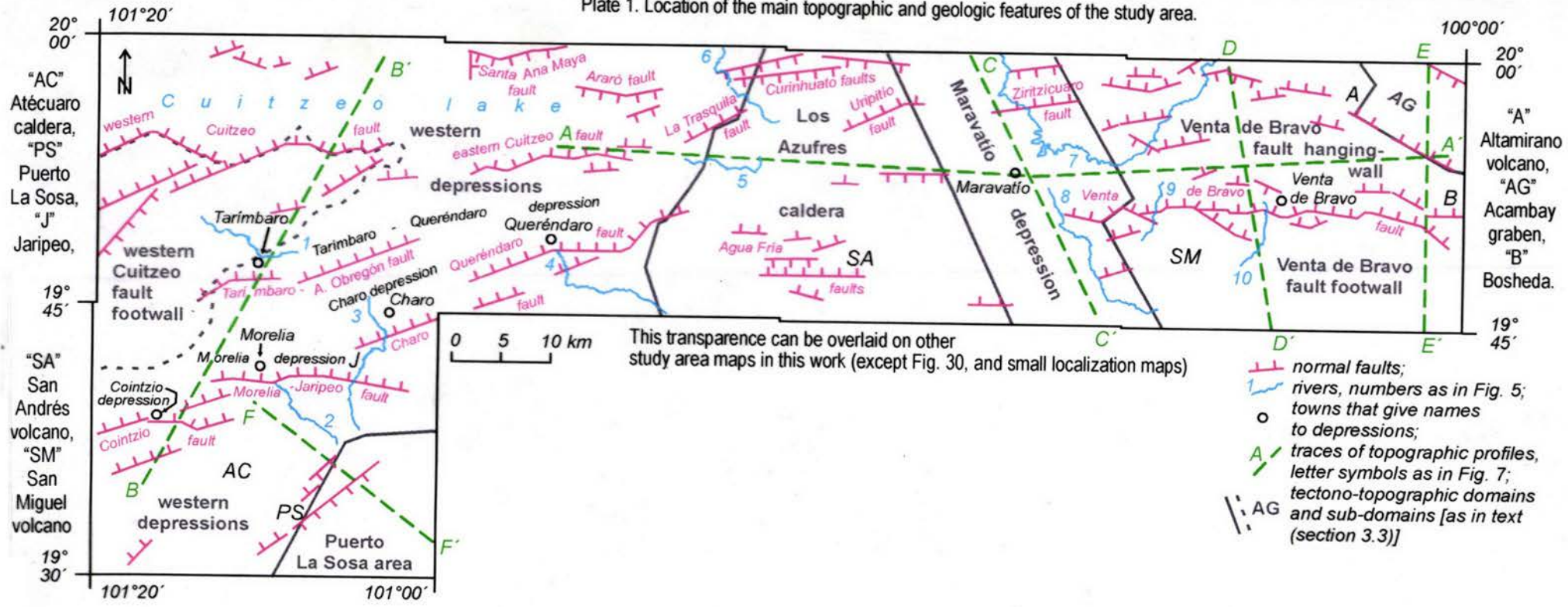


Plate 2. Major topographic lineaments.

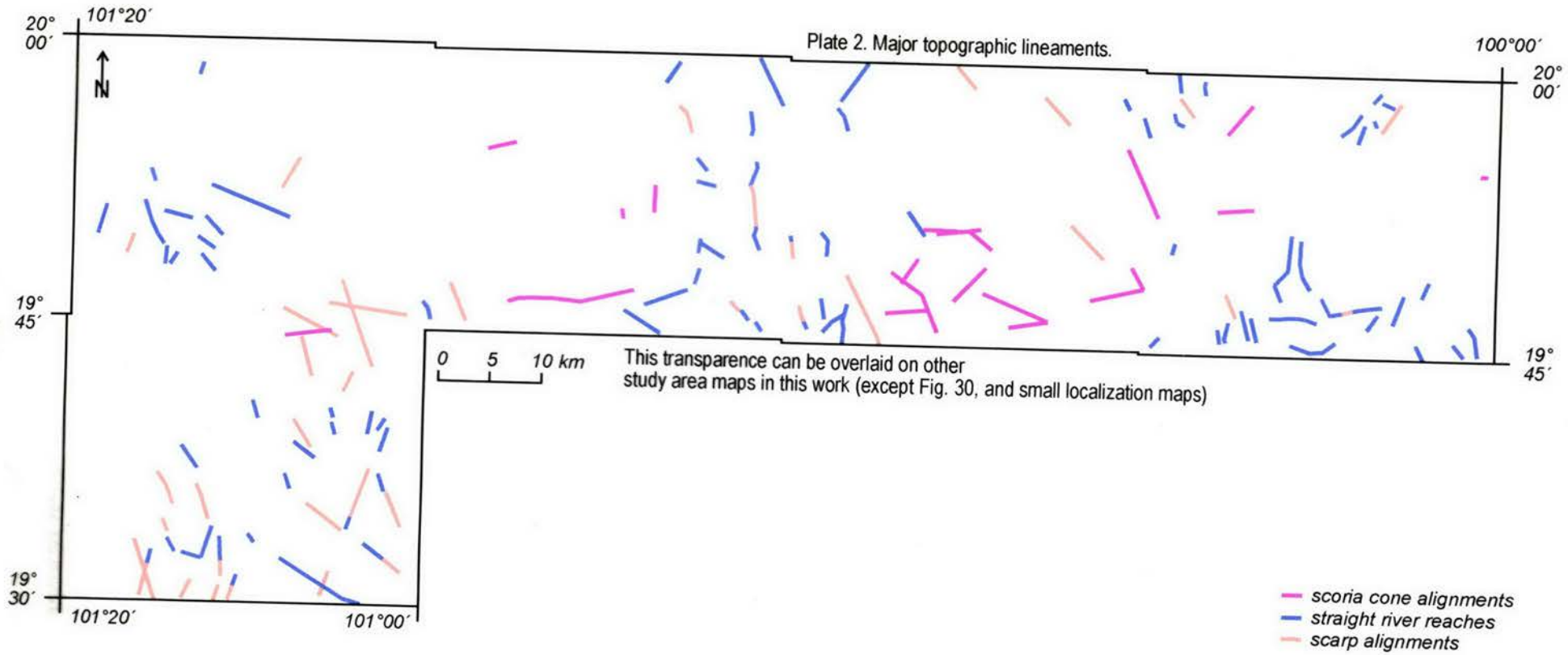
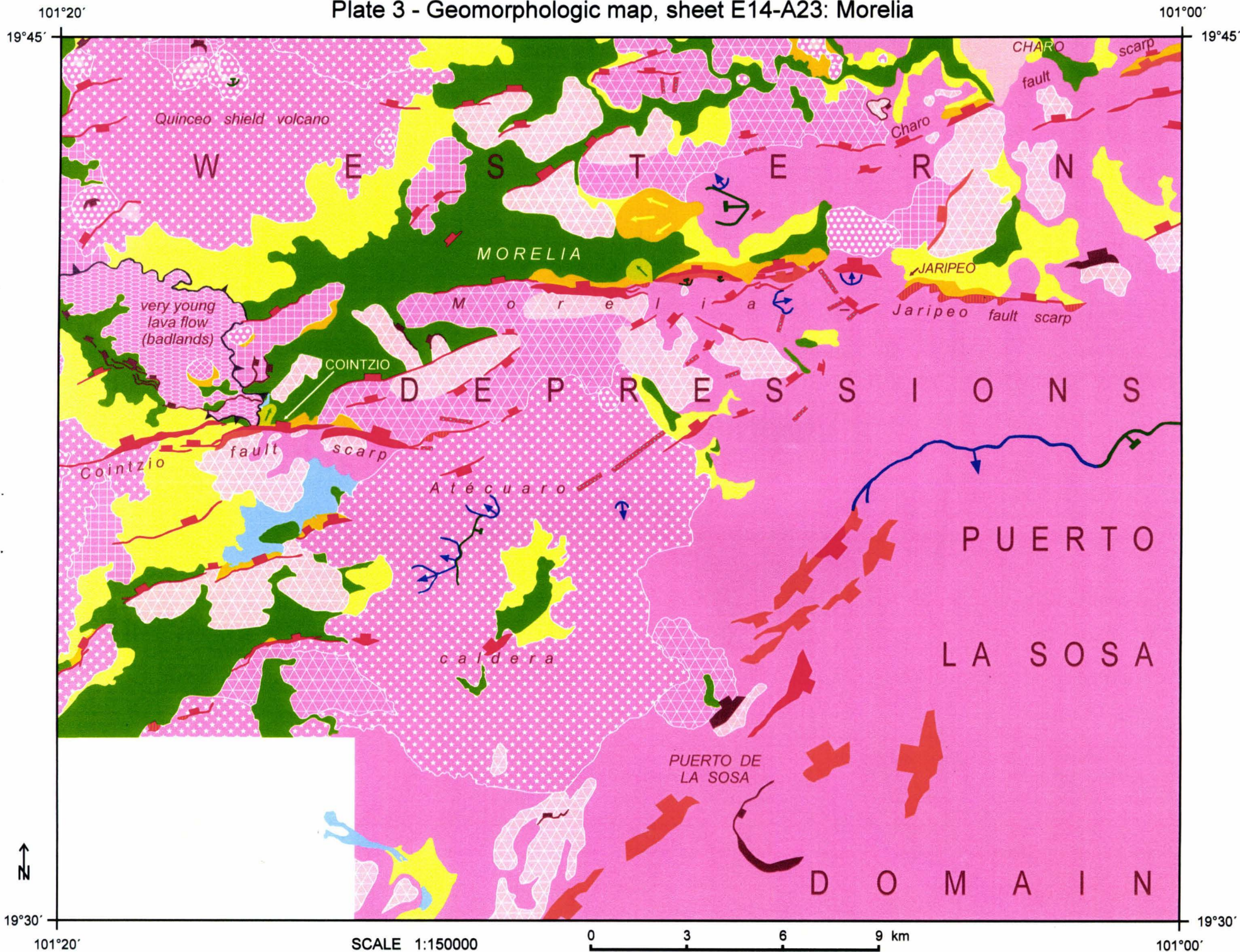


Plate 3 - Geomorphologic map, sheet E14-A23: Morelia



SCALE 1:150000



101°00'

Plate 4 - Geomorphologic map, sheet E14-A13: Cuitzeo

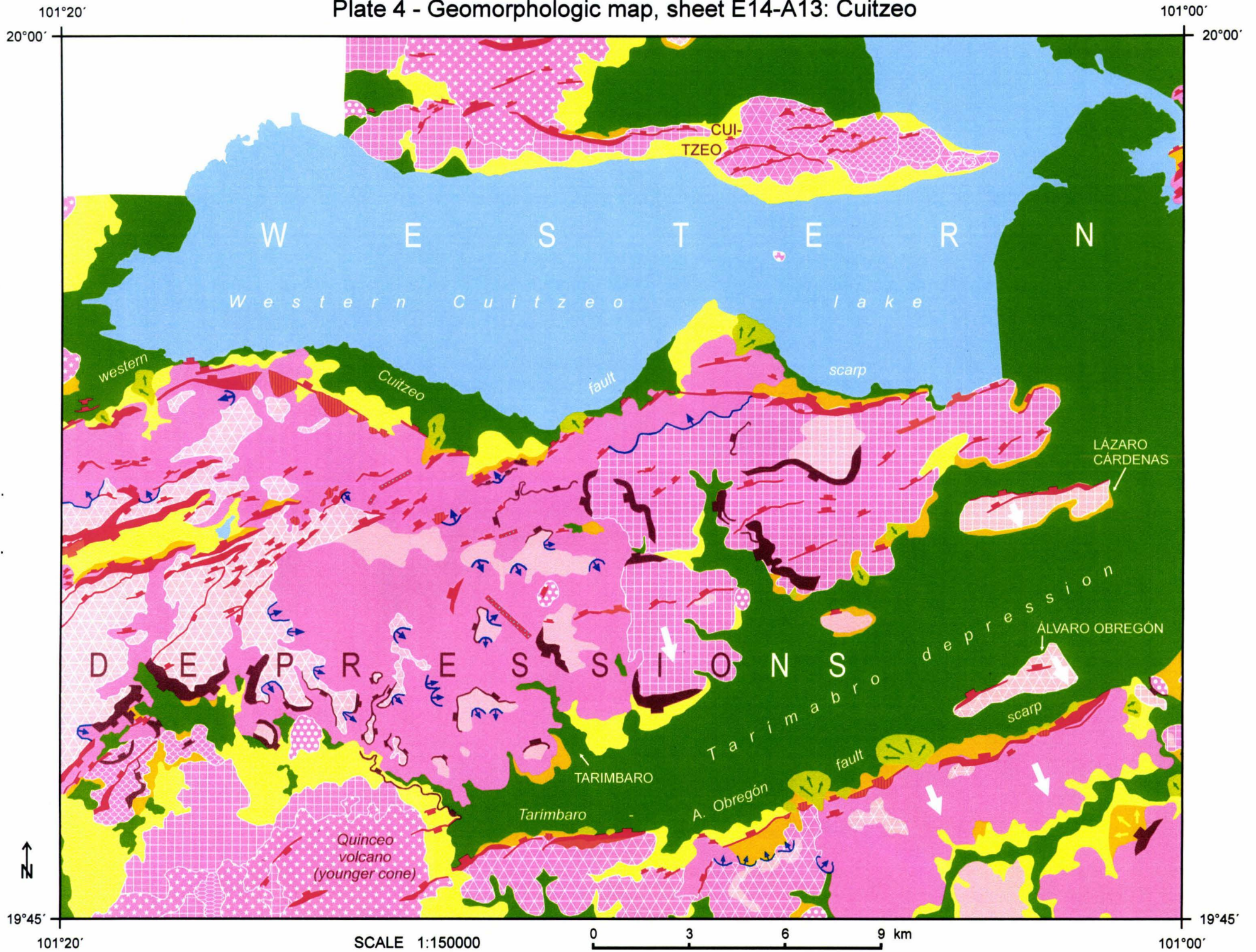


Plate 5 - Geomorphologic map, sheet E14-A14: Zinápecuaro

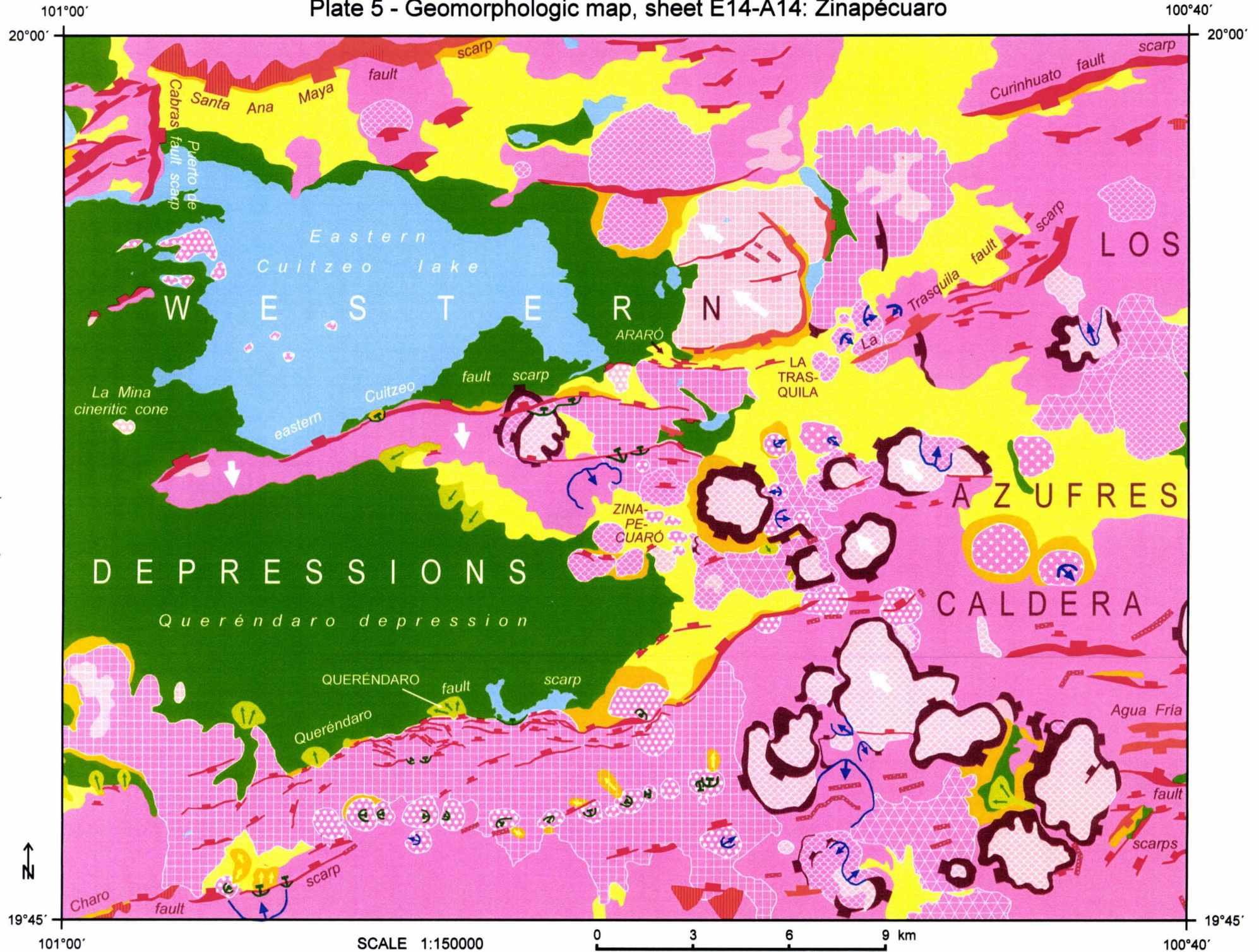
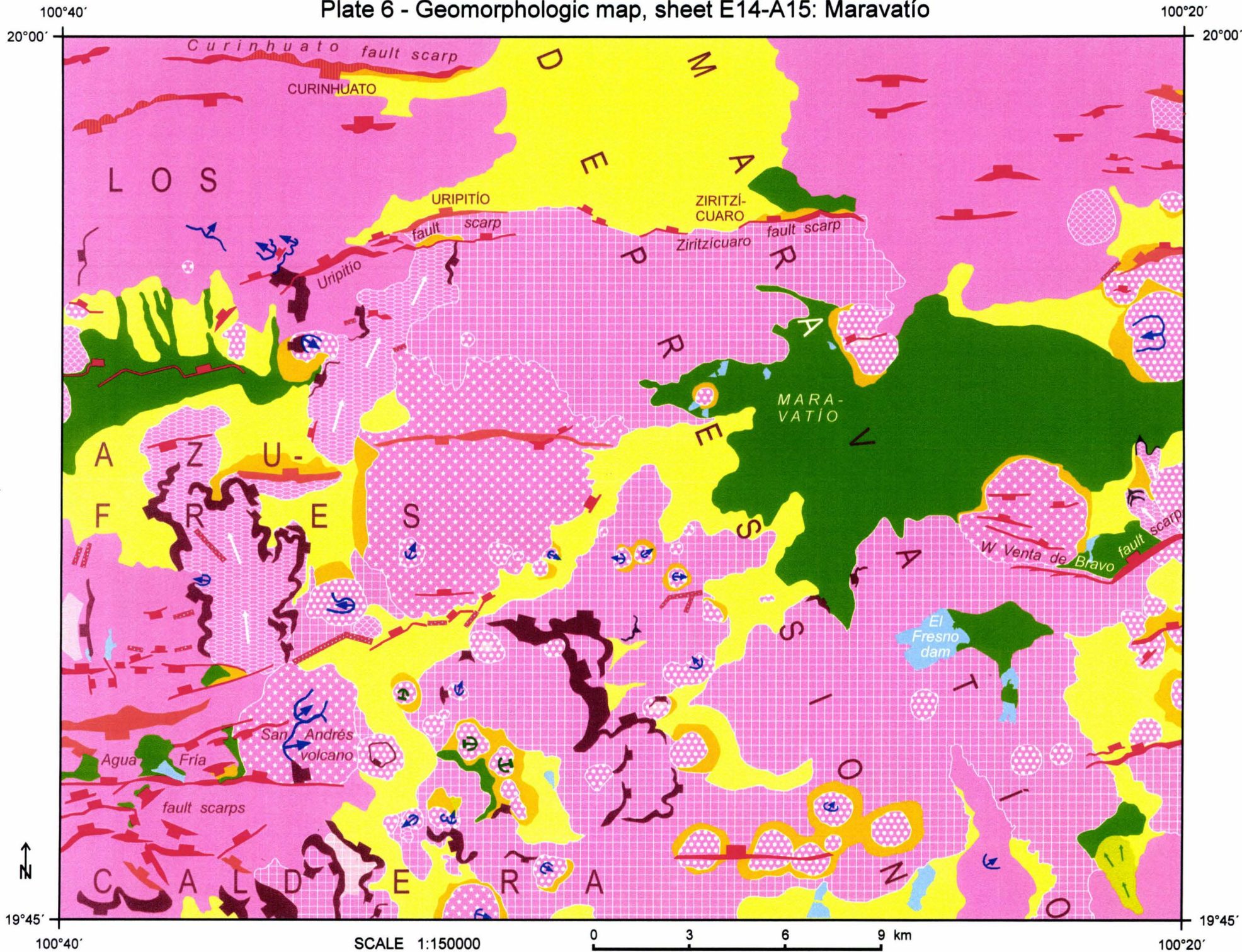


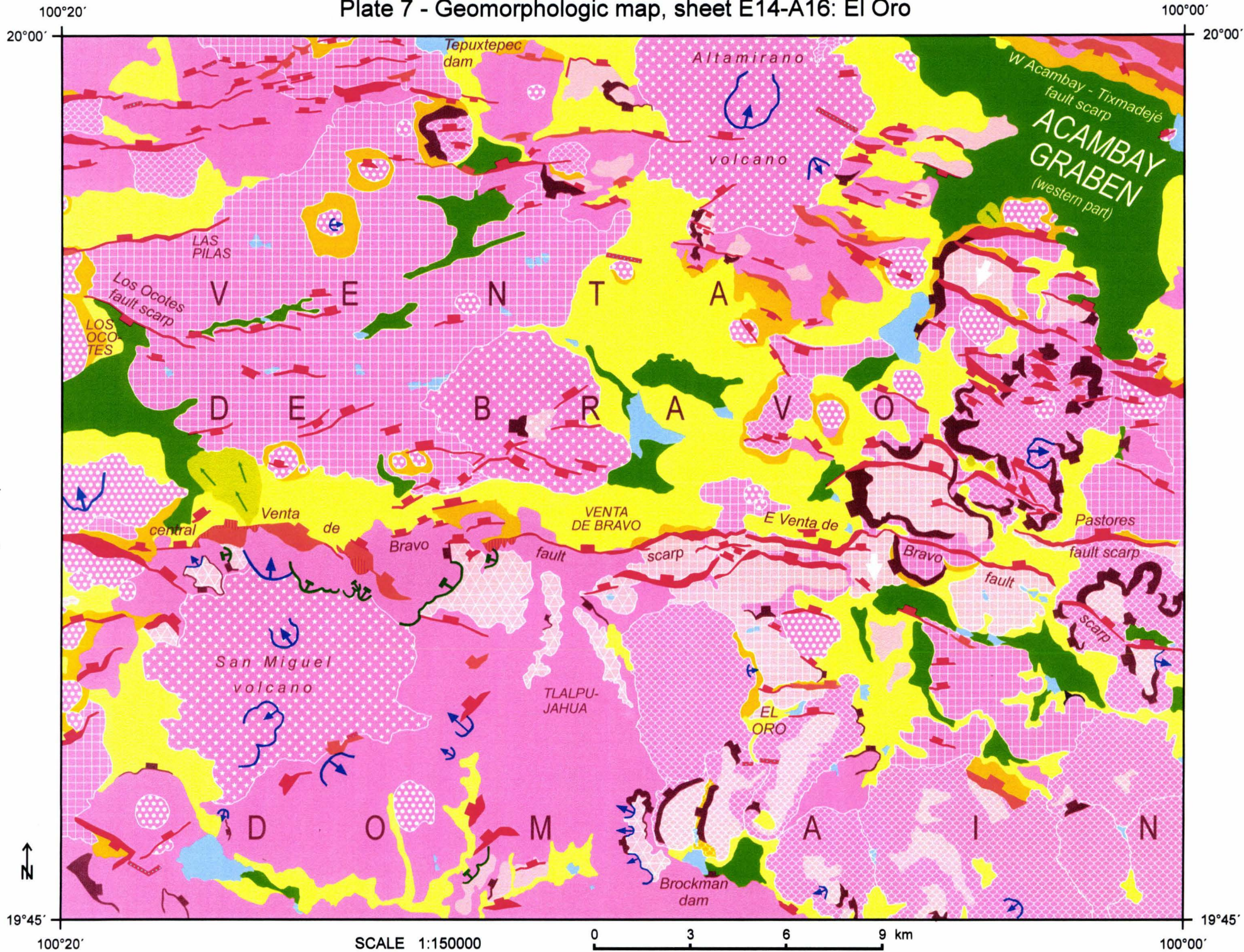
Plate 6 - Geomorphologic map, sheet E14-A15: Maravatío



SCALE 1:150000

0 3 6 9 km

Plate 7 - Geomorphologic map, sheet E14-A16: El Oro



SCALE 1:150000

0 3 6 9 km





# Plate 8 - Explanation of geomorphologic maps (Plates 3-7).

## SURFACE CLASSES




### weathering and erosion dominated:

-  summit surface
-  slope







### transitional:

-  talus or colluvial fan (arrow indicates sediment dispersion direction)
-  footslope










### deposition dominated:

-  aluvial or proluvial fan (arrow indicates sediment dispersion direction)
-  fluvio-lacustrine plain
-  water body

## VOLCANIC LANDFORMS

-  scoria cone
-  lava cone
-  lava dome
-  lava flow (arrow indicates flow direction)
-  lava plain
-  pyroclastic flow and fall deposits (Zinapécuaro map), or ignimbrite plain or mesa (other maps)

## LINEAR FEATURES

-  fault scarp (ticks point downslope)
-  rounded/lowered fault scarp (ticks point downslope)
-  triangular facet
-  entrenched stream reach
-  tilt of topographic surface
-  collapse scar (ticks points downslope)
-  erosion cirque (descriptive term, arrows point downslope)
-  lithologic scarp (ticks point downslope)
-  lava front (ticks point downslope)



features related to deformation

features that may be related to deformation

Features unrelated to deformation

Town names are given in UPPERCASE